Restoring forest resilience in the Sierra Nevada mixed-conifer zone, with a focus on measuring spatial patterns of trees using airborne lidar

Sean Medeiros Alexander Jeronimo

A dissertation

submitted in partial fulfillment of the

requirements for the degree of

Doctor of Philosophy

University of Washington

2018

Reading Committee:

Brian J. Harvey, Chair

Van R. Kane

James A. Lutz

Program Authorized to Offer Degree:

Environmental and Forest Sciences

University of Washington

Abstract

Restoring forest resilience in the Sierra Nevada mixed-conifer zone,

with a focus on measuring spatial patterns of trees using airborne lidar

Sean Medeiros Alexander Jeronimo

Chairs of the Supervisory Committee:
Professor Jerry F. Franklin
Research Assistant Professor Van R. Kane
School of Environmental and Forest Sciences

Forests across the western United States experienced profound changes throughout the 20th century in response to human resource use such as logging, grazing, and mining as well as very effective fire suppression, followed in some areas by fire reintroduction. In the Sierra Nevada of California, these changes include increases in forest density and fuel loads and a compositional shift away from fire tolerant tree species toward fire intolerant species. Many of the ecosystem functions and services that humans rely on in California, such as provision of water and habitat and fire resistance, have been degraded by this forest change. Forest restoration efforts are underway across the state and region, but the pace and scale of restoration lags behind what is necessary to change the course of regional trends. For example, federal forests in the Sierra Nevada currently average 40,163 ha of mechanical, prescribed fire, and wildland fire fuels

reduction annually compared to an estimated 223,000 ha annual rate required to keep up with fuels production. Airborne lidar technology may be able to help increase the pace of restoration by providing detailed measurements of forest structure across hundreds of thousands of contiguous hectares, augmenting and in some cases replacing data collected in ground-based surveys and allowing for more rapid assessment of range-wide forest conditions. In this dissertation I present three studies incorporating lidar data into different aspects of forest restoration. All studies use lidar individual tree detection as source data, in part to enable making measurements of tree spatial patterns in terms of tree clumps and canopy openings. This common focus exists because spatial patterns of trees influence fire and insect behavior, snow retention, tree regeneration, and other key ecosystem functions and services for which humans manage forests.

The nominal goal of forest restoration is often resilient forests. In this context resilience is defined as maintaining or quickly recovering characteristic ecosystem functions after disturbance at scales from forest stands to the Sierra Nevada ecoregion. Forest restoration is often guided by reference conditions describing characteristics of forest structure under resilient active-fire conditions, historical or contemporary. Since resilient forest structure varies depending on physiography, there is a need for a Sierra-wide reference condition dataset that is flexibly able to adapt to local environmental conditions. In Chapter 1 I sought to provide this dataset by asking these questions: (1) What is the geographic and environmental distribution of restored active-fire forest patches in the Sierra Nevada mixed-conifer zone? (2) What are the ranges of variation in structure and spatial patterns across restored patches? (3) How do density, tree clumping, and canopy opening patterns vary by topography and climate in restored patches? I analyzed fire history and environmental conditions over 10.8 million ha, including 3.9 million ha in the Sierra

Nevada mixed-conifer zone, and found that the 30,379 ha of restored patches were distributed throughout the range but were more abundant on National Park lands (81% of restored areas) than National Forest lands and were positively correlated with lightning strike density. Furthermore, 33% of restored areas were located in western Yosemite National Park and met our criteria for inclusion in this study only after being burned at low and moderate severity in the 2013 Rim Fire. Lidar-measured ranges of variation in reference condition structure were broad, with density ranging from 6-320 trees ha^{-1} (median 107 trees ha^{-1}), basal area from 2-113 m^2 ha^{-1} (median 21 m^2 ha^{-1}), average size of closely associated tree clumps from 1 to 207 trees (median 3.1 trees), and average percent of stand area >6 m from the nearest canopy ranging from 0% to 100% (median 5.1%). These ranges matched past studies reporting density and spatial patterns of contemporary and historical active-fire reference stands in the Sierra Nevada, except this study observed longer tails on distributions due to the spatial completeness of lidar sampling. Reference areas in middle-elevation climate zones had lower density (86 vs. 121 trees ha-1), basal area, (13.7 vs. 31 m2 ha-1), and mean clump size (2.7 vs. 4.0 trees) compared to lower- and higher-elevation classes, while ridgetops had lower density (101 vs. 115 trees ha-1), basal area (19.6 vs. 24.1 m2 ha-1), and mean clump size (3.0 vs. 3.3 trees) but more open space (7.4% vs. 5.1%) than other landforms.

In Chapter 2 I developed new methods for integrating lidar data into silvicultural planning at treatment unit and project area scales, with a focus on dry forest restoration treatments. At the stand scale my objective was to delineate the decision space for prescription parameters like density, basal area, and spatial patterns given the soft constraints of reference conditions and the hard constraints of possible transitions given current structure. At the landscape scale my objective was to provide a framework for selecting from available treatment options, stand by

stand, to meet different landscape-level goals. I applied the new methods to a case study area in the Lake Tahoe Basin, California and asked in this context: How do structural departures from reference conditions and associated treatment prescriptions vary with topographic position and aspect? I found that ridges and southwest-facing slopes in the study area had a greater degree of departure from the reference envelope and required more density reduction compared to valleys and northeast-facing slopes.

Reducing the risk of fire mortality is a common restoration goal, but modeling tools currently used for restoration planning do not incorporate spatially explicit stand structure and do not differentiate immediate fire effects from those which are delayed 2-4 years. This leaves silviculturists with the imperative to prescribe spatial patterns that reduce fire damage and mortality but few tools to identify exactly what structural conditions meet these goals. In Chapter 3 I used pre- and post-Rim Fire data from the 25.6 ha Yosemite Forest Dynamics Plot (YFPD) to build a model of tree mortality predicted from lidar individual tree detection structural metrics. I calculated metrics at the scale of lidar-detected trees (termed tree-approximate objects, TAOs), at the scale of 0.1 ha plots centered on each TAO, and at the 90×90 m neighborhood scale. I used these to predict TAO mortality at the neighborhood scale and TAO mortality class – immediate or delayed mortality – at the TAO scale. I also tested the inclusion of a set of topoedaphic and burn weather predictors as well as a cross-scale interaction term between the TAO mortality model and the neighborhood-level mortality model. I asked these questions: (1) How does mortality progress 1-4 years post-fire in terms of rates, demographics, and agents? (2) What elements of forest structure and pattern predict immediate and delayed post-fire mortality at scales from TAOs to neighborhoods? (3) How does the prevalence of different mortality agents vary with changes in the important fine-scale predictors of fire mortality? I found that smaller

trees were killed in the first year with a 40% mortality rate and the average diameter of killed trees increased each subsequent year while the mortality rate decreased. The topoedaphic and burn weather predictors as well as the cross-scale interaction improved model fit and parsimony, but that the improvement was directional, i.e., including neighborhood-level information improved the TAO-level model but not vice-versa. Important predictors fell into categories of fuel amount, fuel configuration, and burning conditions. Amounts of crown damage for immediately killed trees were higher for TAOs shorter than 51 m and in 0.1 ha areas where mean clump sizes was less than 21 TAOs. The amount of delayed mortality that was directly fire-related was higher when TAO crown base heights were less than 28 m and TAO density in 0.1 ha areas was greater than 170 TAOs ha^{-1}. Crown base heights over 18 m and local TAO density of less than 180 TAOs ha^{-1} had more beetle kill and less rot. The model performed similarly well on an independent validation dataset of 48 0.25 ha plots spanning the footprint of the Rim Fire within Yosemite as on the YFDP training data, indicating that the model is widely applicable.

Together, these studies advance the theory and practical tools available to pracitioners of forest restoration in the Sierra Nevada and represent an advance in the integration of lidar analysis with operational forest restoration. This work highlights the value of lidar in landscape analysis of forest ecosystems and provides direction for further integration of new technologies into forest management.

Table of Contents

List of Tables

List of Figures

Acknowledgements

I thank my parents, the late Peter McDonald, and Jerry Franklin for sparking my interest in the natural world, forestry, and forest science. I thank James Freund and Jim Lutz for encouraging me to pursue my interests, teaching me the skills I needed to know, and providing me with continued opportunities. Derek Churchill has been a key person in my academic and professional career as well as a valuable person in my life, and I thank him for that.

I thank Jerry Franklin and Van Kane, my committee chairs, for the excellent guidance I have received. I thank Van especially for his flexibility and his trust in me to get things done, eventually. I thank my other committee members – Brian Harvey, Monika Moskal, Jim Lutz, and Abby Swann – for their prompt and helpful feedback and positive pedagogical attitude.

I thank Bob McGaughey for his large and ongoing efforts to make lidar data more useful and usable for practical applications in forestry. Working and discussing the big ideas behind individual tree detection with Bob has been fun and productive and led to many of the concepts that are foundational to this work.

I thank many past and present Franklin lab members and some associated folks, particularly Miles LeFevre, Russell Kramer, Andrew Larson, Keala Hagmann, Luke Dow, Bob Van Pelt, Linda Winter, and Alina Cansler, for engaging discussions and critical reviews.

I thank my RRAMS and PFC labmates, specifically Jonathan Kane, Tristan O'Mara, Bryce Bartl-Geller, and Hailey Wiggins, for good feedback along the way and for working with me to make the tools presented in this dissertation more operational and useful. Jonathan especially has provided a lot of help with various processing tasks and a lot of thoughtful feedback on methods.

I thank Kendall Becker, Jamie Lydersen, Brandon Collins, and Malcolm North for their insights and advice on criteria for identifying reference areas. I thank Derek Young for many

thoughtful discussions about water balance modeling. I thank Calvin Farris, Lauren Payne, Scott Conway, Malcolm North, Carlos Ramirez, and Hugh Safford for helpful feedback on the lidar silviculture tools. I thank Tucker Furniss, Dustin Mutch, Etta Crowley, Giulio DeFazio, Sara Germain, and Obi for a fun and productive field season that could not have gone better. Luke Dow, Caileigh Shoot, and hundreds of volunteers on the Yosemite Forest Dynamics Plot also contributed to field work for data used in this dissertation.

I thank Amanda Davis, Michelle Trudeau, and David Campbell for making it possible to be a student at the School of Environmental and Forest Sciences.

I thank Melissa Pingree for being an essential partner to me in finishing this big project.

Many thanks to Greg Asner of the Carnegie Institution for Science and Stanford University for sharing his lidar data for Sequoia and King's Canyon National Parks. Chapters 1 and 2 were supported by the USDA Forest Service Pacific Southwest Research Station through Joint Venture Agreement 14-JV-11272139-014 "Using LiDAR to Guide Restoration in Sierra Nevada Forests" and Challenge Cost Share Agreement 13-CS-11052007-055 "Using Light Detection and Ranging (LiDAR) to Guide Burned Landscape Recovery and Restoration in Sierra Nevada Forests," and by the USDA Forest Service Colville National Forest through Joint Venture Agreement 13-JV-11062104-031 "Northeast Washington Vision 2020 Monitoring Plan." Chapter 2 was additionally supported by the Pacific Northwest Cooperative Ecosystem Studies Unit through Task Agreement H8W07110001 "Using LiDAR to Guide Forest Restoration in the Crater Lake Panhandle." Chapter 3 was supported by the Joint Fire Science Program through Grant 16-1-04-02 "Using multi-scale spatial data to improve predictions of immediate and delayed post-fire mortality," and support for the Yosemite Forest Dynamics Plot, which was integral to Chapter 3, is provided by the Utah Agricultural Experiment Station (Project 1153).

Chapter 1: Structure and pattern vary by climate and landform across active-fire landscapes in the montane Sierra Nevada

1. Introduction

Restoration of forest resilience – the ability of a forest ecosystem to maintain or quickly recover functions of management concern after disturbance at scales from stands to ecoregions – is an important goal in contemporary forest management, especially in fire-prone forests of the western United States (North *et al.*, 2009; Churchill *et al.*, 2013; Hessburg *et al.*, 2013; DeRose and Long, 2014; Hessburg *et al.*, 2015; Seidl *et al.*, 2015; Johnstone *et al.*, 2016; Stephens *et al.*, 2016). Restoration planning differs from traditional timber management planning in that the basic goals of restoration are functional ecosystem outcomes rather than measurable commodity outputs (Franklin and Johnson, 2012; Franklin *et al.*, 2018). Reference conditions describing characteristics of ecosystems that portray or embody desired functional outcomes are an invaluable tool in restoration planning, since they can provide a quantifiable link between structure, composition, and desired function (Churchill *et al.*, 2013). Reference conditions can serve as both waypoints that inform measurable restoration targets (Kaufmann *et al.*, 1998; Moore *et al.*, 1999) and benchmarks for evaluating restoration progress (Christensen *et al.*, 1996; Larson and Churchill, 2012). In either case, the purpose of reference conditions is to use a desirable ecosystem as an example for relating function to measurable aspects of structure and composition.

Reference conditions are often drawn from historical data, including recovered historical inventories (Leiburg, 1900; Langille, 1903; Munger, 1912; Collins *et al.*, 2011; Hagmann *et al.*, 2013; Lydersen *et al.*, 2013; Hagmann *et al.*, 2014) as well as reconstructed data (Fulé *et al.*,

1997; Hessburg *et al.*, 1999; Scholl and Taylor, 2010; Churchill *et al.*, 2013; Barth *et al.*, 2015; Churchill *et al.*, 2017; LeFevre *et al.*, in prep). Historical references represent conditions that existed before Euro-American settlement when linkages between process and pattern remained within the bounds of their evolutionary environment (Moore *et al.*, 1999; Hessburg *et al.*, 2005; Larson and Churchill, 2012). There are challenges associated with using historical reference conditions, however. Primary historical data suitable for defining reference conditions are not common and are often limited in spatial extent and data quality (Stephens *et al.*, 2015). Reconstructed data based on analysis of remnant structures (e.g., live trees, snags, and logs) can be quite uncertain for smaller trees, and the uncertainty increases as reconstructions reach farther back in time (Barth *et al.*, 2015). Due to the amount of labor involved, reconstruction studies are also limited in their spatial extent: they are able to characterize stand-level structure adequately but probably do not completely capture landscape-level variation (Hessburg *et al.*, 1999), an important aspect of restoration planning (Hessburg *et al.*, 2015). Because climates have been and are changing, historical reference data describe conditions under a climate different than today's (Millar and Woolfenden, 1999; Stephens *et al.*, 2010; Heyerdahl *et al.*, 2014; Hanberry *et al.*, 2015; Hart *et al.*, 2015; Johnstone *et al.*, 2016). This can be overcome to some extent using climate analog reference conditions, which give conditions for a site with historical climate similar to the contemporary or projected future climate of a departed site (Churchill *et al.*, 2013).

Reference conditions can also be drawn from contemporary forests in areas where resource extraction has been minimal and characteristic disturbance regimes have been maintained or reintroduced (Taylor, 2010; Collins *et al.*, 2016). In fire-prone forests of the western United States, fire is the primary process that structures forests (Brown *et al.*, 2004; Hessburg *et al.*, 2005), maintaining stands characterized by a fine-scale mosaic of tree clumps and canopy

46 openings that is resilient to fire and insect disturbances (Larson and Churchill, 2012; Churchill *et*
47 *al.*, 2013). Thus, contemporary reference conditions are usually drawn from areas where fire
48 regimes were not interrupted or where frequent lower-severity fire regimes have been restored.
49 Contemporary reference conditions are a good supplement to historical reference data, because
50 (1) contemporary measurements do not have uncertainty that varies with tree size, like
51 reconstructed measurements do, (2) contemporary reference conditions inherently incorporate
52 some effects of climatic change on resilience and (3) modern remote sensing tools allow for
53 description of complete reference landscapes at the multiple scales necessary for restoration
54 planning. The major drawback of contemporary reference conditions, however, is that they exist
55 because of a special set of conditions that may be unique to a site. For example, the Illilouette
56 Valley in Yosemite National Park has been studied as a contemporary active-fire landscape, but
57 low productivity and associated low fuel loads, sparse understory, and low regeneration rates
58 made reintroducing lower-severity fire less risky for forest managers in this watershed compared
59 to most of the Sierra Nevada (Collins *et al.*, 2016).
60 The structural conditions associated with resilient forest ecosystems vary with fine-scale
61 changes in topography and environment (Lydersen and North, 2012; Churchill *et al.*, 2017).
62 Thus, a regional reference condition dataset will have a very wide range of variation reflecting
63 the diversity of environmental conditions across the region. A key step in using reference
64 conditions to inform restoration, then, is constraining that wide range of variation in
65 consideration of the biophysical conditions on a given site. That is, the reference conditions used
66 for a given area should be drawn from an environmentally and climatically similar restored site
67 to ensure that resilient conditions in one location will translate to another. This concept is derived

from climate analogs (sensu Churchill *et al.*, 2013), and we refer to it in a broadened sense as biophysical analogs.

The aim of this study is to identify and describe contemporary active-fire reference areas for the Sierra Nevada mixed-conifer zone and to place them in the context of their biophysical setting. This work is intended to support planning, implementing, and monitoring restoration treatments by quantifying the ranges of structural conditions that occur in different environments across restored-fire landscapes. We especially seek to understand the details of how structure and spatial pattern vary with topography and climate. We conceptualize spatial pattern as a fine-scale mosaic of widely space individual trees, clumps of trees closely aggregated in space, and open space between tree crowns (Churchill *et al.*, 2013).

Our specific research questions are:

(1) What is the geographic and environmental distribution of restored active-fire forest patches in the Sierra Nevada mixed-conifer zone?

(2) What are the ranges of variation in structure and spatial patterns across restored patches?

(3) How do density, tree clumping, and canopy opening patterns vary by topography and climate in restored patches?

2. Methods

2.1 Classifying the biophysical environment

2.1.1 Climate classes

We began by defining climate classes across the Sierra Nevada (Figure 1) for two purposes. First, the classes helped us delineate the mixed-conifer zone, which was the focus of this study.

Second, the climate classes provided the basic biophysical context that we used to analyze variation in reference condition structure.

We defined climate classes using climatic variables at the grain size of catchment basins. We chose to use catchment basins because these form ecologically relevant units (a connected watershed) that are familiar to forest managers and are operationally practical in terms of mechanical treatments (e.g., road building and yarding) and fire treatments (e.g., placement of fire line). We used basin data from the National Hydrography Dataset (EPA and USGS, 2018), with catchment sizes ranging from 7-1013 ha. We combined any catchments smaller than 100 ha with their immediate neighbors until a minimum size of 100 ha was reached; the smallest catchment after consolidation was 109.3 ha. For climate classification variables we sought metrics integrating the biophysical conditions experienced by vegetation (Stephenson, 1998). To this end, we followed the definition of climate analogs by Churchill *et al.* (2013) and selected actual evapotranspiration (AET) and climatic water deficit (Deficit) which are integrated measures of productivity and moisture stress, respectively (Lutz *et al.*, 2010). We supplemented these

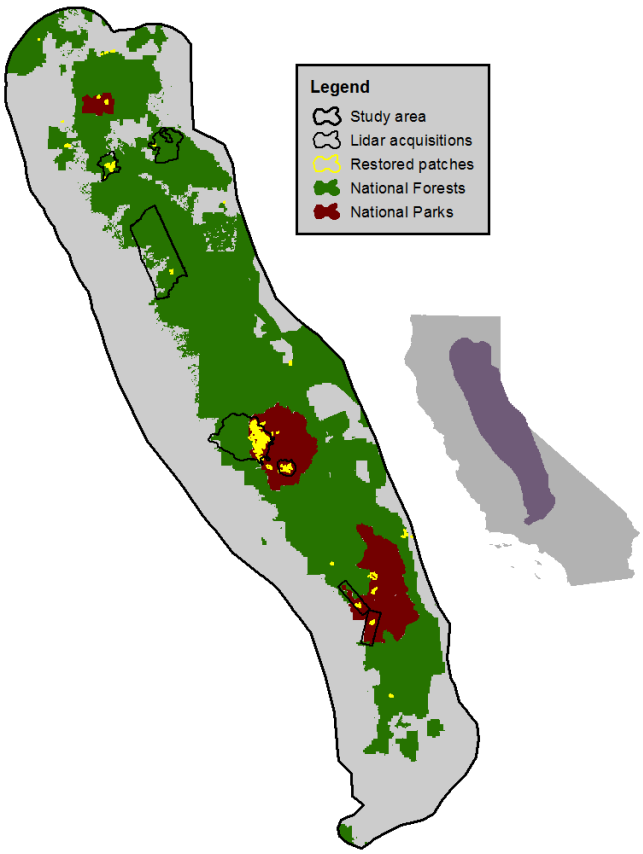

Figure 1 Map of study area showing restored patches across the Sierra Nevada, federal ownership, and lidar acquisitions.

113 with January minimum temperature (T_{min}), which can help to pinpoint limitations on
114 regeneration and growth (Lutz *et al.*, 2010; Dobrowski *et al.*, 2013). We gathered AET, Deficit,
115 and T_{min} data from the publicly available Basin Characterization Model dataset (Flint *et al.*,
116 2013, 2014) and calculated the 25th and 75th percentile values for each metric within each
117 catchment (Figure 2).

118 We used the six resultant variables for each catchment, normalized by global maxima, in a
119 hierarchical classification with Euclidean distances and a complete linkage method. This was
120 implementing using the hclust function in R (R Core Team, 2016). We chose to use 20 classes by
121 inspecting the dendrogram and scree plot (Figure S1.1) as well as by inspecting the classification
122 results for cuts at 4, 8, 12, 16, 20, 24, 28, and 32 classes. Numbers of classes greater than 20
123 began to split up basins in ways that did not make ecological or climatological sense. We

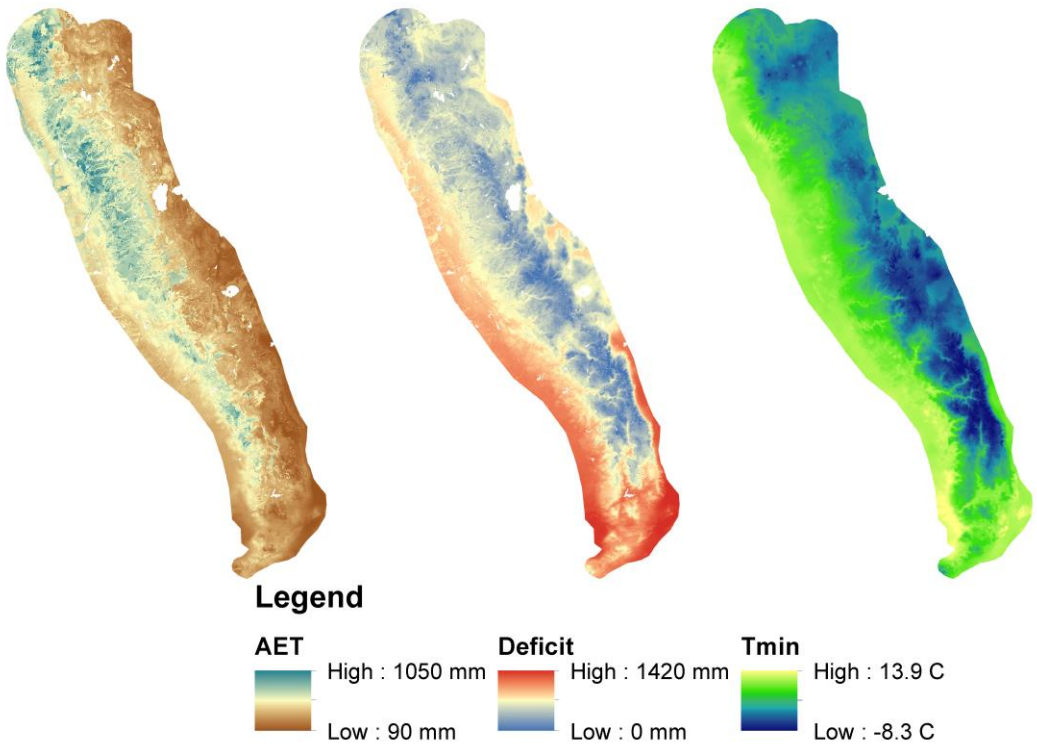

Figure 2 Maps of layers used to classify climate – actual evapotranspiration (AET), climatic water deficit (Deficit), and January minimum temperature (Tmin) – across the study area. Data from Flint *et al.* (2014).

assigned descriptive names to each class based on inspection of the dendrogram and boxplots of class-wise distributions of AET, Deficit, and T_{min} (Table 1, Figure S1.2).

Flint *et al.* (2013) calculated AET and Deficit as a partitioning of potential evapotranspiration based largely on soil water holding capacity. Flint *et al.* (2013) used data from the US General Soil Map (Soil Survey Staff, 2018) to estimate soil water holding, but these data represent soil characteristics as homogeneous values over large polygons (~1000 ha minimum size) even though soil is highly variable at sub-meter scales (Vereecken *et al.*, 2016). We tested the sensitivity of our climate classification to variation in the soil water inputs and found that the classification is adequately robust to variation in soil assumptions (Supplement 2).

We validated the climate classes in terms of their ability to discriminate between forest composition using data from USFS Forest Inventory and Analysis (FIA) plots (Bechtold and Patterson, 2005) throughout the Sierra Nevada. We selected plots that represent native forested communities by enforcing these criteria: (1) minimum 10% forest cover, (2) natural stand origin, and (3) no artificial regeneration. A total of 3217 plots met these criteria. We summarized composition on each plot by calculating proportions of live tree basal area by species and assigned each plot a climate class based on its publicly available fuzzed location (within 1.6 km of the true location).

We used PERMANOVA (McCune *et al.*, 2002) to test whether composition varied significantly by climate class. With the adonis function in the R package vegan (Oksanen *et al.*, 2016), we compared proportionate live basal area by species across climate classes using the Bray-Curtis dissimilarity measure (Bray and Curtis, 1957) and assessed significance with 1000 permutations of climate class labels.

146 **Table 1** Climate class characteristics in terms of climate variables, species composition, and forest type. AET = actual evapotranspiration, T_{min} =
147 annual minimum temperature. Species codes are given in Table S1.1. Ecological zones, forest types, and historical fire return intervals are as
148 defined by van Wagtendonk and Fites-Kaufman (2006).

		Median Values					
Class	**Class Name**	**Elevation (m)**	**AET (mm)**	**Deficit (mm)**	**T_{min} (° C)**	**Species dominant by BA in at least 5% of plots**	**Indicator species**
1	Dry Foothills	270	386	903	9.5	QUDO, QUWI, PISA, QUCH	QUDO, QUWI
2	Hot Southern Foothills	240	276	1145	9.8	QUDO, QUWI, QUCH, AECA	QUDO, AECA
3	Warm Southern Foothills	1280	241	1057	7.4	QUDO, QUCH, QUWI, QUKE, PIMO	JUCA
4	Foothill Valleys	390	553	640	9.4	PIPO, PSME, LIDE, QUWI, QUDO	PSME, PIPO
5	Foothill-Low Montane Transition	770	452	755	7.7	QUCH, PIPO, QUWI, QUKE, QUDO, PSME, CADE	QUKE
6	Very Hot Low Montane	770	545	617	7.6	PSME, PIPO, QUKE, CADE	PSME, QUKE
7	Hot Low Montane	1010	611	482	5.7	PIPO, CADE, PSME, LIDE, QUKE, QUCH, ABCO	LIDE
8	South Sierra Low Montane	1740	160	927	3.9	QUCH, PIMO, PIJE, ABCO, QUWI, QUKE, CADE	PIMO
9	Warm Dry Low Montane	1310	485	573	5.2	PSME, ABCO, PIPO, QUKE, CADE, QUCH	PSME, QUKE
10	Warm Mesic Low Montane	1670	376	620	3.5	ABCO, CADE, PSME, PIPO, PILA, PIJE	CADE
11	Xeric Mid Montane	1470	229	756	1.9	PIJE, JUOC, ABCO, CADE, QUCH, PIPO, PISA	PIJE, JUOC
12	Warm Mesic Mid Montane	1470	507	416	2.7	ABCO, PSME, CADE, PIPO	ABCO, CADE
13	Cool Dry Mid Montane	1810	359	517	1.5	ABCO, ABMA, CADE, PSME, PIPO, PIJE	ABCO, ABMA
14	Xeric High Montane	1850	220	628	0.1	PIJE, ABCO, JUOC, PIPO, ABMA, CADE	PIJE, JUOC
15	Cool Mesic High Montane	2170	443	321	0.0	ABMA, ABCO, PICO, PIMO2, PIJE, TSME	ABMA, ABCO
16	Cool Dry High Montane	2110	298	465	-0.8	ABCO, ABMA, PICO, PIJE, PIPO	ABMA, PICO
17	Cold Dry High Montane	2330	224	523	-2	PIJE, PICO, ABMA, ABCO, JUOC	PIJE, PICO
18	High Sierra	2950	224	353	-3.5	PICO, PIAL, ABMA, PIBA	PICO
19	High Valleys and Meadows	2880	379	155	-3.8	PIBA	PIBA
20	Subalpine	3400	201	252	-5.1	PIAL, PICO, PIBA, TSME	PIAL

Table 1, continued Climate class characteristics in terms of climate variables, species composition, and forest type. AET = actual evapotranspiration, T_{min} = annual minimum temperature. Species codes are given in Table S1.1. Ecological zones, forest types, and historical fire return intervals are as defined by van Wagtendonk and Fites-Kaufman (2006).

Class	Ecological zone	Common forest type(s)	Historical fire return interval
1	Foothill shrubland and woodland	QUDO woodland, PISA-QUWI woodland	Short
2	Foothill shrubland and woodland	QUDO woodland, mixed hardwood woodland	Short
3	Foothill shrubland and woodland	QUDO woodland, mixed hardwood woodland	Short-Medium
4	Foothill shrubland and woodland/ Lower-montane forest transition zone	QUDO woodland, PISA-QUWI woodland, riparian forest	Medium
5	Foothill shrubland and woodland/ Lower-montane forest transition zone	Mixed hardwood woodland, QUDO woodland, mixed evergreen	Short-Medium
6	Lower-montane forest	QUKE-PIPO-ABCO-PSME forest, mixed evergreen	Short
7	Lower-montane forest	QUKE-PIPO-ABCO-PSME forest, mixed evergreen	Short-Medium
8	Lower-montane forest	QUKE-PIPO-ABCO-PSME forest, mixed conifer	Short
9	Lower-montane forest	Mixed evergreen, mixed conifer	Short
10	Lower-montane forest	Mixed conifer	Short
11	Lower-montane forest/ Upper montane forest transition zone	PIJE woodland, JUOC woodland, mixed evergreen	Short
12	Lower-montane forest/ Upper montane forest transition zone	Mixed conifer	Short
13	Lower-montane forest/ Upper montane forest transition zone	Mixed conifer, PIJE woodland	Short-Medium
14	Upper montane forest	PIJE woodland, mixed conifer, JUOC woodland	Medium
15	Upper montane forest	ABMA forest, PIMO2 forest, PIJE woodland	Medium
16	Upper montane forest	ABMA forest, PICO forest, PIJE woodland	Medium-Long
17	Upper montane forest	PIJE woodland, PICO forest, ABMA forest, JUOC woodland	Medium-Long
18	Upper montane forest/Subalpine forest transition zone	PICO forest, PIAL woodland, ABMA forest, PIBA woodland	Long
19	Subalpine forest	PIBA woodland	Long
20	Subalpine forest	PIAL woodland, PICO forest, PIBA woodland, TSME forest	Long

To provide a more specific idea of how composition varied by climate class we took two approaches to associating tree species with each climate class. First, we created lists for each class giving the species that are dominant by basal area on at least 5% of FIA plots, in decreasing order of dominance frequency.

Second, we performed an indicator species analysis (ISA) (McCune *et al.*, 2002) to determine the most characteristic indicator species for each class. We implemented the ISA in R. The ISA calculates indicator values (IVs) for each species in each class representing how faithful and how exclusive the species is to that class (McCune *et al.*, 2002). We assessed significance of IVs using a permutation test, randomly shuffling the climate classes 1000 times. We assigned an indicator species to each class by taking the species with the highest IV that was also significant under the permutation test ($p < 0.05$). When two climate classes had the same indicator species we differentiated them by also considering the species with the second highest significant IV. For pairs of classes where the primary and secondary indicator species were both the same, we tested for differences in composition using a PERMANOVA with contrasts comparing the two classes of interest. As before this was implemented using the adonis function, Bray-Curtis dissimilarities, and 1000 permutations to assess significance.

We used the results of these two composition analyses to make associations between climate classes and the ecological zones and forest types defined by van Wagtendonk and Fites-Kaufman (2006). We also associated the climate classes into five major groups: foothills, low montane, mid-montane, upper montane, and high sierra.

2.1.2 Landscape management units

We subdivided catchments by topographic position to capture localized patterns of change in solar demand, soil depth, and water availability that can influence the biophysical environment

and reference conditions at fine scales (Wiggins, 2017). We classified areas in terms of landscape management unit (LMU, sensu Underwood *et al.*, 2010) using the Landscape Management Unit Tool version 2 (Boynton *et al.*, 2015). This tool operates by classifying a digital elevation model (DEM) by topographic position. We used the simplified output from the tool and created the following simplified classes based on a 30 m resolution DEM and default parameters: ridge, valley, SW slope (135-225° aspect), and NE slope (0-135° and 225-360° aspect). We did not perform validation on the LMU classes since the nature of LMUs has already been described for California (Underwood *et al.*, 2010; Lydersen and North, 2012; Wiggins, 2017).

2.2 Locating restored areas

We located this study in the Sierra Nevada mixed-conifer zone, which we took to include forests dominated by a variable mix of ponderosa pine (*Pinus ponderosa*), Jeffrey pine (*P. jeffreyi*), sugar pine (*P. lambertiana*), white fir (*Abies concolor*), red fir (*A. magnifica*), and incense cedar (*Calocedrus decurrens*). This zone is the center of most contemporary forest management in the Sierra Nevada and has a greater restoration need than other forest types (Weatherspoon and Skinner, 1996; North *et al.*, 2009). Based on the analysis of climate class composition we took the 12 climate classes in the lower montane, mid-montane, and upper montane groups to comprise the Sierra Nevada mixed-conifer zone.

We defined restored areas as patches where forest cover is naturally regenerated, has been minimally modified by Euro-American resource extraction, and has recently had a fire regime similar to that of the pre-Euro-American past, i.e., at least two fires have recently burned with an interval <60 years between them (Lydersen and North, 2012). We restricted the study to federal

198 lands so that we had access to records of past management. This included all or part of 13
199 National Forests and three National Parks (Figure 1).
200 Across the Sierra Nevada we created a raster layer at a 30 m resolution where pixel values
201 were scored as integers from 0-5 representing how restored that pixel was. One point was scored
202 for each of the following criteria:

203 1. No records exist of past timber management (planting, harvest, thinning, etc.);
204 2. The pixel has experienced at least two fires in the last 60 years, so that a "regime" is
205 beginning to be defined (Taylor, 2010; Lydersen and North, 2012; van Wagtendonk *et*
206 *al.*, 2012);
207 3. At least one of these fires occurred within the last 30 years, so that the results of
208 reintroduced fire are still extant (Lydersen and North, 2012);
209 4. At least one of these fires had moderate severity effects on the pixels, because moderate
210 severity fire kills more trees in lower canopy strata than low severity fire, thereby doing
211 more work to return a fire-excluded stand to resilient conditions (Collins *et al.*, 2011;
212 Becker and Lutz, 2016); and
213 5. The pixel has not experienced high severity effects, because high amounts of mortality
214 indicate low fire resistance (North *et al.*, 2012; Stephens *et al.*, 2013).

215 Management history data were retrieved from the Forest Service national geodata clearinghouse
216 (USDA Forest Service, 2018). We did not consider management history for National Parks. Fire
217 history was drawn from the FRAP fire atlas (Cal Fire, 2018) for years 1957-1983 and Monitoring
218 Trends in Burn Severity (Eidenshink *et al.*, 2007) for years 1984-2014. The Cal Fire (2018) data
219 did not include spatially explicit burn severities, so we treated all management ignitions as low
220 severity fires throughout. Fires started by lightning and accidental human ignition were assumed

to be low severity when they were small (<400 ha) and successfully suppressed within a few days. Larger fire areas from 1957-1983 with unknown severity were excluded from the analysis.

Using the raster layer so defined, we drew polygons around restored patches following natural boundaries of fire history and topography to separate patches. We enforced the following criteria for each patch:

1. Patch size is at least 100 ha, due to time constraints on manual patch delineation;
2. Any high-severity patches incorporated into the restored area are no larger than 10 ha, since the majority of high severity patches found historically were no more than a few hectares in size (Kilgore, 1973; Skinner and Chang, 1996; Keeley and Stephenson, 2000);
3. No more than 10% of the polygon has burned at high severity, which is near the high end of the range of variation in historical high severity proportions (Mallek *et al.*, 2013 and references therein; Stephens *et al.*, 2015);
4. The average number of fires in the polygon is ≥2, to ensure that the patch has, on the whole, experienced multiple fires; and
5. The average number of recent fires (<30 yr. old) in the polygon is ≥1, to ensure that the patch has, on the whole, burned recently.

Thus, the polygons are intended to represent patches with a variety of patterns but which are mainly characterized by meeting the pixel criteria (Figure 3). The patch criteria allow for flexibility in several ways. First, even though high severity pixels were not favored in the pixel criteria, we recognize that some amount of high severity fire is expected to occur in restored

Figure 3 Photos exemplifying conditions in reference areas. Top-left shows a hillslope view exhibiting a complex patch mosaic. Top-right and middle row show open, fire-resistant conditions with scattered large trees and very little understory. Bottom row shows sites that have burned fewer times or at lower severity, where stem density appears high but most small trees are dead and surface fuel loads are low.

241

areas (Collins and Stephens, 2010; Mallek *et al.*, 2013) and so some high severity patches are allowed. We chose to make the limits for high severity inclusion within these patches liberal relative to published historical conditions because (1) studies capturing historical conditions likely missed some of the largest patches and, (2) these restored stands have had several fires recently but are still recovering from decades of fire suppression, so we do not expect them to fully match historical conditions. The patch criteria also allow for unburned patches to be incorporated within the matrix of burned lands. This is intentional, since unburned refugia are critical elements of resilience in post-fire landscapes (Kolden *et al.*, 2012; Kolden *et al.*, 2015). In contrast, we did not allow any management activity within the patches.

2.3 Quantifying reference conditions

We used lidar data to characterize the forest structure of the restored areas and provide a set of quantitative reference conditions. Lidar data provides measurements of structure at a resolution of several data points per square meter across areas tens to hundreds of thousands of hectares in size, and so allowed us to quantify structural variation across entire restored patches. We characterized structure on the basis of lidar-identified tree-approximate objects (TAOs) (North *et al.*, 2017; Jeronimo *et al.*, 2018). TAOs are an ecologically meaningful unit of measurement representing a canopy tree that was detected by the lidar along with subordinate trees that cannot be individually resolved. The canopy tree may be an individual with no neighbors or may be associated with a small number of understory trees (mean 1.5 [sd 1.2] undetected trees per TAO; S. Jeronimo, *unpublished data*). Using TAOs allows for a consistent unit of analysis even while tree detection accuracy changes with forest structure (Jeronimo *et al.*, 2018). Since large trees, which are more visible to lidar, dominate basal area and spatial heterogeneity (Lutz *et al.*, 2012; Lutz *et al.*, 2013; Lutz *et al.*, 2018), directly measuring patterns

of TAOs maintains much of the useful information that would be gathered in a traditional tree-based survey. By necessity, this portion of the analysis was limited to areas with available lidar data (Figure 1; Table 2). This included 76% of the identified restored areas, or 23,088 ha.

Across each lidar acquisition area we created ground-normalized canopy height models using a 0.75 m resolution and a 3×3 pixel smoothing window (Jeronimo *et al.*, 2018) and segmented the canopy height model into TAOs using the TreeSeg tool in the FUSION Lidar Toolkit (McGaughey, 2018). The TreeSeg tool associates each TAO with a location and a height. We additionally modeled dbh for each TAO using regressions developed from the 3217 FIA plots described above. We used the following regression model form:

$$\text{dbh} = b_0 \text{height}^{b_1}, \qquad \textbf{Equation 1}$$

fitting a separate set of coefficients for each climate class (Table 3).

We split restored areas into polygons by LMU, and for each polygon calculated summary metrics quantifying conditions in terms of TAO size distributions, stocking, and spatial pattern. Size distributions were quantified in terms of modeled dbh distributions. Stocking was quantified

Table 2 Lidar acquisitions used in this study and their key technical specifications. Vendor abbreviations: WSI = Watershed Sciences, Inc. (today Quantum Spatial), NCALM = National Center for Airborne Laser Mapping, CIS = Carnegie Institution for Science. CAO = Carnegie Airborne Observatory (Asner *et al.*, 2007).

Acquisition	Illilouette Basin	Rim Fire	Sequoia National Park	Storrie Fire 1	Storrie Fire 2	Moonlight Fire	Tahoe National Forest
Mo./yr. acquired	Aug. 2011	Nov. 2013	Aug. 2015	Aug. 2009	Aug. 2013	Aug. 2013	Jun. 2013
Collected by	WSI	NCALM	CIS	WSI	WSI	WSI	NCALM
Instrument	Dual Leica ALS50 ii	Optech Gemini ALTM	CAO	Dual Leica ALS50 ii	Dual Leica ALS50 ii	Dual Leica ALS50 ii	Optech Gemini ALTM
Max. returns per pulse	4	4	4	4	4	4	4
Average pulse density (# m^{-2})	12	12	14	7	11	11	8.5
Laser pulse frequency (kHz)	83	125	100	90	90	90	100
Field of view (°)	±14	±14	±17	±14	±14	±14	±18

by TAO density and basal area based on modeled dbh. Spatial pattern metrics followed the Individuals, Clumps, and Openings method (ICO) (Churchill *et al.*, 2013). TAOs were considered members of the same clump if their high points were within 6 m of one another, and TAOs with no neighbors within 6 m were considered individuals. This limiting distance was chosen to represent the average crown width of a mature conifer and was validated using plot data from Yosemite (n = 97 trees, data not shown). Clump size distributions were reported as proportions of TAOs in clumps of different sizes: individuals, small clumps (2-4 TAOs), medium clumps (5-9 TAOs), large clumps (10-14 TAOs), super clumps (15-30 TAOs), and mega clumps (>30 TAOs). Open space was considered to be any area with no vegetation taller than 2 m according to the canopy height model. Open space distributions were created to describe the amount of open space at varying distances from the nearest canopy: 0-10 m in 2 m bins, 10-20 m, and >20 m. Canopy gaps were delineated using methods from Lydersen *et al.* (2013), which uses image morphology operations to identify gaps at least 60 m^2 in size and cut off long meandering gaps at ecologically relevant thresholds. Gaps were summarized in terms of gap density and gap size distributions.

2.5 Differences in reference structure across biophysical environments

To assess how structure of restored areas changes across different biophysical environments we tested for differences between climate and LMU classes, including an interaction term, using analysis of variance (ANOVA) and structural indices. We used data from the six climate classes that had at least 100 ha of restored patches with lidar coverage. The structural indices were TAO density, TAO basal area, mean clump size, and proportion of open space >6 m from the nearest canopy. These metrics are a good summary of stocking and pattern (Churchill *et al.*, 2013). The indices were calculated on the basis of LMU patches within each restored area. We confirmed

that the distributions of the indices met the assumptions of ANOVA, which required log-transforming the clump and opening indices. We then tested for significant differences between climate and LMU classes for each of these metrics in separate univariate two-way ANOVAs. For any tests that gave significant results we used a Tukey HSD post-hoc test to find significant differences between pairs of classes.

3. Results

3.1 Climate classes

The 20 climate classes identified across the Sierra Nevada were distinctly different in terms of AET, Deficit, T_{min}, and species composition (Figure S1.2). The warmest, driest class, Dry Foothills, had a median AET of 386 mm (range 229-856 mm, mean 396 mm), a median Deficit of 903 mm (range 317-1202 mm, mean 893 mm), and a median T_{min} of 9.5° C (range 2.1-12.5° C, mean 9.4° C). In contrast, the coldest, wettest class, Subalpine, had a similar median AET of 379 mm (range 100-483 mm, mean 207 mm), a much lower median Deficit of 155 mm (range 12-767, mean 255 mm), and a median T_{min} of -3.8° C (range –8.3-0.9° C, mean –5.2° C) (Table 2). Five classes fell into the foothills category, five were low montane, three were mid-montane, four were upper montane, and three were high Sierra. Geographically, climate class groupings followed two major gradients: latitude and elevation. A noticeable break in classification occurred around 38° N latitude, with some higher-Deficit classes introduced south of that line. The elevation gradient is clear, and is expressed in roughly parallel bands running north-south along the range (Figure 4).

Composition of FIA plots was significantly different among climate classes ($p < 0.01$). Classes in the Foothills group were dominated by oaks (*Quercus* spp.) and gray pine (*Pinus sabiniana*), with California buckeye (*Aesculus californica*) and single-leaf pinyon (*P.*

Table 3 Model coefficients and statistics for height-diameter regressions on forest inventory and analysis plots within each climate class. Model form is $\mathrm{dbh} = b_0 \mathrm{height}^{b_1}$, with dbh in cm and height in m.

					Data used to build model					
Class	**b_0**	**b_1**	**r^2**	**RMSE (cm)**	**N plots**	**N trees**	**DBH min (cm)**	**DBH max (cm)**	**Height min (m)**	**Height max (m)**
1	1.538561	1.146477	0.64	3.99	216	3179	2.5	121.2	1.2	45.1
2	2.722830	1.023248	0.61	3.38	31	304	3.6	101.3	2.7	30.5
3	2.056479	1.158301	0.70	4.29	69	1310	2.5	115.1	0.9	34.4
4	1.147980	1.120285	0.86	5.09	21	654	2.5	149.6	2.7	64.6
5	1.376703	1.109428	0.79	4.73	460	13524	2.5	209.0	1.8	68.9
6	1.192055	1.128306	0.86	5.06	88	3311	2.5	182.6	1.8	68.9
7	1.077415	1.160679	0.84	5.16	27	1091	2.5	161.0	2.1	60.4
8	3.031823	0.957971	0.64	5.64	30	723	2.5	158.2	1.5	46.3
9	1.446733	1.087456	0.86	4.74	335	13501	2.5	203.2	0.9	70.1
10	1.693278	1.057848	0.86	5.10	224	8712	2.5	245.6	1.5	75.6
11	2.316709	1.003102	0.81	5.60	113	2251	2.5	157.5	1.2	51.8
12	1.404125	1.108035	0.86	4.78	62	2414	2.5	177.8	1.8	60.7
13	1.783197	1.049170	0.85	5.32	356	13568	2.5	216.7	0.6	80.5
14	2.825456	0.922265	0.75	5.58	312	8589	2.5	164.6	0.3	59.4
15	1.930723	1.042319	0.84	5.77	127	4231	2.5	201.4	0.9	59.4
16	1.914989	1.060524	0.83	6.33	328	10398	2.5	261.9	0.6	59.4
17	2.052697	1.064319	0.79	6.15	233	6498	2.5	176.8	0.9	67.1
18	2.580526	1.009084	0.74	7.68	164	5082	2.5	196.3	1.2	57.9
19	15.647173	0.672207	0.44	5.68	1	34	56.4	127.3	8.2	17.4
20	2.960294	1.029713	0.72	8.15	44	990	2.5	154.2	1.5	33.2

monophylla) in the Southern Foothills. Ponderosa pine, Douglas-fir (*Pseudotsuga menziesii*), and tanoak (*Lithocarpus densiflorus*) occurred in Foothill Valleys and incense-cedar additionally occurred in the Foothills-Low Montane Transition zone. Low Montane classes were dominated by Douglas-fir, white fir, sugar pine, incense cedar, and ponderosa pine, but red fir was notably absent. California black oak (*Q. kelloggii*) was also common and canyon live oak (*Q. chrysolepis*) was present. Sugar pine was most dominant in the Warm Mesic Low Montane class. Mid Montane classes had a similar species assemblage but also included red fir, and Jeffrey pine was dominant in the Xeric Mid Montane class. High Montane classes were dominated by red fir, Jeffrey pine, and white fir, with some of the other pines still present. Lastly, the High Sierra

group was dominated by high-altitude pines (*P. contorta*, *P. albicaulis*, and *P. balfouriana*) with some red fir and mountain hemlock (*Tsuga mertensiana*) (Table 2).

The indicator species analysis (ISA) yielded significant results for all climate classes. Within the Montane classes Douglas-fir and California black oak were indicators for warmer, drier classes (high AET and high Deficit) while incense cedar indicated cooler classes (lower T_{min}). Edaphically xeric classes (low AET with high Deficit) were indicated by Jeffrey pine and western juniper (*Juniperus occidentalis*). Red fir and lodgepole pine (*P. contorta*) indicated classes with T_{min} values at or below 0° C (Table 2).

There were two cases when pairs of classes shared the same primary and secondary indicator species. The Very Hot Low Montane class and the Warm Dry Low Montane class both had

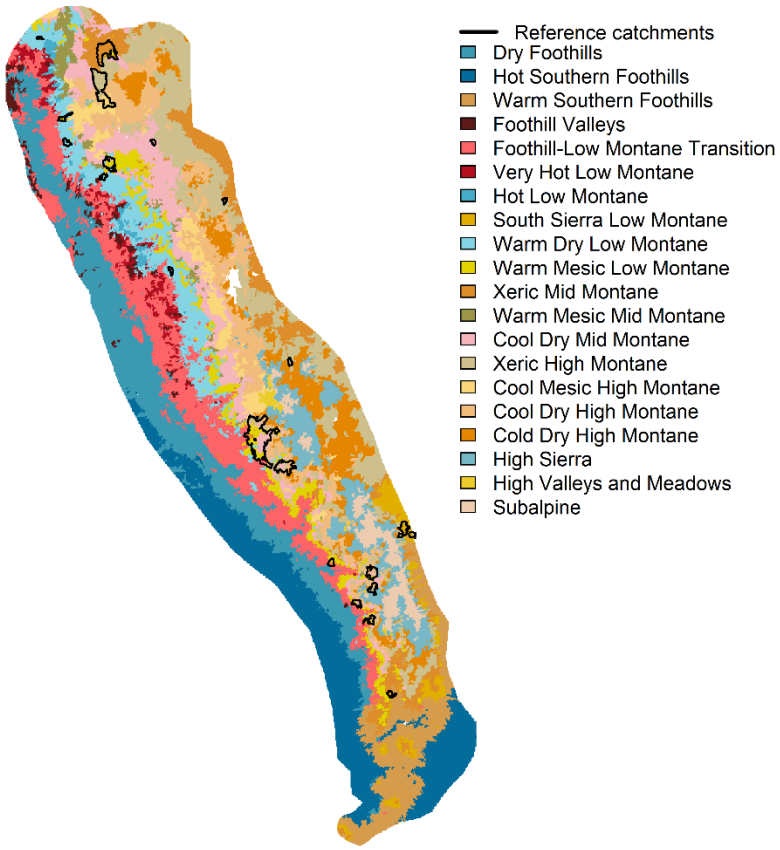

Figure 4 Map of climate classes with catchments containing at least one restored patch indicated.

Douglas-fir and California black oak as indicators, and the Xeric Mid Montane and Xeric High Montane classes shared Jeffrey pine and western juniper. In both cases PERMANOVA tests with pairwise contrasts showed significant differences in FIA plot composition ($p < 0.01$).

3.2 Restored areas

We identified a total of 30,379 ha of restored patches across the Sierra Nevada mixed-conifer zone. Median contiguous patch size was 260 ha and the maximum was 5500 ha (Supplement 3). Patches were distributed across the latitudinal and altitudinal ranges of our study area, mostly on the west slope of the Sierra Nevada (Figure 1). By far the majority of restored area was in the central and southern Sierra (25,663 ha), concentrated in Yosemite National Park (19,990 ha) and Sequoia-Kings Canyon National Park (3,927 ha), along with 1,380 ha on the Sierra, Sequoia, and Inyo National Forests. The majority of restored patches in the northern Sierra were on the Plumas and Lassen National Forests (3,532 ha) and Lassen National Park (701 ha).

Restored patches were identified within nine of the twelve montane climate classes. The two hottest, driest low montane classes and the Warm Mesic Mid Montane class did not have any restored area, and the Cold Dry High Montane class had only 45 ha of restored area. The other eight montane classes had at least 500 ha of restored area each. By far the majority of restored area was in the Warm Mesic Low Montane (10,112 ha) and Cool Dry Mid Montane (10,187 ha) classes.

3.3 Reference conditions

The reference envelope of restored patch structure was broad and variable (Figure 5). TAO density varied from 6 to 320 trees ha^{-1} distributed widely across diameter classes. Typical LMU patches had up to 42.9 trees ha^{-1} <20 cm dbh, up to 29.2 trees ha^{-1} 20-40 cm dbh, up to 26.0 trees ha^{-1} 40-60 cm, up to 21.6 trees ha^{-1} 60-80 cm, up to 15.3 trees ha^{-1} 80-100 cm, and up to 7.4 trees

367 ha^{-1} 100-120 cm dbh (all values given are 75th percentile values). Overall density was normally

368 distributed (Figure 5) with a mean of 111 trees ha^{-1} and a standard deviation of 40 trees ha^{-1}.

369 Basal area was distributed as a zero-inflated normal with a mode at 25 m^2 ha^{-1} (standard

370 deviation 17 m^2 ha^{-1}) and a right skew. Five percent of LMU patches had less than 2 m^2 ha^{-1} of

371 basal area (Figure 5).

372 Spatial patterns of TAOs in restored patches had some consistent patterns of variation. TAOs

373 were most commonly arranged as individuals with no close neighbors and in clumps of 15-30

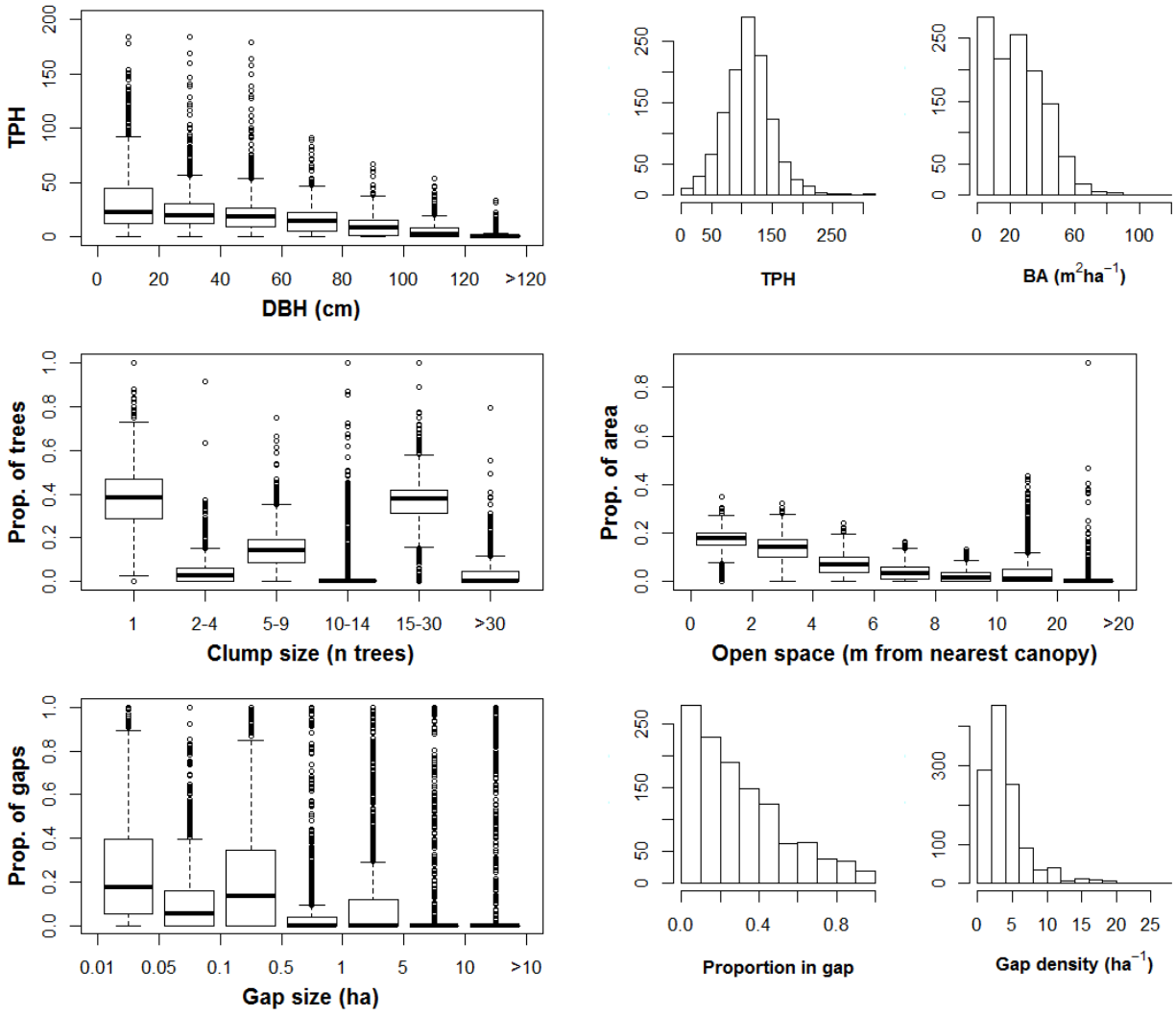

Figure 5 Ranges of variation in reference condition structure across all restored patches with available lidar data. TPH = trees per hectare, DBH = diameter at breast height, BA = basal area.

374 (both median 38% of TAOs per LMU patch). LMU patches with many clumps of 2-14 or >30
375 TAOs were less common (Figure 5). Between 25% and 40% of stand area was usually situated in
376 openings <4 m from the nearest canopy, whereas less than 15% was usually >6 m from the
377 nearest canopy. However, as indicated by the zero-inflation of the basal area distribution, some
378 LMU patches were very open and it was not rare for 10-20% of the patch area to be located >10
379 m from the nearest canopy (Figure 5). Delineated gaps at least 12 m in diameter were present on
380 94% of patches, usually representing <50% of patch area. On most patches the majority of gaps
381 were under 0.5 ha in size (median 72%), with 25% under 0.05 ha (Figure 5). However, larger
382 gaps were often present, including commonly up to 13% of gaps in the 1-5 ha size class. Most
383 LMU patches had 2-5 gaps ha^{-1}, and up to 8 gaps ha^{-1} was common (Figure 5). The highest
384 observed gap density was 26 ha^{-1}.

385 *3.4 Variation in reference structure across biophysical environments*

386 All of the stocking and spatial pattern indices we tested varied significantly by climate class
387 and LMU. Density and mean clump size also had significant climate class-LMU interaction
388 terms (Figure 6). Of the six climate classes analyzed the lowest- and highest-elevation classes
389 had the highest densities (median 121 trees ha^{-1}), following a roughly U-shaped distribution
390 across the elevation gradient. The Xeric Mid Montane class had significantly lower density than
391 any other class (median 86 trees ha^{-1}). Density was also significantly lower on ridges compared
392 to valleys, but the absolute difference was not large (medians 101 vs. 115 trees ha^{-1}). Ridges and
393 valleys diverged from the general U-shaped distribution in the highest elevation class, Cold Dry
394 High Montane, where densities were almost as low as for the Xeric Mid Montane class (Figure
395 6). Basal area followed density in its response to topography (slightly lower on ridges), but its
396 relationship with climate was more complex. The two edaphically xeric classes had lower basal

area (median 3.7 and 22 $m^2 ha^{-1}$) as did the Warm Mesic Low Montane class (median 13.7 $m^2 ha^{-1}$). However, the Cool Dry Mid Montane class, which had relatively low density, had the highest basal area (median 31 $m^2 ha^{-1}$). There was no significant climate class-LMU interaction for basal area.

Mean clump size was statistically indistinguishable among five of the six tested climate classes (Figure 6). The Cool Dry Mid Montane class had a significantly lower mean clump size than the rest (median 2.7 vs. 4.0 trees). A small but significant difference in mean clump size existed between ridges (median 3.0 trees) and other landforms (median 3.3 trees). More pronounced was the interactive effect of climate class and LMU on mean clump size. Clump sizes were much larger in valleys compared to other landforms in the Warm Dry Low Montane, Xeric Mid Montane, and Xeric High Montane climate classes (Figure 6). Southwest-facing slopes also had higher mean clump sizes in the Xeric High Montane climate class. The open space index, measuring the proportion of stand area greater than 6 m from the nearest canopy edge, varied across climate classes and LMUs almost as a mirror image of basal area when plotted on a log scale (Figure 6). The open space index was lowest in the Warm Dry Low Montane class (median 0.01) and highest in the Xeric Mid Montane class (median 0.29). Open space was significantly higher on ridges (median 0.074) and significantly lower on NE-facing slopes (median 0.046), while valleys and SW slopes were transitional (median 0.056).

4. Discussion

4.1 Geographic and environmental distribution of restored patches

The geographic distribution of restored active-fire patches was primarily a result of management practices associated with different land ownerships. There are two obvious factors contributing to this. First, we required that restored patches have no history of active forest

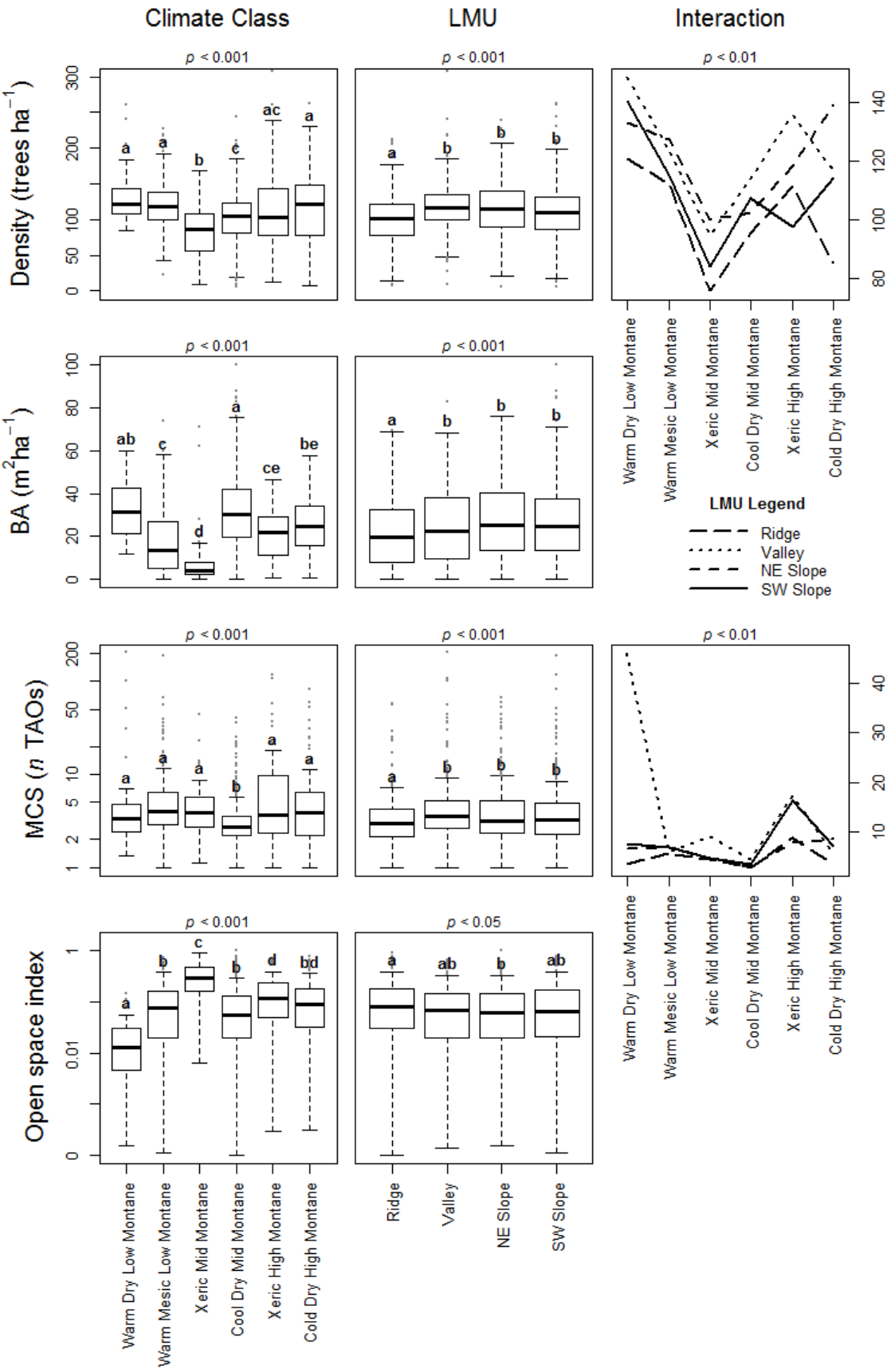

Figure 6 Structure and pattern indices varying by climate class and landscape management unit (LMU). Interaction terms are shown where significant. BA = basal area, MCS = mean clump size, TAO = tree-approximate object.

management such as planting, thinning, or harvesting timber. Timber management has been widespread across National Forests of the Sierra Nevada since the early 1900s (Laudenslayer and Darr, 1990), but has generally not occurred in the National Parks which were protected from most resource extraction starting in 1890 (Yosemite and Sequoia-Kings Canyon) and 1907 (Lassen) (Parsons and van Wagtendonk, 1996). Logging that did occur before the parks were protected was mostly opportunistic and small-scale (Laudenslayer and Darr, 1990). Second, fire policy has been very different between National Forests versus National Parks in the Sierra Nevada, especially since the early 1970s when the parks began phasing out full suppression policies and adopting instead active prescribed and wildland use fire programs (Parsons and Botti, 1996; van Wagtendonk, 2007; van Wagtendonk and Lutz, 2007). In contrast, National Forests started using prescribed burning more recently and have adopted wildland fire use policies primarily for management of designated wilderness (Stephens and Ruth, 2005). This in large part accounts for the fact that 81% of the restored area in the Sierra Nevada mixed-conifer zone is in National Parks, even while the parks represent less than 13% of the federal land base in the Sierra Nevada.

Some part of the distribution of restored areas can also be attributed to environmental conditions, in particular, lightning strikes. Lightning strike density varies with elevation across the Sierra Nevada, peaking in the 1800-2400 m elevation band (van Wagtendonk, 1994; van Wagtendonk and Cayan, 2008). This may explain why there were no restored areas in the two lowest-altitude montane climate classes. The elevation band that these classes primarily occupy, 600-1200 m, receives less than half as many lightning strikes of any of the other montane classes, and less than a quarter as many strikes as the three highest-elevation montane classes (van Wagtendonk and Cayan, 2008). Lightning ignitions are an important environmental factor

444 in Sierra Nevada fire regimes, since essentially all of the montane forest is dry enough to burn
445 during the annual summer drought (Lutz *et al.*, 2009).

446 A final factor that influenced the distribution of restored areas was the 2013 Rim fire. The
447 Rim fire burned a large swath of western Yosemite (Lydersen *et al.*, 2014), reburning a series of
448 fires from the 1980s-2000s that had substantial lower-severity components. This initial series of
449 fires primed western Yosemite for a subsequent lower-severity burn. Although the Rim fire had
450 drastic high-severity effects on the adjacent Stanislaus National Forest, severity in Yosemite was
451 much more mixed presumably because of the previous fire history (Lydersen *et al.*, 2014; Kane
452 *et al.*, 2015a; Lydersen *et al.*, 2017). Over half of the restored areas in Yosemite only met our
453 criteria after being burned by the Rim fire.

454 *4.2 Ranges of variation in restored stand structure and pattern*

455 The ranges of variation in density that we measured in restored patches generally matched
456 ranges reported by past studies quantifying active-fire Sierra Nevada forest structure. For
457 example, several reconstructed and historical datasets report mean densities ranging from 60-314
458 trees ha^{-1}, with total density ranges from 16-650 trees ha^{-1} (North *et al.*, 2007; Scholl and Taylor,
459 2010; Collins *et al.*, 2011; Van de Water and North, 2011; Knapp *et al.*, 2013; Barth *et al.*, 2015;
460 Stephens *et al.*, 2015). This matches well with our measured mean density of 111 TAOs ha^{-1}
461 (range 6-320), even when considering that each TAO may represent up to a few trees. These
462 same studies report mean basal area between 21 and 54 $m^2 ha^{-1}$ with a range of 0.3-89 $m^2 ha^{-1}$,
463 compared to our mean basal area of 25 $m^2 ha^{-1}$ (range 0.01-113). This alignment indicates that
464 the patches we identified as restored do exhibit some of the key structural features associated
465 with historically resilient stands, namely, lower densities than contemporary fire-suppressed
466 forests and dominance by large trees (North *et al.*, 2009; Stephens *et al.*, 2015).

In contrast, correspondence between our measurements of spatial pattern and reported measurements for historical Sierra Nevada forests was mixed. We are aware of only one study using spatially explicit data to describe historical spatial patterns in the Sierra Nevada: Lydersen *et al.* (2013) used 1929 stem map data from the "Methods of Cutting" experiment on the Stanislaus-Tuolumne Experimental Forest to quantify tree clumps and canopy opening patterns. Our measurements of TAO clumps did not directly align with their measurements of tree clumps. Specifically, we measured a higher proportion of individuals (38% vs. 5.6%) and a lower proportion of small clumps of 2-4 trees/TAOs (4.2% vs. 13.4%). This is probably because many TAOs counted as individuals actually represent two or three trees. In this sense our data and the data from Lydersen *et al.* (2013) are not directly comparable. However, measurements of open space do not rely on tree counts and so can be directly compared. Our average measurements were similar to the Methods of Cutting plots. Lydersen *et al.* (2013) found 40% of plot area was in open space <3 m from the nearest canopy compared to our finding of 25-40% within 4 m. The Methods of Cutting plots averaged 5.2 delineated gaps ha^{-1} compared to our 4.1 ha^{-1}, and the distributions of gap sizes were also comparable. However, we additionally identified many large gaps (>10 ha) that have no parallel in the Lydersen *et al.* (2013) dataset.

Contemporary measurements of spatial pattern in the active-fire Sierra San Pedro Martir in northern Baja California, Mexico provide another point of reference. Fry *et al.* (2014) found that 10-14% of trees in Jeffrey pine-mixed conifer stands were individuals with no close neighbors, while 20-25% of trees were in small clumps and 18-24% of trees were in medium clumps of 5-9 trees. These proportions represent a somewhat less clumped stand than the Lydersen *et al.* (2013) data (more individuals and small clumps, fewer large clumps), but compare to our findings

similarly. That is, we found higher proportions of individuals and lower proportions of small clumps overall.

4.3 Variation in reference structure across biophysical environments

Patterns of variation in active-fire forest structure are very complex, driven by multiple interactions between fire, topography, and moisture (Kane *et al.*, 2013; Collins *et al.*, 2016). Some of this variation can be explained by elevation, water balance, and topographic position. For example, Collins *et al.* (2015) found that elevation and AET strongly differentiated between different classes of tree size and stand basal area, Kane *et al.* (2015b) found that AET and Deficit, along with slope and topographic position, were good predictors of canopy cover and tree height in twice-burned stands, and Lydersen and North (2012) found gradients of tree size and density associated with slope position, which differentiated between structural conditions better than aspect did. However, there was residual variation around these patterns in all cases. Our results suggest that the way the biophysical environment drives structure in active-fire landscapes is context-dependent, which may partially account for high amounts of unexplained variation in earlier research. Here we provide examples illustrating the complex context dependency in relationships between the biophysical environment and structure.

We found that ridgetops had lower density, lower basal area, smaller tree clumps, and more open space than other landforms (Figure 6). This matches descriptions by Lydersen and North (2012), who suggest that ridges uniquely combine lower productivity with more severe fire effects (i.e., more fire mortality) to result in a fundamentally different growing environment than other landforms. However, climate conditions can alter or enhance this relationship. For instance, the basic relationship between landform and density is reversed in the Xeric High Montane climate class, where ridges are similar to NE slopes while SW slopes have the lowest density

(Figure 6). One possible explanation is that this climate class is characterized by shallow, rocky soils throughout, so ridgetop soil conditions are not very different from other landforms. This normalization of landform effects may allow the (usually less important) effect of aspect on insolation to be expressed in the form of reduced density on SW slopes. In contrast, the relationship between landform and density is enhanced in the Cold Dry High Montane class, where ridgetop density was lower than density on other landforms by a much greater margin than in any other climate class (Figure 6). One possible explanation for this pattern is that ridges in this climate class, which was the only sampled climate class with average T_{min} values below 0° C (Figure S1.2), experience strong winds carrying damaging ice crystals more commonly than warmer classes, and so the uniquely difficult growing environment found on ridges is made even more difficult relative to other climate classes.

A strongly context-dependent relationship was observed between landform and mean clump size. Overall, clump sizes in valleys were not significantly different than for any other landform; however, in the warmest and driest climate classes valleys had significantly larger clumps on average. For the Xeric Mid Montane and Xeric High Montane classes the difference was approximately a factor of 2, while the Warm Dry Low Montane class, the hottest class sampled, the difference was a factor of over 100 (Figure 6). This pattern, along with the patterns related to ridgetops discussed above, suggests that while broad conclusions about structural variation across elevation, water balance, and topography may be helpful guideposts, the signs and magnitudes of relationships between these factors and structure are not consistent across biophysical space.

4.4 Using reference condition data in forest management

The structural data for Sierra Nevada reference areas presented here are intended to be applied to forest restoration planning and treatments. The envelopes of forest structure indices (Figure 5) as well as more detailed reference area descriptions (Supplement 3) can provide quantitative waypoints for interpreting current conditions and planning restoration treatments or comparing to post-treatment conditions for monitoring. The most consistent finding from studies investigating the structure of contemporary frequent-fire forests is that both the kinds and proportions of structural conditions are extremely variable at landscape scales. Thus, it is important to manage for wide and flexible ranges of variation at multiple scales rather than managing for one specific condition at any scale (Larson and Churchill, 2012; Hessburg *et al.*, 2015; Collins *et al.*, 2016).

Given the complex relationships between environmental setting and reference condition structure, it is valuable to use the most biophysically analogous data available for evaluating departure from reference conditions. We regard the climate classes as a coarse-scale filter and the LMUs as a fine-scale filter for matching biophysical analogs. In this framework, a departed landscape is first matched to a suitable set of reference areas based on matching climate classes. Then comparisons are made between matching LMU facets within the departed and reference areas, i.e., ridges are compared to ridges and valleys are compared to valleys, etc. This approach should ensure that the reference ranges of variation selected represent resilient conditions for the departed site in question.

Evaluating departure from the results presented here is more straightforward if lidar data are available for the departed area under analysis. This allows for consistent data processing and direct comparisons between two TAO-based sets of metrics. However, the reference conditions we report can also be compared to ground-based measurements (i.e., tree lists) as long as the

limitations of lidar measurements are accounted for. Specifically, each TAO may represent between one and several trees, and so measures of TAO density and clump sizes will be smaller than measures of tree density and clump sizes. For these measures our results can be taken as a lower range estimate. On the other hand, our results for basal area should be close to the actual values, since lidar accurately captures the larger trees that constitute most of the basal area (Lutz *et al.*, 2012; Jeronimo *et al.*, 2018). Similarly, since lidar is very effective at measuring canopy gaps our results for the open space index should be very similar to results from a field-measured stem map (Koukoulas and Blackburn, 2004).

5. Conclusions

Measuring reference conditions across contemporary active-fire landscapes using lidar affords some key advantages over historical reference conditions and field-based sampling. Forest structure in active-fire landscapes is highly variable at multiple scales (Fry *et al.*, 2014; Belote *et al.*, 2015; Collins *et al.*, 2016). By studying contemporary conditions of restored areas over hundreds or thousands of contiguous hectares we were able to capture the full range of variability present today, including dense aggregations of hundreds of trees as well as large meandering openings snaking across dozens of hectares. These features would not have been practically measureable with reconstruction techniques or using ground-based surveys.

In this study we have analyzed and presented results representing ranges of structure at scales of topographic facets with areas around 2-20 ha. However, spatial heterogeneity in forest structure also occurs across broader scales: landscape conditions are a mix of a tree clump and canopy opening patch mosaic, shrubland and herbland covering dozens of hectares of potential forest sites, and some large aggregations of closed-canopy forest (Hessburg *et al.*, 2005; Kane *et al.*, 2014). Analyzing these reference areas in terms of landscape patches (e.g. seral stages *sensu*

Gärtner *et al.*, 2008) would be a valuable complement to the finer-scale data we have presented here.

An important drawback to using lidar measurements as the sole data source is that there are no composition data to go along with the structural measurements. Composition data must come from other sources such as modeling or imputation from structure, Landsat or other spectral data sources, or field surveys (Jeronimo *et al.*, 2018). Lidar is also only able to characterize the shrub layer in general terms (Martinuzzi *et al.*, 2009), which can be a problem since shrubs, as angiosperms, are a key element of mammal and bird diets in the Sierra Nevada (Lutz *et al.*, 2014; Lutz *et al.*, 2017). However, the reference conditions we provide here are associated with species assemblages (Table 2). Since restoration treatments typically favor fire- and drought-tolerant species it should be clear what species will be expected for retention in a given climate class. Nevertheless, field visits and silvicultural knowledge will still be necessary to set realistic composition targets.

While the reference areas we present here have experienced some reintroduction to fire, they also previously experienced decades of fire suppression and other anthropogenic disturbances (e.g., grazing). We do not claim that these forests are fully restored nor that they are in the most resilient condition possible. Nevertheless, these areas have burned multiple times and are still forested with a degree of heterogeneity comparable to historical measurements. They are the best extant examples of Sierra Nevada mixed-conifer forests under an active fire regime.

References

Asner, G.P., Knapp, D.E., Kennedy-Bowdoin, T., Jones, M.O., Martin, R.E., Boardman, J.W., Field, C.B., 2007. Carnegie airborne observatory: in-flight fusion of hyperspectral imaging and waveform light detection and ranging for three-dimensional studies of ecosystems. Journal of Applied Remote Sensing 1, 013536.

Barth, M.A., Larson, A.J., Lutz, J.A., 2015. A forest reconstruction model to assess changes to Sierra Nevada mixed-conifer forest during the fire suppression era. Forest Ecology and Management 354, 104-118.

Bechtold, W.A., Patterson, P.L., 2005. The enhanced forest inventory and analysis program: national sampling design and estimation procedures. US Department of Agriculture Forest Service, Southern Research Station Asheville, North Carolina.

Becker, K.M., Lutz, J.A., 2016. Can low-severity fire reverse compositional change in montane forests of the Sierra Nevada, California, USA? Ecosphere 7.

Belote, R.T., Larson, A.J., Dietz, M.S., 2015. Tree survival scales to community-level effects following mixed-severity fire in a mixed-conifer forest. Forest Ecology and Management 353, 221-231.

Boynton, R., Shipley, K., Roth, N., Underwood, E., 2015. The Landscape Management Unit (LMU) Tool. URL: http://ice.ucdavis.edu/project/landscape_management_unit_lmu_tool. Accessed 12/1/2017.

Bray, J.R., Curtis, J.T., 1957. An Ordination of the Upland Forest Communities of Southern Wisconsin. Ecological Monographs 27, 325-349.

Brown, J.H., Gillooly, J.F., Allen, A.P., Savage, V.M., West, G.B., 2004. Toward a metabolic theory of ecology. Ecology 85, 1771-1789.

623 Cal Fire, 2018. FRAP - Data Fire Perimeters. In.
624 Christensen, N.L., Bartuska, A.M., Brown, J.H., Carpenter, S., D'Antonio, C., Francis, R.,
625 Franklin, J.F., MacMahon, J.A., Noss, R.F., Parsons, D.J., 1996. The report of the
626 Ecological Society of America committee on the scientific basis for ecosystem
627 management. Ecological Applications 6, 665-691.
628 Churchill, D.J., Carnwath, G.C., Larson, A.J., Jeronimo, S.M.A., 2017. Historical forest
629 structure, composition, and spatial pattern in dry conifer forests of the western Blue
630 Mountains, Oregon. General Technical Report PNW-GTR-956. USDA Forest Service
631 Pacific Northwest Research Station, Portland, OR.
632 Churchill, D.J., Larson, A.J., Dahlgreen, M.C., Franklin, J.F., Hessburg, P.F., Lutz, J.A., 2013.
633 Restoring forest resilience: from reference spatial patterns to silvicultural prescriptions
634 and monitoring. Forest Ecology and Management 291, 442-457.
635 Collins, B.M., Everett, R.G., Stephens, S.L., 2011. Impacts of fire exclusion and recent managed
636 fire on forest structure in old growth Sierra Nevada mixed-conifer forests. Ecosphere 2,
637 1-14.
638 Collins, B.M., Lydersen, J.M., Everett, R.G., Fry, D.L., Stephens, S.L., 2015. Novel
639 characterization of landscape-level variability in historical vegetation structure. In.
640 Collins, B.M., Lydersen, J.M., Fry, D.L., Wilkin, K., Moody, T., Stephens, S.L., 2016.
641 Variability in vegetation and surface fuels across mixed-conifer-dominated landscapes
642 with over 40 years of natural fire. Forest Ecology and Management 381, 74-83.
643 Collins, B.M., Stephens, S.L., 2010. Stand-replacing patches within a ‘mixed severity’fire
644 regime: quantitative characterization using recent fires in a long-established natural fire
645 area. Landscape Ecology 25, 927-939.

DeRose, R.J., Long, J.N., 2014. Resistance and resilience: A conceptual framework for silviculture. Forest Science 60, 1205-1212.

Dobrowski, S.Z., Abatzoglou, J., Swanson, A.K., Greenberg, J.A., Mynsberge, A.R., Holden, Z.A., Schwartz, M.K., 2013. The climate velocity of the contiguous United States during the 20th century. Global Change Biology 19, 241-251.

Eidenshink, J., Schwind, B., Brewer, K., Zhu, Z., Quayle, B., Howard, S., 2007. A project for monitoring trends in burn severity. Fire Ecology 3 (1): 3-21. Fire Ecology Special Issue Vol 3, 4.

EPA, USGS, 2018. National Hydrography Dataset Plus Version 2. URL: https://www.epa.gov/waterdata/nhdplus-national-hydrography-dataset-plus. Accessed 12/1/2017.

Flint, L.E., Flint, A.L., Thorne, J.H., Boynton, R., 2013. Fine-scale hydrologic modeling for regional landscape applications: the California Basin Characterization Model development and performance. Ecological Processes 2, 25.

Flint, L.E., Flint, A.L., Thorne, J.H., Boynton, R., 2014. 2014 California BCM (Basin Characterization Model) Downscaled Climate and Hydrology - 30-year Summaries. California Climate Commons.

Franklin, J.F., Johnson, K.N., 2012. A restoration framework for federal forests in the Pacific Northwest. Journal of Forestry 110, 429-439.

Franklin, J.F., Johnson, K.N., Johnson, D.L., 2018. Ecological Forest Management. Waveland Press, Long Grove, IL.

667 Fry, D.L., Stephens, S.L., Collins, B.M., North, M.P., Franco-Vizcaíno, E., Gill, S.J., 2014.
668 Contrasting spatial patterns in active-fire and fire-suppressed Mediterranean climate old-
669 growth mixed conifer forests. PLoS One 9, e88985.
670 Fulé, P.Z., Covington, W.W., Moore, M.M., 1997. Determining reference conditions for
671 ecosystem management of southwestern ponderosa pine forests. Ecological Applications
672 7, 895-908.
673 Gärtner, S., Reynolds, K., Hessburg, P., Hummel, S., Twery, M., 2008. Decision support for
674 evaluating landscape departure and prioritizing forest management activities in a
675 changing environment. Forest Ecology and Management 256, 1666-1676.
676 Hagmann, R.K., Franklin, J.F., Johnson, K.N., 2013. Historical structure and composition of
677 ponderosa pine and mixed-conifer forests in south-central Oregon. Forest Ecology and
678 Management 304, 492-504.
679 Hagmann, R.K., Franklin, J.F., Johnson, K.N., 2014. Historical conditions in mixed-conifer
680 forests on the eastern slopes of the northern Oregon Cascade Range, USA. Forest
681 Ecology and Management 330, 158-170.
682 Hanberry, B.B., Noss, R.F., Safford, H.D., Allison, S.K., Dey, D.C., Hart, J.L., Buchanan, M.L.,
683 Cox, L.E., Dumroese, R.K., Palik, B.J., 2015. Restoration is preparation for the future.
684 Journal of Forestry 113, 425-429.
685 Hart, J.L., Buchanan, M.L., Cox, L.E., 2015. Has Forest Restoration Been Freed from the Bonds
686 of History? Journal of Forestry 113, 429-430.
687 Hessburg, P., Reynolds, K., Salter, R., Dickinson, J., Gaines, W., Harrod, R., 2013. Landscape
688 Evaluation for Restoration Planning on the Okanogan-Wenatchee National Forest, USA.
689 Sustainability 5, 805.

690 Hessburg, P.F., Agee, J.K., Franklin, J.F., 2005. Dry forests and wildland fires of the inland
691 Northwest USA: contrasting the landscape ecology of the pre-settlement and modern
692 eras. Forest Ecology and Management 211, 117-139.
693 Hessburg, P.F., Churchill, D.J., Larson, A.J., Haugo, R.D., Miller, C., Spies, T.A., North, M.P.,
694 Povak, N.A., Belote, R.T., Singleton, P.H., Gaines, W.L., Keane, R.E., Aplet, G.H.,
695 Stephens, S.L., Morgan, P., Bisson, P.A., Rieman, B.E., Salter, R.B., Reeves, G.H., 2015.
696 Restoring fire-prone Inland Pacific landscapes: seven core principles. Landscape Ecology
697 30, 1805-1835.
698 Hessburg, P.F., Smith, B.G., Salter, R.B., 1999. Using Estimates of Natural Variation to Detect
699 Ecologically Important Change in Forest Spatial Patterns: A Case Study, Cascade Range,
700 Eastern Washington. In: United States Department of Agriculture, F.S. (Ed.). Pacific
701 Northwest Research Station, Portland, OR.
702 Heyerdahl, E.K., Loehman, R.A., Falk, D.A., 2014. Mixed-severity fire in lodgepole pine
703 dominated forests: are historical regimes sustainable on Oregon's Pumice Plateau, USA?
704 Canadian Journal of Forest Research 44, 593-603.
705 Jeronimo, S.M.A., Kane, V.R., Churchill, D.J., McGaughey, R.J., Franklin, J.F., 2018. Applying
706 lidar individual tree detection to management of structurally diverse forest landscapes.
707 Journal of Forestry 116, 336-346.
708 Johnstone, J.F., Allen, C.D., Franklin, J.F., Frelich, L.E., Harvey, B.J., Higuera, P.E., Mack,
709 M.C., Meentemeyer, R.K., Metz, M.R., Perry, G.L., 2016. Changing disturbance regimes,
710 ecological memory, and forest resilience. Frontiers in Ecology and the Environment 14,
711 369-378.

712 Kane, V.R., Cansler, C.A., Povak, N.A., Kane, J.T., McGaughey, R.J., Lutz, J.A., Churchill,
713 D.J., North, M.P., 2015a. Mixed severity fire effects within the Rim fire: relative
714 importance of local climate, fire weather, topography, and forest structure. Forest
715 Ecology and Management 358, 62-79.
716 Kane, V.R., Lutz, J.A., Cansler, C.A., Povak, N.A., Churchill, D.J., Smith, D.F., Kane, J.T.,
717 North, M.P., 2015b. Water balance and topography predict fire and forest structure
718 patterns. Forest Ecology and Management 338, 1-13.
719 Kane, V.R., Lutz, J.A., Roberts, S.L., Smith, D.F., McGaughey, R.J., Povak, N.A., Brooks, M.L.,
720 2013. Landscape-scale effects of fire severity on mixed-conifer and red fir forest
721 structure in Yosemite National Park. Forest Ecology and Management 287, 17-31.
722 Kane, V.R., North, M.P., Lutz, J.A., Churchill, D.J., Roberts, S.L., Smith, D.F., McGaughey,
723 R.J., Kane, J.T., Brooks, M.L., 2014. Assessing fire effects on forest spatial structure
724 using a fusion of Landsat and airborne LiDAR data in Yosemite National Park. Remote
725 Sensing of Environment 151, 89-101.
726 Kaufmann, M.R., Huckaby, L.S., Regan, C.M., Popp, J., 1998. Forest reference conditions for
727 ecosystem management in the Sacramento Mountains, New Mexico.
728 Keeley, J.E., Stephenson, N.L., 2000. Restoring natural fire regimes to the Sierra Nevada in an
729 era of global change. In: Cole, D.N., McCool, S.F., Borrie, W.T., O'Loughlin, J. (Eds.),
730 Wilderness science in a time of change conference Volume 5: Wilderness ecosystems,
731 threats, and management. Proceedings. RMRS-P-15-VOL5. USDA Forest Service Rocky
732 Mountain Research Station, Missoula, MT.
733 Kilgore, B.M., 1973. The ecological role of fire in Sierran conifer forests: its application to
734 national park management. Quaternary Research 3, 496-513.

735 Knapp, E.E., Skinner, C.N., North, M.P., Estes, B.L., 2013. Long-term overstory and understory
736 change following logging and fire exclusion in a Sierra Nevada mixed-conifer forest.
737 Forest Ecology and Management 310, 903-914.
738 Kolden, C.A., Abatzoglou, J.T., Lutz, J.A., Cansler, C.A., Kane, J.T., Van Wagtendonk, J.W.,
739 Key, C.H., 2015. Climate contributors to forest mosaics: ecological persistence following
740 wildfire. Northwest Science 89, 219-238.
741 Kolden, C.A., Lutz, J.A., Key, C.H., Kane, J.T., van Wagtendonk, J.W., 2012. Mapped versus
742 actual burned area within wildfire perimeters: characterizing the unburned. Forest
743 Ecology and Management 286, 38-47.
744 Koukoulas, S., Blackburn, G.A., 2004. Quantifying the spatial properties of forest canopy gaps
745 using LiDAR imagery and GIS. International Journal of Remote Sensing 25, 3049-3072.
746 Langille, H.D., 1903. Forest conditions in the Cascade Range forest reserve, Oregon. United
747 States Geological Survey, Government Printing Office, Washington, DC.
748 Larson, A.J., Churchill, D.J., 2012. Tree spatial patterns in fire-frequent forests of western North
749 America, including mechanisms of pattern formation and implications for designing fuel
750 reduction and restoration treatments. Forest Ecology and Management 267, 74-92.
751 Laudenslayer, W.F., Darr, H.H., 1990. Historical effects of logging on forests of the Cascade and
752 Sierra Nevada Ranges of California.
753 LeFevre, M.E., Churchill, D.J., Larson, A.J., Kane, V.R., in prep. An application of spatial
754 reference conditions of the Colville National Forest, Washington.
755 Leiburg, J., 1900. Cascade Range and Ashland forest reserves and adjacent regions. In, Twenty-
756 first annual report of the United States Geological Survey to the Secretary of the United
757 States 1899-1900. Government Printing Office, Washington, DC.

Lutz, J.A., Furniss, T.J., Germain, S.J., Becker, K.M., Blomdahl, E.M., Jeronimo, S., Cansler, C.A., Freund, J.A., Swanson, M.E., Larson, A.J., 2017. Shrub communities, spa-tial patterns, and shrub-mediated tree mortality following reintroduced fire in Yosemite National Park, California, USA. Fire Ecology 13, 104-126.

Lutz, J.A., Furniss, T.J., Johnson, D.J., Davies, S.J., Allen, D., Alonso, A., Anderson-Teixeira, K.J., Andrade, A., Baltzer, J., Becker, K.M.L., Blomdahl, E.M., Bourg, N.A., Bunyavejchewin, S., Burslem, D.F.R.P., Cansler, C.A., Cao, K., Cao, M., Cárdenas, D., Chang, L.W., Chao, K.J., Chao, W.C., Chiang, J.M., Chu, C., Chuyong, G.B., Clay, K., Condit, R., Cordell, S., Dattaraja, H.S., Duque, A., Ewango, C.E.N., Fischer, G.A., Fletcher, C., Freund, J.A., Giardina, C., Germain, S.J., Gilbert, G.S., Hao, Z., Hart, T., Hau, B.C.H., He, F., Hector, A., Howe, R.W., Hsieh, C.F., Hu, Y.H., Hubbell, S.P., Inman-Narahari, F.M., Itoh, A., Janík, D., Kassim, A.R., Kenfack, D., Korte, L., Král, K., Larson, A.J., Li, Y., Lin, Y., Liu, S., Lum, S., Ma, K., Makana, J.R., Malhi, Y., McMahon, S.M., McShea, W.J., Memiaghe, H.R., Mi, X., Morecroft, M., Musili, P.M., Myers, J.A., Novotny, V., de Oliveira, A., Ong, P., Orwig, D.A., Ostertag, R., Parker, G.G., Patankar, R., Phillips, R.P., Reynolds, G., Sack, L., Song, G.Z.M., Su, S.H., Sukumar, R., Sun, I.F., Suresh, H.S., Swanson, M.E., Tan, S., Thomas, D.W., Thompson, J., Uriarte, M., Valencia, R., Vicentini, A., Vrška, T., Wang, X., Weiblen, G.D., Wolf, A., Wu, S.H., Xu, H., Yamakura, T., Yap, S., Zimmerman, J.K., 2018. Global importance of large-diameter trees. Global Ecology and Biogeography 27, 849-864.

Lutz, J.A., Larson, A.J., Freund, J.A., Swanson, M.E., Bible, K.J., 2013. The importance of large-diameter trees to forest structural heterogeneity. PLoS One 8, e82784.

780 Lutz, J.A., Larson, A.J., Swanson, M.E., Freund, J.A., 2012. Ecological importance of large-
781 diameter trees in a temperate mixed-conifer forest. PLoS One 7, e36131.
782 Lutz, J.A., Schwindt, K.A., Furniss, T.J., Freund, J.A., Swanson, M.E., Hogan, K.I., Kenagy,
783 G.E., Larson, A.J., 2014. Community composition and allometry of Leucothoe davisiae,
784 Cornus sericea, and Chrysolepis sempervirens. Canadian Journal of Forest Research 44,
785 677-683.
786 Lutz, J.A., van Wagtendonk, J.W., Franklin, J.F., 2010. Climatic water deficit, tree species
787 ranges, and climate change in Yosemite National Park. Journal of Biogeography 37, 936-
788 950.
789 Lutz, J.A., Van Wagtendonk, J.W., Thode, A.E., Miller, J.D., Franklin, J.F., 2009. Climate,
790 lightning ignitions, and fire severity in Yosemite National Park, California, USA.
791 International Journal of Wildland Fire 18, 765-774.
792 Lydersen, J., North, M., 2012. Topographic variation in structure of mixed-conifer forests under
793 an active-fire regime. Ecosystems 15, 1134-1146.
794 Lydersen, J.M., Collins, B.M., Brooks, M.L., Matchett, J.R., Shive, K.L., Povak, N.A., Kane,
795 V.R., Smith, D.F., 2017. Evidence of fuels management and fire weather influencing fire
796 severity in an extreme fire event. Ecological Applications.
797 Lydersen, J.M., North, M.P., Collins, B.M., 2014. Severity of an uncharacteristically large
798 wildfire, the Rim Fire, in forests with relatively restored frequent fire regimes. Forest
799 Ecology and Management 328, 326-334.
800 Lydersen, J.M., North, M.P., Knapp, E.E., Collins, B.M., 2013. Quantifying spatial patterns of
801 tree groups and gaps in mixed-conifer forests: reference conditions and long-term

changes following fire suppression and logging. Forest Ecology and Management 304, 370-382.

Mallek, C., Safford, H., Viers, J., Miller, J., 2013. Modern departures in fire severity and area vary by forest type, Sierra Nevada and southern Cascades, California, USA. Ecosphere 4, 1-28.

Martinuzzi, S., Vierling, L.A., Gould, W.A., Falkowski, M.J., Evans, J.S., Hudak, A.T., Vierling, K.T., 2009. Mapping snags and understory shrubs for a LiDAR-based assessment of wildlife habitat suitability. Remote Sensing of Environment 113, 2533-2546.

McCune, B., Grace, J.B., Urban, D.L., 2002. Analysis of ecological communities. MjM software design Gleneden Beach, OR.

McGaughey, R.J., 2018. FUSION/LDV: Software for LIDAR Data Analysis and Visualization: Version 3.70. USDA Forest Service Pacific Northwest Research Station, Seattle, WA.

Millar, C.I., Woolfenden, W.B., 1999. The role of climate change in interpreting historical variability. Ecological Applications 9, 1207-1216.

Moore, M.M., Wallace Covington, W., Fule, P.Z., 1999. Reference conditions and ecological restoration: a southwestern ponderosa pine perspective. Ecological Applications 9, 1266-1277.

Munger, T.T., 1912. The future yield of yellow pine stands in Oregon. Unpublished report. Transcript of archived original available from fs.usda.gov/detail/umatilla/learning/history-culture. In. Government Printing Office, Washington, DC.

North, M., Collins, B.M., Stephens, S., 2012. Using fire to increase the scale, benefits, and future maintenance of fuels treatments. Journal of Forestry 110, 392-401.

North, M., Innes, J., Zald, H., 2007. Comparison of thinning and prescribed fire restoration treatments to Sierran mixed-conifer historic conditions. Canadian Journal of Forest Research 37, 331-342.

North, M., Stine, P., O'Hara, K., Zielinski, W., Stephens, S., 2009. An ecosystem management strategy for Sierran mixed-conifer forests, General Technical Report PSW-GTR-220. USDA Forest Service Pacific Southwest Research Station. Albany, CA.

North, M.P., Kane, J.T., Kane, V.R., Asner, G.P., Berigan, W., Churchill, D.J., Conway, S., Gutiérrez, R.J., Jeronimo, S., Keane, J., Koltunov, A., Mark, T., Moskal, M., Munton, T., Peery, Z., Ramirez, C., Sollmann, R., White, A., Whitmore, S., 2017. Cover of tall trees best predicts California spotted owl habitat. Forest Ecology and Management 405, 166-178.

Oksanen, J., Blanchet, F.G., Kindt, R., Legendre, P., Minchin, P.R., O'Hara, R.B., Simpson, G.L., Solymos, P., Stevens, M.H.H., Wagner, H., 2016. vegan: Community Ecology Package.

Parsons, D.J., Botti, S.J., 1996. Restoration of Fire in National Parks. In: Hardy, C.C., Arno, S.F. (Eds.), The use of fire in forest restoration. General Technical Report INT-GTR-341. USDA Forest Service Intermountain Research Station, Ogden, UT.

Parsons, D.J., van Wagtendonk, J.W., 1996. Fire research and management in the Sierra Nevada National Parks. Science and ecosystem management in the national parks. University of Arizona Press, Tucson, Arizona, USA, 25-48.

R Core Team, 2016. R: A language and environment for statistical computing. R Foundation for Statistical Computing, Vienna, Austria.

847 Scholl, A.E., Taylor, A.H., 2010. Fire regimes, forest change, and self-organization in an old-
848 growth mixed-conifer forest, Yosemite National Park, USA. Ecological Applications 20,
849 362-380.
850 Seidl, R., Spies, T.A., Peterson, D.L., Stephens, S.L., Hicke, J.A., 2015. Searching for resilience:
851 addressing the impacts of changing disturbance regimes on forest ecosystem services.
852 Journal of applied ecology.
853 Skinner, C.N., Chang, C., 1996. Fire regimes, past and present. In, Sierra Nevada Ecosystem
854 Project: Final report to Congress, vol II. Assessments and scientific basis for management
855 options. University of California Center for Water and Wildland Resources, Davis,
856 California.
857 Soil Survey Staff, 2018. U.S. General Soil Map (STATSGO2). Natural Resources Conservation
858 Service, United States Department of Agriculture.
859 Stephens, S.L., Agee, J.K., Fulé, P., North, M., Romme, W., Swetnam, T., Turner, M.G., 2013.
860 Managing forests and fire in changing climates. Science 342, 41-42.
861 Stephens, S.L., Collins, B.M., Biber, E., Fulé, P.Z., 2016. US federal fire and forest policy:
862 emphasizing resilience in dry forests. Ecosphere 7.
863 Stephens, S.L., Lydersen, J.M., Collins, B.M., Fry, D.L., Meyer, M.D., 2015. Historical and
864 current landscape-scale ponderosa pine and mixed conifer forest structure in the Southern
865 Sierra Nevada. Ecosphere 6, 1-63.
866 Stephens, S.L., Millar, C.I., Collins, B.M., 2010. Operational approaches to managing forests of
867 the future in Mediterranean regions within acontext of changing climates. Environmental
868 Research Letters 5, 024003.

869 Stephens, S.L., Ruth, L.W., 2005. FEDERAL FOREST-FIRE POLICY IN THE UNITED
870 STATES. Ecological Applications 15, 532-542.
871 Stephenson, N., 1998. Actual evapotranspiration and deficit: biologically meaningful correlates
872 of vegetation distribution across spatial scales. Journal of Biogeography 25, 855-870.
873 Taylor, A.H., 2010. Fire disturbance and forest structure in an old-growth Pinus ponderosa
874 forest, southern Cascades, USA. Journal of Vegetation Science 21, 561-572.
875 Underwood, E.C., Viers, J.H., Quinn, J.F., North, M., 2010. Using topography to meet wildlife
876 and fuels treatment objectives in fire-suppressed landscapes. Environmental Management
877 46, 809-819.
878 USDA Forest Service, 2018. FSGeodata Clearinghouse. In.
879 Van de Water, K., North, M., 2011. Stand structure, fuel loads, and fire behavior in riparian and
880 upland forests, Sierra Nevada Mountains, USA; a comparison of current and
881 reconstructed conditions. Forest Ecology and Management 262, 215-228.
882 van Wagtendonk, J., Fites-Kaufman, J.A., 2006. Sierra Nevada bioregion. In: Sugihara, N.G.,
883 van Wagtendonk, J.W., Shaffer, K.E., Fites-Kaufman, J.A., Thode, A.D. (Eds.), Fire in
884 California's Ecosystems. University of California Press, Berkeley, CA, pp. 264–294.
885 van Wagtendonk, J.W., 1994. Spatial patterns of lightning strikes and fires in Yosemite National
886 Park. In, Proceedings of the 12th conference on fire and forest meteorology, pp. 223-231.
887 van Wagtendonk, J.W., 2007. The History and Evolution of Wildland Fire Use. Fire Ecology 3,
888 3-17.
889 van Wagtendonk, J.W., Cayan, D.R., 2008. Temporal and spatial distribution of lightning strikes
890 in California in relation to large-scale weather patterns. Fire Ecology 4, 34-56.

van Wagtendonk, J.W., Lutz, J.A., 2007. Fire regime attributes of wildland fires in Yosemite National Park, USA. Fire Ecology 3, 34-52.

van Wagtendonk, J.W., van Wagtendonk, K.A., Thode, A.E., 2012. Factors associated with the severity of intersecting fires in Yosemite National Park, California, USA. Fire Ecology 8, 11-31.

Vereecken, H., Schnepf, A., Hopmans, J.W., Javaux, M., Or, D., Roose, T., Vanderborght, J., Young, M., Amelung, W., Aitkenhead, M., 2016. Modeling soil processes: Review, key challenges, and new perspectives. Vadose Zone Journal 15.

Weatherspoon, C.P., Skinner, C.N., 1996. Landscape-level strategies for forest fuel management.

Wiggins, H.L., 2017. The influence of tree height on lidar's ability to accurately characterize forest structure and spatial pattern across reference landscapes. Master of Science Thesis. University of Montana, Missoula, MT.

Supplements to Chapter 1: Structure and pattern vary by climate and landform across active-fire landscapes in the montane Sierra Nevada

Table of Contents for Supplements

Supplement 1: Additional table and figures

Table S1.1 Species codes, Latin names, and common names key for Table 2.

Species code	Latin name	Common name
ABCO	*Abies concolor*	White fir
ABMA	*Abies magnifica*	Red fir
AECA	*Aesculus californica*	California buckeye
CADE	*Calocedrus decurrens*	Incense-cedar
JUCA	*Juniperus californica*	California juniper
JUOC	*Juniperus occidentalis*	Western juniper
LIDE	*Lithocarpus densiflorus*	Tanoak
PIAL	*Pinus ablicaulis*	Whitebark pine
PIBA	*Pinus baulforiana*	Foxtail pine
PICO	*Pinus contorta*	Lodgepole pine
PIJE	*Pinus jeffreyi*	Jeffrey pine
PILA	*Pinus lambertiana*	Sugar pine
PIMO	*Pinus monophylla*	Single-leaf pinyon
PIMO2	*Pinus monticola*	Western white pine
PIPO	*Pinus ponderosa*	Ponderosa pine
PISA	*Pinus sabiniana*	Gray pine
PSME	*Pseudotsuga menziesii*	Douglas-fir
QUCH	*Quercus chrysolepis*	Canyon live oak
QUDO	*Quercus douglasii*	Blue oak
QUKE	*Quercus kelloggii*	Black oak
QUWI	*Quercus wislizeni*	Interior live oak
TSME	*Tsuga mertensiana*	Mountain hemlock

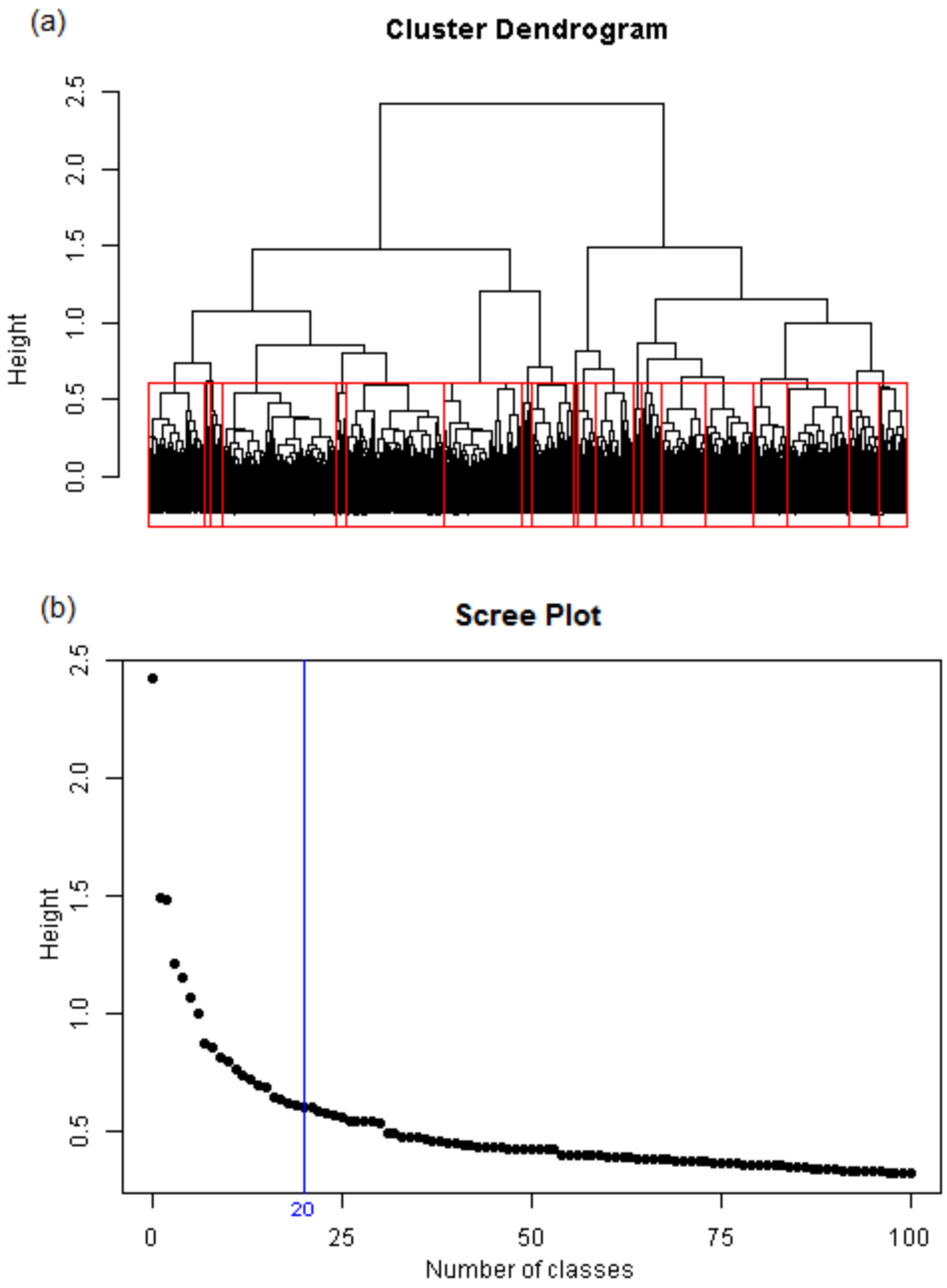

Figure S1.1 Dendrogram (a) and scree plot (b) for hierarchical classification of climate (actual evapotranspiration, climatic water deficit, and January minimum temperature) on the basis of catchments.

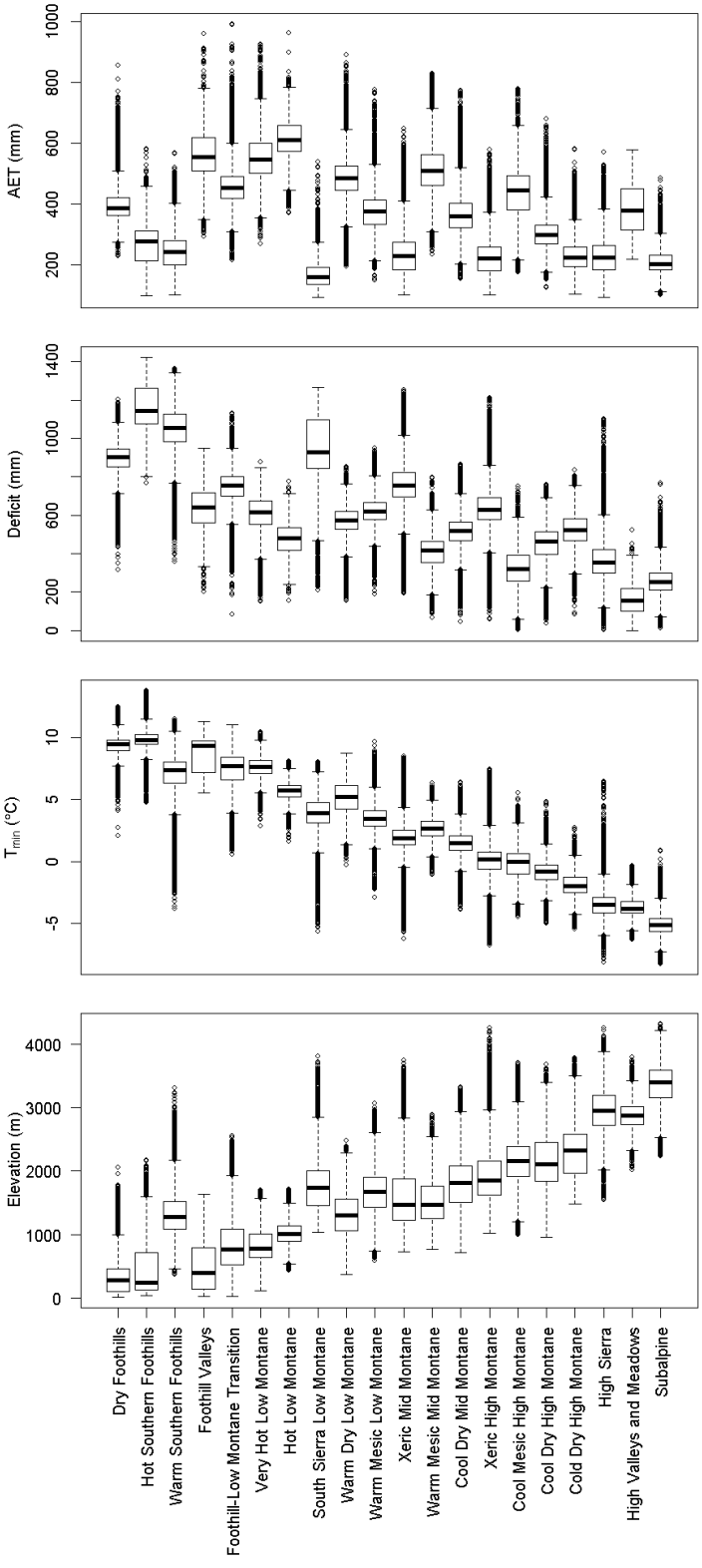

Figure S1.2 Characteristics of the 20 climate classes in terms of actual evapotranspiration (AET), climatic water deficit (Deficit) and January minimum temperature (T_{min}), which were the input variables for the classification, as well as elevation, for reference. See Table 2 for class descriptions.

Supplement 2: Analyzing the sensitivity of climate classification to plausible variation in soil water holding capacity

Introduction

Our climate classification for defining biophysical analogs was defined on the basis of January minimum temperature (T_{min}), actual evapotranspiration (AET), and climatic water deficit (Deficit). We drew this inputs from the California Climate Commons database (Flint *et al.*, 2014), and they were originally calculated by Flint *et al.* (2013) as part of the Basin Characterization Model (BCM). The Flint *et al.* (2013) methodology models AET and Deficit as the decomposition of potential evapotranspiration (PET), which is in turn a function of air temperature and solar radiation. How PET is partitioned into AET and Deficit depends on water input from precipitation and water storage in the soil. Thus, the primary inputs into our climate classification are air temperature, solar radiation, precipitation, and soil water holding capacity.

Of these four inputs, the three climate-related variables have well-known error characteristics and were evaluated against weather station data by Flint and Flint (2008). In contrast, the soil water holding capacity (WHC) inputs, which were drawn from the US General Soil Map (STATSGO2) (Soil Survey Staff, 2018), do not have well-known error associated with them and were not evaluated against any other data source by Flint and Flint (2008) or Flint *et al.* (2013). Furthermore, these inputs are highly oversimplified: the STATSGO2 data represent soil characteristics as homogeneous values over large polygons (>1000 ha) even though soil properties like WHC are highly variable at fine scales (Vereecken *et al.*, 2016). Here we test the sensitivity of our climate classification to variation in WHC inputs using a Monte Carlo simulation approach.

Methods

Our approach to testing the sensitivity of our climate classification to variation in WHC followed these steps (1) associate each STATSGO2 map unit with a distribution of plausible WHC values, (2) simulate many WHC layers for the Sierra Nevada by making draws from the plausible distributions, (3) estimate new partitioning of PET into AET and Deficit based on simulated WHC layers, (4) create a new set of climate classes for each simulated WHC layer, and (5) assess agreement among new climate classes.

Plausible WHC distributions and Monte Carlo simulation

Each STATSGO2 polygon is associated with a soil map unit that theoretically represents a relatively homogeneous set of soil properties (Soil Survey Staff, 2018). Each map unit is composed of one or more components in different proportions, where a component represents a single soil series. Values like WHC are calculated for map units by taking averages among constituent components, weighted by the proportion of the map unit assigned to each component. In the STATSGO database, each component has a low, representative (modal), and high value for WHC (Natural Resources Conservation Service, 2014); it is the representative value that is averaged into the map unit-level WHC metric.

We wanted to represent the actual variation of WHC as a distribution for each map unit. We started by representing WHC for each component as a distribution. We chose to use gamma distributions because WHC values are positive real numbers and gamma provided better fits than lognormal and other tested distributions. We took the low, representative, and high values for each component to represent the 5^{th}, 50^{th}, and 95^{th} percentile WHC values, respectively, assuming that the soil surveys captured most but not all of the actual range of variation in soil

characteristics. We fit a gamma distribution to these three values at the given quantiles using the optim function in R (R Core Team, 2016) with a finite-difference gradient approximation and a variable metric optimizing algorithm (Shanno, 1970). We brought the component-level distributions up to the map unit level by combining the components in a mixture distribution weighted by component proportions. The final distribution of map unit WHC followed this form:

$$\mathrm{WHC}_i \sim \sum_{j=1}^{n_i} \varphi_{ij}\mathrm{Gamma}\left(\alpha_{ij}, \beta_{ij}\right), \;\; i = 1 \ldots N \qquad \text{Equation S2.1}$$

where WHC_i is the WHC for map unit i, N is the number of map units, n_i is the number of components within map unit i, φ_{ij} is the proportion (summing to 1 for each i) of component j in map unit i, and α_{ij} and β_{ij} are the scale and rate parameters of the gamma distribution as estimated for component j of map unit i (Figure S2.1).

We made 200 simulated WHC maps for the Sierra Nevada using the same 270 m grid as the AET and Deficit inputs. We assigned each grid cell to a map unit based on the STATSGO2 polygon that the grid cell center fell into and made draws on a grid cell basis from the corresponding map unit-level WHC distributions. Importantly, this resulted in WHC layers varying at the grid cell scale, compared to the homogeneous polygon-wide values given by STATSGO2 (Figure S2.2).

Carrying new WHC through to AET and Deficit and climate classes

Because we did not have access to the actual implementation of the BCM and did not have resources to replicate it, we were not able to simply input the new WHC values into existing BCM calculations. Instead, we modeled the effect of WHC on AET and Deficit and used that model to create new AET and Deficit layers from the WHC draws. Since AET and Deficit sum to equal PET and PET is invariant to WHC, we modeled the proportion of PET assigned to AET (AET%) as a function of WHC. We also included precipitation data from BCM (Flint *et al.*,

2014) in the model, since this is the other major input affecting water balance. The model form we used was:

$$\mathrm{AET\%} = \beta_0 \mathrm{WHC}^{\beta_1} \mathrm{PPT}^{\beta_2} \qquad \text{Equation S2.2}$$

with WHC in cm and PPT representing total annual precipitation in cm. We fit the model using the lm function in R (R Core Team, 2016) and obtained the following parameter estimates: $\beta_0 = -5.190$, $\beta_1 = 0.0666$, $\beta_2 = 0.000233$ ($r^2 = 0.82$, $p < 0.001$). We used this model to estimate AET% for each of the 200 simulated WHC layers, then multiplied AET% by PET to get AET estimates and subtracted those results from PET to get Deficit estimates. We ran the climate classification again on each of the new AET/Deficit pairs together with the original T_{min} layers using the same methods as in the main study. As in the main study, we cut the hierarchical classification trees at 20 classes.

Assessing agreement among classification results

Because hierarchical classification is unsupervised the classes resulting from each run do not necessarily align one-to-one with the classes from any other runs. However, we wanted to assess error in terms of one-to-one correspondence between each of the simulations and the original "reference" classes, so we relabeled classes to create correspondence after the fact. For each of the simulation runs we created a confusion matrix between the simulation classification and the reference classification. We permuted rows of the confusion matrix to maximize the sum of the major diagonal using a brute force approach. This yielded the class labeling with optimal class-wise correspondence. We assessed agreement between each simulation and the reference classification using Cohen's κ (Cohen, 1968) calculated from the optimized confusion matrices. We inspected the full distribution of κ values and visually analyzed maps of the simulations with the lowest, median, and highest κ values compared to the reference map.

Results and Discussion

The Monte Carlo simulation of variation in WHC led to classifications that matched the reference classification acceptably well. Values of κ ranged from 0.39 to 0.60 with a median of 0.53 (Figure S2.3), and were greater than 0.44 for 95% of simulations. Interpretation of κ values varies (Cohen, 1968; Fleiss, 1971; Randolph, 2005), but values in the range observed are typically considered moderate to good agreement. At the same time, higher numbers of classes lead to lower κ values for similar levels of agreement (Randolph, 2005). Given the relatively large number of classes we were testing (20) and the high degree of variability in soil inputs, we took the distribution of κ values to indicate that our climate classification is acceptably robust to uncertainty in the WHC input.

This finding agreed with our visual interpretation of the classifications with the best, median, and worst κ values (Figure S2.4), which showed largely consistent classification patterns. Areas where classification varied were consistently on the edges of class patches. This indicated that classification is less stable in transition zones, where changes in WHC tipped a classification one way or the other. Inspection of many of the confusion matrices confirmed this, showing that misclassification was most often into an environmentally adjacent class.

In future work it may be beneficial to quantitatively analyze which areas have the most stable classification and which areas are more sensitive. The stable areas could be considered more certain and the areas sensitive to changes in WHC input could be considered to be transition zones between the stable classes.

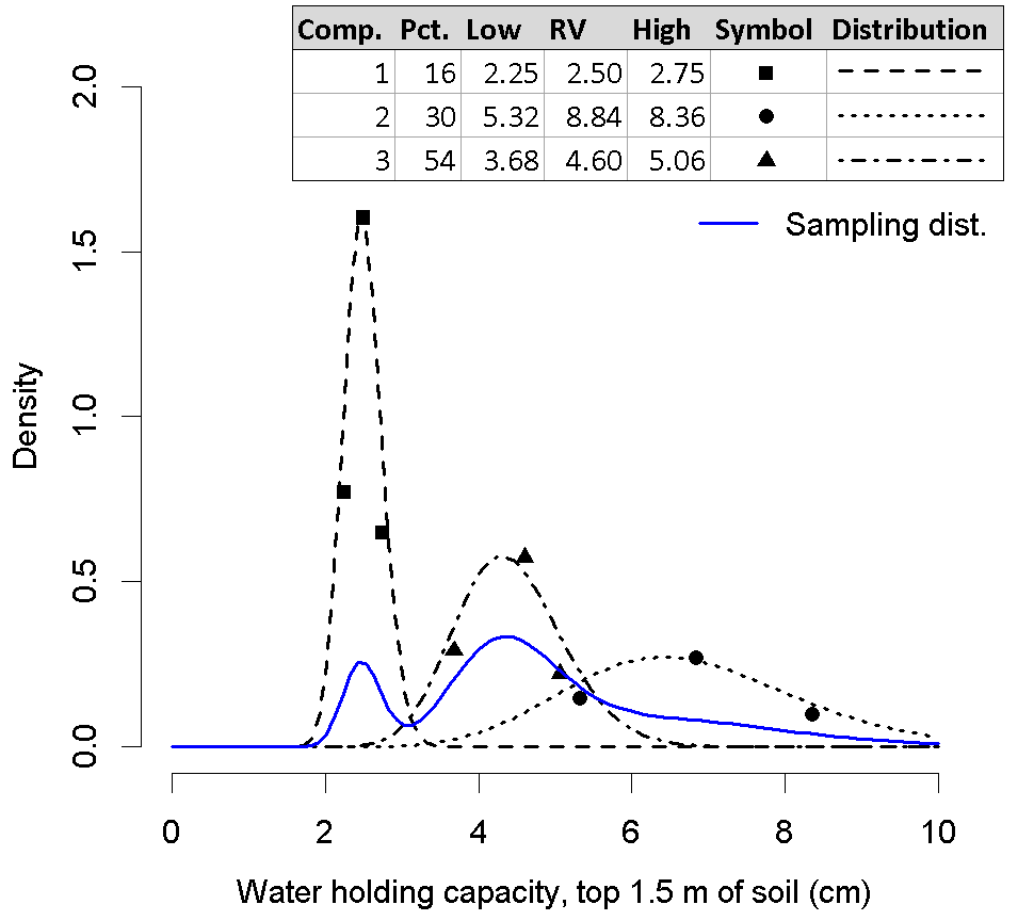

Figure S2.1 Example of expressing soil map unit-level water holding capacity as a distribution instead of as a single average value. Gamma distributions are fit to each of the several components ("Comp.") comprising the map unit on the basis of the low, representative ("RV"), and high water holding capacity values for that component. The distributions are then combined into the map unit-level mixture distribution (blue line) on the basis of each component's abundance ("Pct.").

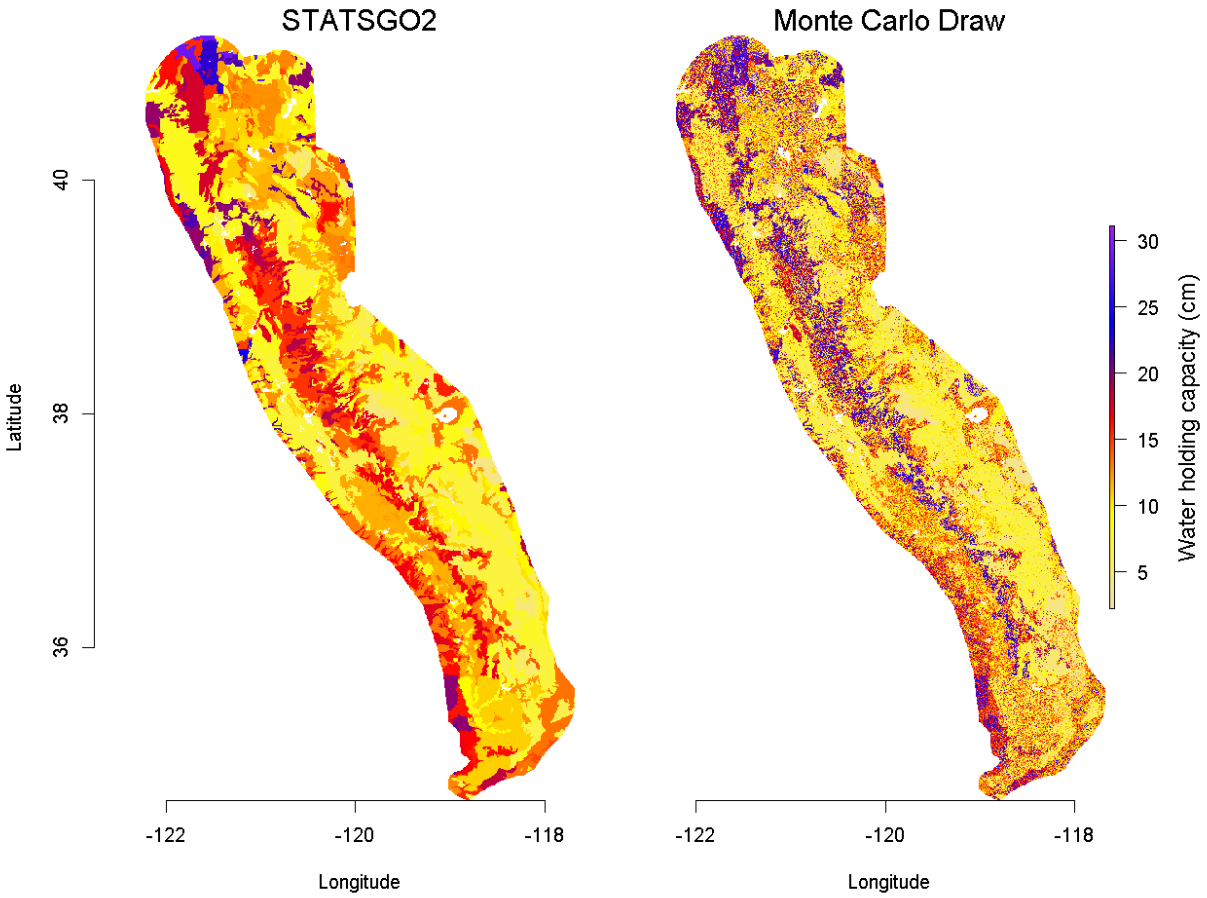

Figure S2.2 Comparison of basic STATSGO2 dataset where each soil map unit is characterized by a single water holding capacity value (left) versus one of the 200 draws from the Monte Carlo analysis (right). Making random draws from water holding capacity distributions on a pixel basis adds a substantial amount of variation to the map, but maintains many of the general patterns.

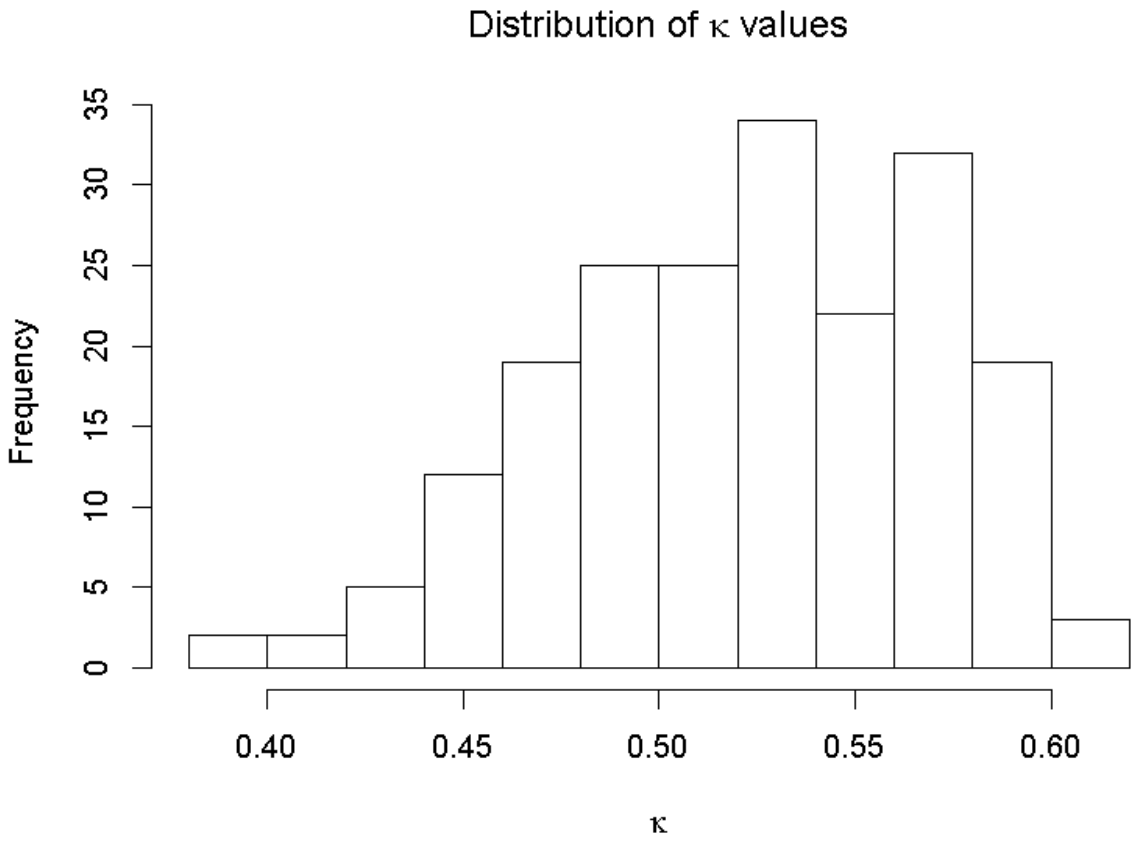

Figure S2.3 Distribution of κ values indicating level of pixel-wise agreement between the climate classification map and the 200 new classifications calculated with varying soil data in the Monte Carlo analysis.

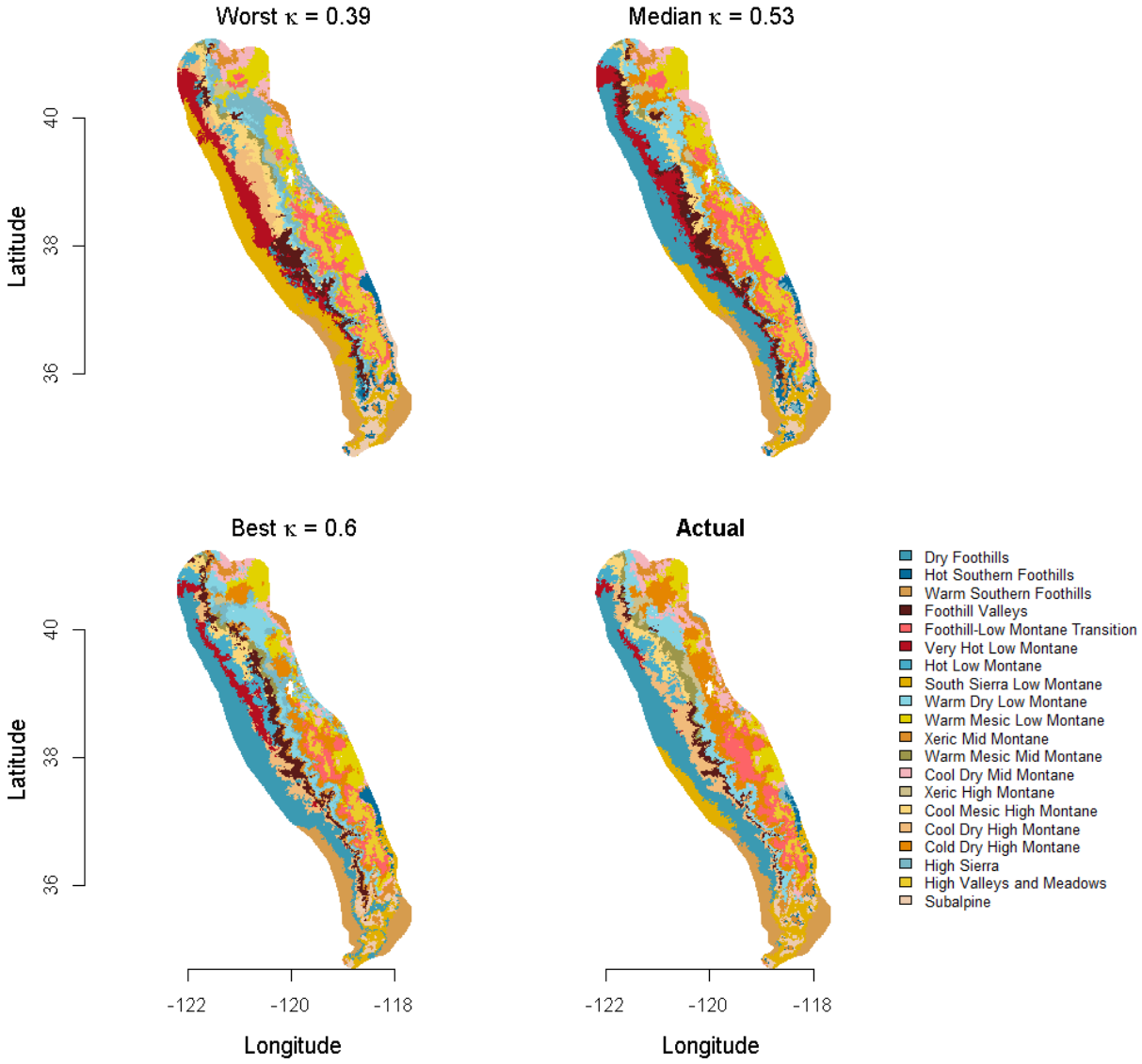

Figure S2.4 Comparison of climate classification map with three example new classifications from the Monte Carlo analysis representing the worst, median, and best agreement.

References

Cohen, J., 1968. Weighted kappa: Nominal scale agreement provision for scaled disagreement or partial credit. Psychological Bulletin 70, 213.

Fleiss, J.L., 1971. Measuring nominal scale agreement among many raters. Psychological Bulletin 76, 378.

Flint, L.E., Flint, A.L., 2008. A basin-scale approach to estimating stream temperatures of tributaries to the Lower Klamath River, California. Journal of Environmental Quality 37, 57-68.

Flint, L.E., Flint, A.L., Thorne, J.H., Boynton, R., 2013. Fine-scale hydrologic modeling for regional landscape applications: the California Basin Characterization Model development and performance. Ecological Processes 2, 25.

Flint, L.E., Flint, A.L., Thorne, J.H., Boynton, R., 2014. 2014 California BCM (Basin Characterization Model) Downscaled Climate and Hydrology - 30-year Summaries. California Climate Commons.

Natural Resources Conservation Service, 2014. SSURGO Table Column Descriptions. United States Department of Agriculture.

R Core Team, 2016. R: A language and environment for statistical computing. R Foundation for Statistical Computing, Vienna, Austria.

Randolph, J.J., 2005. Free-Marginal Multirater Kappa (multirater Kfree): An Alternative to Fleiss' Fixed-Marginal Multirater Kappa, Joensuu University Learning and Instruction Symposium 2005. Joenssu, Finland.

Shanno, D.F., 1970. Conditioning of quasi-Newton methods for function minimization. Mathematics of Computation 24, 647-656.

Soil Survey Staff, 2018. U.S. General Soil Map (STATSGO2). Natural Resources Conservation Service, United States Department of Agriculture.

Vereecken, H., Schnepf, A., Hopmans, J.W., Javaux, M., Or, D., Roose, T., Vanderborght, J., Young, M., Amelung, W., Aitkenhead, M., 2016. Modeling soil processes: Review, key challenges, and new perspectives. Vadose Zone Journal 15.

Supplement 3: Profiles of contemporary reference areas in the Sierra Nevada mixed-conifer forest zone

This supplement provides detailed information about areas in the Sierra Nevada mixed-conifer zone with restored fire regimes and available lidar data. For each patch, the following data are provided:

- Reference area name
- Ownership
- Land area
- Proportion of area in different landforms (ridge, valley, NE slopes, SW slopes)
- Minimum, mean, and maximum actual evapotranspiration, climatic water deficit, January minimum temperature, and elevation
- Maps, including location within California, elevation, climate class, and canopy height
- Photos, when available
- Graphs of ranges of variation in structure and pattern measured from lidar

Table of Contents for Supplement 3

Ackerson

Ownership	Yosemite National Park			
Hectares	147			
	Ridges	**Valleys**	**NE slopes**	**SW slopes**
Landform proportions	0.22	0.13	0.22	0.43

	Minimum	**Mean**	**Maximum**
AET (mm)	340	387	410
Deficit (mm)	493	539	579
T_{min} (°C)	2.5	2.9	3.4
Elevation (m)	1820	2067	2183

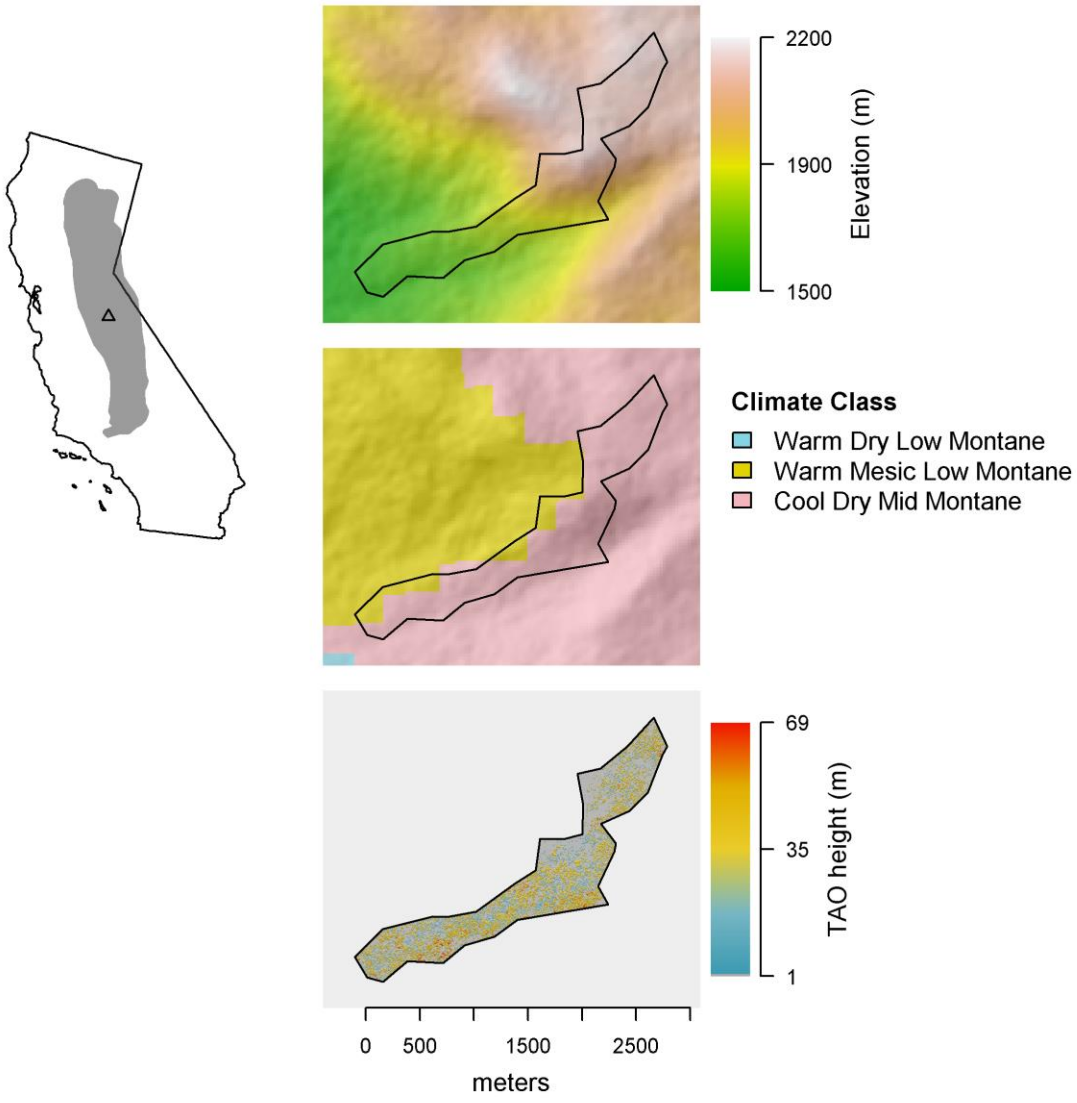

Ackerson

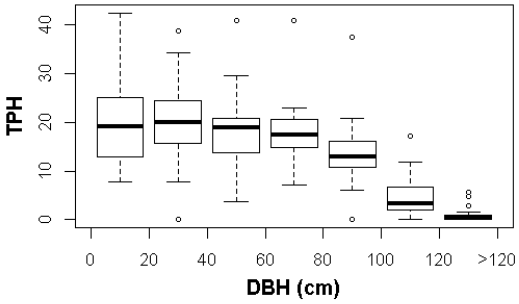
TPH
0 10 20 30 40
0 20 40 60 80 100 120 >120
DBH (cm)

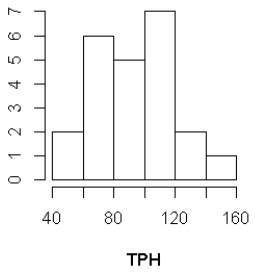
0 1 2 3 4 5 6 7
40 80 120 160
TPH

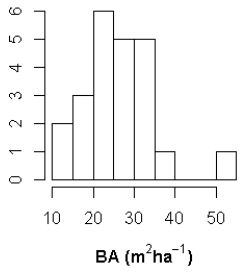
0 1 2 3 4 5 6
10 20 30 40 50
BA (m2ha-1)

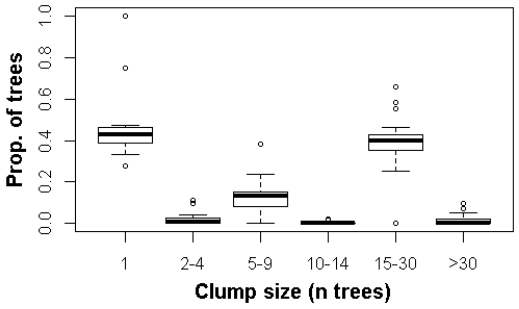
Prop. of trees
0.0 0.2 0.4 0.6 0.8 1.0
1 2-4 5-9 10-14 15-30 >30
Clump size (n trees)

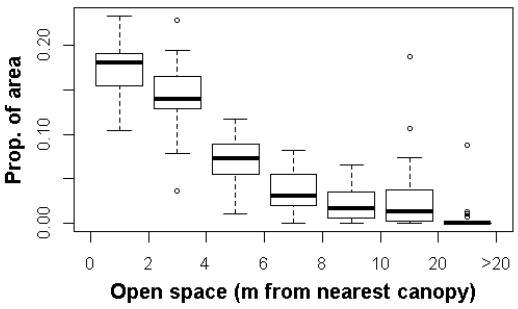
Prop. of area
0.00 0.10 0.20
0 2 4 6 8 10 20 >20
Open space (m from nearest canopy)

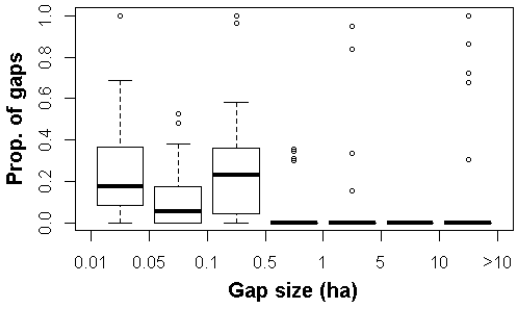
Prop. of gaps
0.0 0.2 0.4 0.6 0.8 1.0
0.01 0.05 0.1 0.5 1 5 10 >10
Gap size (ha)

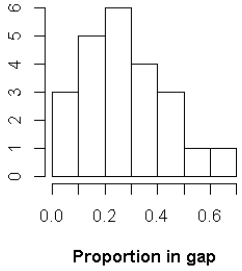
0 1 2 3 4 5 6
0.0 0.2 0.4 0.6
Proportion in gap

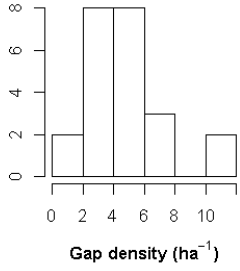
0 2 4 6 8
0 2 4 6 8 10
Gap density (ha-1)

Aspen

Ownership	Yosemite National Park
Hectares	218

	Ridges	**Valleys**	**NE slopes**	**SW slopes**
Landform proportions	0.27	0.23	0.18	0.32

	Minimum	**Mean**	**Maximum**
AET (mm)	387	402	462
Deficit (mm)	447	494	506
T_{min} (°C)	2.2	2.6	3.0
Elevation (m)	1799	1965	2069

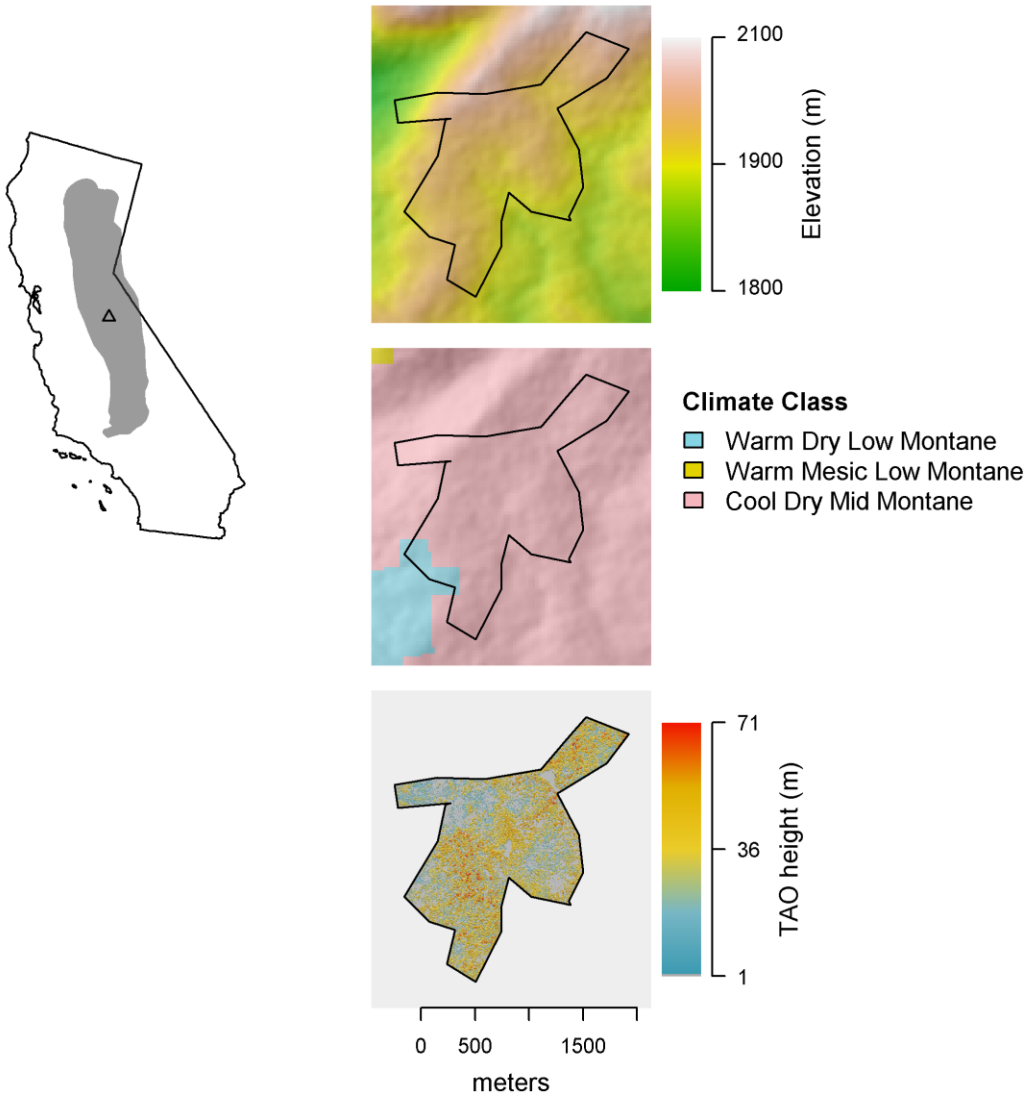

Aspen

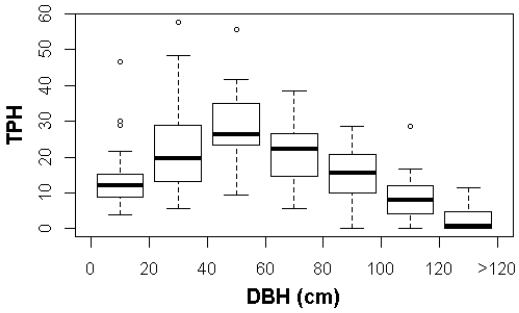
TPH
0 10 20 30 40 50 60
0 20 40 60 80 100 120 >120
DBH (cm)

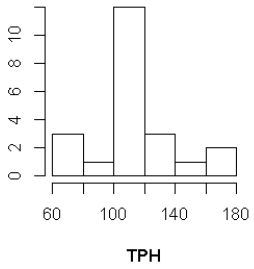
0 2 4 6 8 10
60 100 140 180
TPH

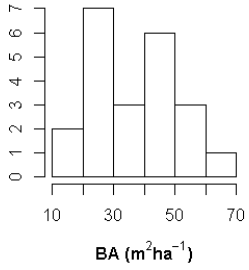
0 1 2 3 4 5 6 7
10 30 50 70
BA (m2ha−1)

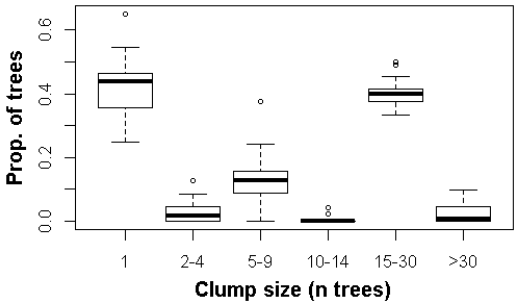
Prop. of trees
0.0 0.2 0.4 0.6
1 2-4 5-9 10-14 15-30 >30
Clump size (n trees)

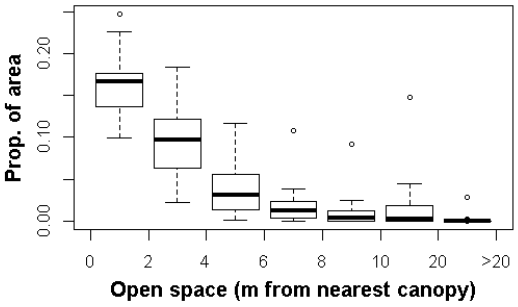
Prop. of area
0.00 0.10 0.20
0 2 4 6 8 10 20 >20
Open space (m from nearest canopy)

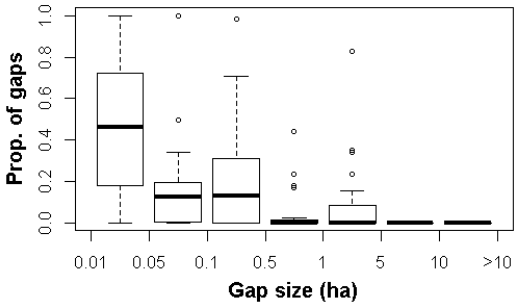
Prop. of gaps
0.0 0.2 0.4 0.6 0.8 1.0
0.01 0.05 0.1 0.5 1 5 10 >10
Gap size (ha)

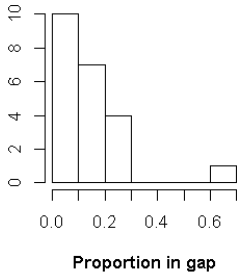
0 2 4 6 8 10
0.0 0.2 0.4 0.6
Proportion in gap

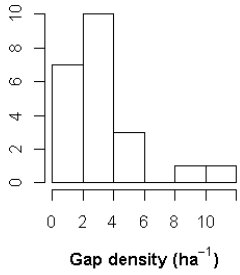
0 2 4 6 8 10
0 2 4 6 8 10
Gap density (ha−1)

Bald

Ownership	Yosemite National Park			
Hectares	289			
	Ridges	**Valleys**	**NE slopes**	**SW slopes**
Landform proportions	0.28	0.07	0.17	0.48

	Minimum	**Mean**	**Maximum**
AET (mm)	292	397	422
Deficit (mm)	483	509	625
T_{min} (°C)	2.8	3.2	3.5
Elevation (m)	1790	1841	1895

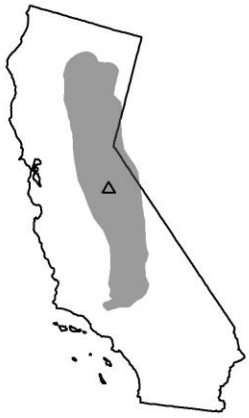

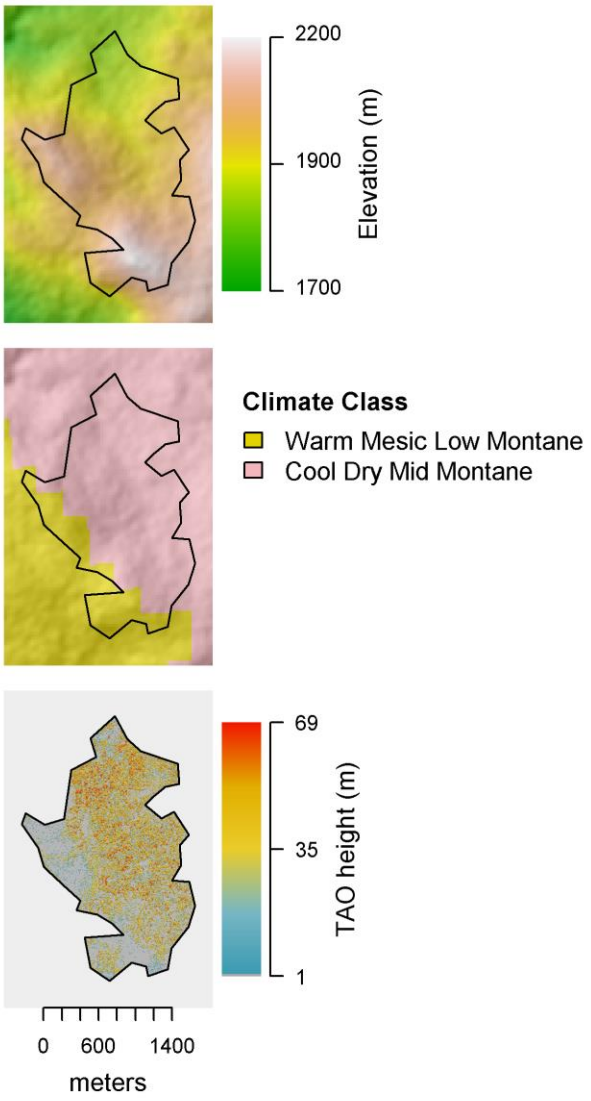

Bald

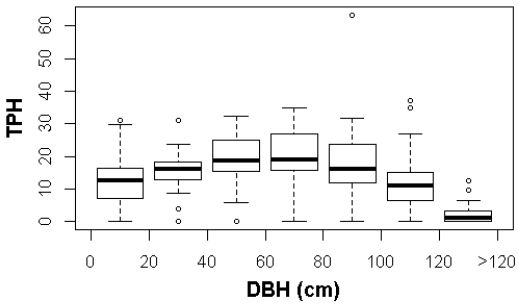
TPH
0 10 20 30 40 50 60
0 20 40 60 80 100 120 >120
DBH (cm)

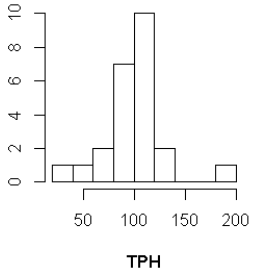
0 2 4 6 8 10
50 100 150 200
TPH

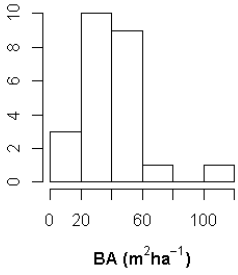
0 2 4 6 8 10
0 20 60 100
BA (m2ha−1)

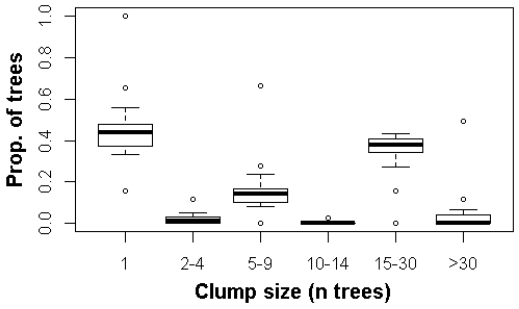
Prop. of trees
0.0 0.2 0.4 0.6 0.8 1.0
1 2-4 5-9 10-14 15-30 >30
Clump size (n trees)

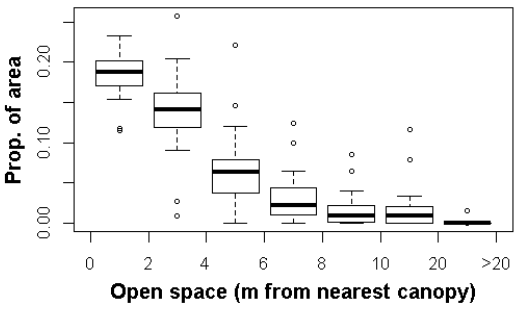
Prop. of area
0.00 0.10 0.20
0 2 4 6 8 10 20 >20
Open space (m from nearest canopy)

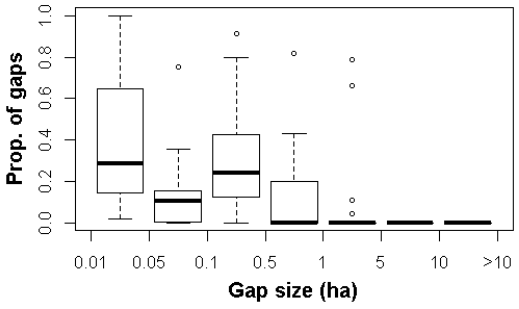
Prop. of gaps
0.0 0.2 0.4 0.6 0.8 1.0
0.01 0.05 0.1 0.5 1 5 10 >10
Gap size (ha)

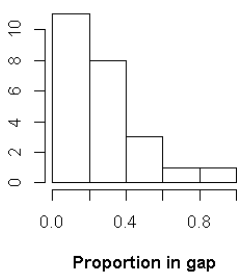
0 2 4 6 8 10
0.0 0.4 0.8
Proportion in gap

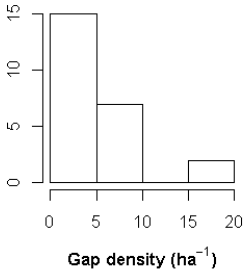
0 5 10 15
0 5 10 15 20
Gap density (ha−1)

Bear

Ownership	Yosemite National Park			
Hectares	286			
	Ridges	**Valleys**	**NE slopes**	**SW slopes**
Landform proportions	0.33	0.13	0.17	0.37
	Minimum	**Mean**	**Maximum**	
AET (mm)	342	394	452	
Deficit (mm)	443	492	547	
T_{min} (°C)	2.3	2.7	3.1	
Elevation (m)	1843	1925	1986	

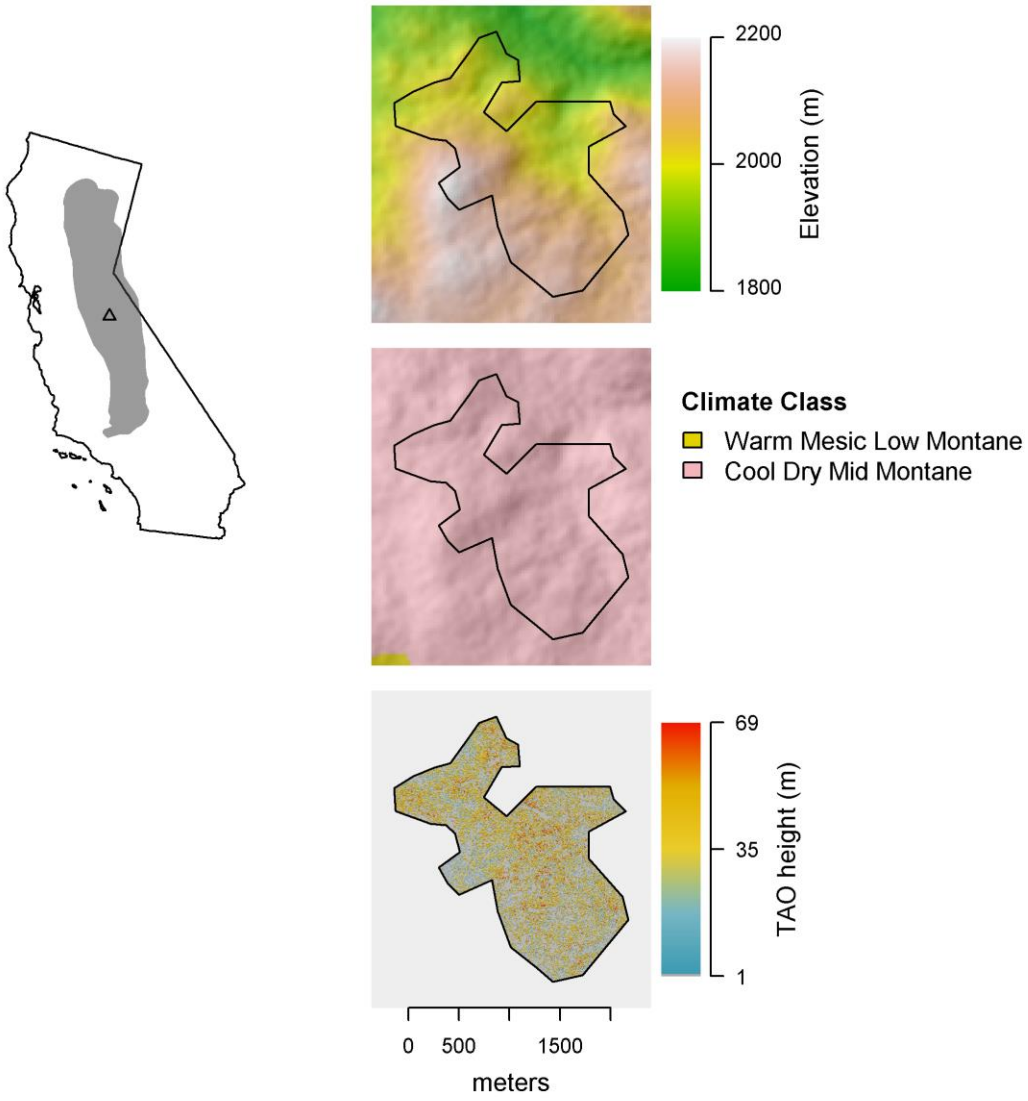

Bear

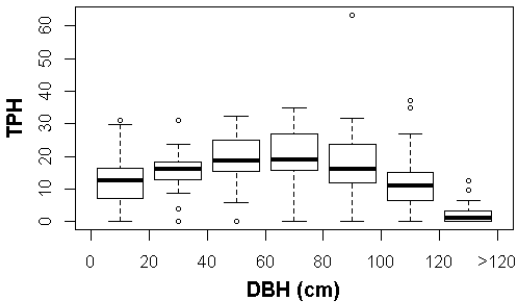
TPH
0 10 20 30 40 50 60
0 20 40 60 80 100 120 >120
DBH (cm)

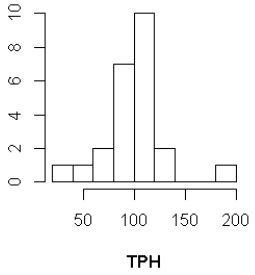
0 2 4 6 8 10
50 100 150 200
TPH

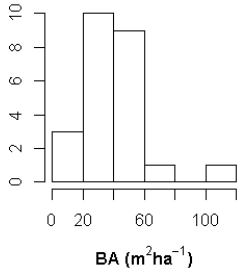
0 2 4 6 8 10
0 20 60 100
BA (m2ha-1)

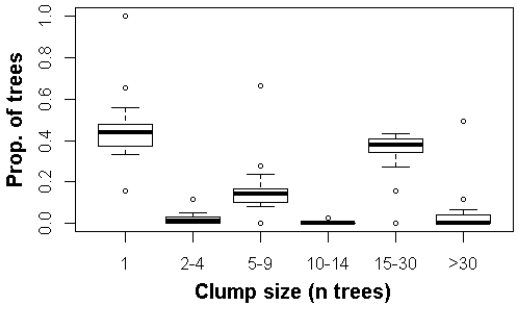
Prop. of trees
0.0 0.2 0.4 0.6 0.8 1.0
1 2-4 5-9 10-14 15-30 >30
Clump size (n trees)

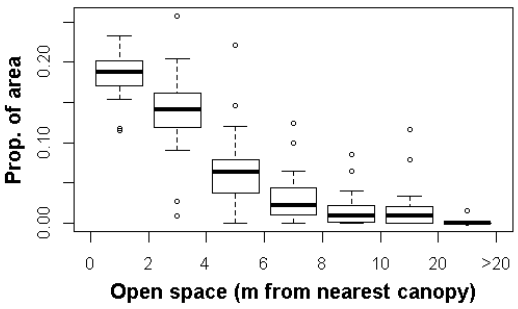
Prop. of area
0.00 0.10 0.20
0 2 4 6 8 10 20 >20
Open space (m from nearest canopy)

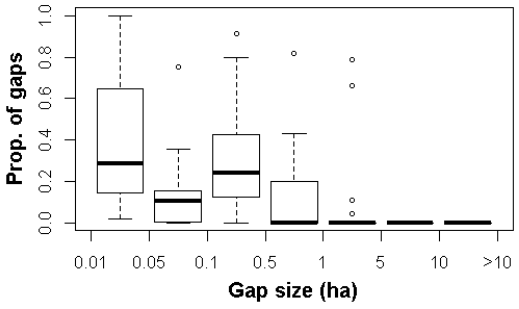
Prop. of gaps
0.0 0.2 0.4 0.6 0.8 1.0
0.01 0.05 0.1 0.5 1 5 10 >10
Gap size (ha)

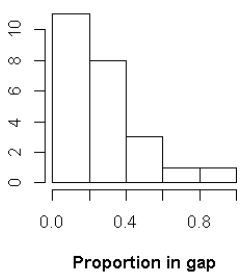
0 2 4 6 8 10
0.0 0.4 0.8
Proportion in gap

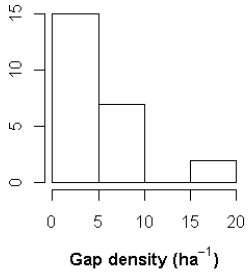
0 5 10 15
0 5 10 15 20
Gap density (ha-1)

Buena Vista

Ownership	Yosemite National Park
Hectares	132

	Ridges	**Valleys**	**NE slopes**	**SW slopes**
Landform proportions	0.11	0.08	0.42	0.39

	Minimum	**Mean**	**Maximum**
AET (mm)	216	262	334
Deficit (mm)	437	524	580
T_{min} (°C)	-0.47	-0.02	0.29
Elevation (m)	2192	2260	2339

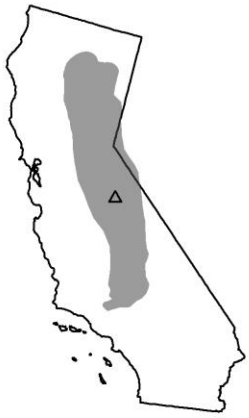

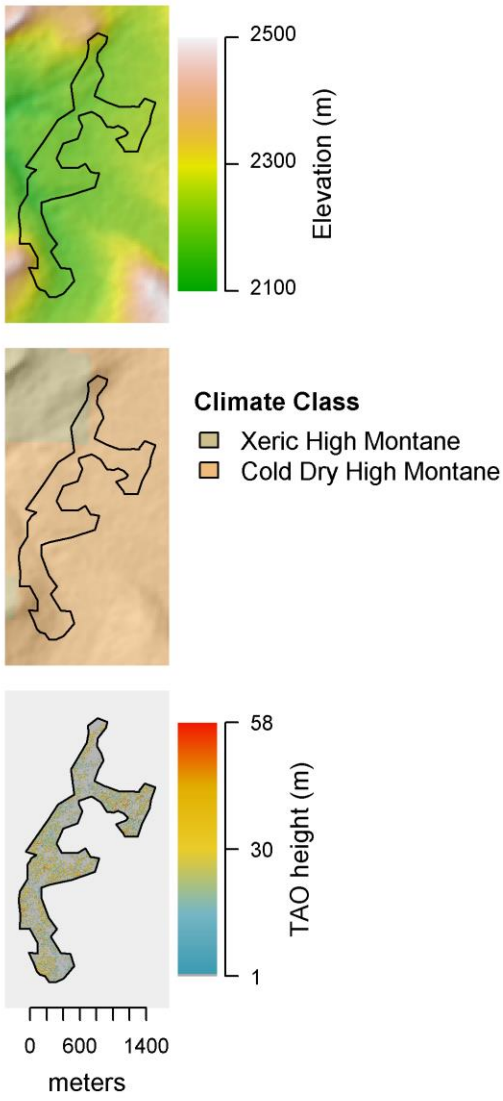

Buena Vista

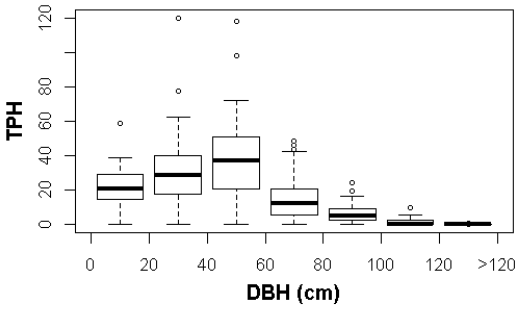
TPH
0 20 40 60 80 100 120
0 20 40 60 80 100 120 >120
DBH (cm)

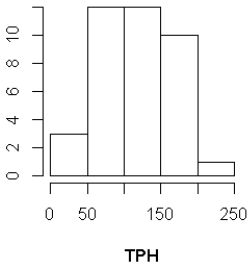
0 2 4 6 8 10
0 50 150 250
TPH

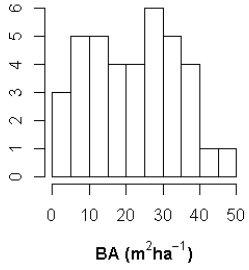
0 1 2 3 4 5 6
0 10 20 30 40 50
BA (m2ha−1)

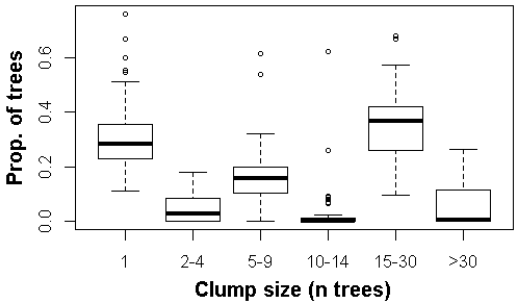
Prop. of trees
0.0 0.2 0.4 0.6
1 2-4 5-9 10-14 15-30 >30
Clump size (n trees)

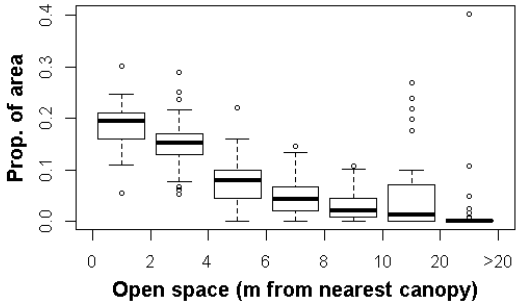
Prop. of area
0.0 0.1 0.2 0.3 0.4
0 2 4 6 8 10 20 >20
Open space (m from nearest canopy)

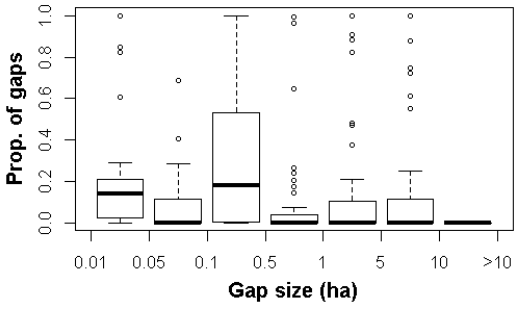
Prop. of gaps
0.0 0.2 0.4 0.6 0.8 1.0
0.01 0.05 0.1 0.5 1 5 10 >10
Gap size (ha)

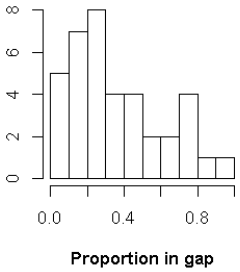
0 2 4 6 8
0.0 0.4 0.8
Proportion in gap

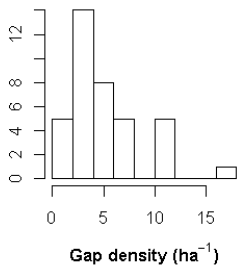
0 2 4 6 8 12
0 5 10 15
Gap density (ha−1)

Cascade

Ownership	Sequoia National Park
Hectares	419

	Ridges	**Valleys**	**NE slopes**	**SW slopes**
Landform proportions	0.34	0.13	0.16	0.37

	Minimum	**Mean**	**Maximum**
AET (mm)	301	338	428
Deficit (mm)	522	587	653
T_{min} (°C)	0.28	1.6	2.5
Elevation (m)	2066	2210	2285

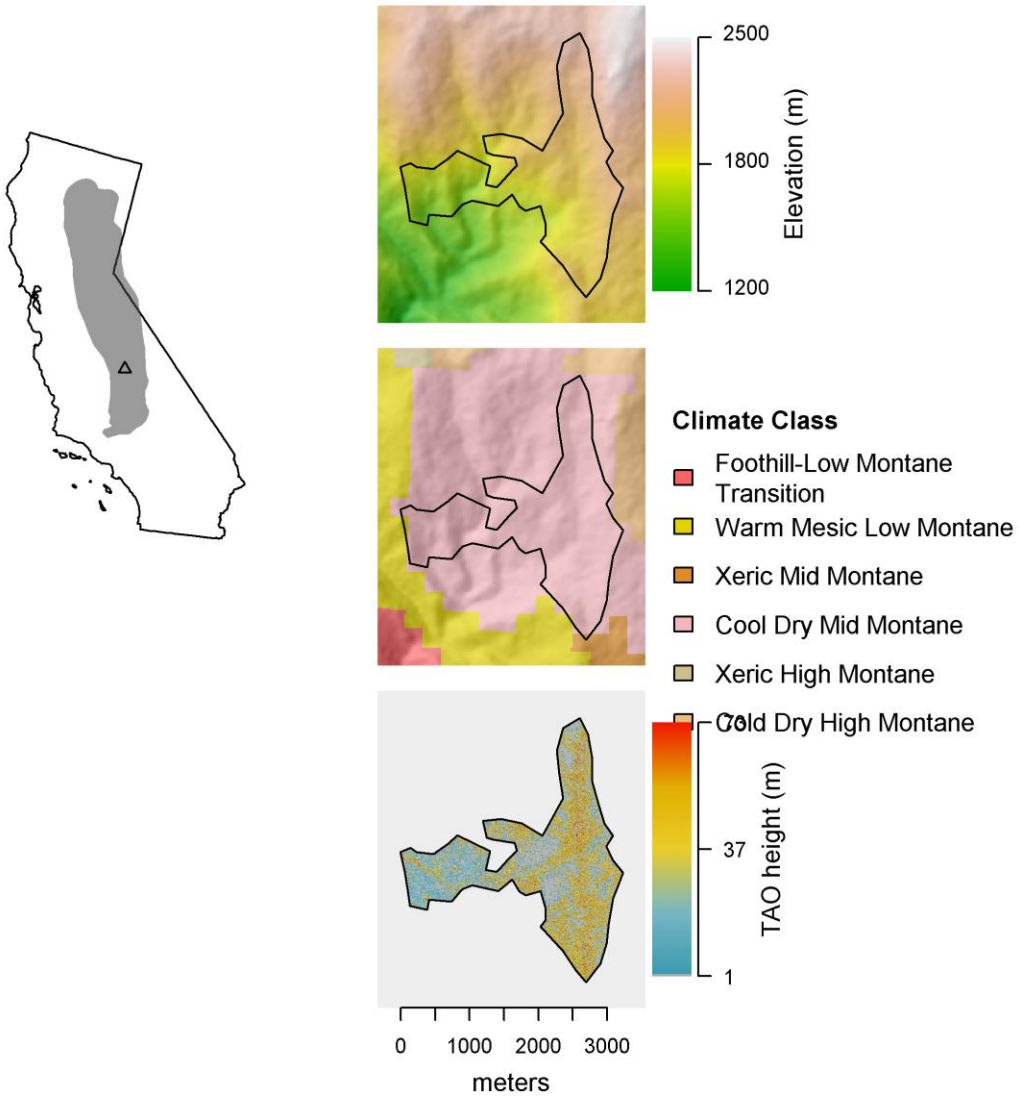

Cascade

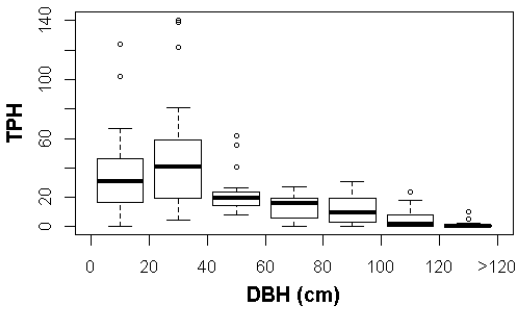
TPH
0 20 60 100 140
0 20 40 60 80 100 120 >120
DBH (cm)

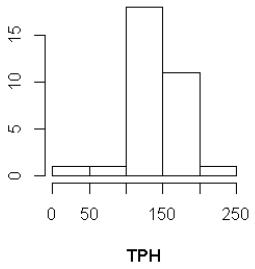
0 5 10 15
0 50 150 250
TPH

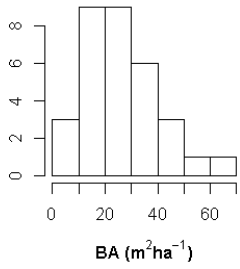
0 2 4 6 8
0 20 40 60
BA (m2ha-1)

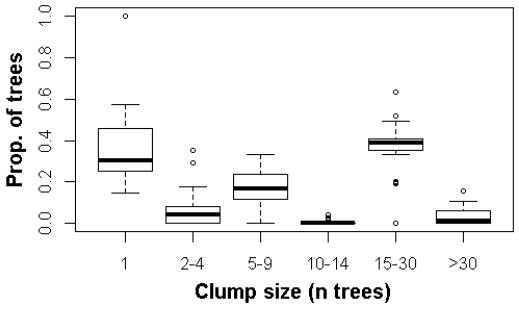
Prop. of trees
0.0 0.2 0.4 0.6 0.8 1.0
1 2-4 5-9 10-14 15-30 >30
Clump size (n trees)

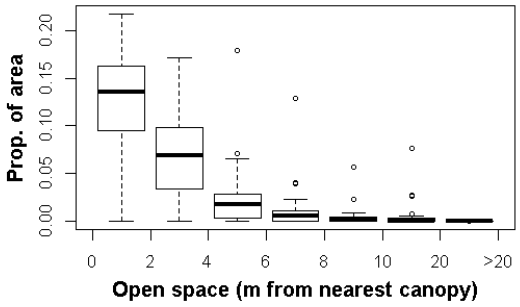
Prop. of area
0.00 0.05 0.10 0.15 0.20
0 2 4 6 8 10 20 >20
Open space (m from nearest canopy)

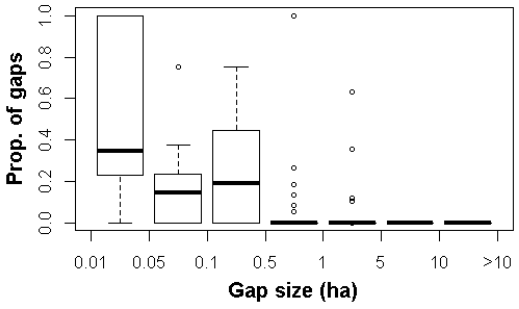
Prop. of gaps
0.0 0.2 0.4 0.6 0.8 1.0
0.01 0.05 0.1 0.5 1 5 10 >10
Gap size (ha)

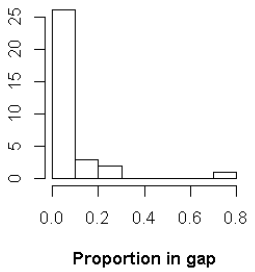
0 5 10 15 20 25
0.0 0.2 0.4 0.6 0.8
Proportion in gap

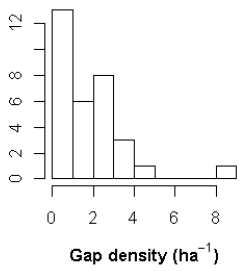
0 2 4 6 8 12
0 2 4 6 8
Gap density (ha-1)

Ceanothus

Ownership	Yosemite National Park and Stanislaus National Forest			
Hectares	183			
	Ridges	**Valleys**	**NE slopes**	**SW slopes**
Landform proportions	0.36	0.08	0.28	0.28

	Minimum	**Mean**	**Maximum**
AET (mm)	387	406	464
Deficit (mm)	455	553	619
T_{min} (°C)	2.7	3.4	4.2
Elevation (m)	1463	1514	1619

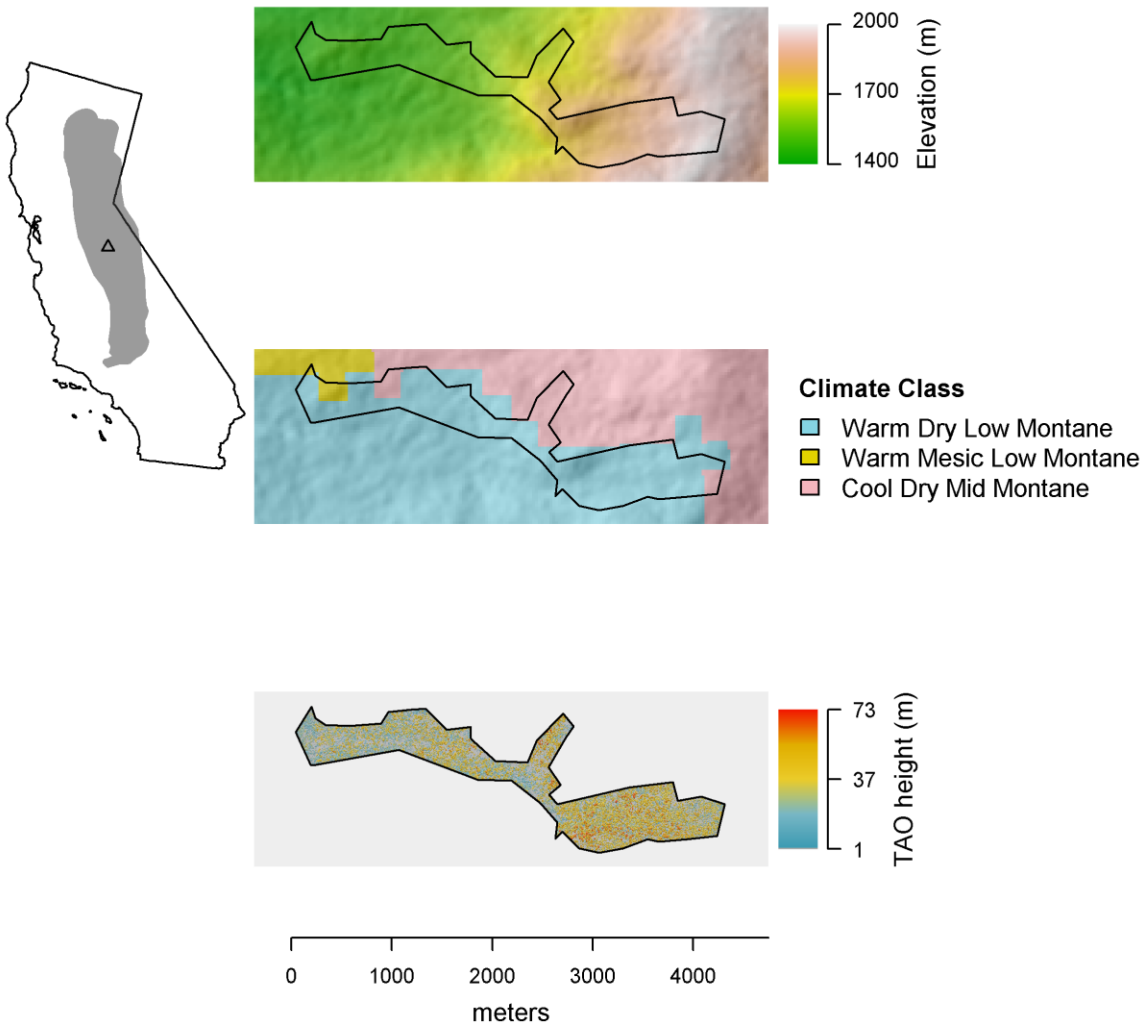

Ceanothus

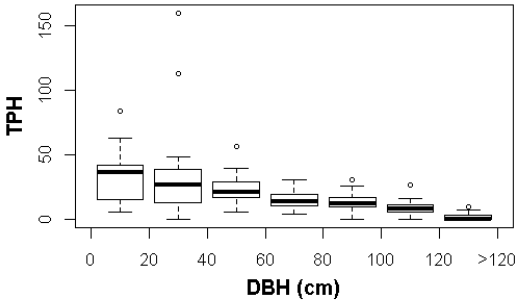
TPH
0
50
100
150
0
20
40
60
80
100
120
>120
DBH (cm)

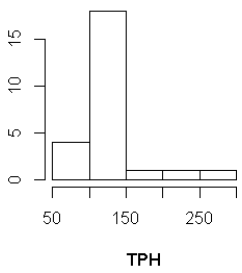
0
5
10
15
50
150
250
TPH

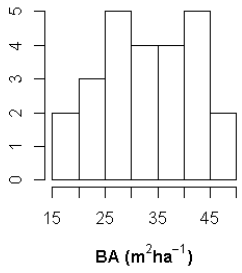
0
1
2
3
4
5
15
25
35
45
BA (m2ha−1)

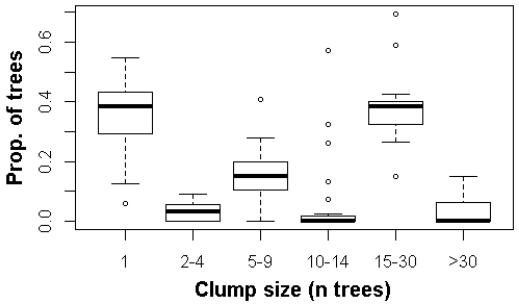
Prop. of trees
0.0
0.2
0.4
0.6
1
2-4
5-9
10-14
15-30
>30
Clump size (n trees)

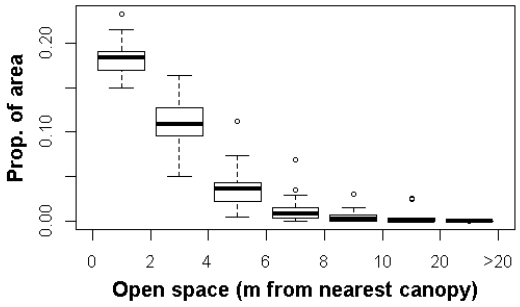
Prop. of area
0.00
0.10
0.20
0
2
4
6
8
10
20
>20
Open space (m from nearest canopy)

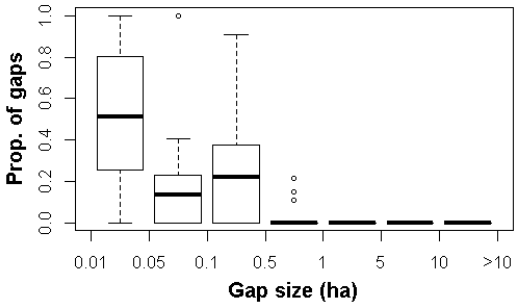
Prop. of gaps
0.0
0.2
0.4
0.6
0.8
1.0
0.01
0.05
0.1
0.5
1
5
10
>10
Gap size (ha)

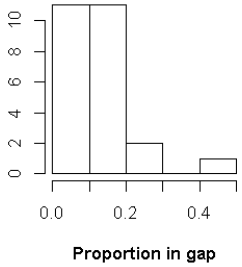
0
2
4
6
8
10
0.0
0.2
0.4
Proportion in gap

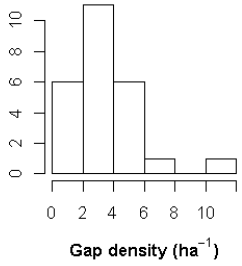
0
2
4
6
8
10
0
2
4
6
8
10
Gap density (ha−1)

Chicken

Ownership	Yosemite National Park			
Hectares	476			
	Ridges	**Valleys**	**NE slopes**	**SW slopes**
Landform proportions	0.32	0.20	0.24	0.24

	Minimum	**Mean**	**Maximum**
AET (mm)	248	346	438
Deficit (mm)	400	516	604
T_{min} (°C)	0.02	1.8	2.8
Elevation (m)	2069	2152	2366

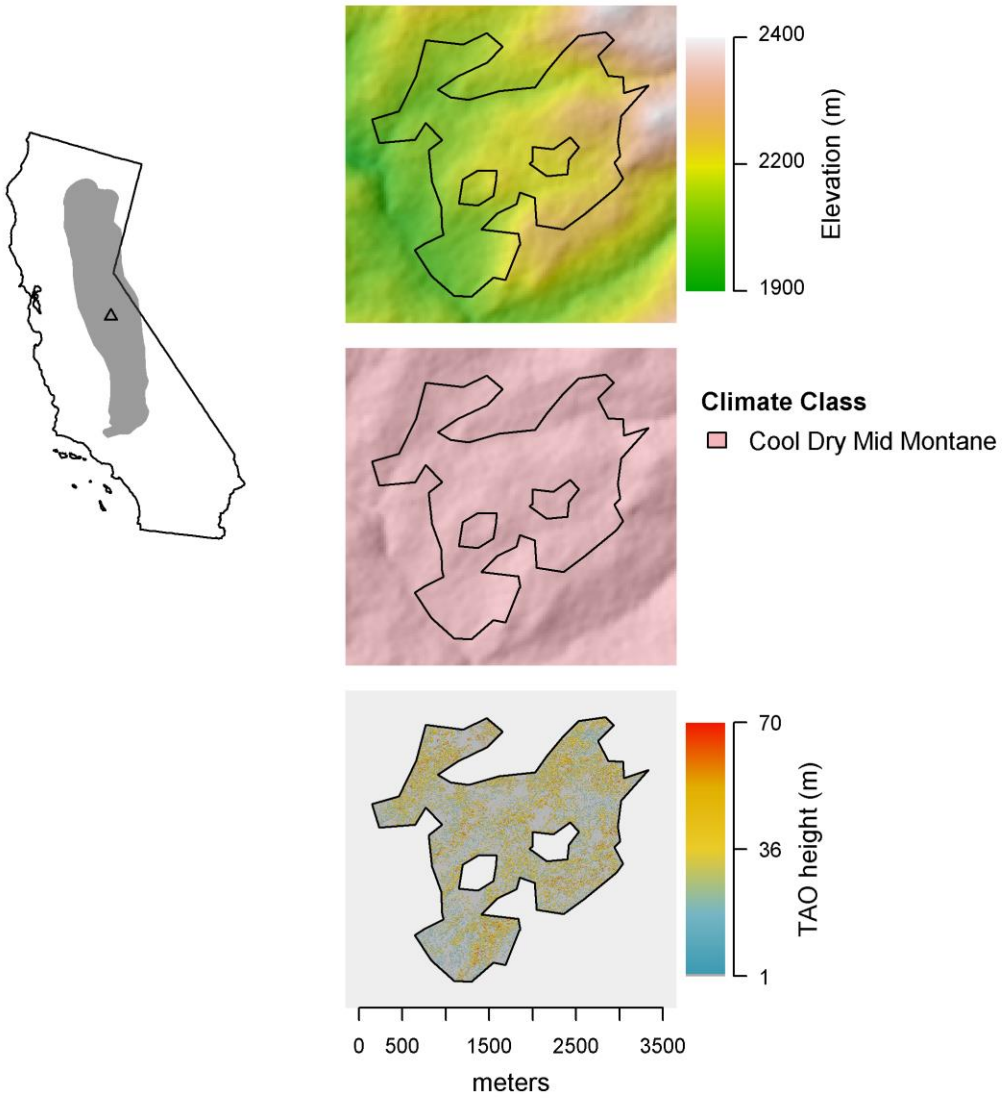

Chicken

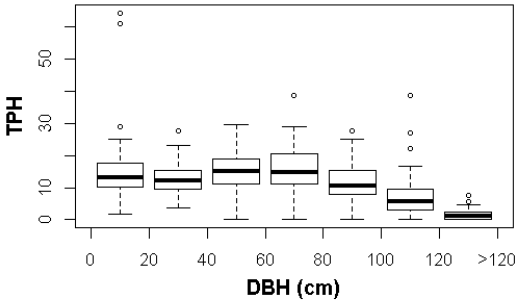
TPH
0 10 30 50
0 20 40 60 80 100 120 >120
DBH (cm)

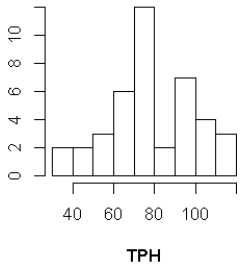
0 2 4 6 8 10
40 60 80 100
TPH

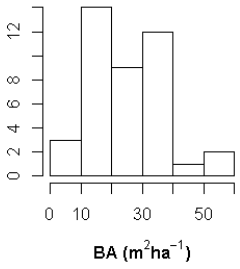
0 2 4 6 8 12
0 10 30 50
BA (m2ha−1)

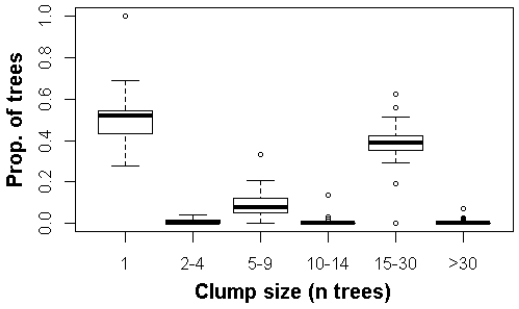
Prop. of trees
0.0 0.2 0.4 0.6 0.8 1.0
1 2-4 5-9 10-14 15-30 >30
Clump size (n trees)

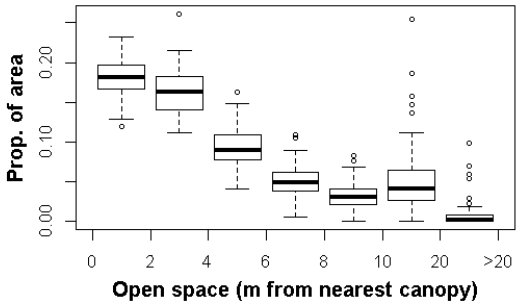
Prop. of area
0.00 0.10 0.20
0 2 4 6 8 10 20 >20
Open space (m from nearest canopy)

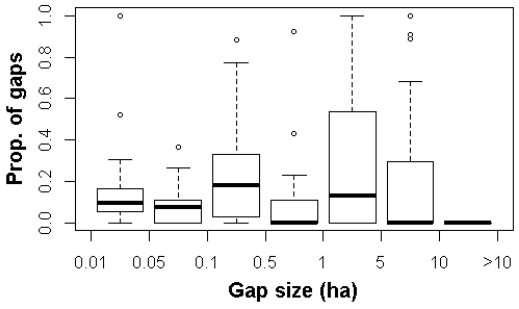
Prop. of gaps
0.0 0.2 0.4 0.6 0.8 1.0
0.01 0.05 0.1 0.5 1 5 10 >10
Gap size (ha)

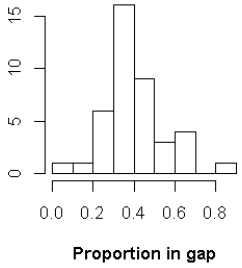
0 5 10 15
0.0 0.2 0.4 0.6 0.8
Proportion in gap

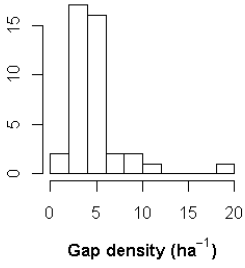
0 5 10 15
0 5 10 15 20
Gap density (ha−1)

Clark

Ownership	Yosemite National Park			
Hectares	234			
	Ridges	**Valleys**	**NE slopes**	**SW slopes**
Landform proportions	0.15	0.24	0.37	0.24
	Minimum	**Mean**	**Maximum**	
AET (mm)	219	287	354	
Deficit (mm)	456	515	577	
T_{min} (°C)	0.21	0.71	1.3	
Elevation (m)	2121	2148	2190	

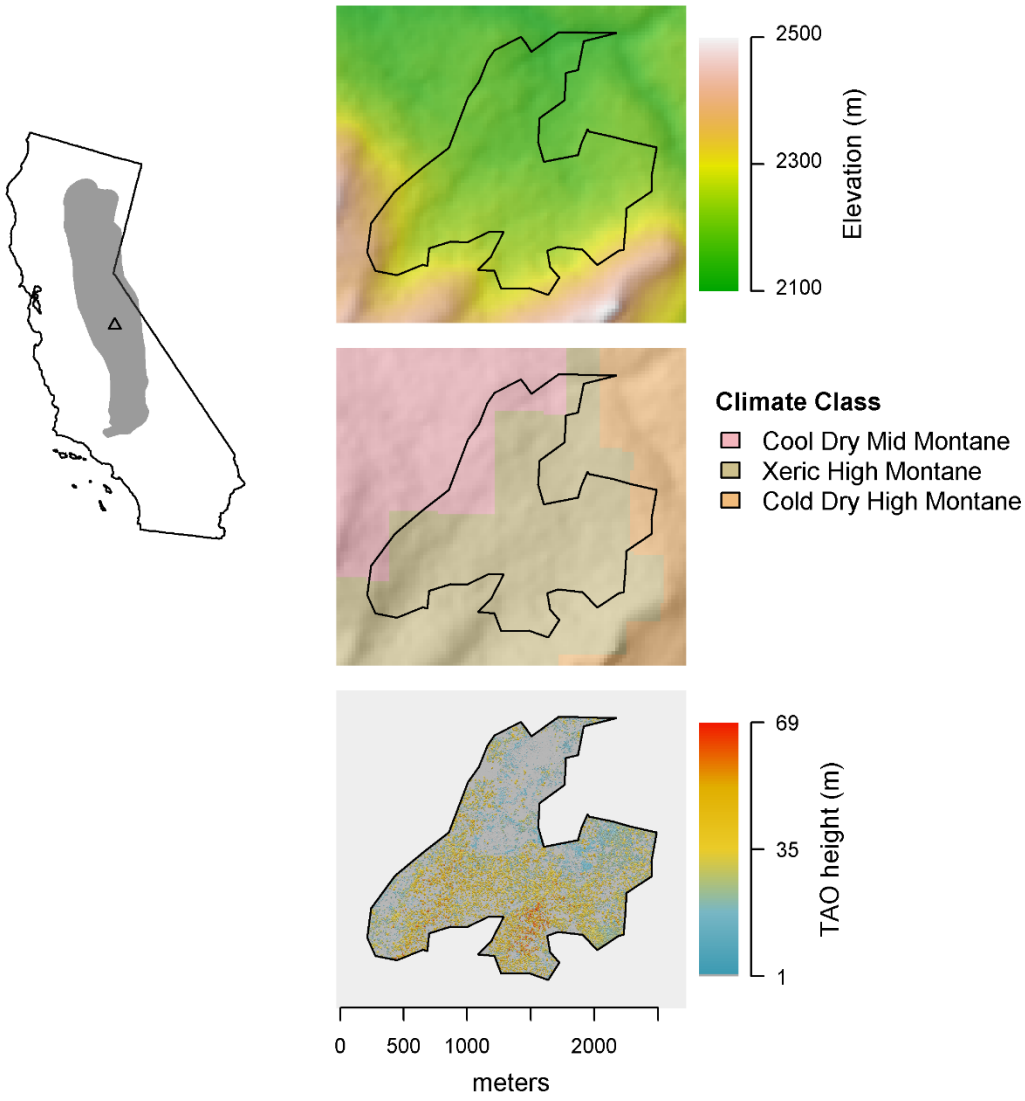

Clark

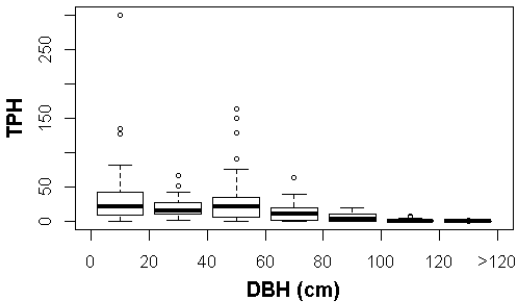
TPH
0
50
150
250
0
20
40
60
80
100
120
>120
DBH (cm)

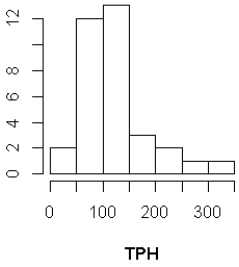
0
2
4
6
8
12
0
100
200
300
TPH

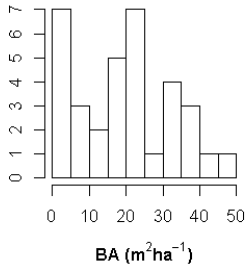
0
1
2
3
4
5
6
7
0
10
20
30
40
50
BA (m2ha−1)

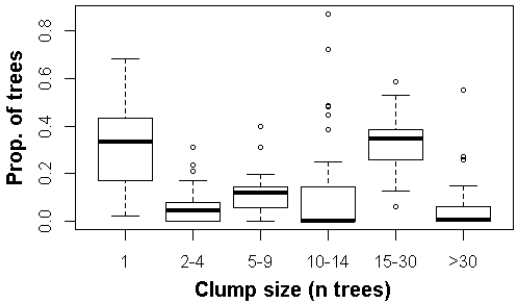
Prop. of trees
0.0
0.2
0.4
0.6
0.8
1
2-4
5-9
10-14
15-30
>30
Clump size (n trees)

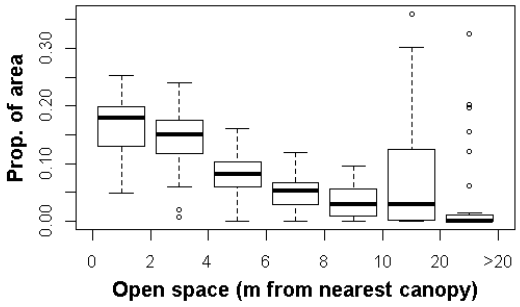
Prop. of area
0.00
0.10
0.20
0.30
0
2
4
6
8
10
20
>20
Open space (m from nearest canopy)

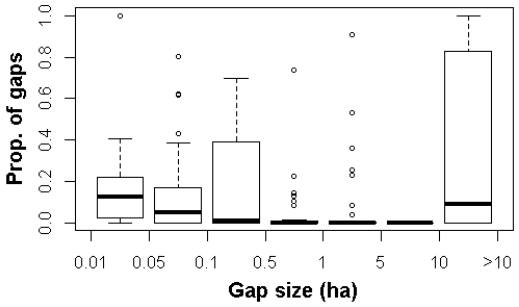
Prop. of gaps
0.0
0.2
0.4
0.6
0.8
1.0
0.01
0.05
0.1
0.5
1
5
10
>10
Gap size (ha)

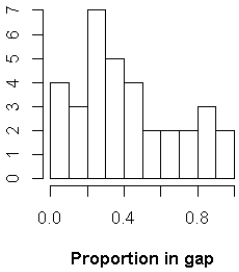
0
1
2
3
4
5
6
7
0.0
0.4
0.8
Proportion in gap

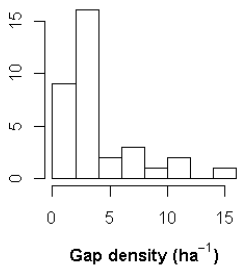
0
5
10
15
0
5
10
15
Gap density (ha−1)

Cottonwood Meadow

Ownership	Yosemite National Park
Hectares	479

	Ridges	**Valleys**	**NE slopes**	**SW slopes**
Landform proportions	0.17	0.09	0.32	0.42

	Minimum	**Mean**	**Maximum**
AET (mm)	330	405	467
Deficit (mm)	413	502	549
T_{min} (°C)	2.3	2.7	2.9
Elevation (m)	1673	1843	1958

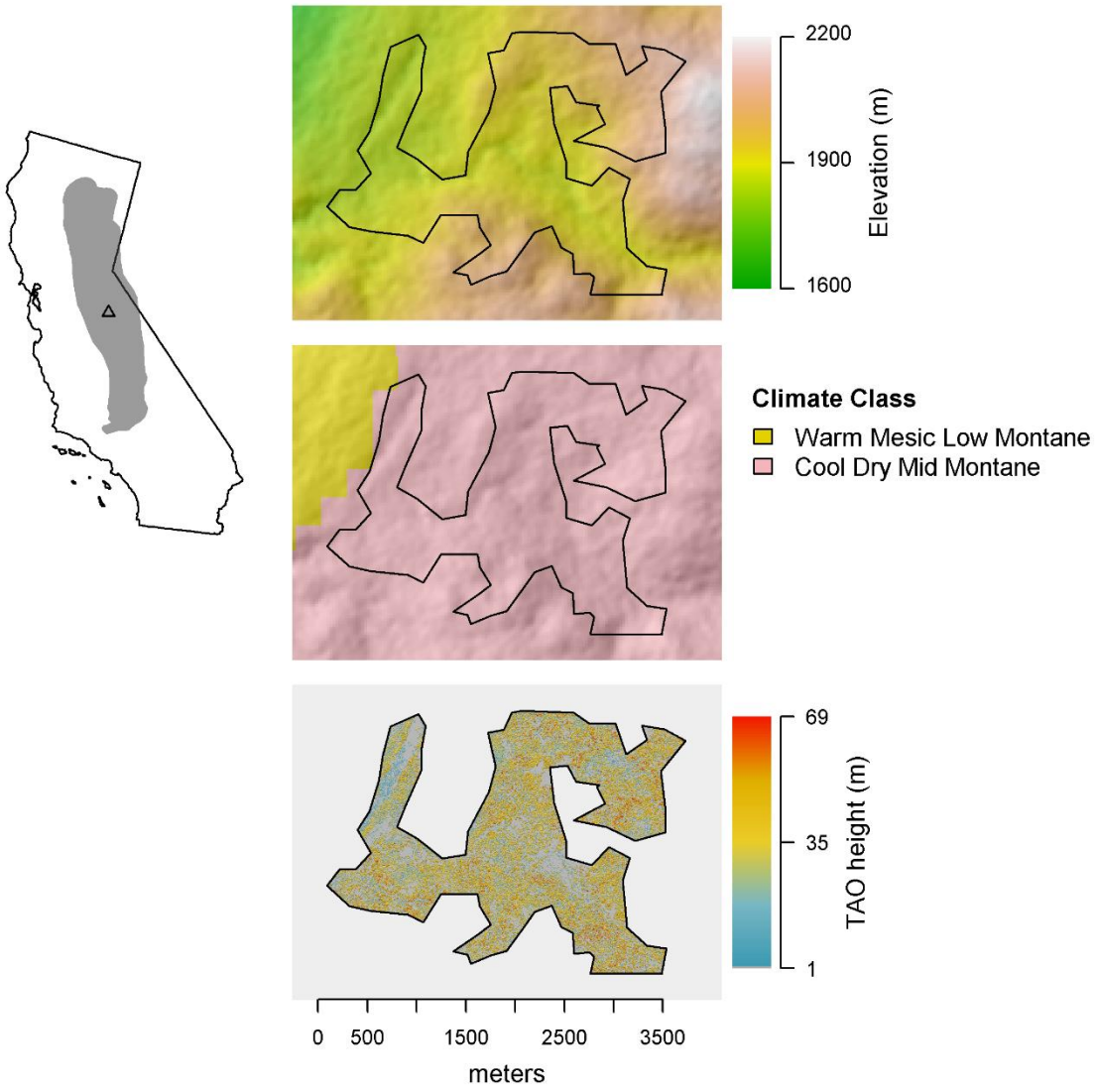

Cottonwood Meadow

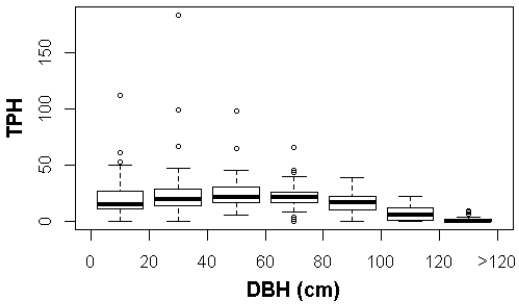

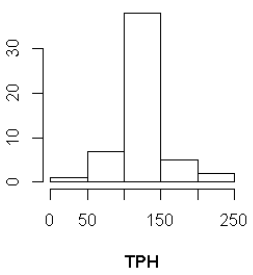

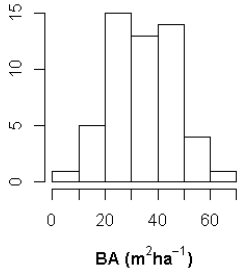

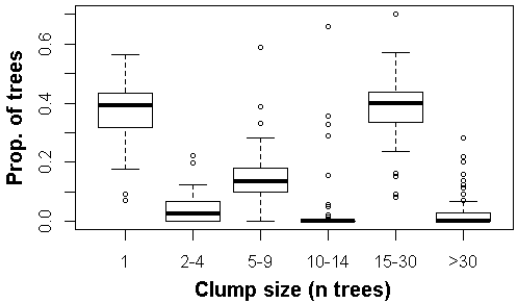

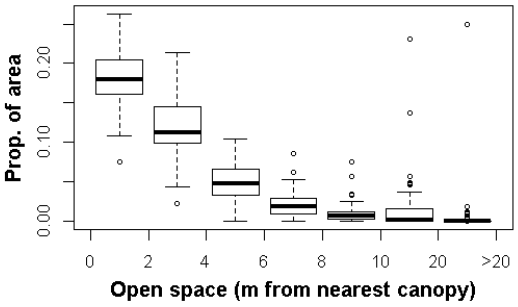

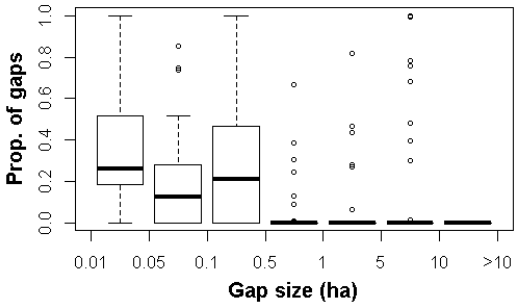

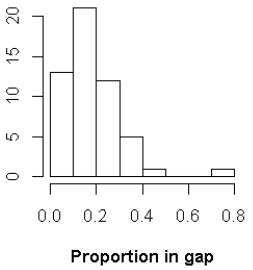

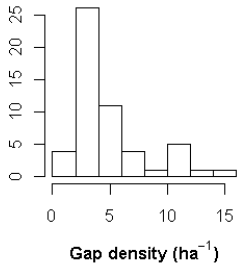

Crane

Ownership	Yosemite National Park and Stanislaus National Forest			
Hectares	119			
	Ridges	**Valleys**	**NE slopes**	**SW slopes**
Landform proportions	0.67	0.07	0.13	0.13

	Minimum	**Mean**	**Maximum**
AET (mm)	312	429	472
Deficit (mm)	557	596	750
T_{min} (°C)	4.7	5.2	6.3
Elevation (m)	1882	1904	1957

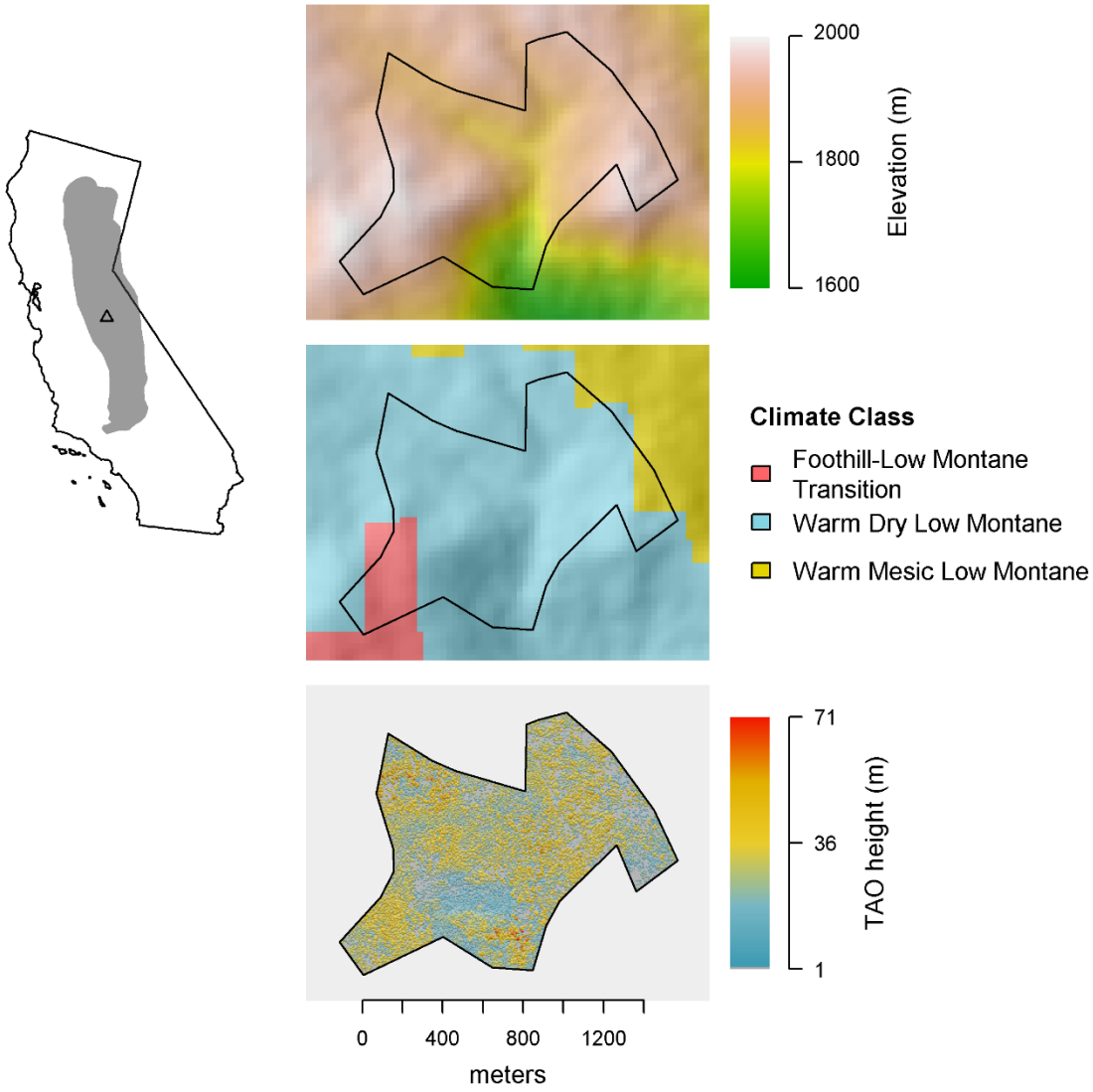

Crane

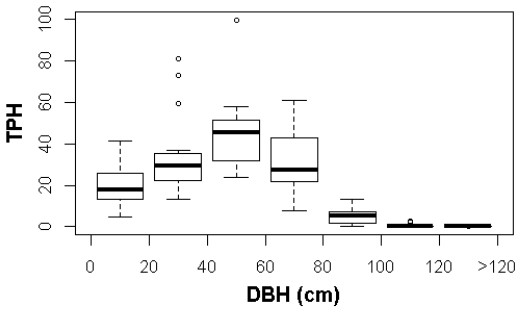
TPH
0 20 40 60 80 100
0 20 40 60 80 100 120 >120
DBH (cm)

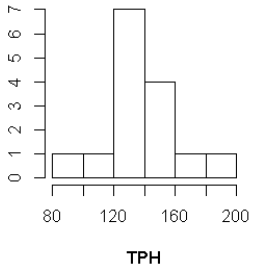
0 1 2 3 4 5 6 7
80 120 160 200
TPH

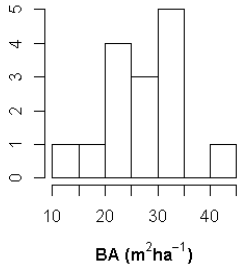
0 1 2 3 4 5
10 20 30 40
BA (m2ha−1)

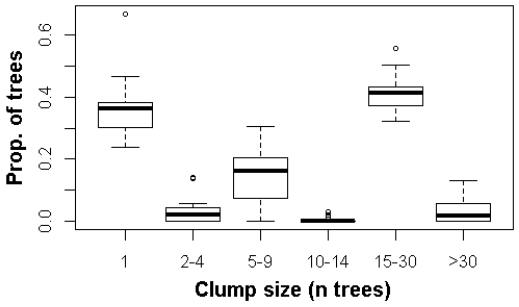
Prop. of trees
0.0 0.2 0.4 0.6
1 2-4 5-9 10-14 15-30 >30
Clump size (n trees)

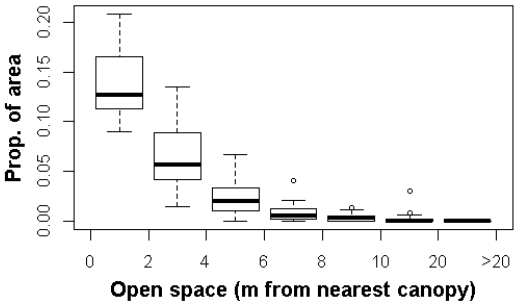
Prop. of area
0.00 0.05 0.10 0.15 0.20
0 2 4 6 8 10 20 >20
Open space (m from nearest canopy)

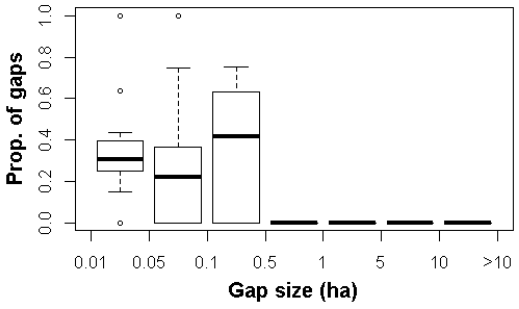
Prop. of gaps
0.0 0.2 0.4 0.6 0.8 1.0
0.01 0.05 0.1 0.5 1 5 10 >10
Gap size (ha)

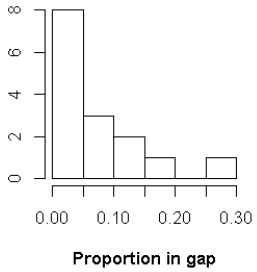
0 2 4 6 8
0.00 0.10 0.20 0.30
Proportion in gap

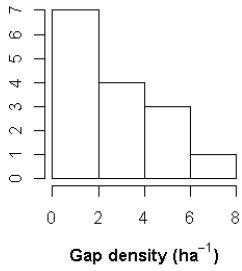
0 1 2 3 4 5 6 7
0 2 4 6 8
Gap density (ha−1)

Dimond O

Ownership	Yosemite National Park and Stanislaus National Forest
Hectares	629

	Ridges	**Valleys**	**NE slopes**	**SW slopes**
Landform proportions	0.26	0.26	0.25	0.23

	Minimum	**Mean**	**Maximum**
AET (mm)	305	400	541
Deficit (mm)	512	595	679
T_{min} (°C)	2.7	3.3	4.2
Elevation (m)	1380	1646	1822

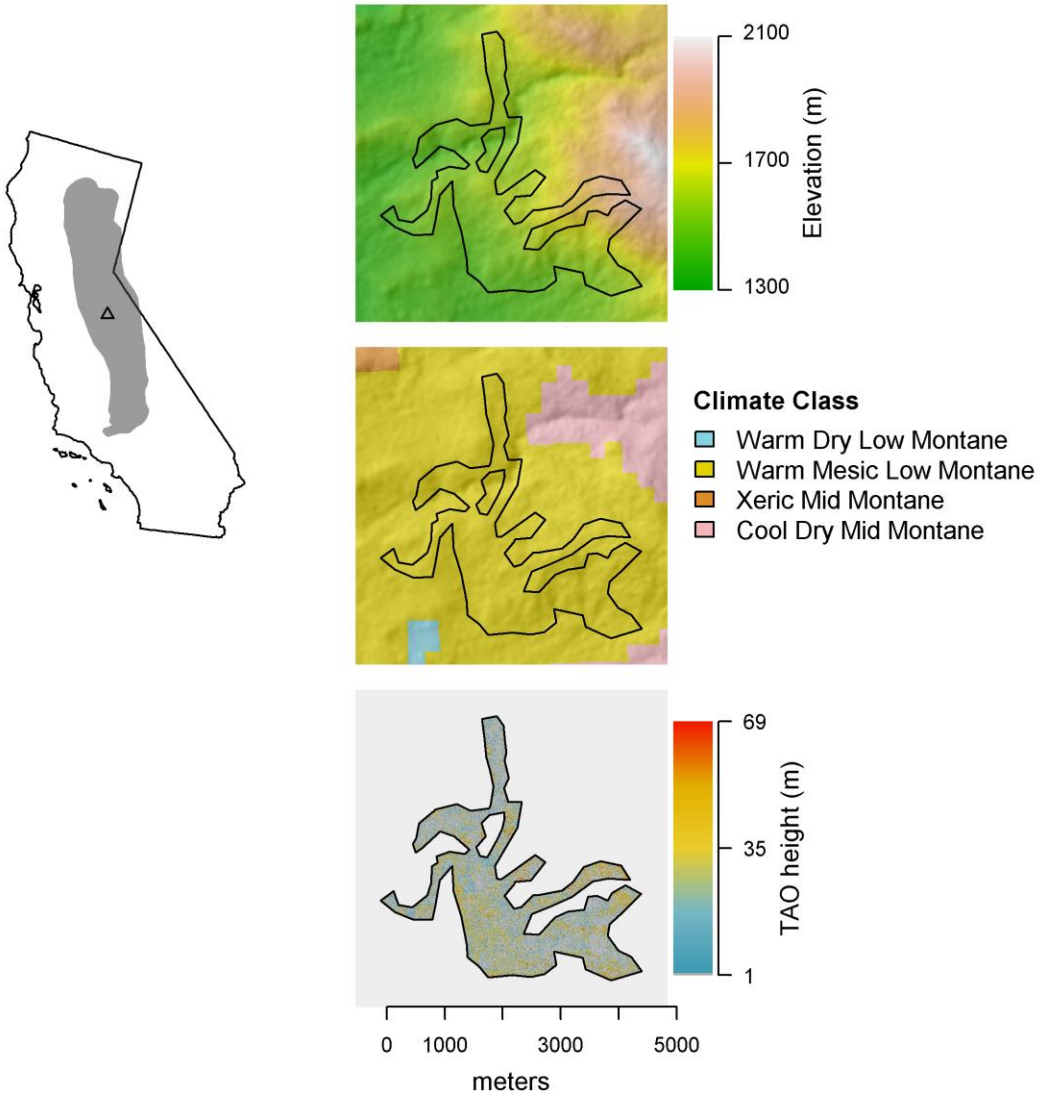

Dimond O

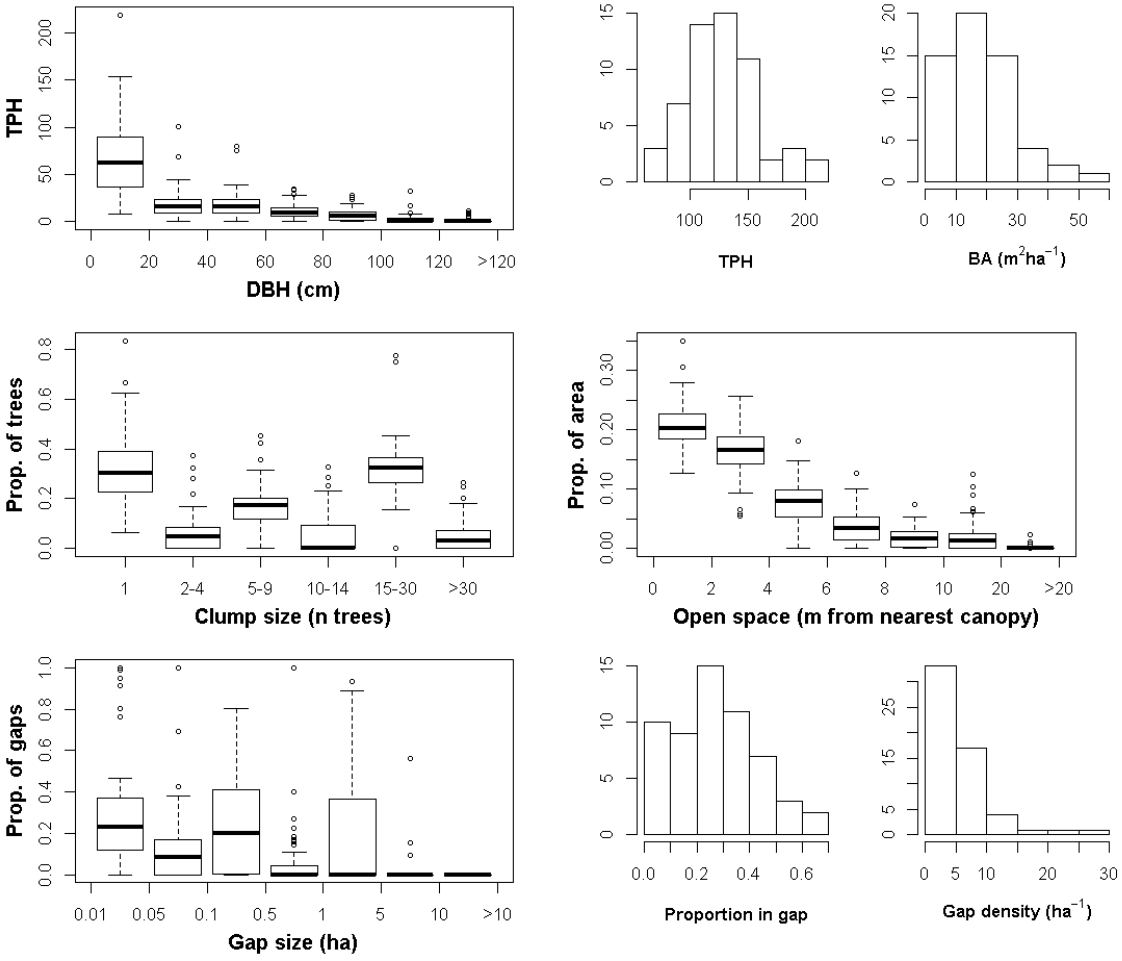
TPH
DBH (cm)
TPH
BA (m²ha⁻¹)
Prop. of trees
Clump size (n trees)
Prop. of area
Open space (m from nearest canopy)
Prop. of gaps
Gap size (ha)
Proportion in gap
Gap density (ha⁻¹)

Edson

Ownership	Yosemite National Park
Hectares	120

	Ridges	**Valleys**	**NE slopes**	**SW slopes**
Landform proportions	0.24	0.15	0.46	0.15

	Minimum	**Mean**	**Maximum**
AET (mm)	231	259	321
Deficit (mm)	416	513	579
T_{min} (°C)	-1.0	-0.24	0.74
Elevation (m)	2371	2419	2480

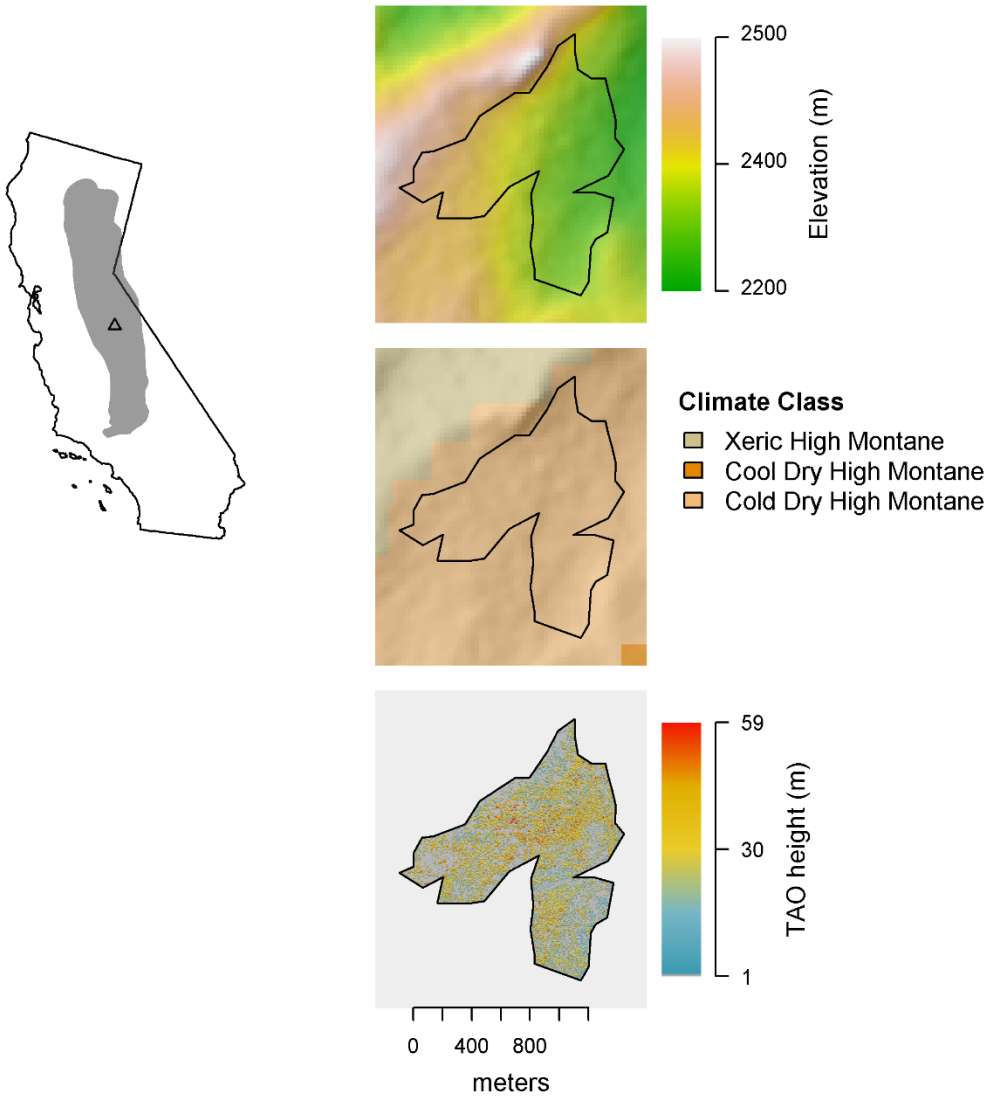

Edson

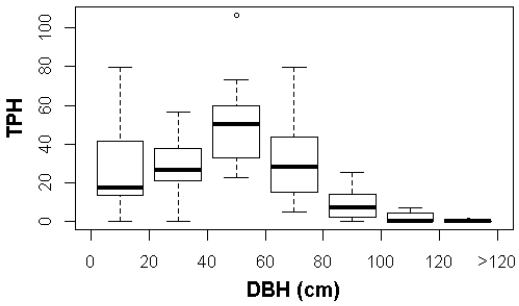
TPH
0 20 40 60 80 100
0 20 40 60 80 100 120 >120
DBH (cm)

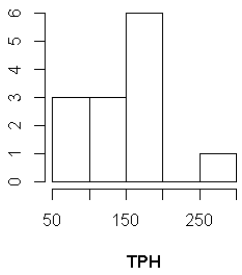
0 1 2 3 4 5 6
50 150 250
TPH

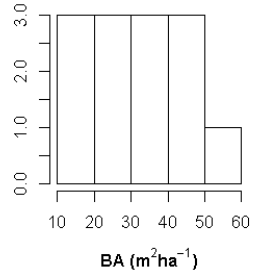
0.0 1.0 2.0 3.0
10 20 30 40 50 60
BA (m2ha-1)

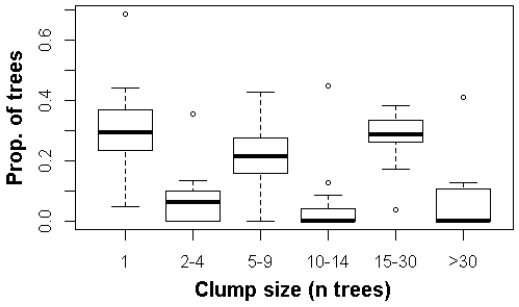
Prop. of trees
0.0 0.2 0.4 0.6
1 2-4 5-9 10-14 15-30 >30
Clump size (n trees)

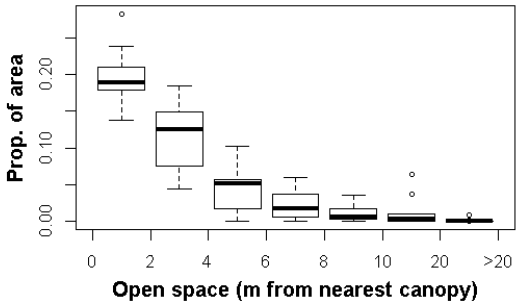
Prop. of area
0.00 0.10 0.20
0 2 4 6 8 10 20 >20
Open space (m from nearest canopy)

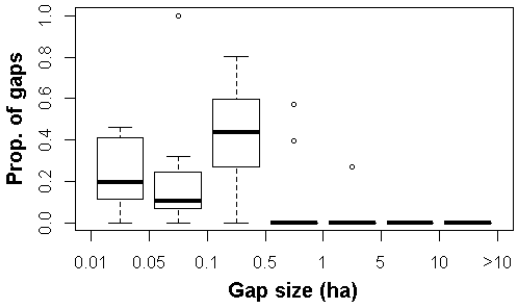
Prop. of gaps
0.0 0.2 0.4 0.6 0.8 1.0
0.01 0.05 0.1 0.5 1 5 10 >10
Gap size (ha)

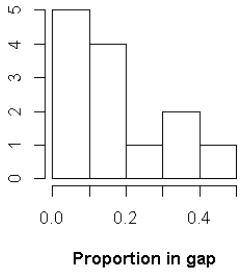
0 1 2 3 4 5
0.0 0.2 0.4
Proportion in gap

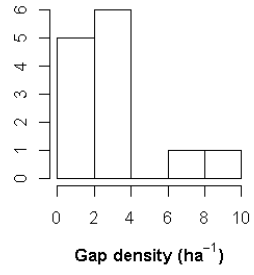
0 1 2 3 4 5 6
0 2 4 6 8 10
Gap density (ha-1)

Generals

Ownership	Sequoia National Park
Hectares	161

	Ridges	**Valleys**	**NE slopes**	**SW slopes**
Landform proportions	0.31	0.19	0.12	0.38

	Minimum	**Mean**	**Maximum**
AET (mm)	409	418	424
Deficit (mm)	547	574	600
T_{min} (°C)	2.2	2.4	2.9
Elevation (m)	1846	1985	2165

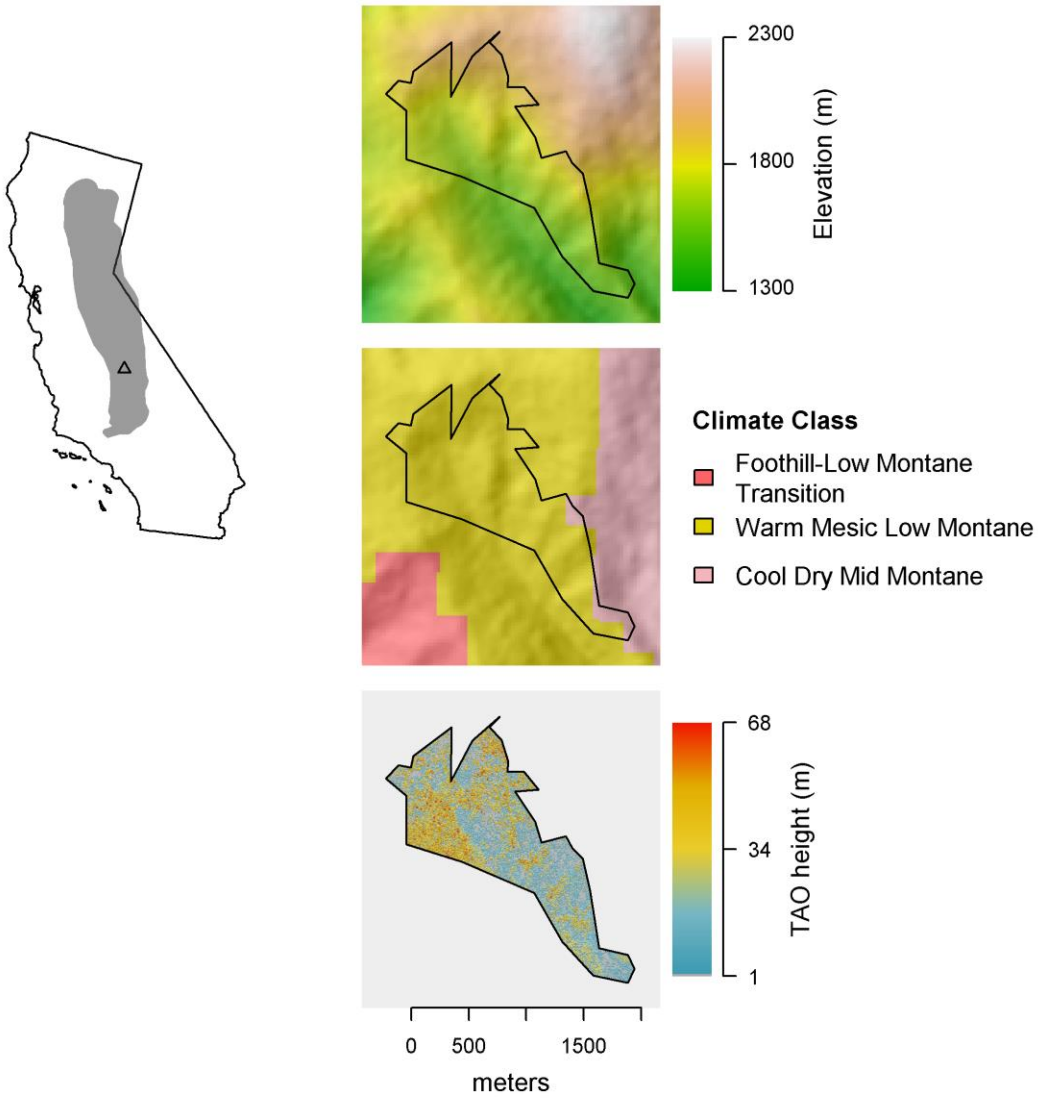

Generals

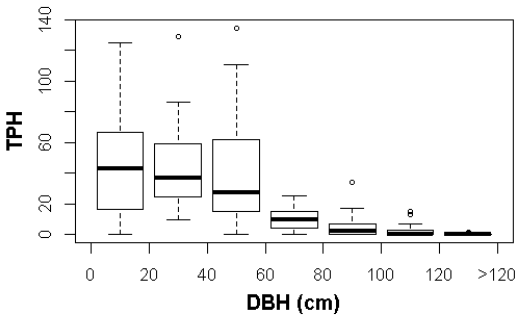
TPH
0 20 60 100 140
0 20 40 60 80 100 120 >120
DBH (cm)

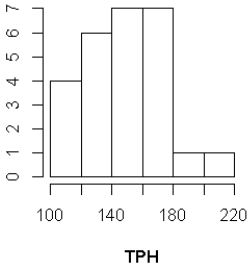
0 1 2 3 4 5 6 7
100 140 180 220
TPH

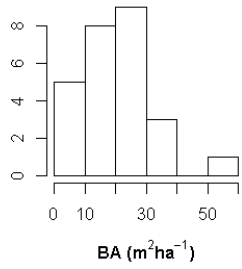
0 2 4 6 8
0 10 30 50
BA (m2ha-1)

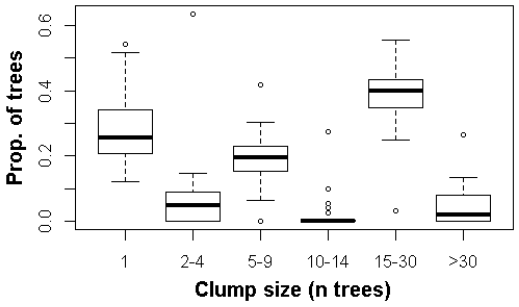
Prop. of trees
0.0 0.2 0.4 0.6
1 2-4 5-9 10-14 15-30 >30
Clump size (n trees)

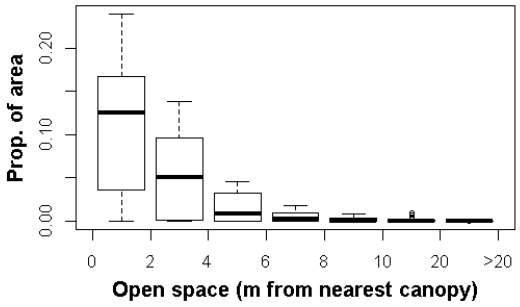
Prop. of area
0.00 0.10 0.20
0 2 4 6 8 10 20 >20
Open space (m from nearest canopy)

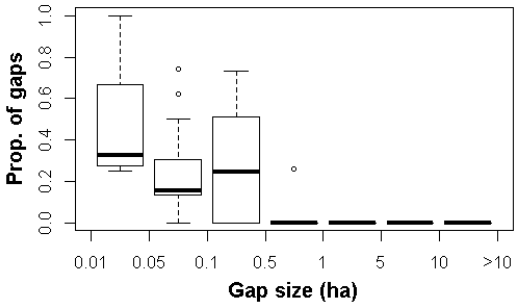
Prop. of gaps
0.0 0.2 0.4 0.6 0.8 1.0
0.01 0.05 0.1 0.5 1 5 10 >10
Gap size (ha)

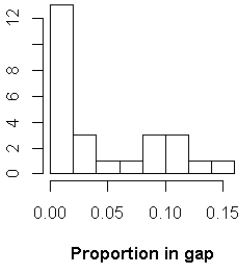
0 2 4 6 8 12
0.00 0.05 0.10 0.15
Proportion in gap

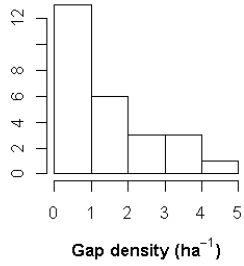
0 2 4 6 8 12
0 1 2 3 4 5
Gap density (ha-1)

Gin

Ownership	Yosemite National Park?			
Hectares	135			
	Ridges	**Valleys**	**NE slopes**	**SW slopes**
Landform proportions	0.47	0.21	0.16	0.16

	Minimum	**Mean**	**Maximum**
AET (mm)	301	329	372
Deficit (mm)	533	580	602
T_{min} (°C)	3.0	3.5	4.0
Elevation (m)	1629	1669	1739

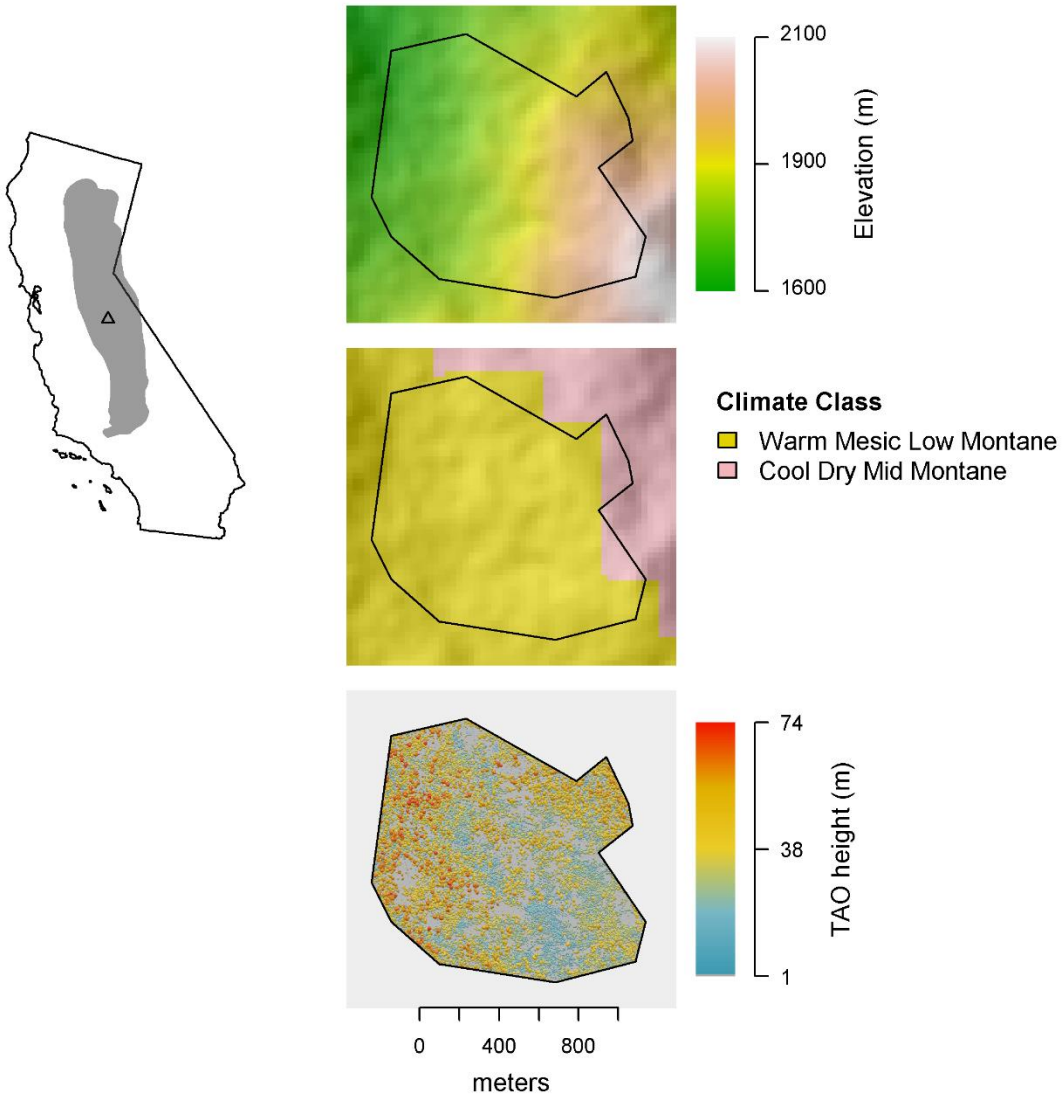

Gin

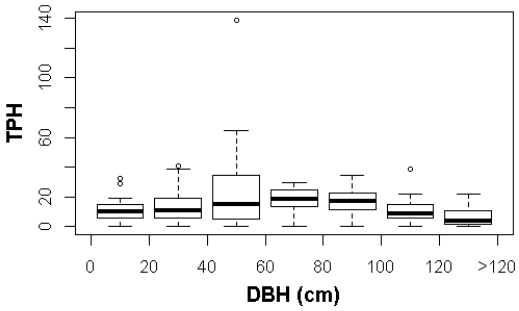
TPH
0 20 60 100 140
0 20 40 60 80 100 120 >120
DBH (cm)

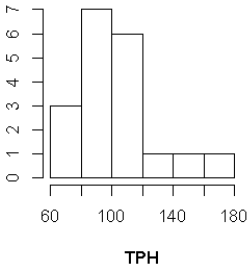
0 1 2 3 4 5 6 7
60 100 140 180
TPH

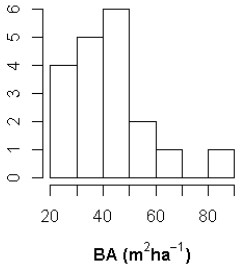
0 1 2 3 4 5 6
20 40 60 80
BA (m2ha−1)

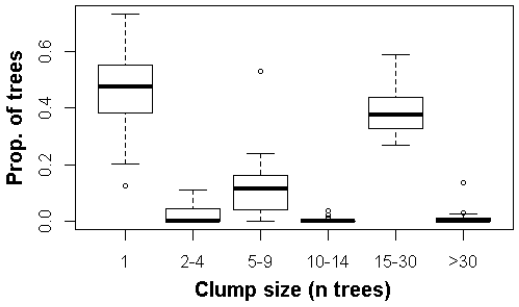
Prop. of trees
0.0 0.2 0.4 0.6
1 2-4 5-9 10-14 15-30 >30
Clump size (n trees)

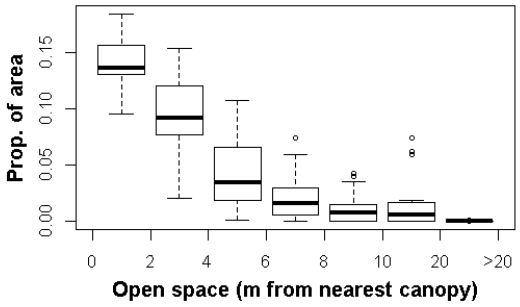
Prop. of area
0.00 0.05 0.10 0.15
0 2 4 6 8 10 20 >20
Open space (m from nearest canopy)

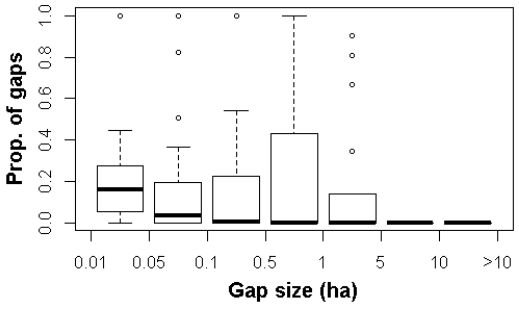
Prop. of gaps
0.0 0.2 0.4 0.6 0.8 1.0
0.01 0.05 0.1 0.5 1 5 10 >10
Gap size (ha)

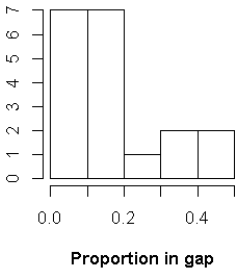
0 1 2 3 4 5 6 7
0.0 0.2 0.4
Proportion in gap

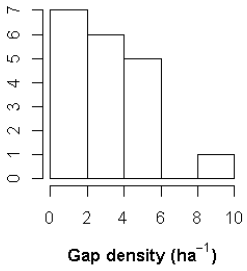
0 1 2 3 4 5 6 7
0 2 4 6 8 10
Gap density (ha−1)

Grayling

Ownership	Yosemite National Park
Hectares	152

	Ridges	**Valleys**	**NE slopes**	**SW slopes**
Landform proportions	0.16	0.05	0.21	0.58

	Minimum	**Mean**	**Maximum**
AET (mm)	276	322	342
Deficit (mm)	359	417	445
T_{min} (°C)	-1.4	-0.90	-0.25
Elevation (m)	2240	2267	2329

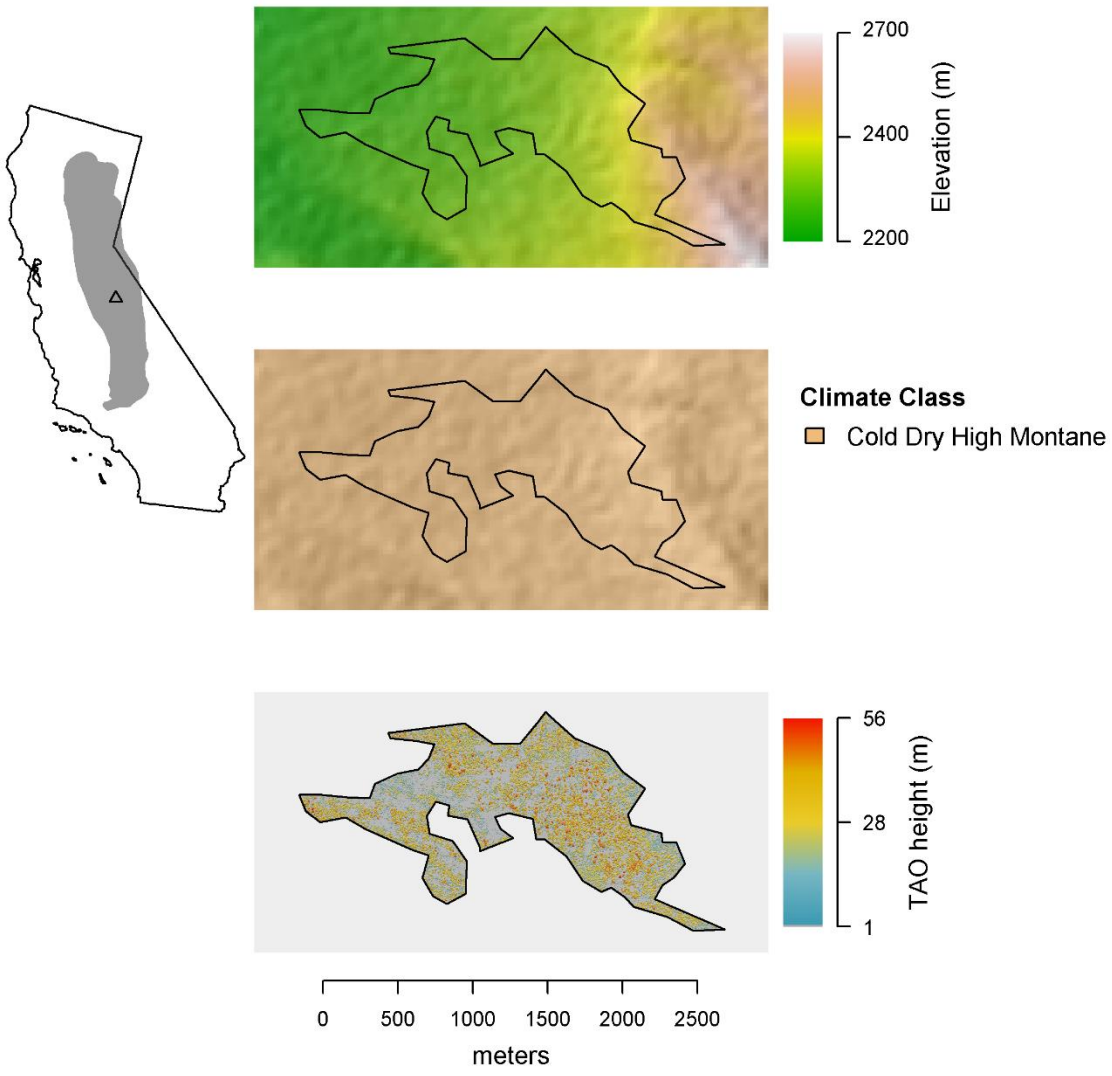

Grayling

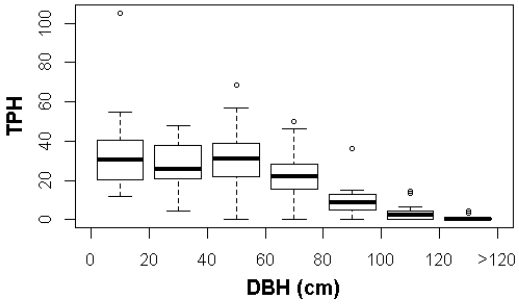
TPH
0 20 40 60 80 100
0 20 40 60 80 100 120 >120
DBH (cm)

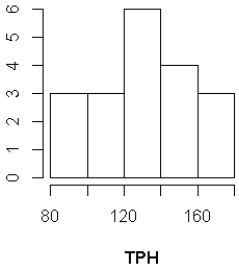
0 1 2 3 4 5 6
80 120 160
TPH

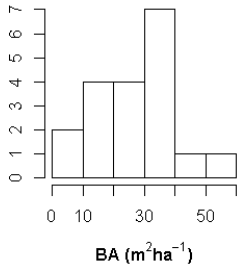
0 1 2 3 4 5 6 7
0 10 30 50
BA (m2ha-1)

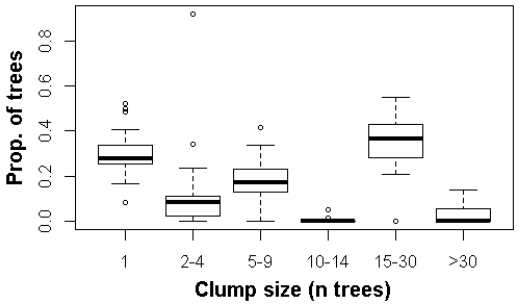
Prop. of trees
0.0 0.2 0.4 0.6 0.8
1 2-4 5-9 10-14 15-30 >30
Clump size (n trees)

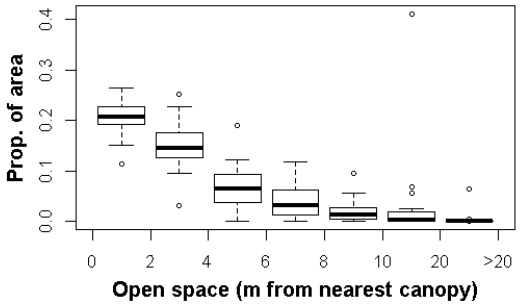
Prop. of area
0.0 0.1 0.2 0.3 0.4
0 2 4 6 8 10 20 >20
Open space (m from nearest canopy)

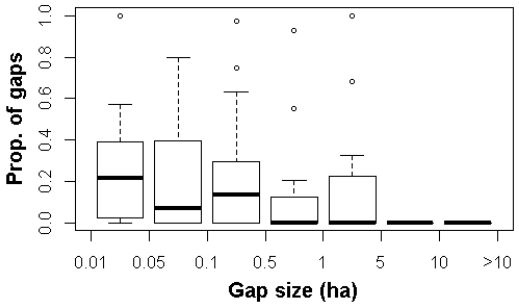
Prop. of gaps
0.0 0.2 0.4 0.6 0.8 1.0
0.01 0.05 0.1 0.5 1 5 10 >10
Gap size (ha)

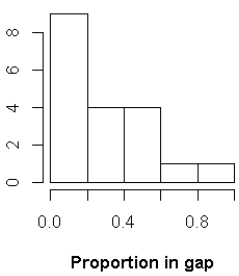
0 2 4 6 8
0.0 0.4 0.8
Proportion in gap

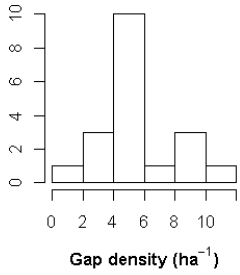
0 2 4 6 8 10
0 2 4 6 8 10
Gap density (ha-1)

Harden

Ownership	Yosemite National Park
Hectares	202

	Ridges	**Valleys**	**NE slopes**	**SW slopes**
Landform proportions	0.18	0.09	0.30	0.42

	Minimum	**Mean**	**Maximum**
AET (mm)	262	295	302
Deficit (mm)	485	500	513
T_{min} (°C)	-0.07	0.16	0.46
Elevation (m)	2269	2385	2435

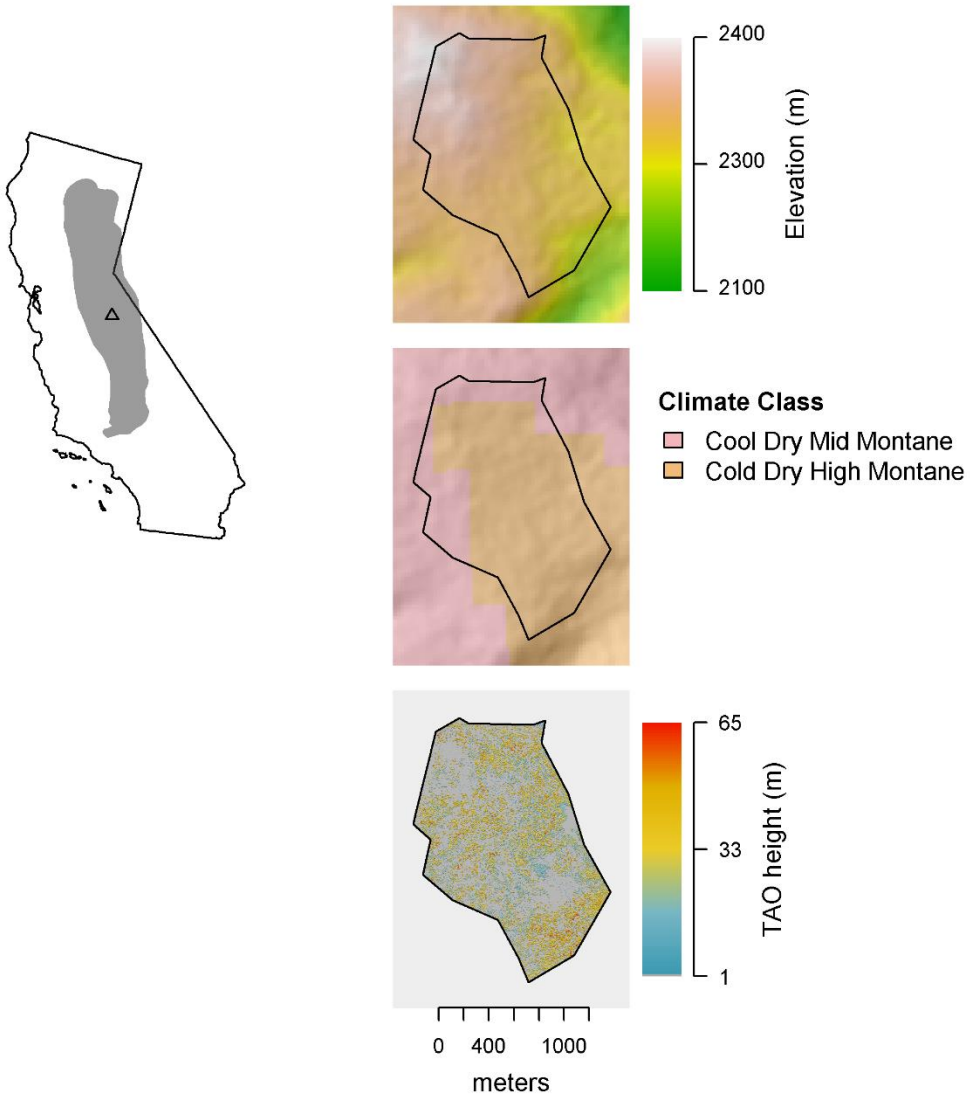

Harden

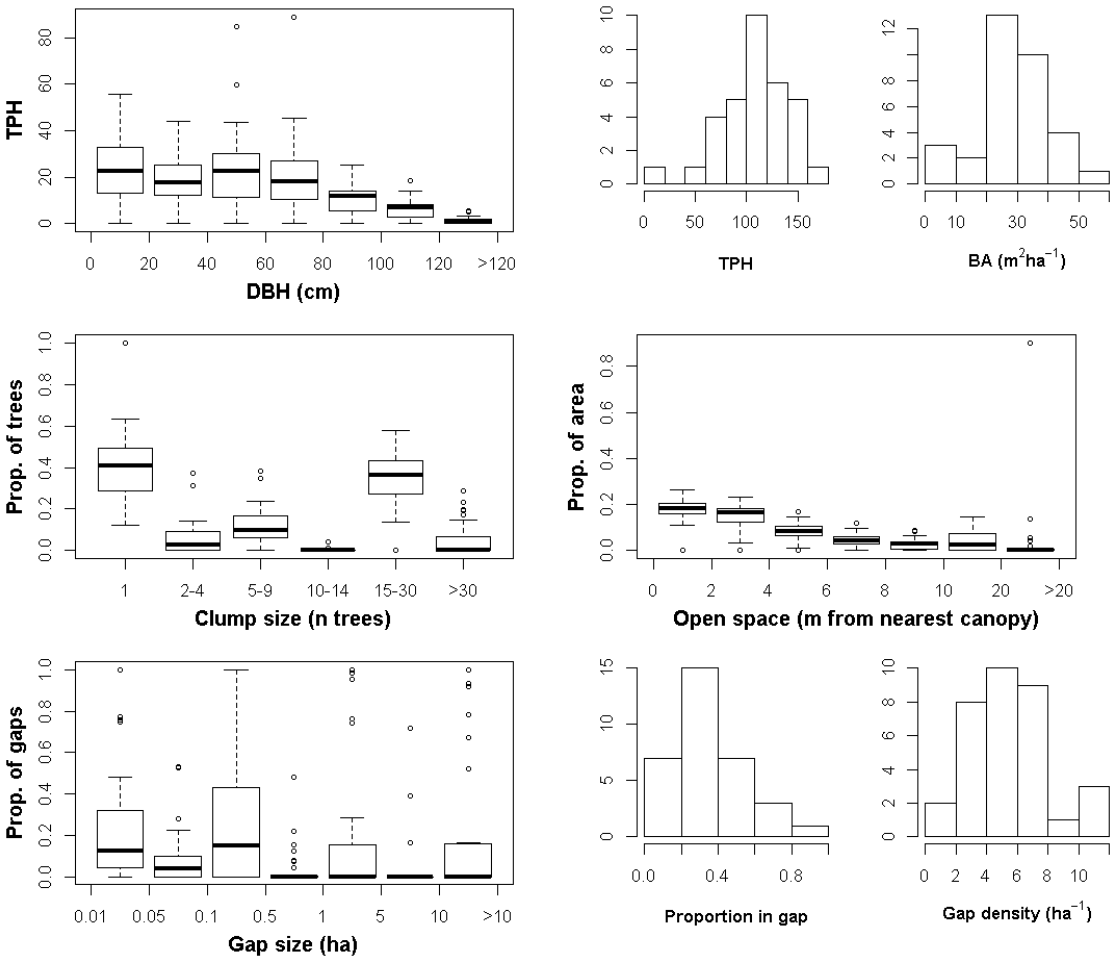
TPH
0 20 40 60 80
0 20 40 60 80 100 120 >120
DBH (cm)
0 2 4 6 8 10
0 50 100 150
TPH
0 2 4 6 8 10 12
0 10 30 50
BA (m2ha-1)
Prop. of trees
0.0 0.2 0.4 0.6 0.8 1.0
1 2-4 5-9 10-14 15-30 >30
Clump size (n trees)
Prop. of area
0.0 0.2 0.4 0.6 0.8
0 2 4 6 8 10 20 >20
Open space (m from nearest canopy)
Prop. of gaps
0.0 0.2 0.4 0.6 0.8 1.0
0.01 0.05 0.1 0.5 1 5 10 >10
Gap size (ha)
0 5 10 15
0.0 0.4 0.8
Proportion in gap
0 2 4 6 8 10
0 2 4 6 8 10
Gap density (ha-1)

Hetch Hetchy

Ownership	Yosemite National Park
Hectares	1314

	Ridges	**Valleys**	**NE slopes**	**SW slopes**
Landform proportions	0.28	0.25	0.25	0.22

	Minimum	**Mean**	**Maximum**
AET (mm)	264	304	376
Deficit (mm)	510	676	758
T_{min} (°C)	2.8	4.6	5.9
Elevation (m)	1091	1339	1650

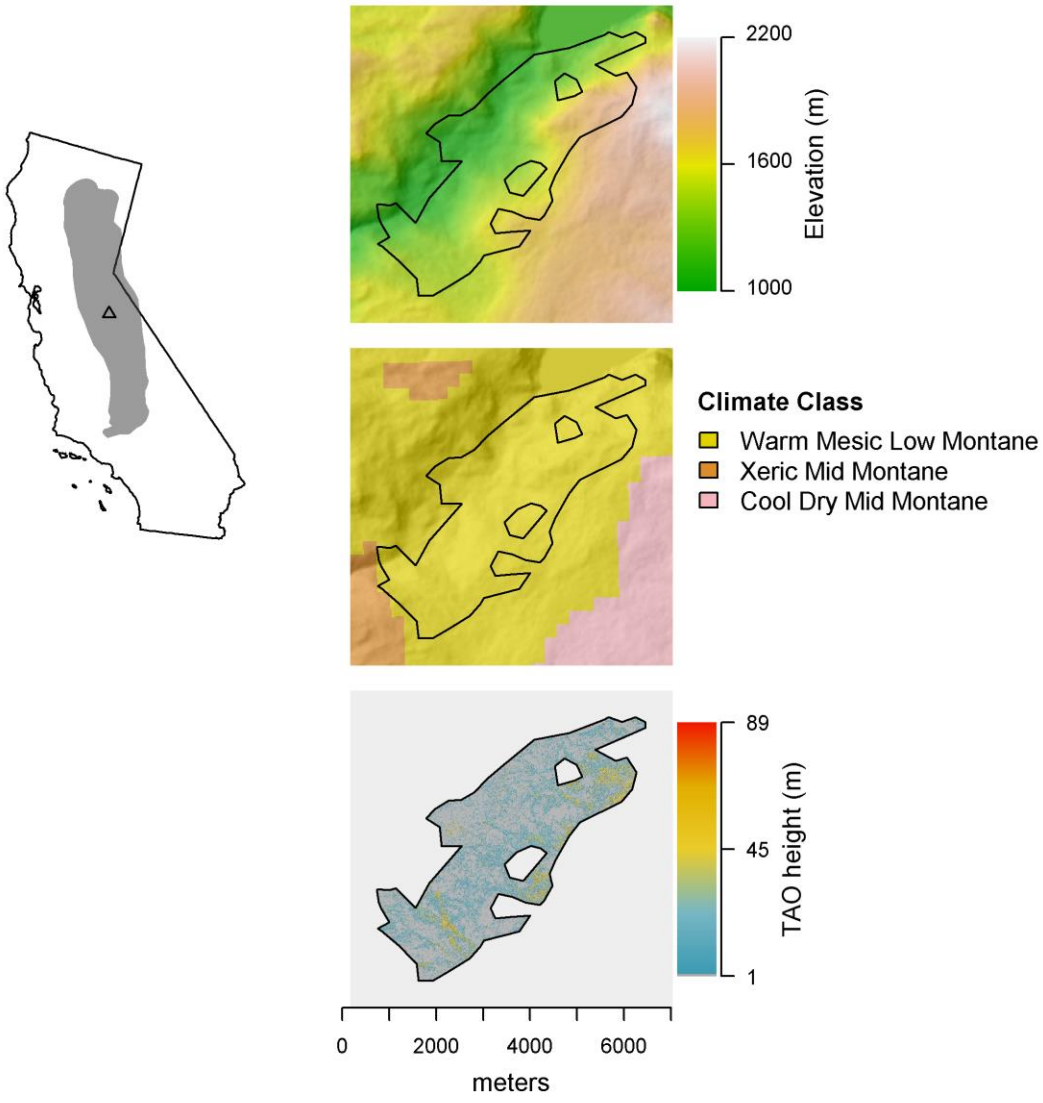

Hetch Hetchy

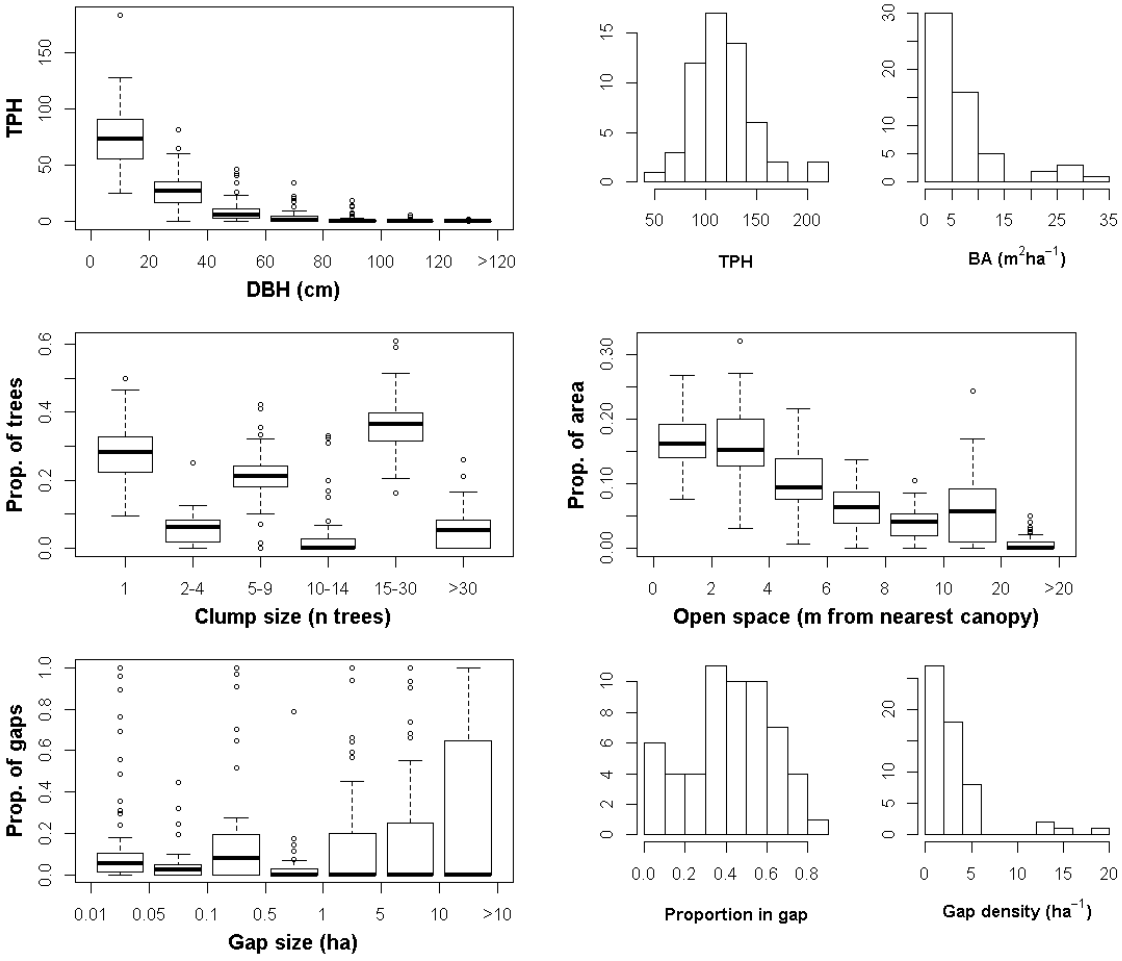

Hetchy View

Ownership	Yosemite National Park
Hectares	105

	Ridges	**Valleys**	**NE slopes**	**SW slopes**
Landform proportions	0.11	0.04	0.33	0.52

	Minimum	**Mean**	**Maximum**
AET (mm)	369	375	384
Deficit (mm)	538	543	550
T_{min} (°C)	2.7	2.8	3.0
Elevation (m)	1714	1748	1783

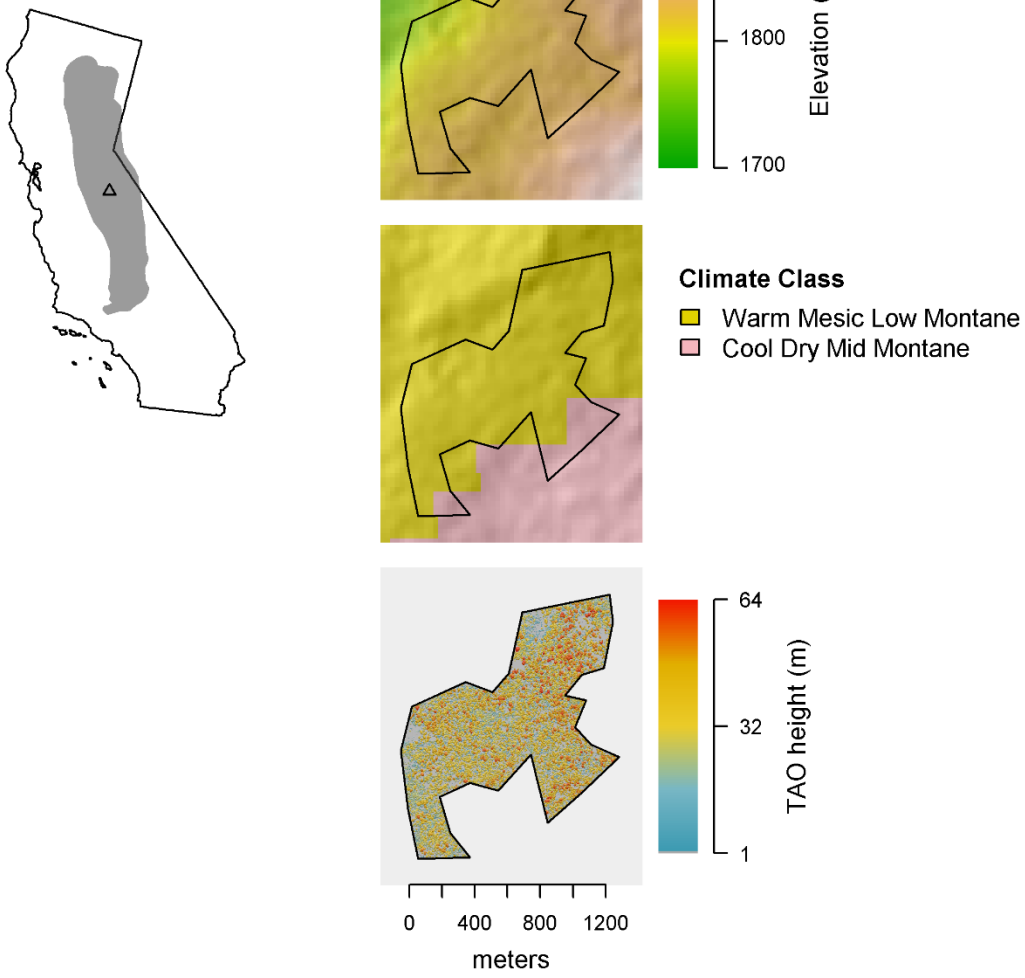

Hetchy View

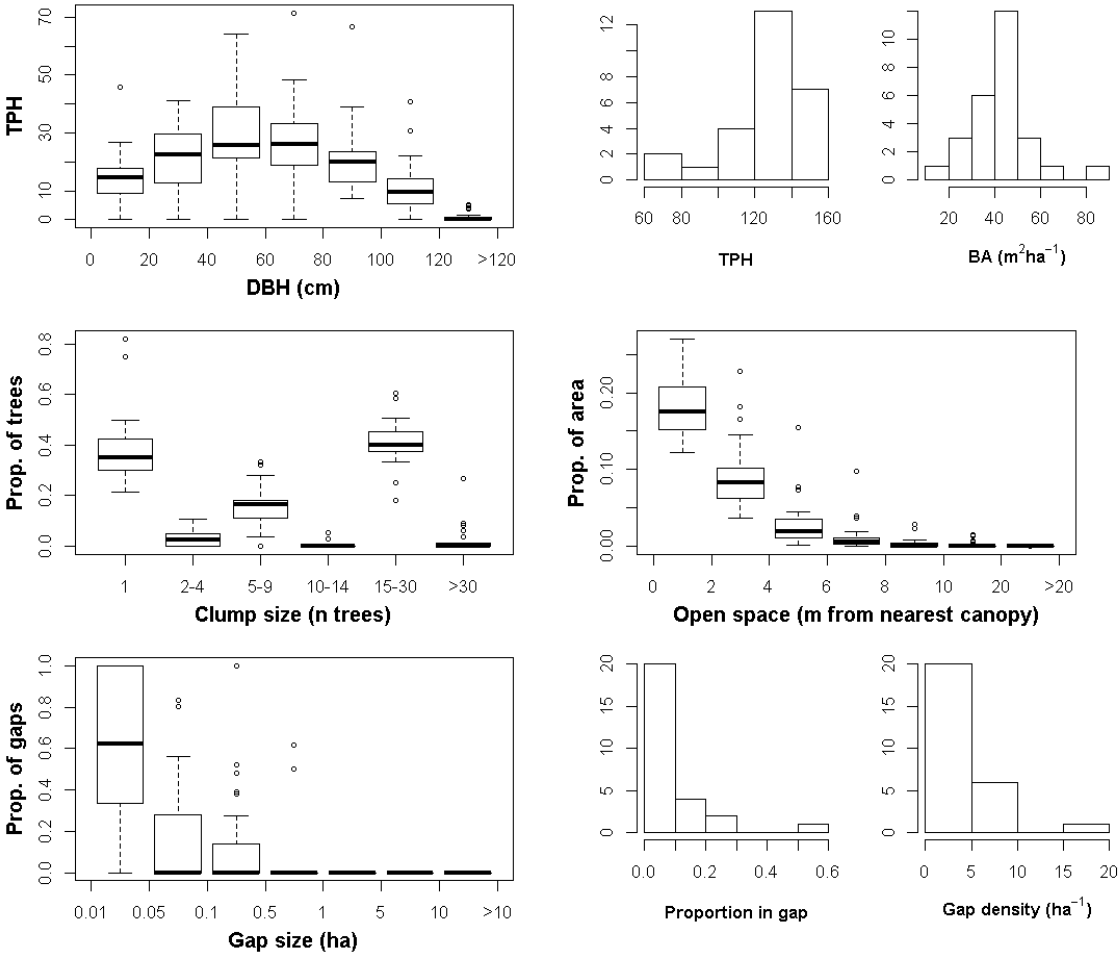
TPH
DBH (cm)
TPH
BA (m²ha⁻¹)
Prop. of trees
Clump size (n trees)
Prop. of area
Open space (m from nearest canopy)
Prop. of gaps
Gap size (ha)
Proportion in gap
Gap density (ha⁻¹)

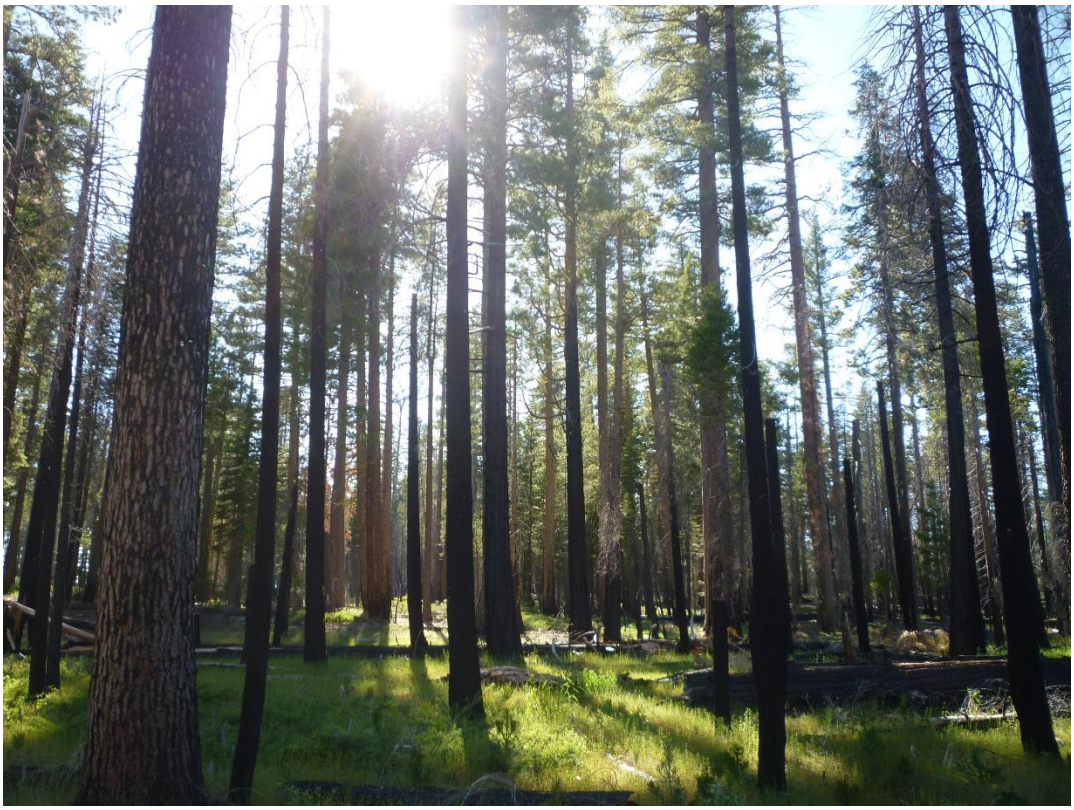

Hodgdon

Ownership	Yosemite National Park
Hectares	675

	Ridges	**Valleys**	**NE slopes**	**SW slopes**
Landform proportions	0.39	0.13	0.26	0.22

	Minimum	**Mean**	**Maximum**
AET (mm)	261	407	506
Deficit (mm)	451	556	688
T_{min} (°C)	2.1	3.3	4.4
Elevation (m)	1622	1708	1935

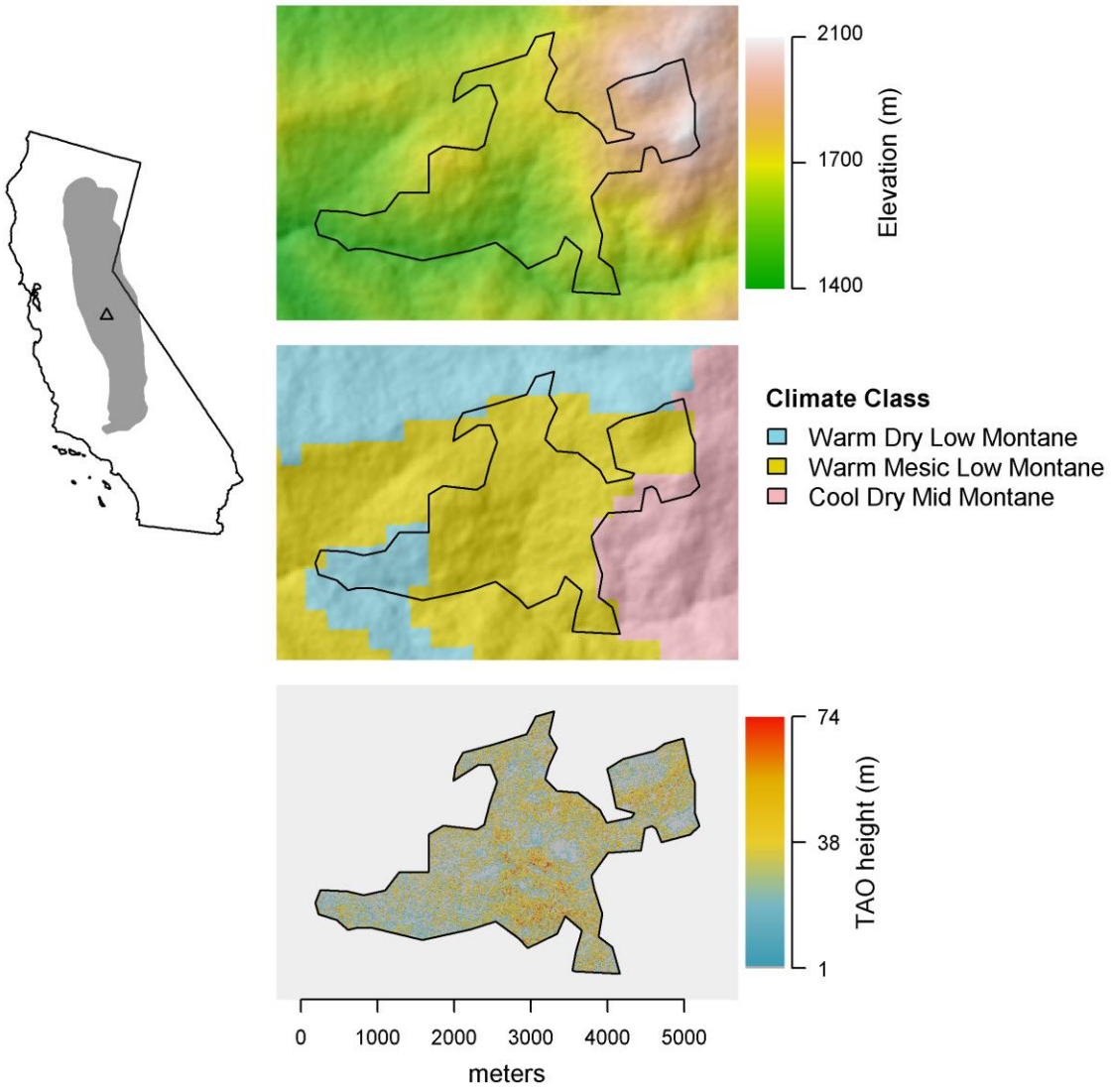

Hodgdon

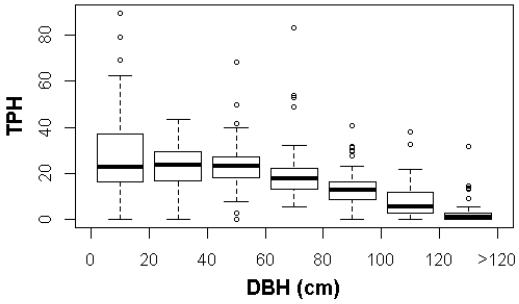
TPH
0 20 40 60 80
0 20 40 60 80 100 120 >120
DBH (cm)

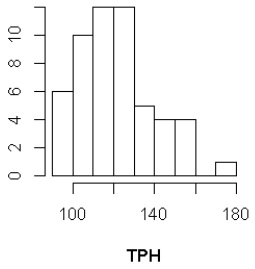
0 2 4 6 8 10
100 140 180
TPH

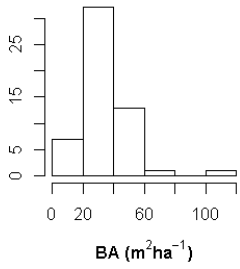
0 5 15 25
0 20 60 100
BA (m2ha−1)

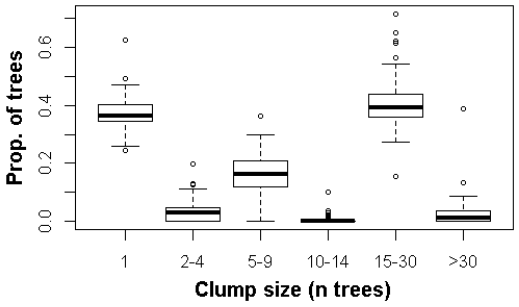
Prop. of trees
0.0 0.2 0.4 0.6
1 2-4 5-9 10-14 15-30 >30
Clump size (n trees)

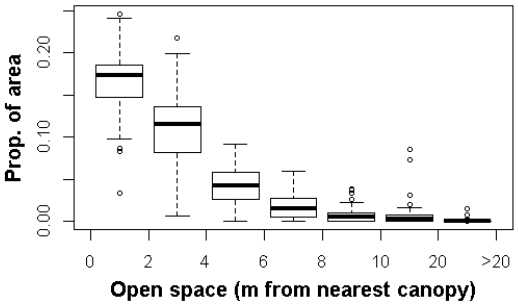
Prop. of area
0.00 0.10 0.20
0 2 4 6 8 10 20 >20
Open space (m from nearest canopy)

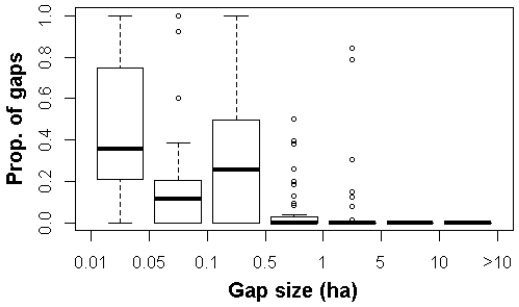
Prop. of gaps
0.0 0.2 0.4 0.6 0.8 1.0
0.01 0.05 0.1 0.5 1 5 10 >10
Gap size (ha)

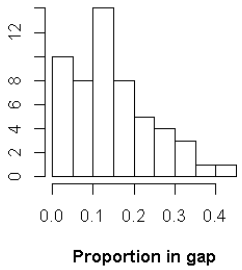
0 2 4 6 8 12
0.0 0.1 0.2 0.3 0.4
Proportion in gap

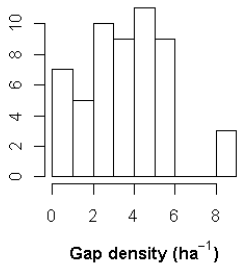
0 2 4 6 8 10
0 2 4 6 8
Gap density (ha−1)

Hoover

Ownership	Yosemite National Park
Hectares	110

	Ridges	**Valleys**	**NE slopes**	**SW slopes**
Landform proportions	0.16	0.23	0.23	0.38

	Minimum	**Mean**	**Maximum**
AET (mm)	230	257	293
Deficit (mm)	407	454	516
T_{min} (°C)	-1.8	-1.4	-0.62
Elevation (m)	2235	2275	2410

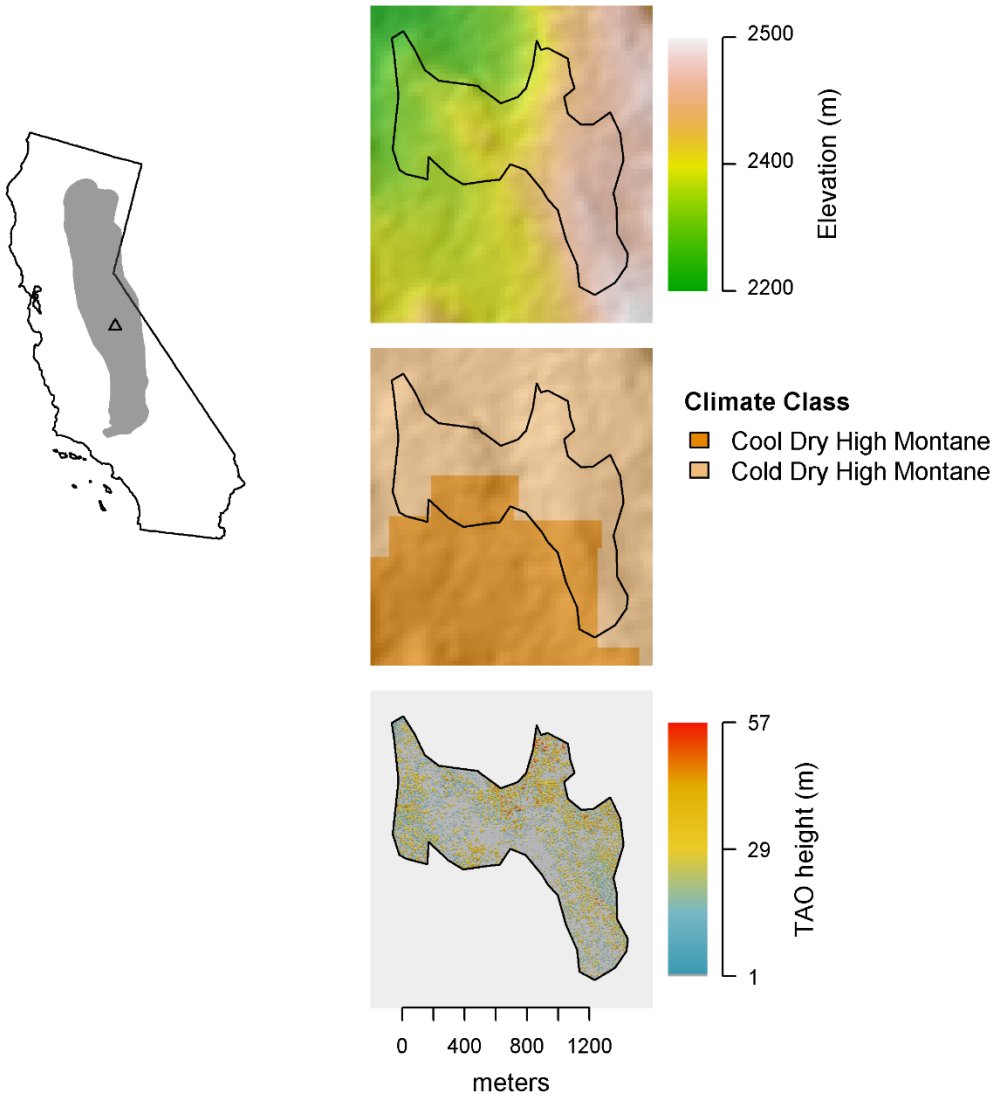

Hoover

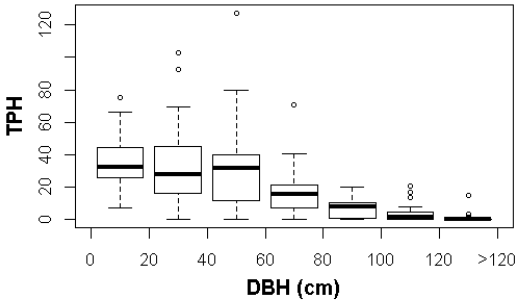
TPH
0 20 40 60 80 100 120
0 20 40 60 80 100 120 >120
DBH (cm)

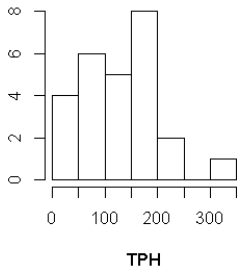
0 2 4 6 8
0 100 200 300
TPH

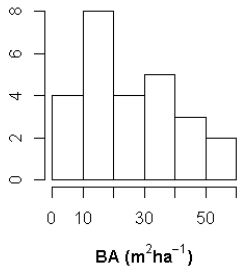
0 2 4 6 8
0 10 30 50
BA (m2ha-1)

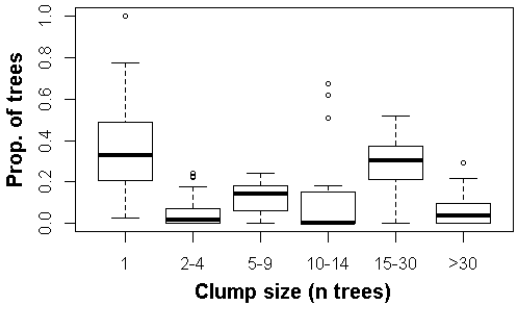
Prop. of trees
0.0 0.2 0.4 0.6 0.8 1.0
1 2-4 5-9 10-14 15-30 >30
Clump size (n trees)

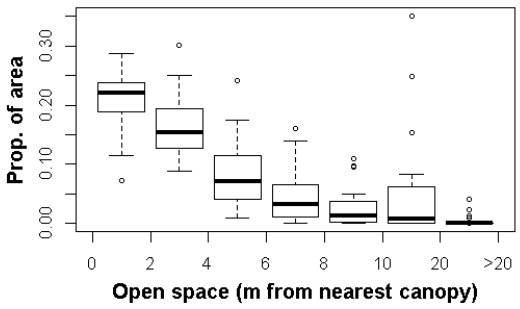
Prop. of area
0.00 0.10 0.20 0.30
0 2 4 6 8 10 20 >20
Open space (m from nearest canopy)

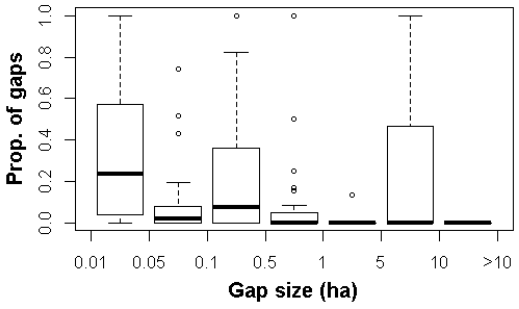
Prop. of gaps
0.0 0.2 0.4 0.6 0.8 1.0
0.01 0.05 0.1 0.5 1 5 10 >10
Gap size (ha)

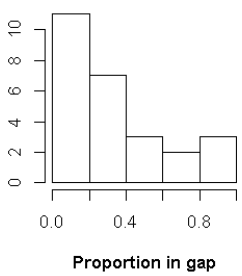
0 2 4 6 8 10
0.0 0.4 0.8
Proportion in gap

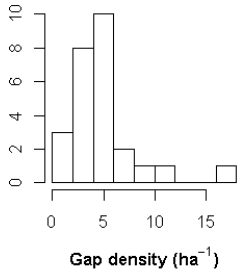
0 2 4 6 8 10
0 5 10 15
Gap density (ha-1)

Horizon				
Ownership	Yosemite?			
Hectares	114			
	Ridges	**Valleys**	**NE slopes**	**SW slopes**
Landform proportions	0.11	0.28	0.28	0.33

	Minimum	**Mean**	**Maximum**
AET (mm)	207	298	367
Deficit (mm)	483	543	633
T_{min} (°C)	0.60	1.4	2.1
Elevation (m)	2281	2352	2394

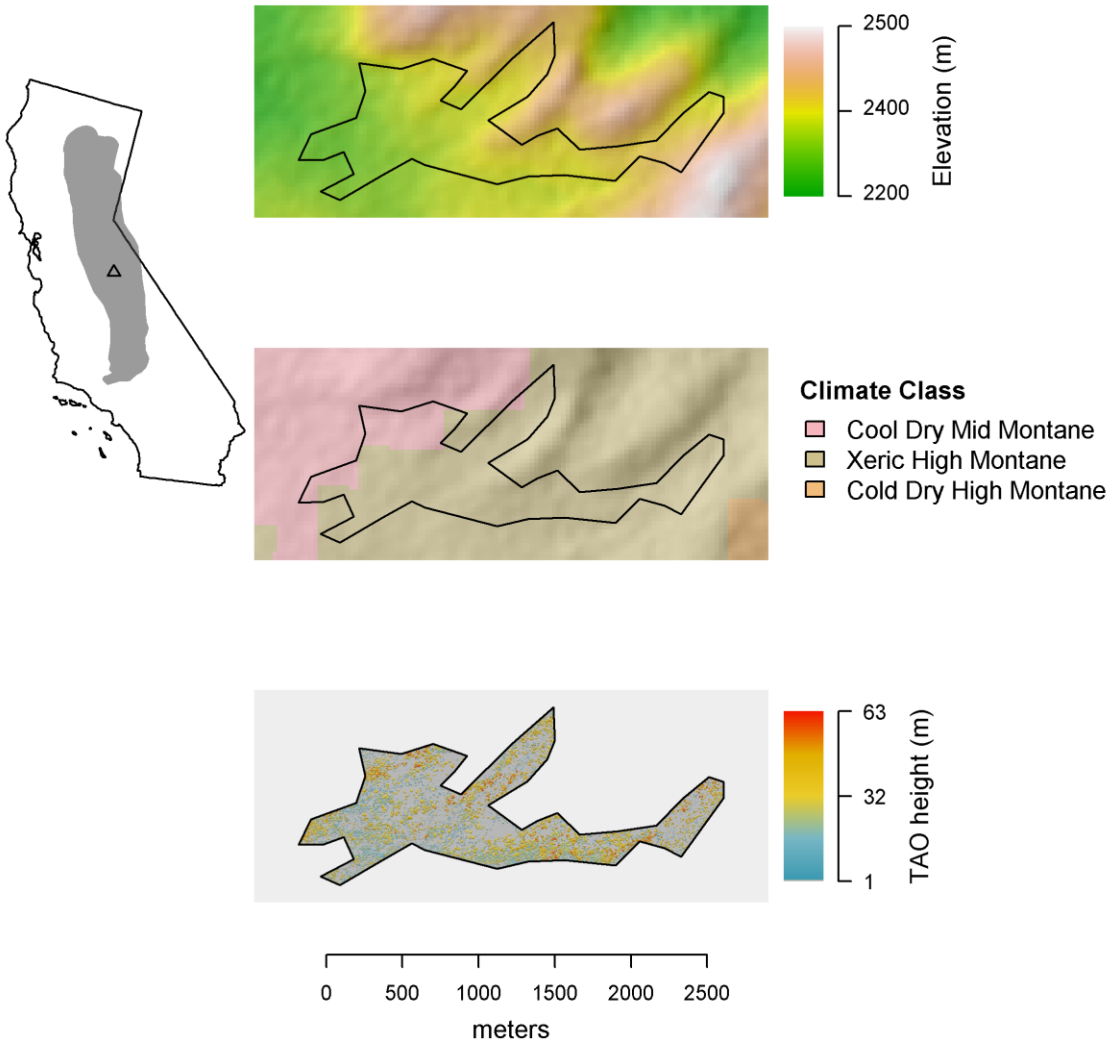

Horizon

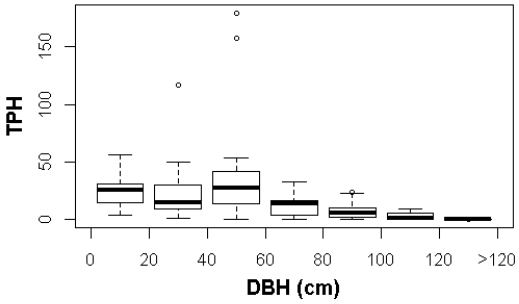
TPH
0 50 100 150
0 20 40 60 80 100 120 >120
DBH (cm)

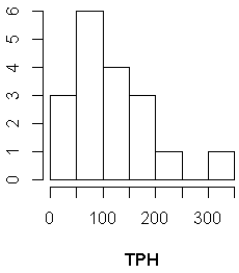
0 1 2 3 4 5 6
0 100 200 300
TPH

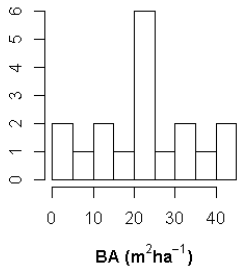
0 1 2 3 4 5 6
0 10 20 30 40
BA (m2ha-1)

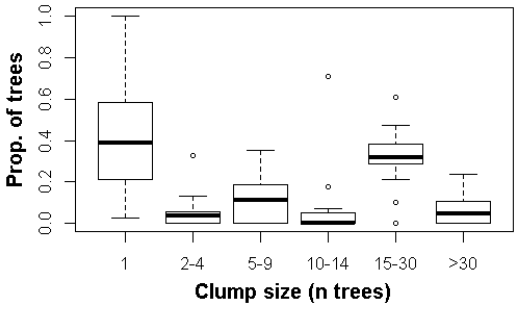
Prop. of trees
0.0 0.2 0.4 0.6 0.8 1.0
1 2-4 5-9 10-14 15-30 >30
Clump size (n trees)

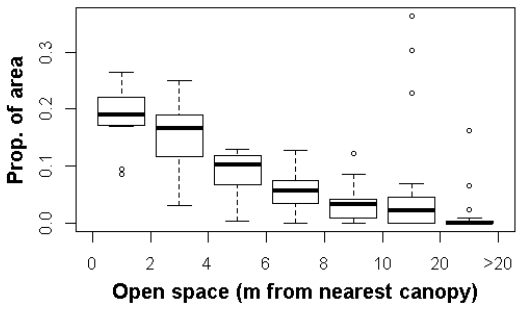
Prop. of area
0.0 0.1 0.2 0.3
0 2 4 6 8 10 20 >20
Open space (m from nearest canopy)

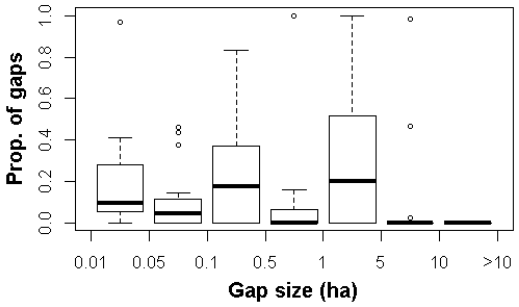
Prop. of gaps
0.0 0.2 0.4 0.6 0.8 1.0
0.01 0.05 0.1 0.5 1 5 10 >10
Gap size (ha)

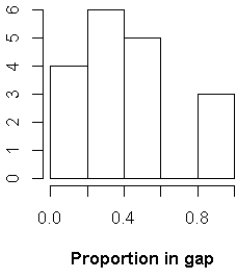
0 1 2 3 4 5 6
0.0 0.4 0.8
Proportion in gap

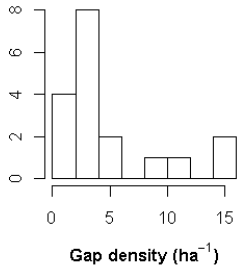
0 2 4 6 8
0 5 10 15
Gap density (ha-1)

Illilouette Creek

Ownership	Yosemite National Park
Hectares	113

	Ridges	**Valleys**	**NE slopes**	**SW slopes**
Landform proportions	0.16	0.21	0.26	0.37

	Minimum	**Mean**	**Maximum**
AET (mm)	355	360	369
Deficit (mm)	479	496	511
T_{min} (°C)	0.94	1.6	2.0
Elevation (m)	1957	2016	2104

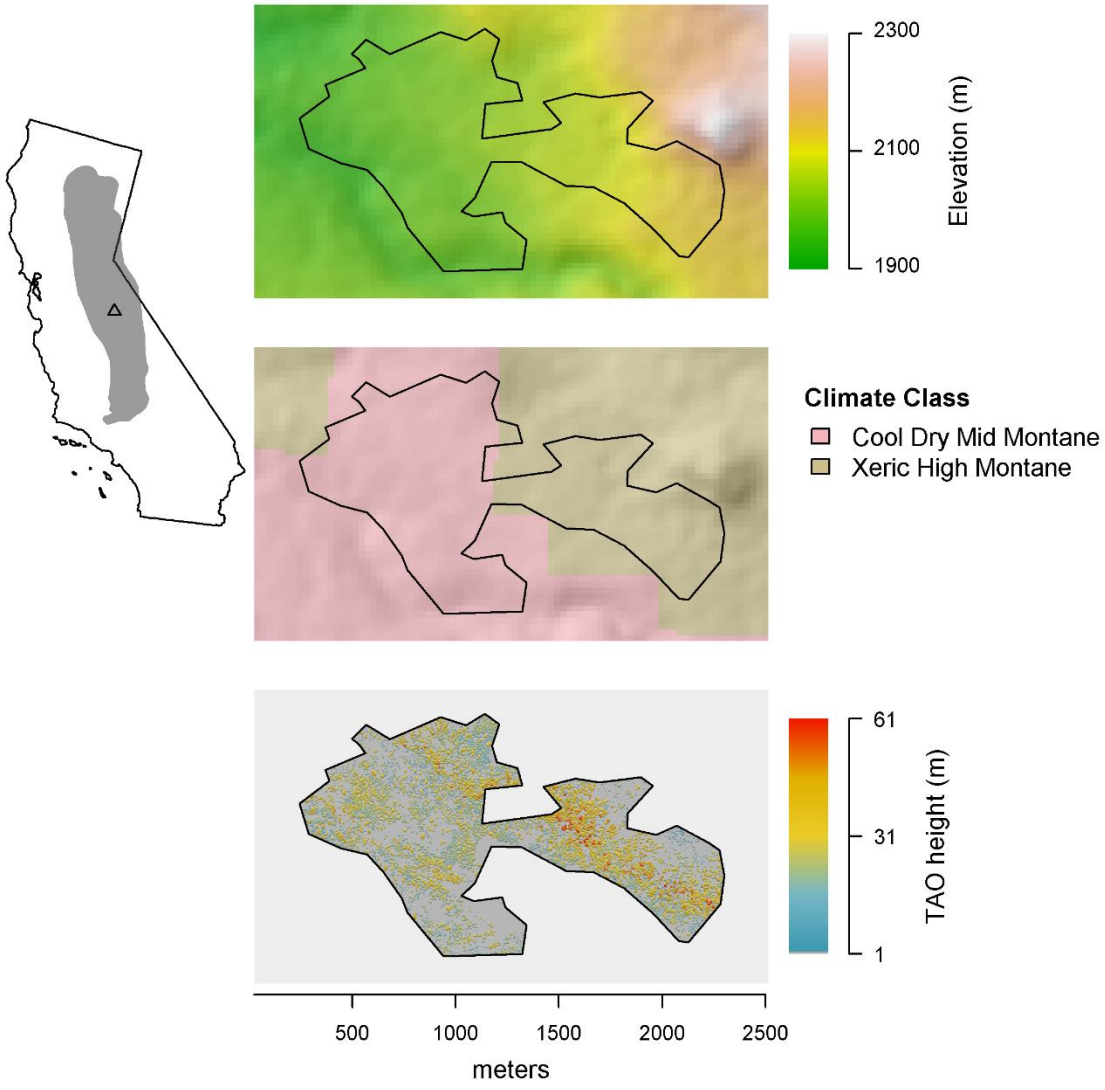

Illilouette Creek

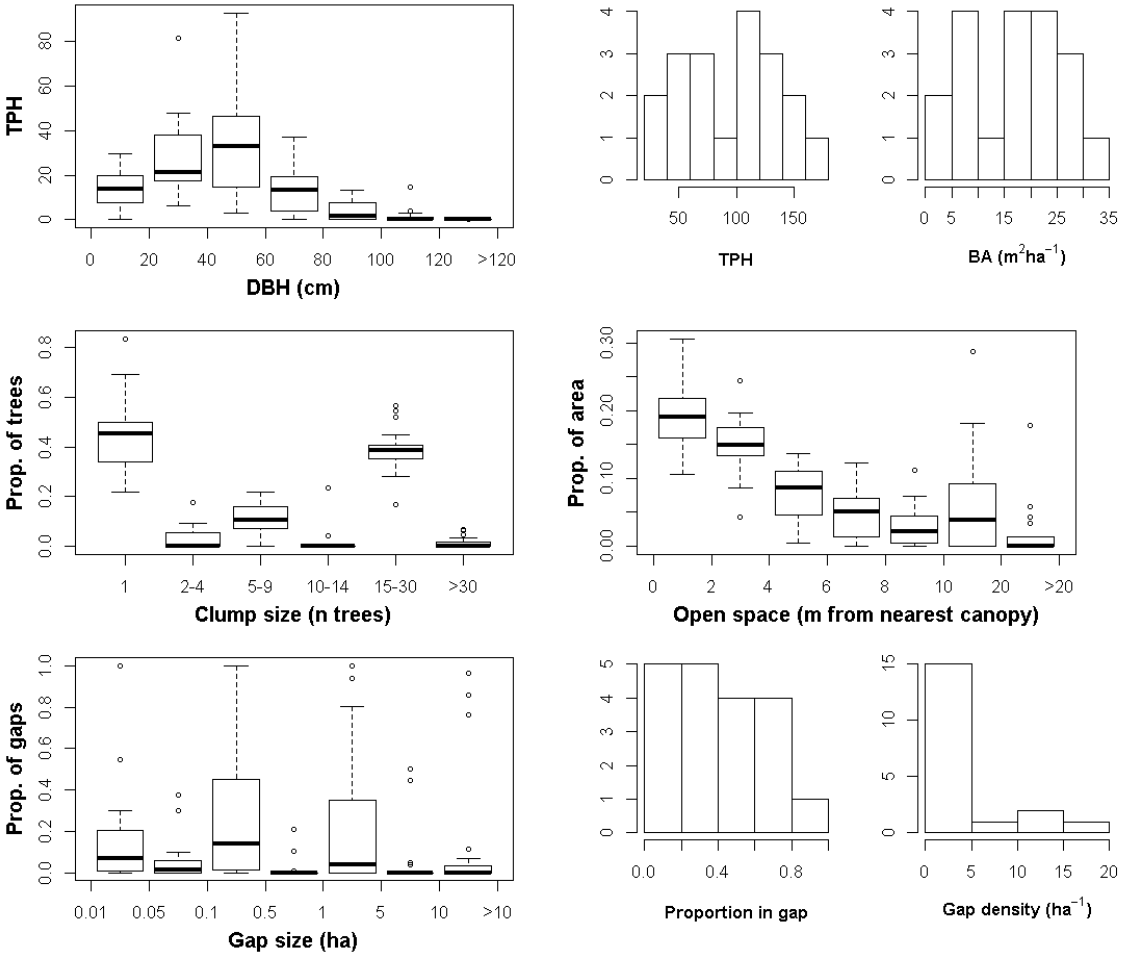

Illilouette Ridge

Ownership	Yosemite National Park
Hectares	128

	Ridges	**Valleys**	**NE slopes**	**SW slopes**
Landform proportions	0.18	0.10	0.36	0.36

	Minimum	**Mean**	**Maximum**
AET (mm)	260	298	372
Deficit (mm)	494	568	604
T_{min} (°C)	0.52	1.8	2.4
Elevation (m)	2275	2357	2403

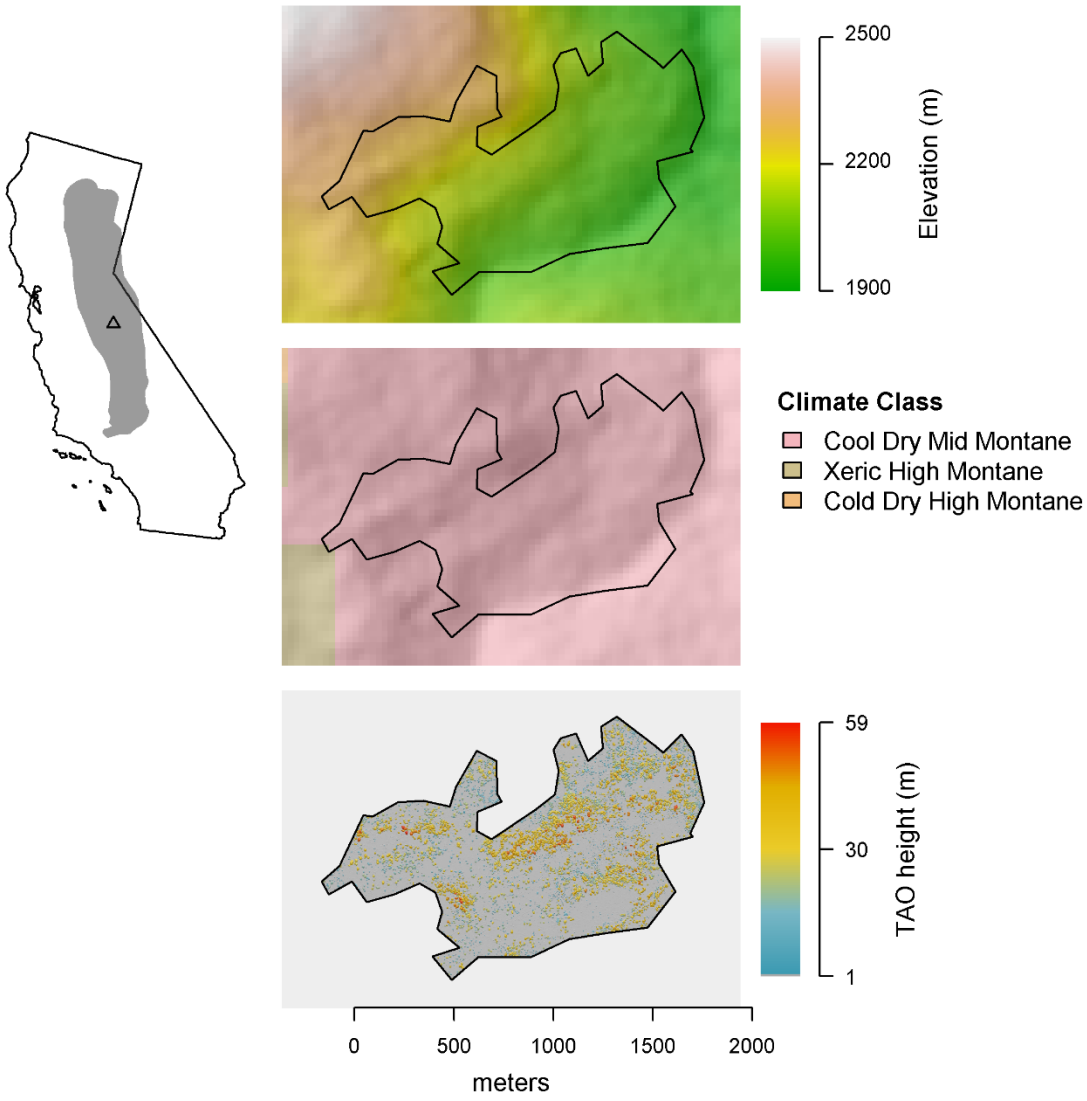

Illilouette Ridge

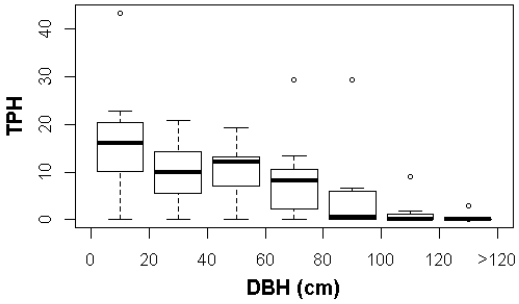

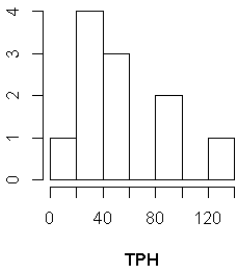

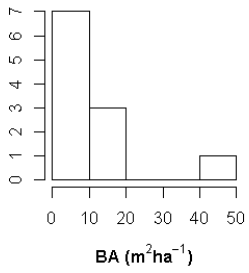

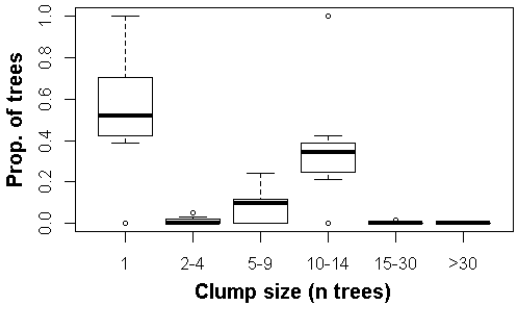

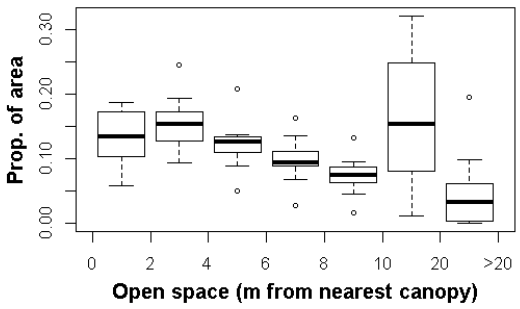

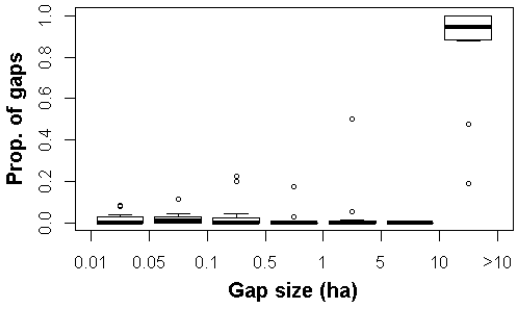

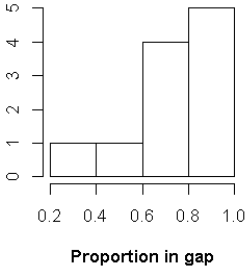

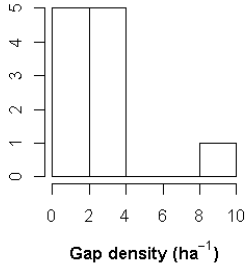

Kolana

Ownership	Yosemite National Park
Hectares	224

	Ridges	**Valleys**	**NE slopes**	**SW slopes**
Landform proportions	0.32	0.32	0.32	0.04

	Minimum	**Mean**	**Maximum**
AET (mm)	250	300	586
Deficit (mm)	359	584	636
T_{min} (°C)	2.5	4.2	5.2
Elevation (m)	1150	1356	1643

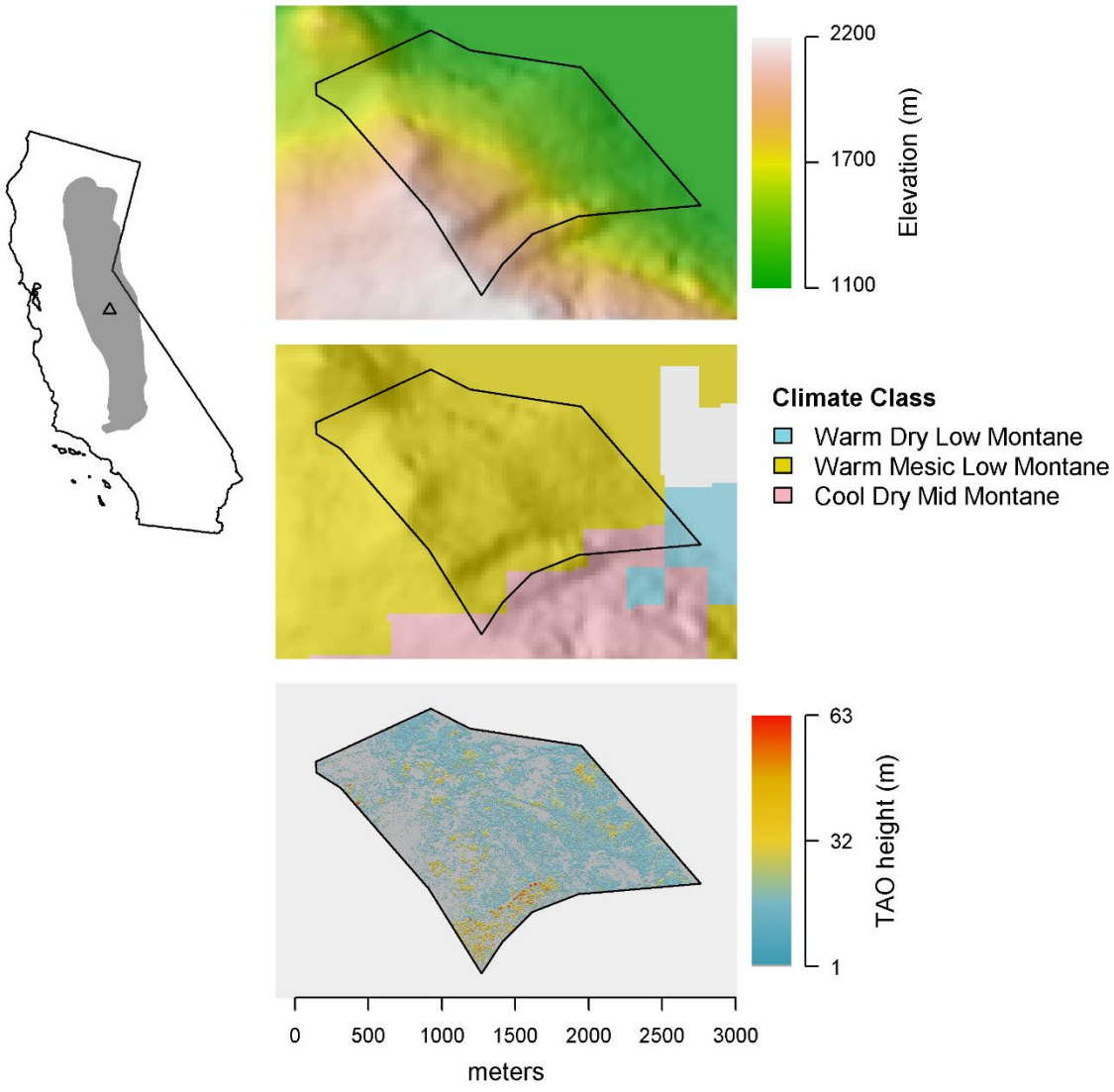

Kolana

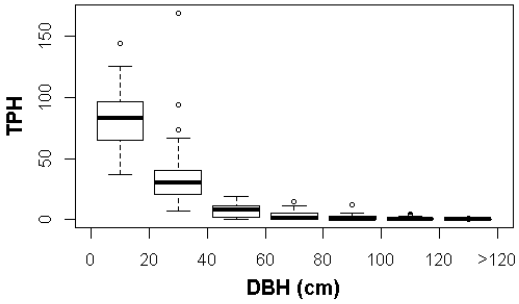
TPH
0 50 100 150
0 20 40 60 80 100 120 >120
DBH (cm)

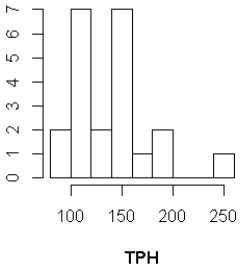
0 1 2 3 4 5 6 7
100 150 200 250
TPH

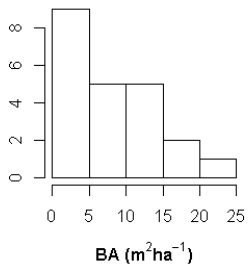
0 2 4 6 8
0 5 10 15 20 25
BA (m2ha−1)

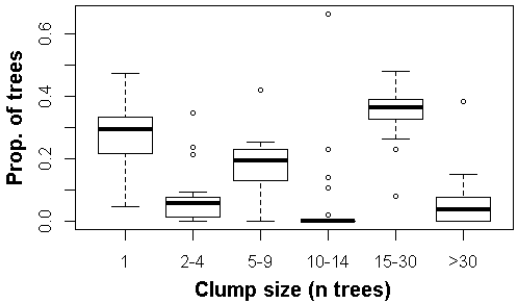
Prop. of trees
0.0 0.2 0.4 0.6
1 2-4 5-9 10-14 15-30 >30
Clump size (n trees)

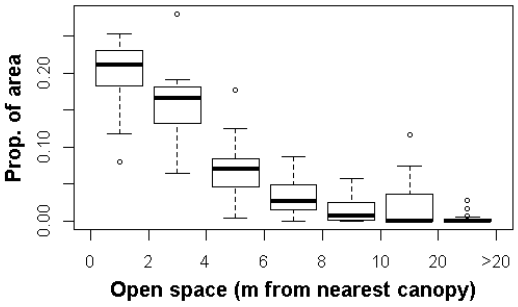
Prop. of area
0.00 0.10 0.20
0 2 4 6 8 10 20 >20
Open space (m from nearest canopy)

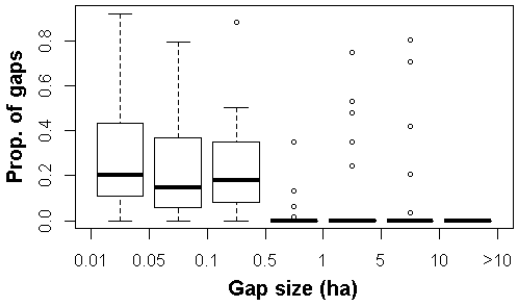
Prop. of gaps
0.0 0.2 0.4 0.6 0.8
0.01 0.05 0.1 0.5 1 5 10 >10
Gap size (ha)

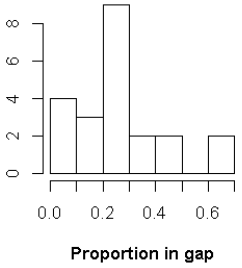
0 2 4 6 8
0.0 0.2 0.4 0.6
Proportion in gap

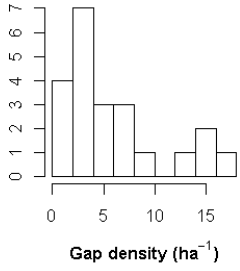
0 1 2 3 4 5 6 7
0 5 10 15
Gap density (ha−1)

Long Gulch

Ownership	Yosemite National Park
Hectares	363

	Ridges	**Valleys**	**NE slopes**	**SW slopes**
Landform proportions	0.15	0.24	0.46	0.15

	Minimum	**Mean**	**Maximum**
AET (mm)	265	372	419
Deficit (mm)	470	519	598
T_{min} (°C)	2.1	2.6	2.9
Elevation (m)	2007	2081	2165

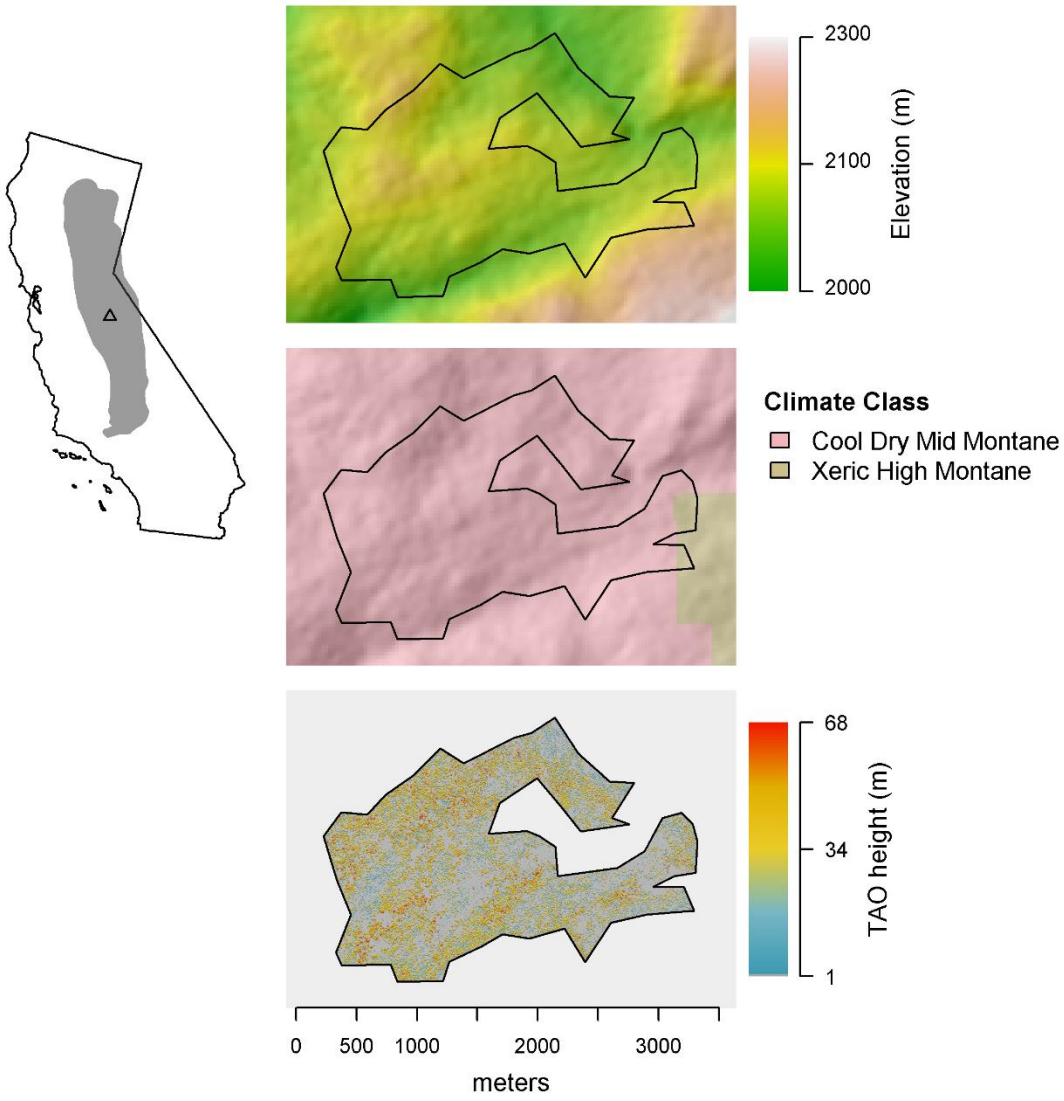

Long Gulch

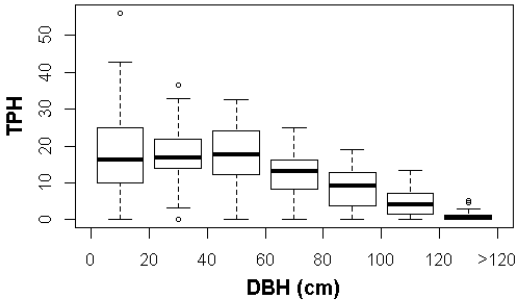
TPH
0 10 20 30 40 50
0 20 40 60 80 100 120 >120
DBH (cm)

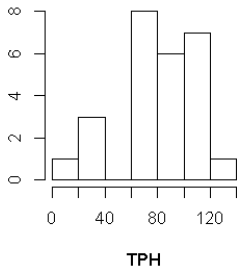
0 2 4 6 8
0 40 80 120
TPH

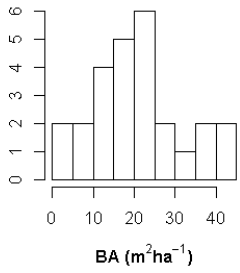
0 1 2 3 4 5 6
0 10 20 30 40
BA (m2ha−1)

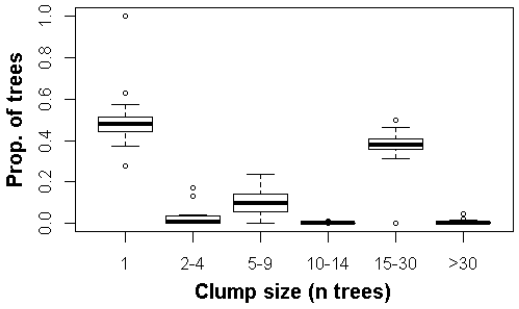
Prop. of trees
0.0 0.2 0.4 0.6 0.8 1.0
1 2-4 5-9 10-14 15-30 >30
Clump size (n trees)

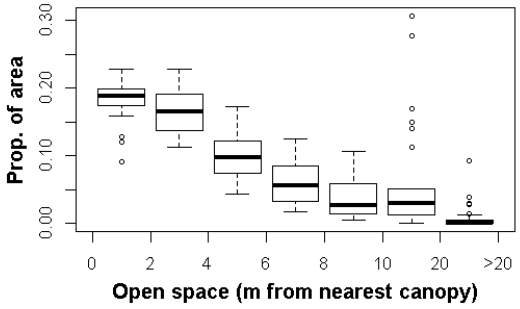
Prop. of area
0.00 0.10 0.20 0.30
0 2 4 6 8 10 20 >20
Open space (m from nearest canopy)

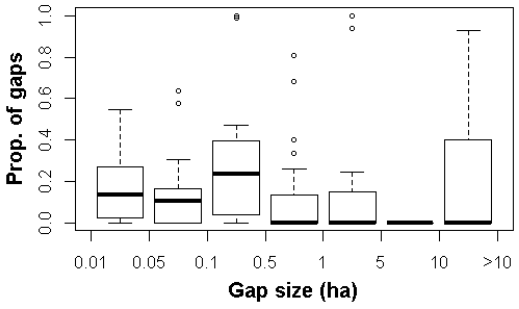
Prop. of gaps
0.0 0.2 0.4 0.6 0.8 1.0
0.01 0.05 0.1 0.5 1 5 10 >10
Gap size (ha)

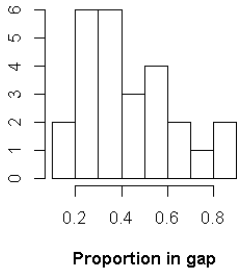
0 1 2 3 4 5 6
0.2 0.4 0.6 0.8
Proportion in gap

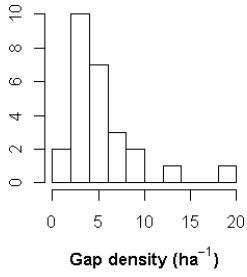
0 2 4 6 8 10
0 5 10 15 20
Gap density (ha−1)

Long Gulch South

Ownership	Yosemite National Park
Hectares	202

	Ridges	**Valleys**	**NE slopes**	**SW slopes**
Landform proportions	0.33	0.27	0.13	0.27

	Minimum	**Mean**	**Maximum**
AET (mm)	273	360	391
Deficit (mm)	466	49.	538
T_{min} (°C)	1.3	1.8	2.2
Elevation (m)	1992	2034	2066

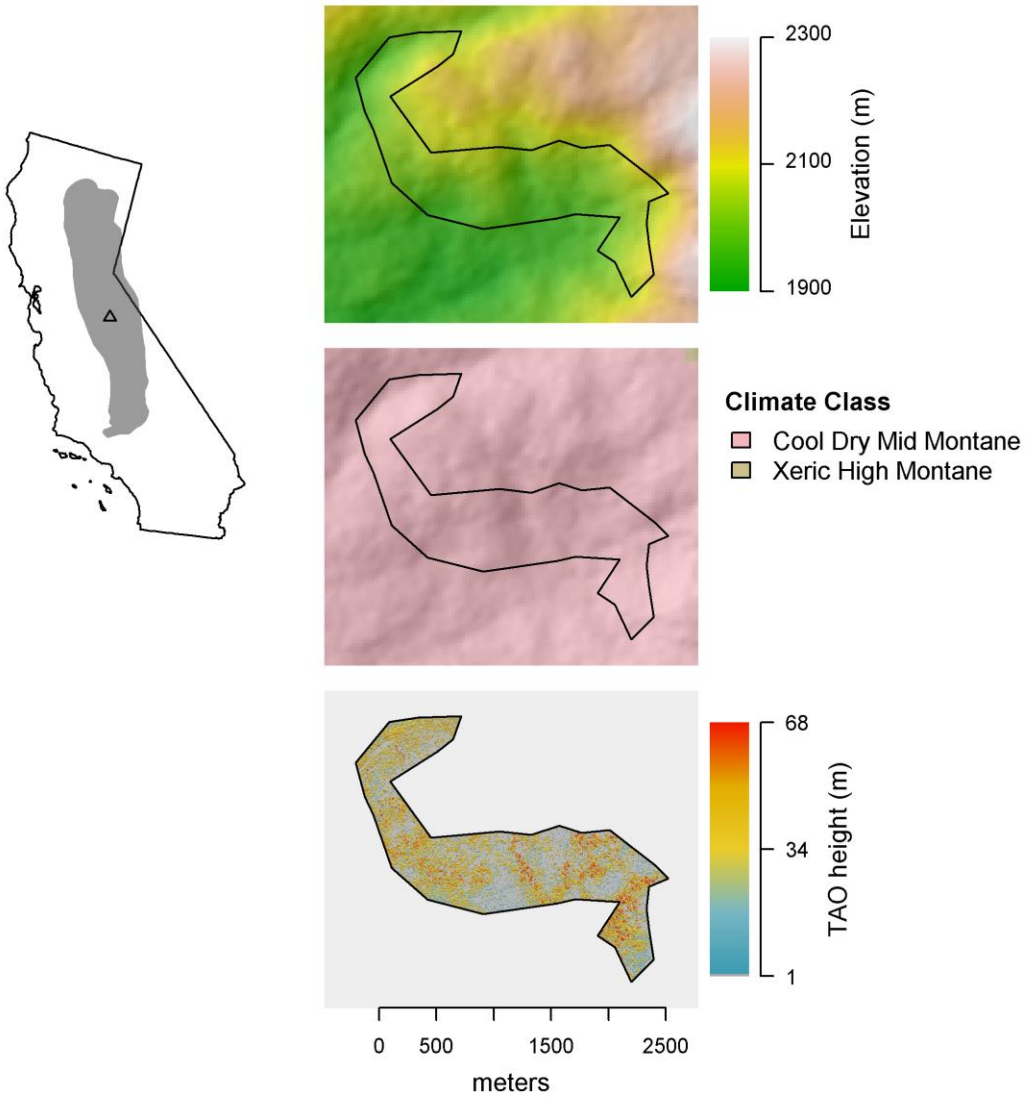

Long Gulch South

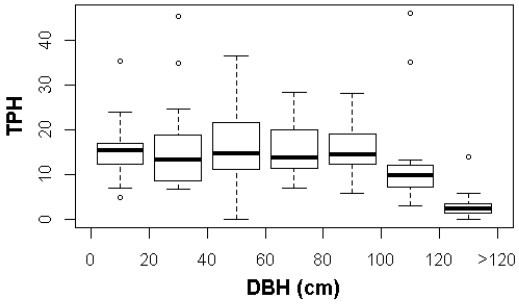

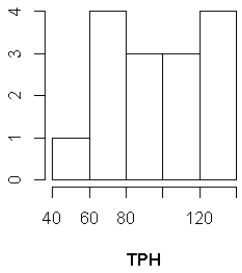

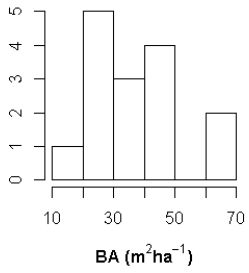

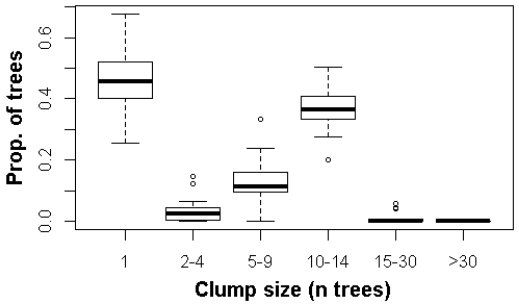

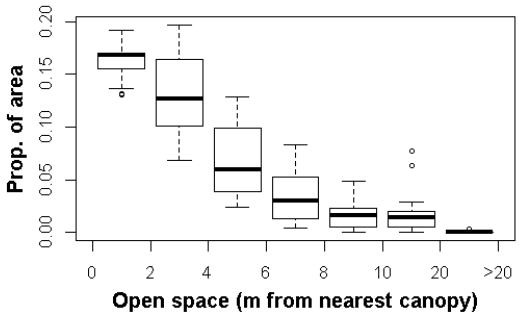

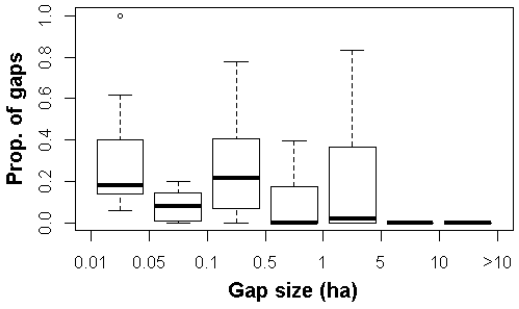

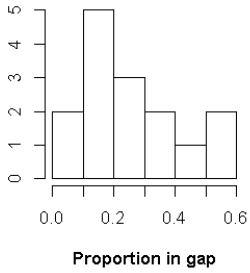

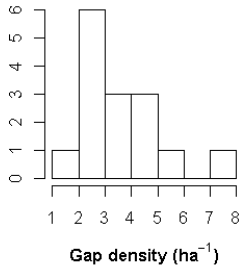

Lower Cottonwood

Ownership	Yosemite National Park
Hectares	511

	Ridges	**Valleys**	**NE slopes**	**SW slopes**
Landform proportions	0.27	0.05	0.27	0.41

	Minimum	**Mean**	**Maximum**
AET (mm)	258	385	472
Deficit (mm)	401	495	479
T_{min} (°C)	0.71	2.3	3.0
Elevation (m)	1826	1955	2076

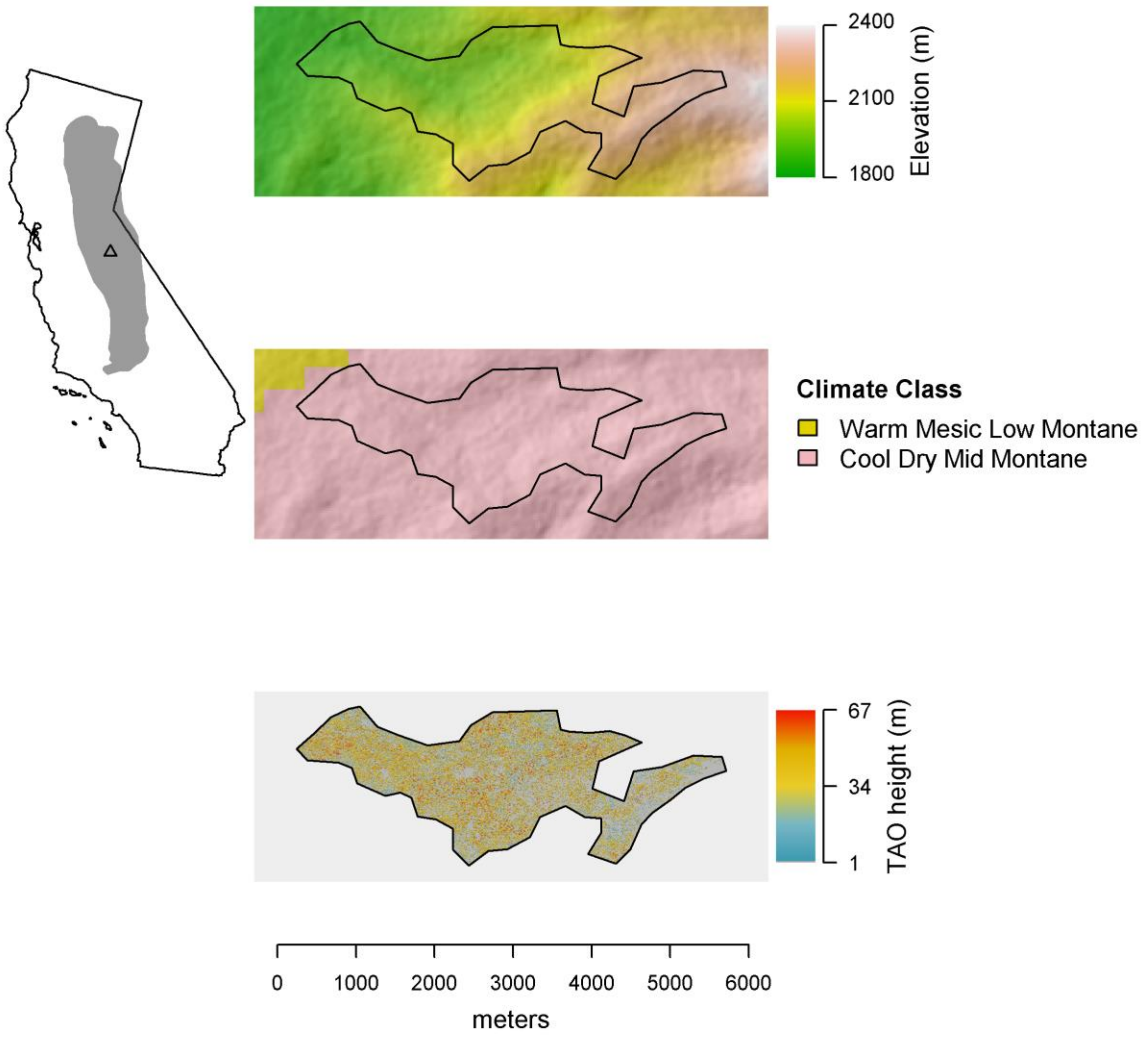

Lower Cottonwood

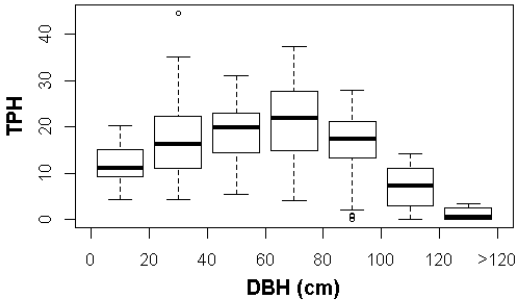

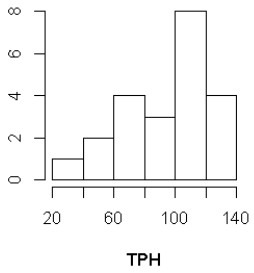

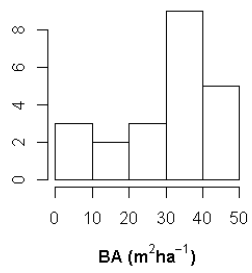

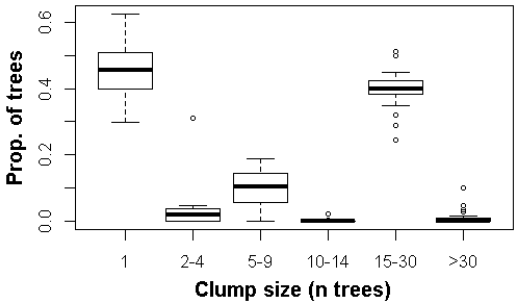

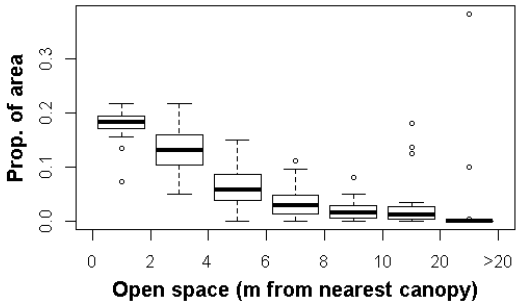

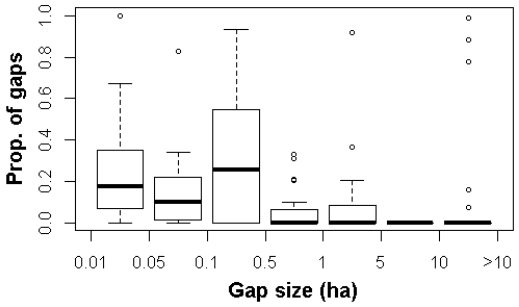

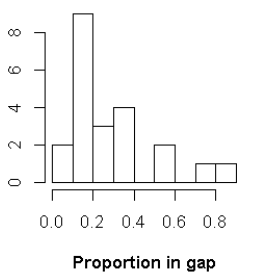

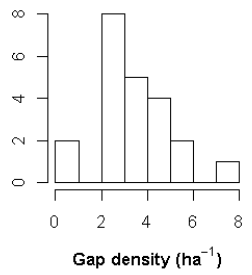

Mather

Ownership	Yosemite National Park and Stanislaus National Forest			
Hectares	975			
	Ridges	**Valleys**	**NE slopes**	**SW slopes**
Landform proportions	0.32	0.17	0.21	0.30

	Minimum	**Mean**	**Maximum**
AET (mm)	271	335	473
Deficit (mm)	573	707	804
T_{min} (°C)	2.9	4.5	6.9
Elevation (m)	1361	1522	1593

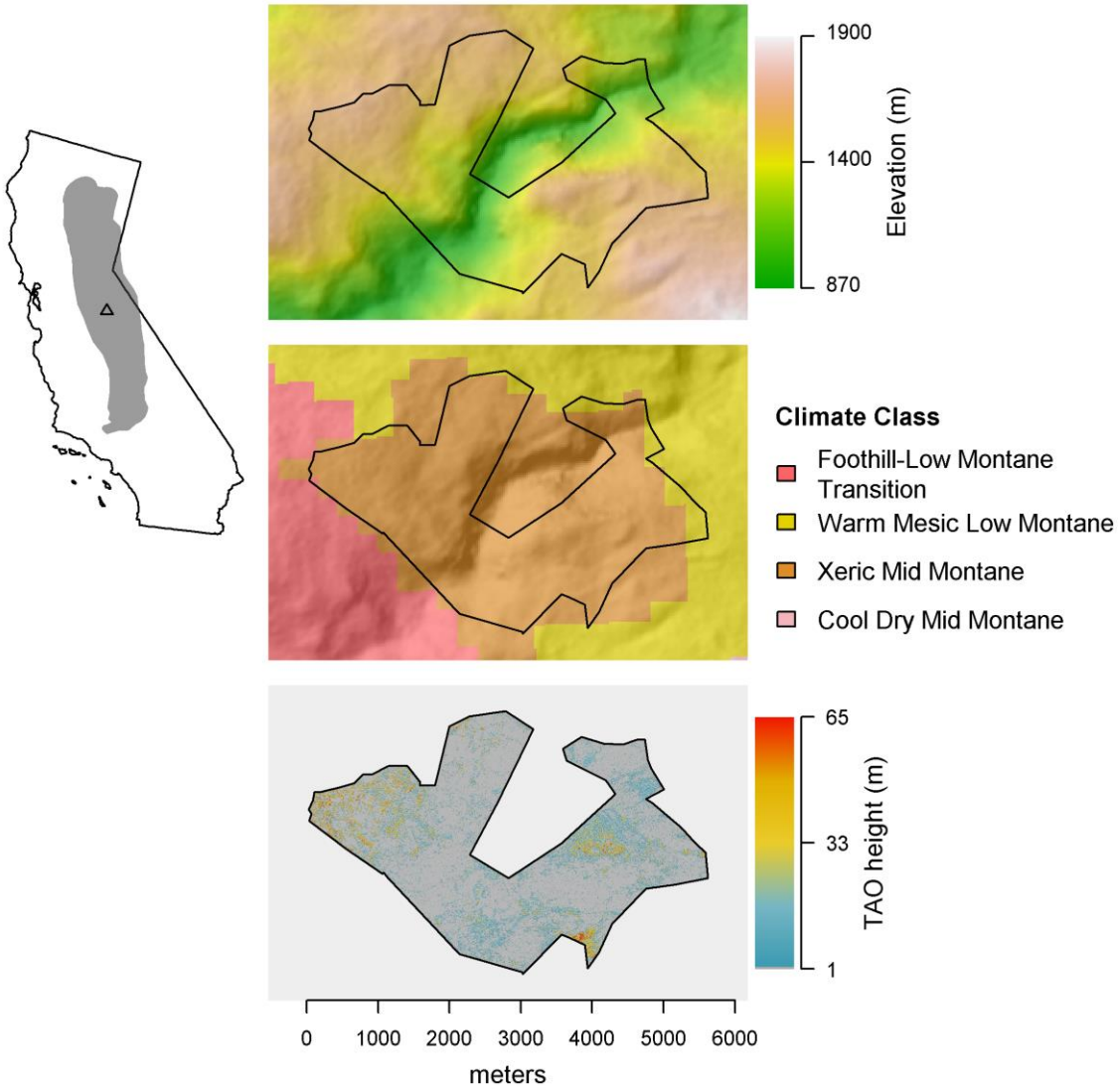

Mather

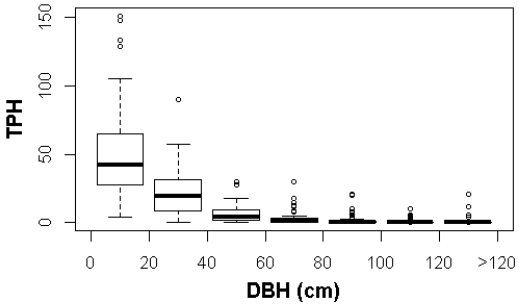
TPH
0
50
100
150
0
20
40
60
80
100
120
>120
DBH (cm)

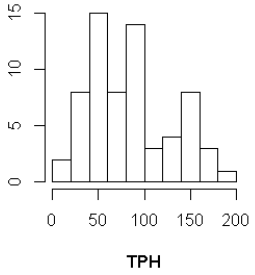
0
5
10
15
0
50
100
150
200
TPH

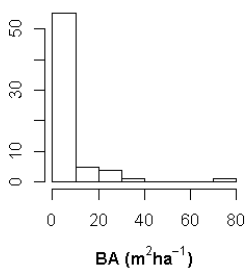
0
10
30
50
0
20
40
60
80
BA (m2ha−1)

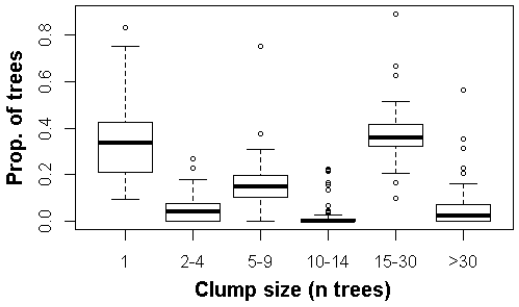
Prop. of trees
0.0
0.2
0.4
0.6
0.8
1
2-4
5-9
10-14
15-30
>30
Clump size (n trees)

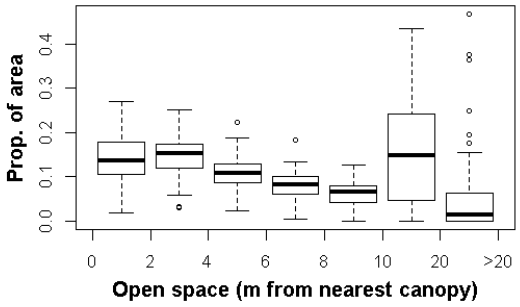
Prop. of area
0.0
0.1
0.2
0.3
0.4
0
2
4
6
8
10
20
>20
Open space (m from nearest canopy)

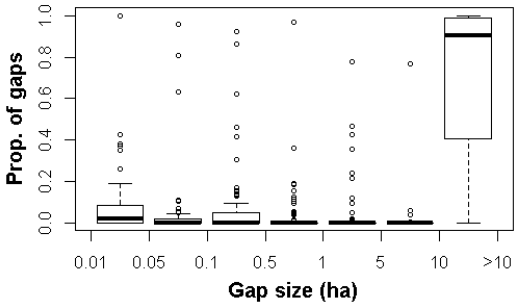
Prop. of gaps
0.0
0.2
0.4
0.6
0.8
1.0
0.01
0.05
0.1
0.5
1
5
10
>10
Gap size (ha)

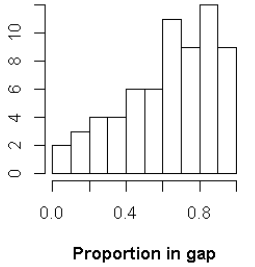
0
2
4
6
8
10
0.0
0.4
0.8
Proportion in gap

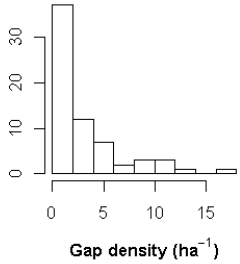
0
10
20
30
0
5
10
15
Gap density (ha−1)

Middle T

Ownership	Yosemite National Park
Hectares	337

	Ridges	**Valleys**	**NE slopes**	**SW slopes**
Landform proportions	0.23	0.08	0.27	0.42

	Minimum	**Mean**	**Maximum**
AET (mm)	268	389	471
Deficit (mm)	407	496	600
T_{min} (°C)	1.6	2.3	2.8
Elevation (m)	1949	2095	2189

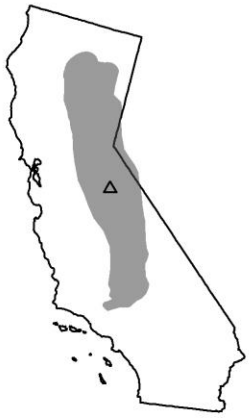

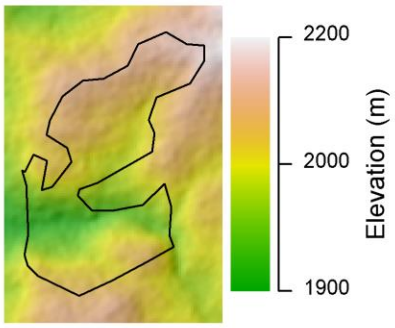

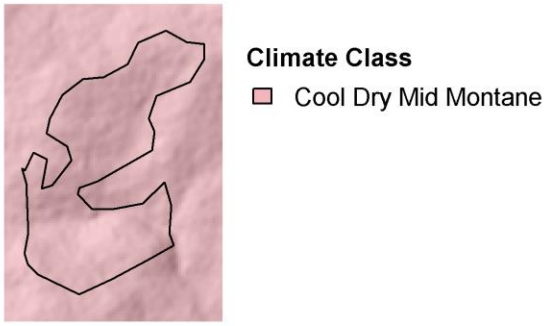

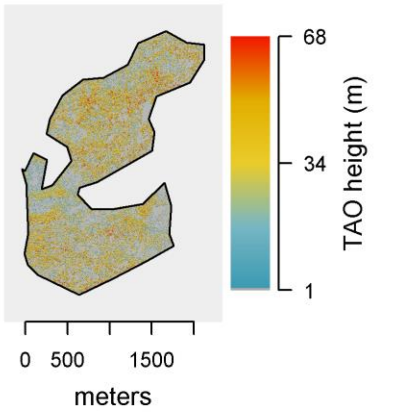

Middle T

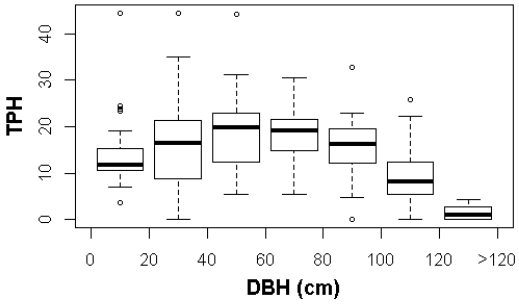
TPH
0 10 20 30 40
0 20 40 60 80 100 120 >120
DBH (cm)

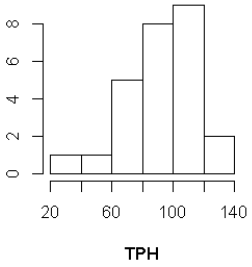
0 2 4 6 8
20 60 100 140
TPH

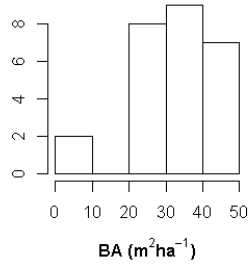
0 2 4 6 8
0 10 20 30 40 50
BA (m2ha-1)

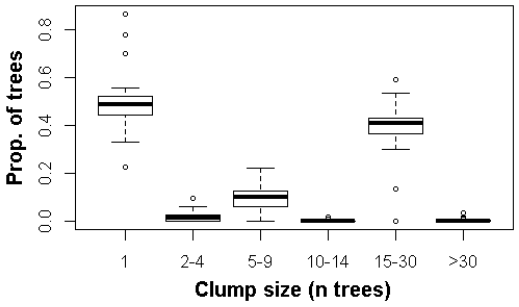
Prop. of trees
0.0 0.2 0.4 0.6 0.8
1 2-4 5-9 10-14 15-30 >30
Clump size (n trees)

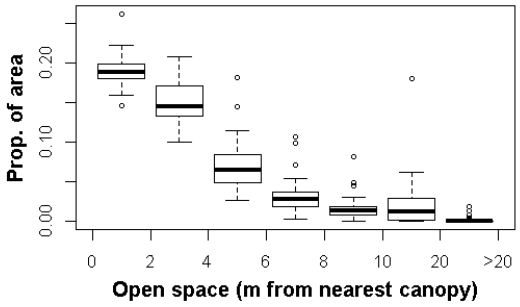
Prop. of area
0.00 0.10 0.20
0 2 4 6 8 10 20 >20
Open space (m from nearest canopy)

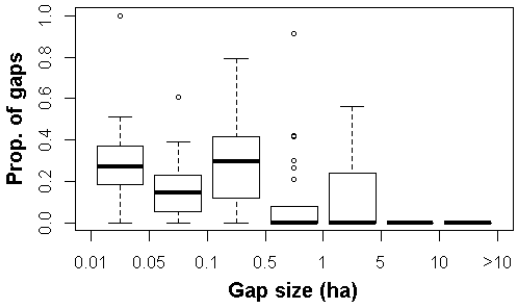
Prop. of gaps
0.0 0.2 0.4 0.6 0.8 1.0
0.01 0.05 0.1 0.5 1 5 10 >10
Gap size (ha)

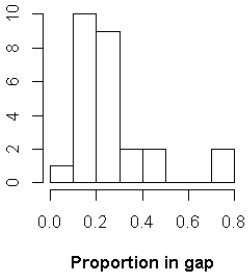
0 2 4 6 8 10
0.0 0.2 0.4 0.6 0.8
Proportion in gap

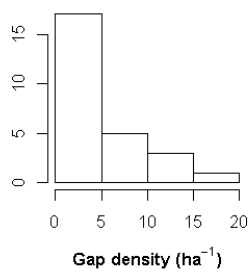
0 5 10 15
0 5 10 15 20
Gap density (ha-1)

Miguel

Ownership	Yosemite National Park			
Hectares	685			
	Ridges	**Valleys**	**NE slopes**	**SW slopes**
Landform proportions	0.16	0.14	0.35	0.35
	Minimum	**Mean**	**Maximum**	
AET (mm)	273	362	504	
Deficit (mm)	526	636	722	
T_{min} (°C)	2.3	3.3	4.9	
Elevation (m)	1427	1525	1905	

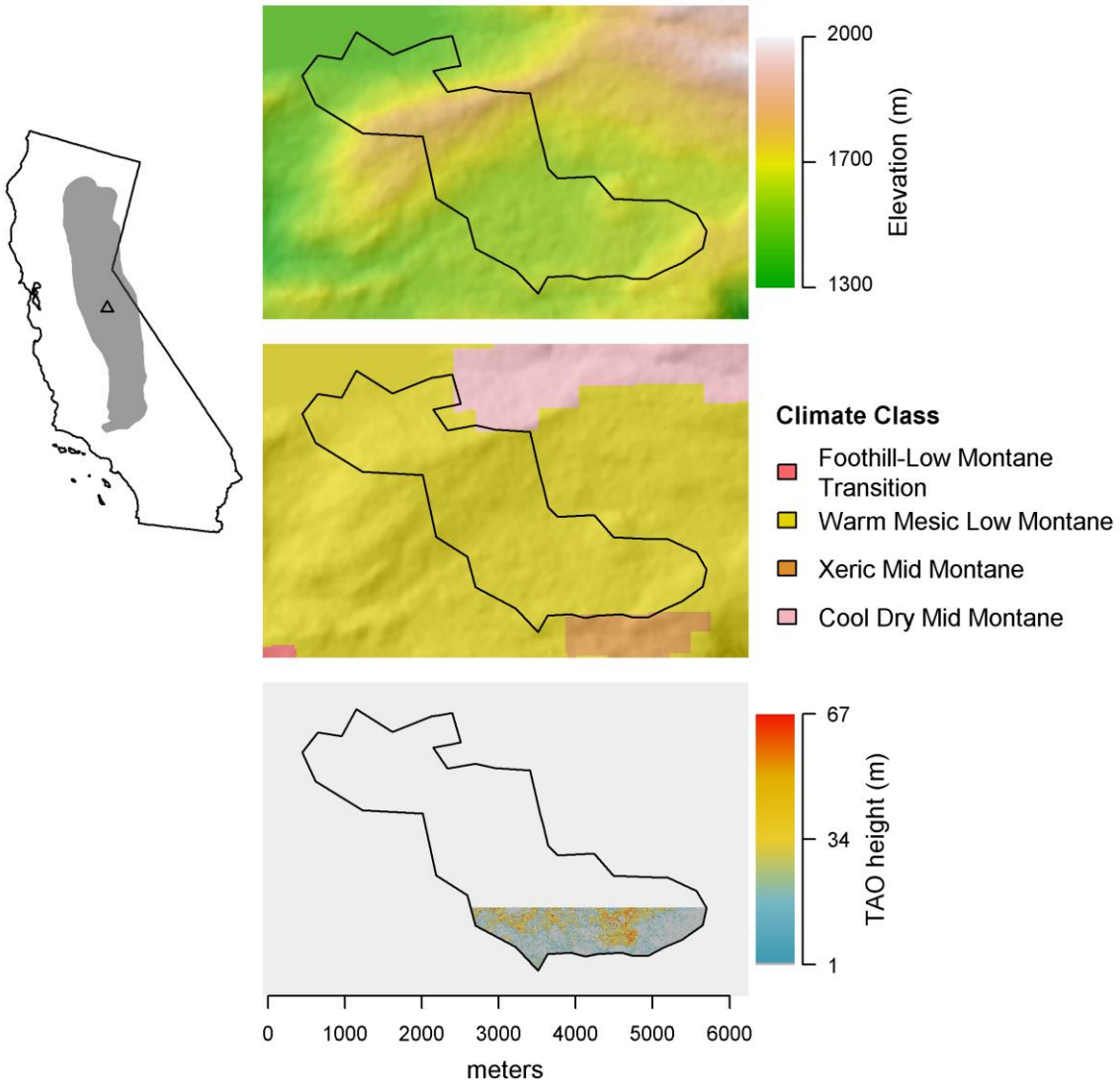

Miguel

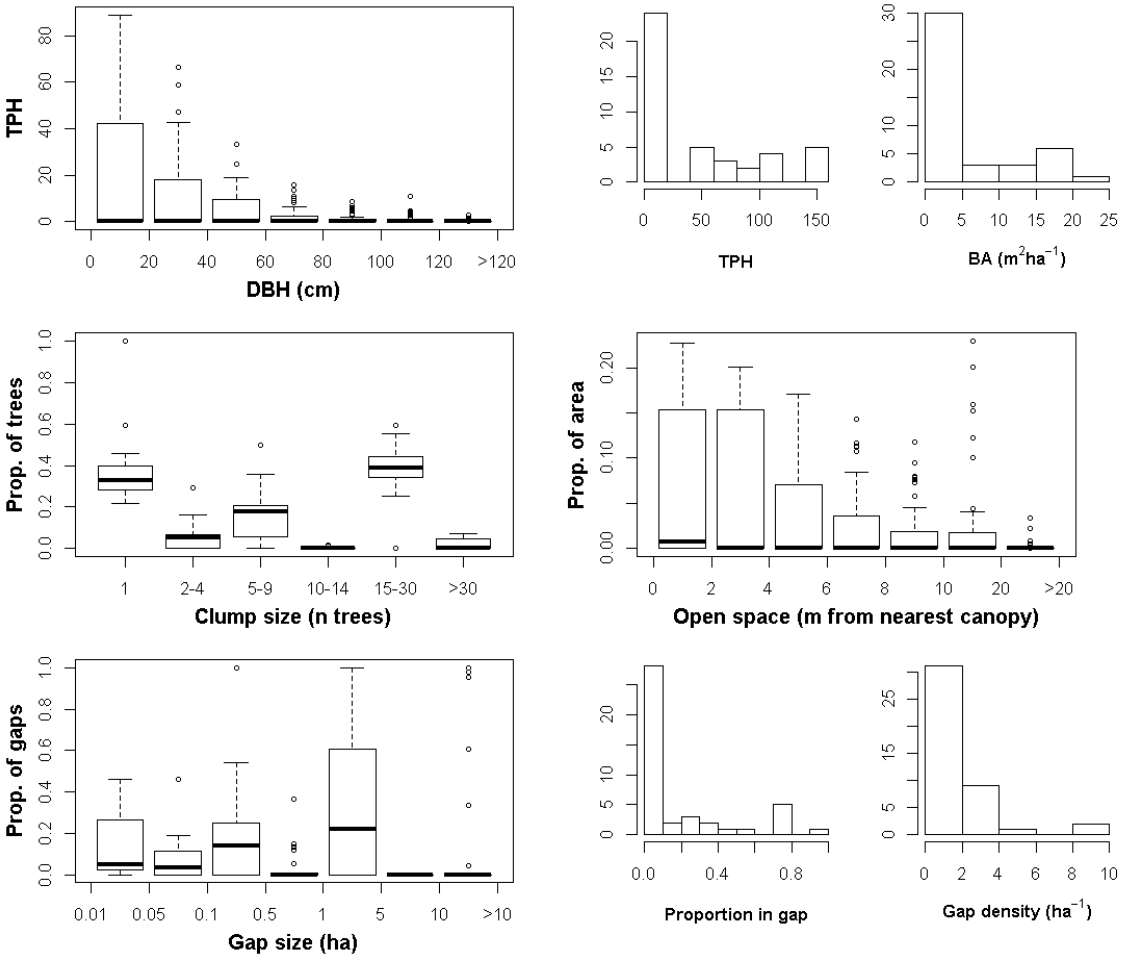
TPH
DBH (cm)
TPH
BA (m²ha⁻¹)
Prop. of trees
Clump size (n trees)
Prop. of area
Open space (m from nearest canopy)
Prop. of gaps
Gap size (ha)
Proportion in gap
Gap density (ha⁻¹)

Park				
Ownership	Yosemite National Park			
Hectares	316			
	Ridges	**Valleys**	**NE slopes**	**SW slopes**
Landform proportions	0.21	0.15	0.32	0.32
	Minimum	**Mean**	**Maximum**	
AET (mm)	230	302	361	
Deficit (mm)	460	522	611	
T_{min} (°C)	0.81	1.3	1.8	
Elevation (m)	1980	2029	2108	

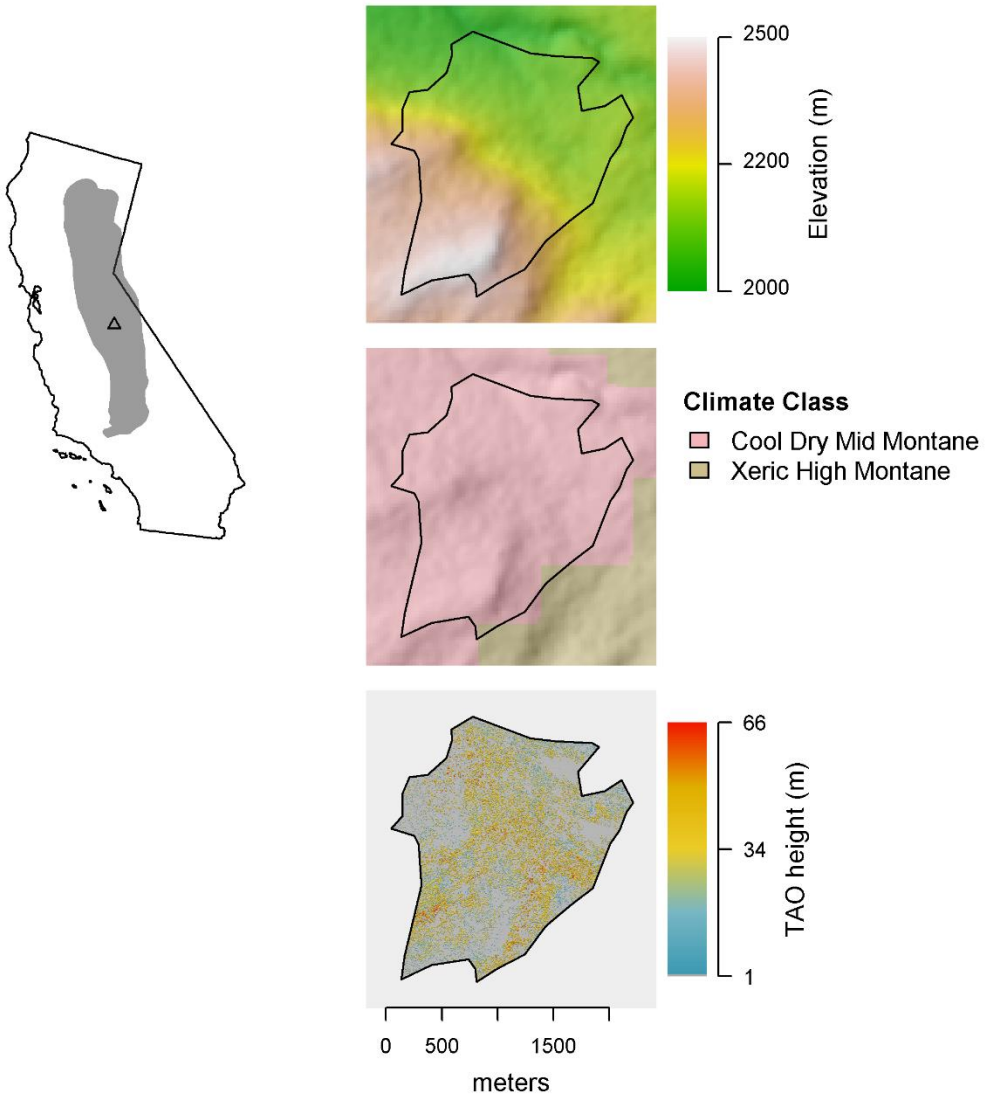

Park

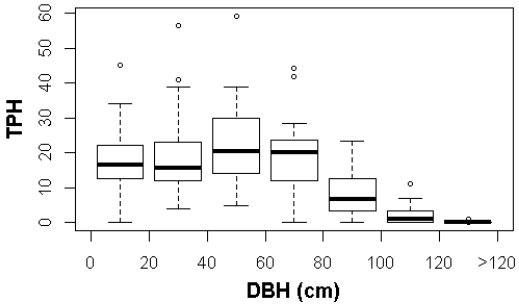
TPH
0 10 20 30 40 50 60
0 20 40 60 80 100 120 >120
DBH (cm)

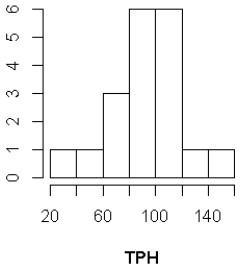
0 1 2 3 4 5 6
20 60 100 140
TPH

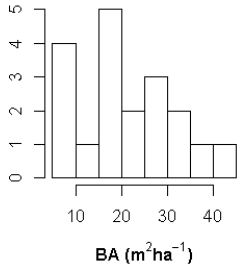
0 1 2 3 4 5
10 20 30 40
BA (m2ha−1)

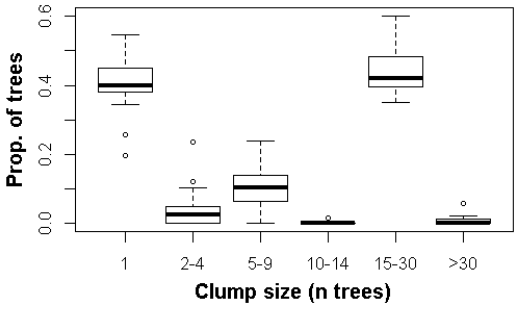
Prop. of trees
0.0 0.2 0.4 0.6
1 2-4 5-9 10-14 15-30 >30
Clump size (n trees)

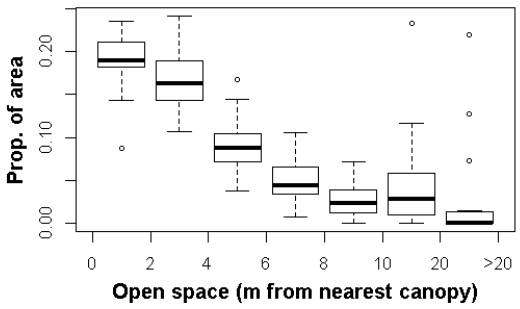
Prop. of area
0.00 0.10 0.20
0 2 4 6 8 10 20 >20
Open space (m from nearest canopy)

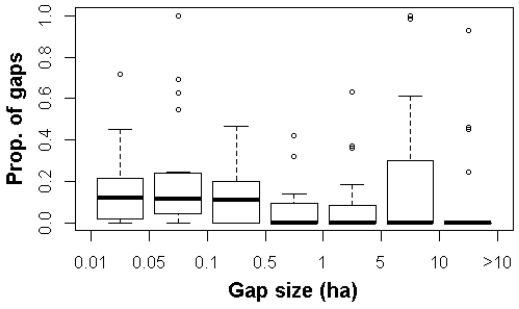
Prop. of gaps
0.0 0.2 0.4 0.6 0.8 1.0
0.01 0.05 0.1 0.5 1 5 10 >10
Gap size (ha)

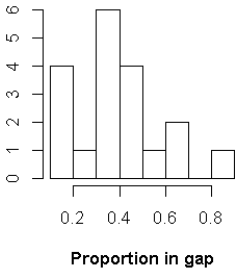
0 1 2 3 4 5 6
0.2 0.4 0.6 0.8
Proportion in gap

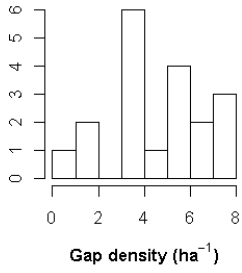
0 1 2 3 4 5 6
0 2 4 6 8
Gap density (ha−1)

Pohono

Ownership	Yosemite National Park			
Hectares	277			
	Ridges	**Valleys**	**NE slopes**	**SW slopes**
Landform proportions	0.21	0.17	0.33	0.29

	Minimum	**Mean**	**Maximum**
AET (mm)	213	249	359
Deficit (mm)	489	597	622
T_{min} (°C)	1.1	1.7	2.0
Elevation (m)	2156	2213	2266

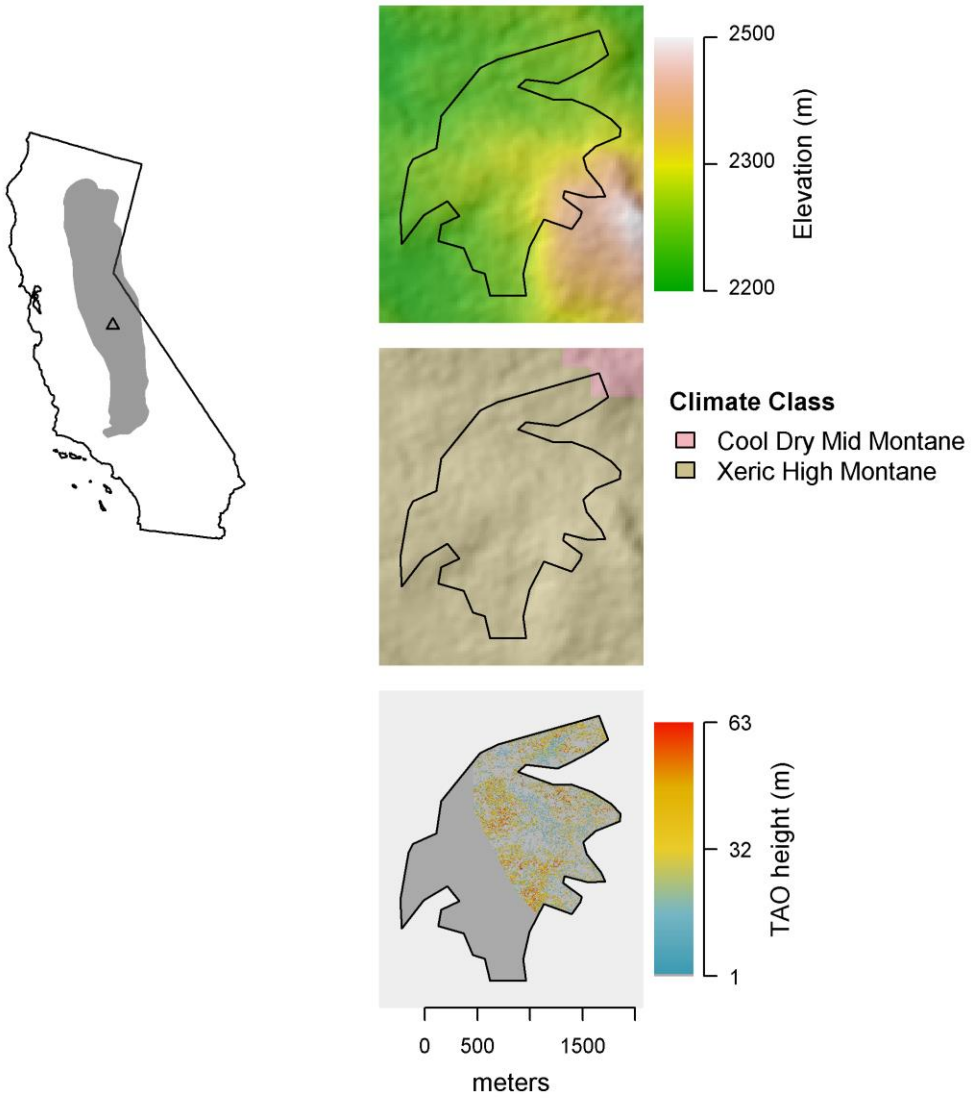

Pohono

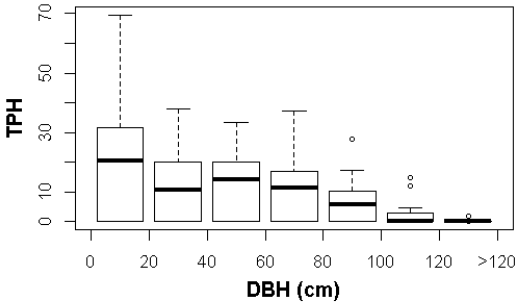
TPH
0
10
30
50
70
0
20
40
60
80
100
120
>120
DBH (cm)

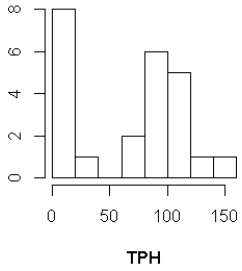
0
2
4
6
8
0
50
100
150
TPH

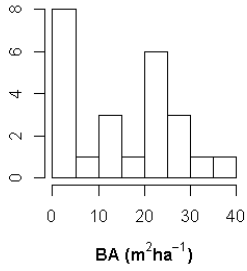
0
2
4
6
8
0
10
20
30
40
BA (m2ha−1)

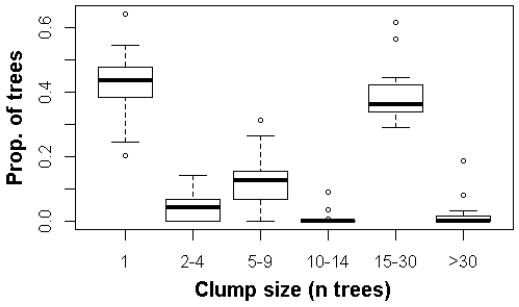
Prop. of trees
0.0
0.2
0.4
0.6
1
2-4
5-9
10-14
15-30
>30
Clump size (n trees)

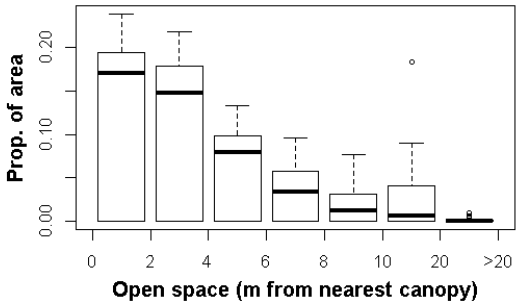
Prop. of area
0.00
0.10
0.20
0
2
4
6
8
10
20
>20
Open space (m from nearest canopy)

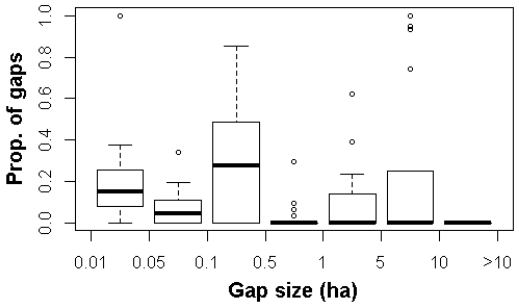
Prop. of gaps
0.0
0.2
0.4
0.6
0.8
1.0
0.01
0.05
0.1
0.5
1
5
10
>10
Gap size (ha)

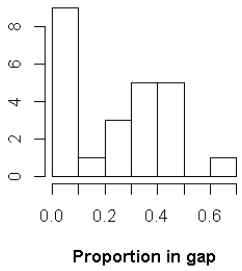
0
2
4
6
8
0.0
0.2
0.4
0.6
Proportion in gap

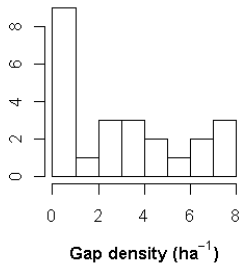
0
2
4
6
8
0
2
4
6
8
Gap density (ha−1)

Poopenaut

Ownership	Yosemite
Hectares	1112

	Ridges	**Valleys**	**NE slopes**	**SW slopes**
Landform proportions	0.24	0.19	0.35	0.22

	Minimum	**Mean**	**Maximum**
AET (mm)	277	358	443
Deficit (mm)	567	677	769
T_{min} (°C)	2.6	3.8	5.9
Elevation (m)	1518	1563	1641

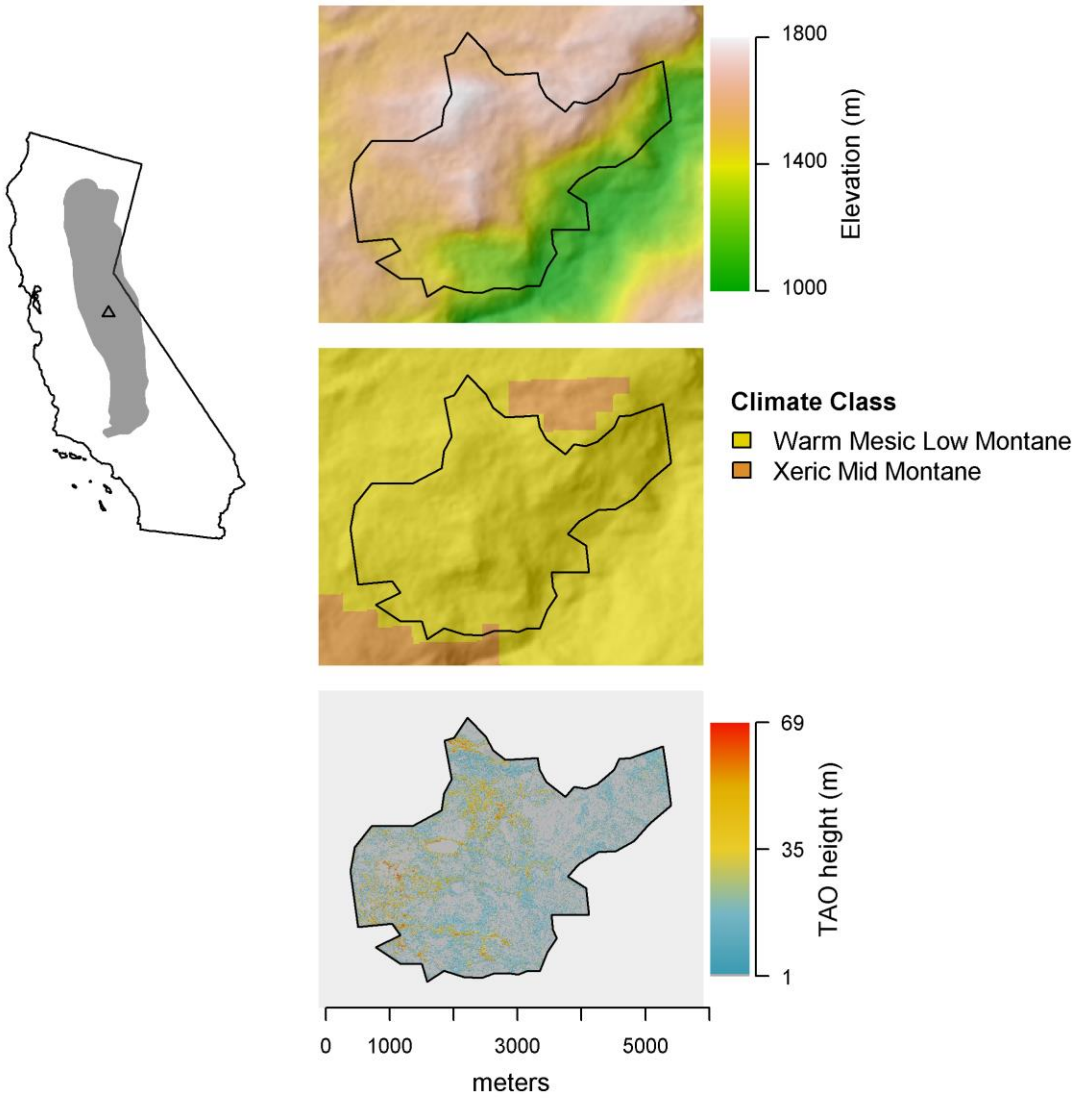

Poopenaut

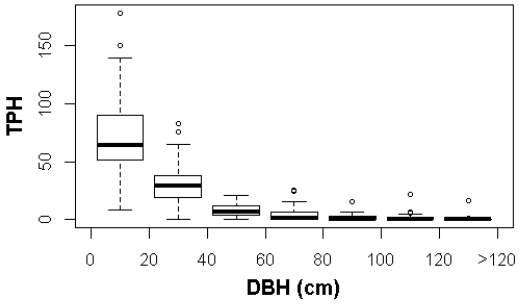
TPH
0
50
100
150
0
20
40
60
80
100
120
>120
DBH (cm)

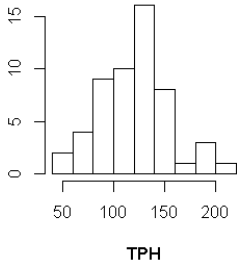
0
5
10
15
50
100
150
200
TPH

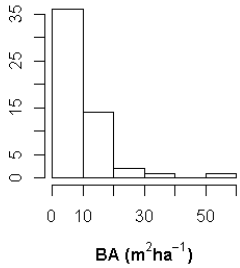
0
5
15
25
35
0
10
30
50
BA (m2ha−1)

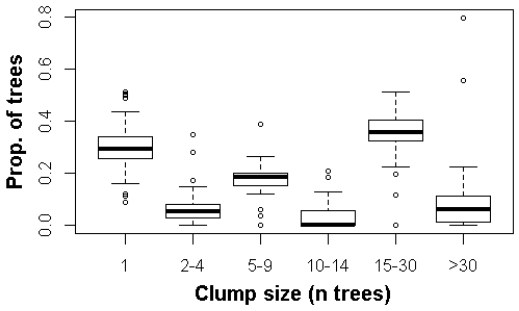
Prop. of trees
0.0
0.2
0.4
0.6
0.8
1
2-4
5-9
10-14
15-30
>30
Clump size (n trees)

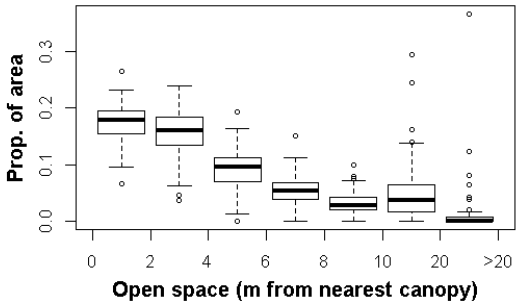
Prop. of area
0.0
0.1
0.2
0.3
0
2
4
6
8
10
20
>20
Open space (m from nearest canopy)

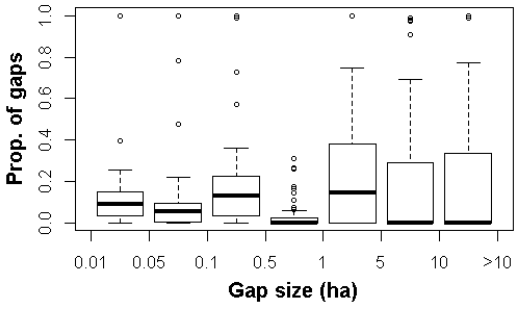
Prop. of gaps
0.0
0.2
0.4
0.6
0.8
1.0
0.01
0.05
0.1
0.5
1
5
10
>10
Gap size (ha)

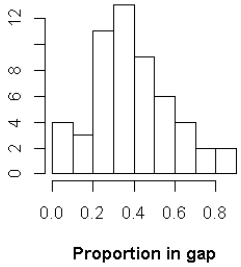
0
2
4
6
8
12
0.0
0.2
0.4
0.6
0.8
Proportion in gap

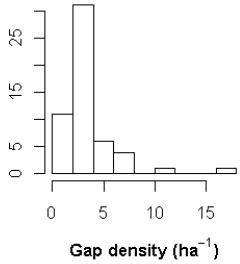
0
5
15
25
0
5
10
15
Gap density (ha−1)

Smith Meadow

Ownership	Yosemite National Park
Hectares	603

	Ridges	**Valleys**	**NE slopes**	**SW slopes**
Landform proportions	0.34	0.16	0.32	0.18

	Minimum	**Mean**	**Maximum**
AET (mm)	246	369	442
Deficit (mm)	462	517	594
T_{min} (°C)	2.0	2.9	4.5
Elevation (m)	1150	1560	1846

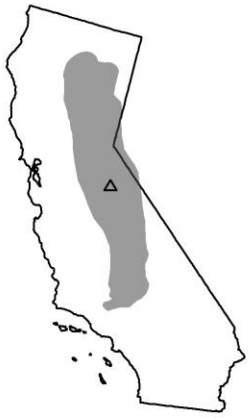

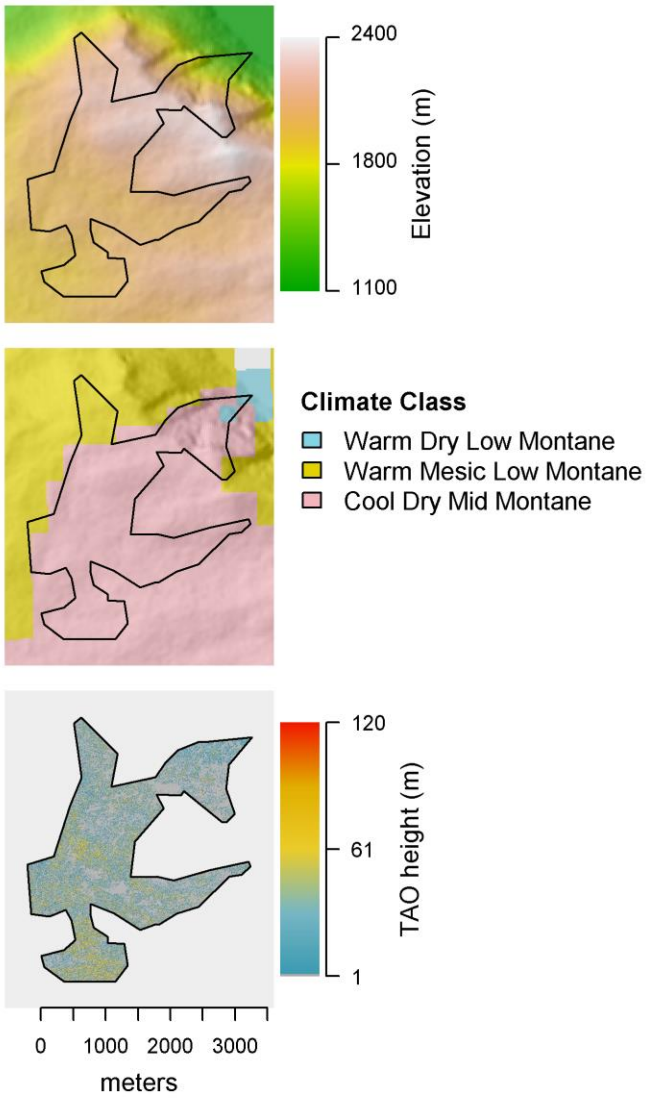

Smith Meadow

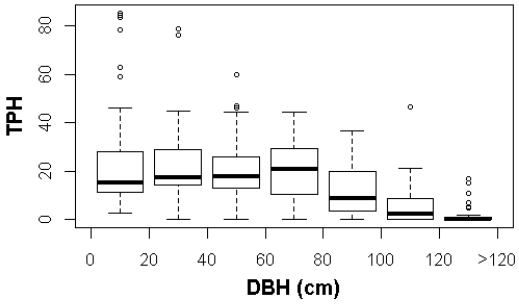

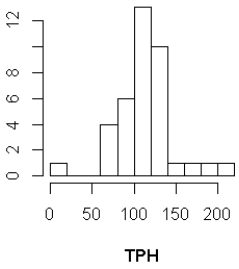

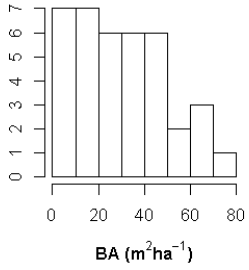

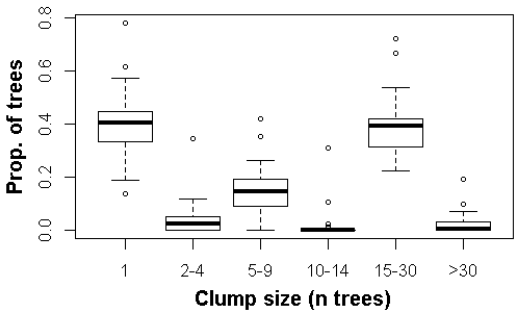

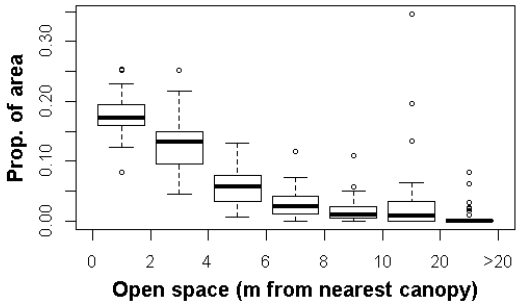

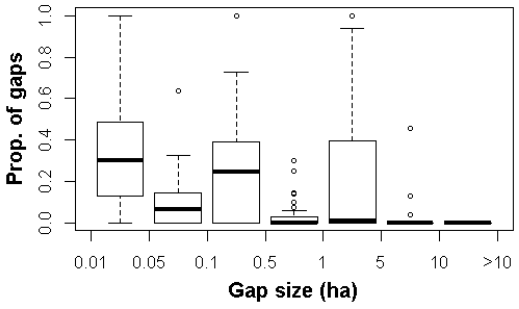

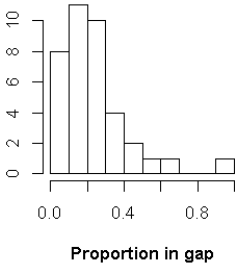

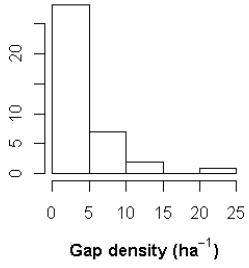

Smith Peak

Ownership	Yosemite National Park
Hectares	182

	Ridges	**Valleys**	**NE slopes**	**SW slopes**
Landform proportions	0.22	0.26	0.30	0.22

	Minimum	**Mean**	**Maximum**
AET (mm)	246	339	401
Deficit (mm)	384	477	573
T_{min} (°C)	0.77	1.8	2.8
Elevation (m)	1583	1774	2219

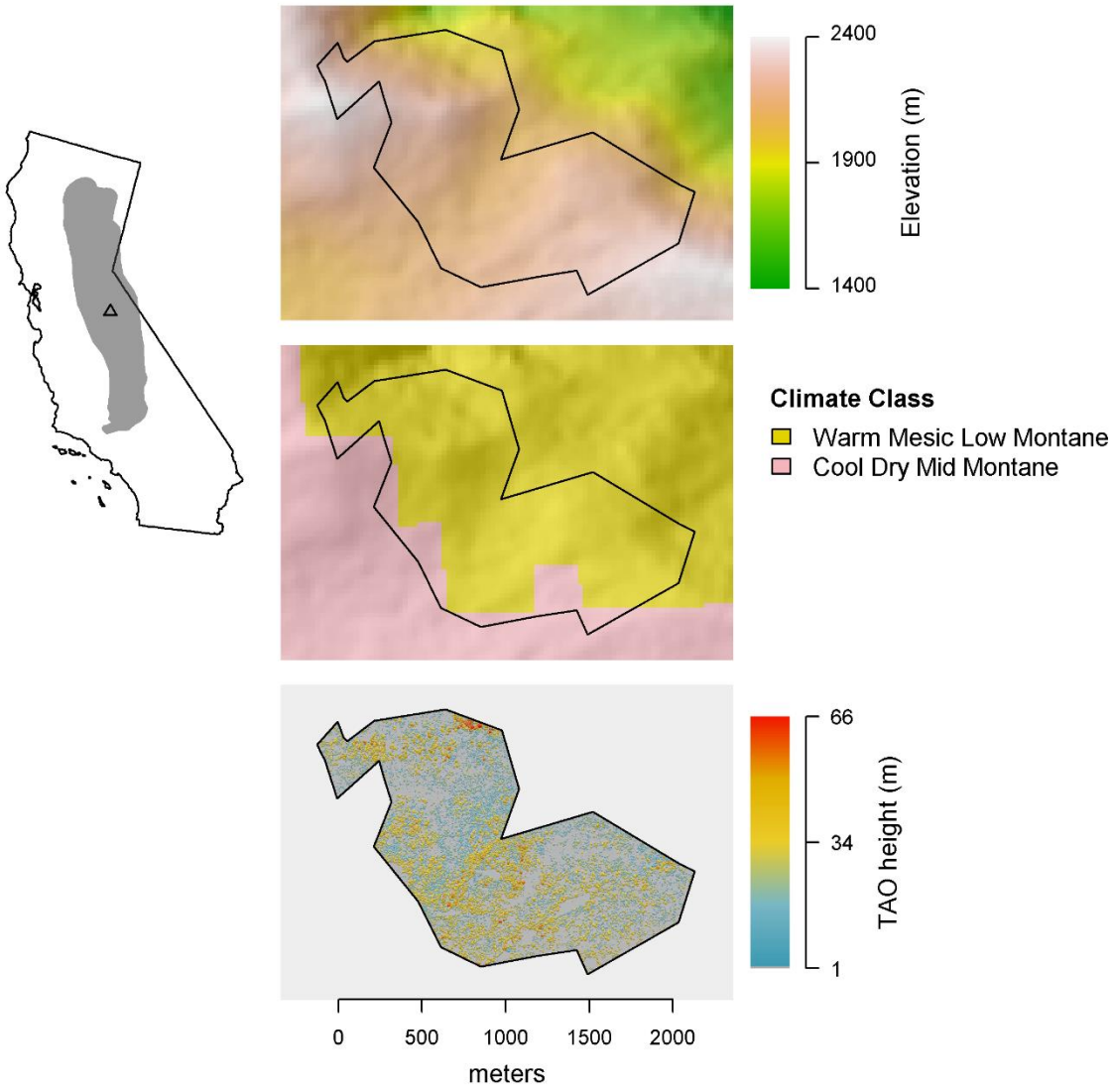

Smith Peak

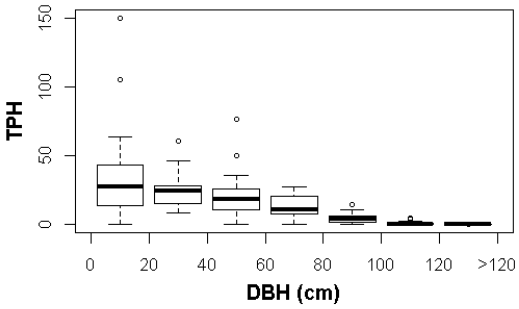
TPH
0
50
100
150
0
20
40
60
80
100
120
>120
DBH (cm)

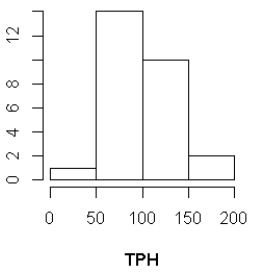
0
2
4
6
8
12
0
50
100
150
200
TPH

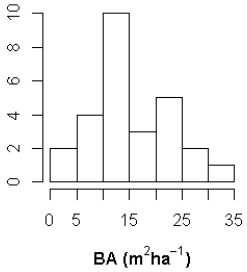
0
2
4
6
8
10
0
5
15
25
35
BA (m2ha−1)

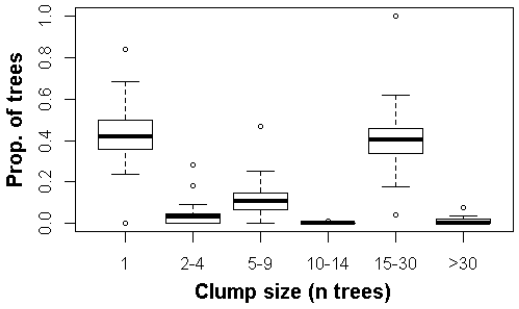
Prop. of trees
0.0
0.2
0.4
0.6
0.8
1.0
1
2-4
5-9
10-14
15-30
>30
Clump size (n trees)

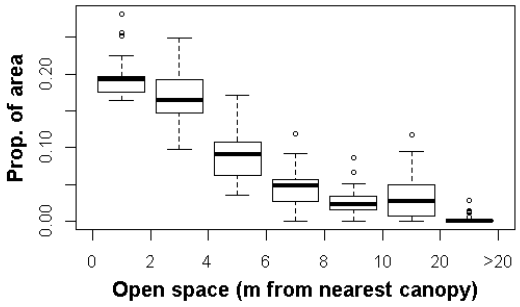
Prop. of area
0.00
0.10
0.20
0
2
4
6
8
10
20
>20
Open space (m from nearest canopy)

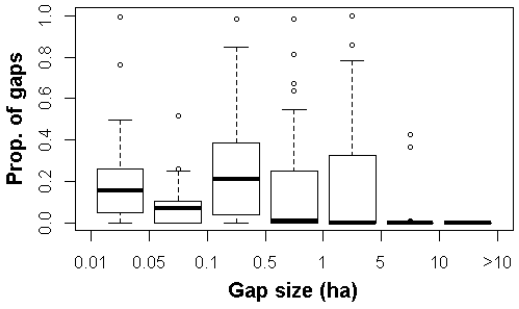
Prop. of gaps
0.0
0.2
0.4
0.6
0.8
1.0
0.01
0.05
0.1
0.5
1
5
10
>10
Gap size (ha)

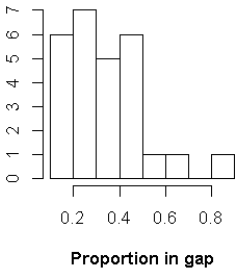
0
1
2
3
4
5
6
7
0.2
0.4
0.6
0.8
Proportion in gap

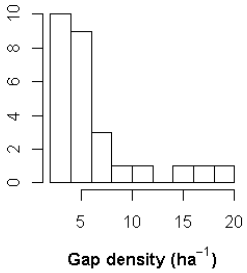
0
2
4
6
8
10
5
10
15
20
Gap density (ha−1)

South Fork

Ownership	Yosemite National Park
Hectares	149

	Ridges	**Valleys**	**NE slopes**	**SW slopes**
Landform proportions	0.42	0.08	0.33	0.17

	Minimum	**Mean**	**Maximum**
AET (mm)	304	349	372
Deficit (mm)	499	521	557
T_{min} (°C)	1.9	2.3	2.9
Elevation (m)	1712	1845	1936

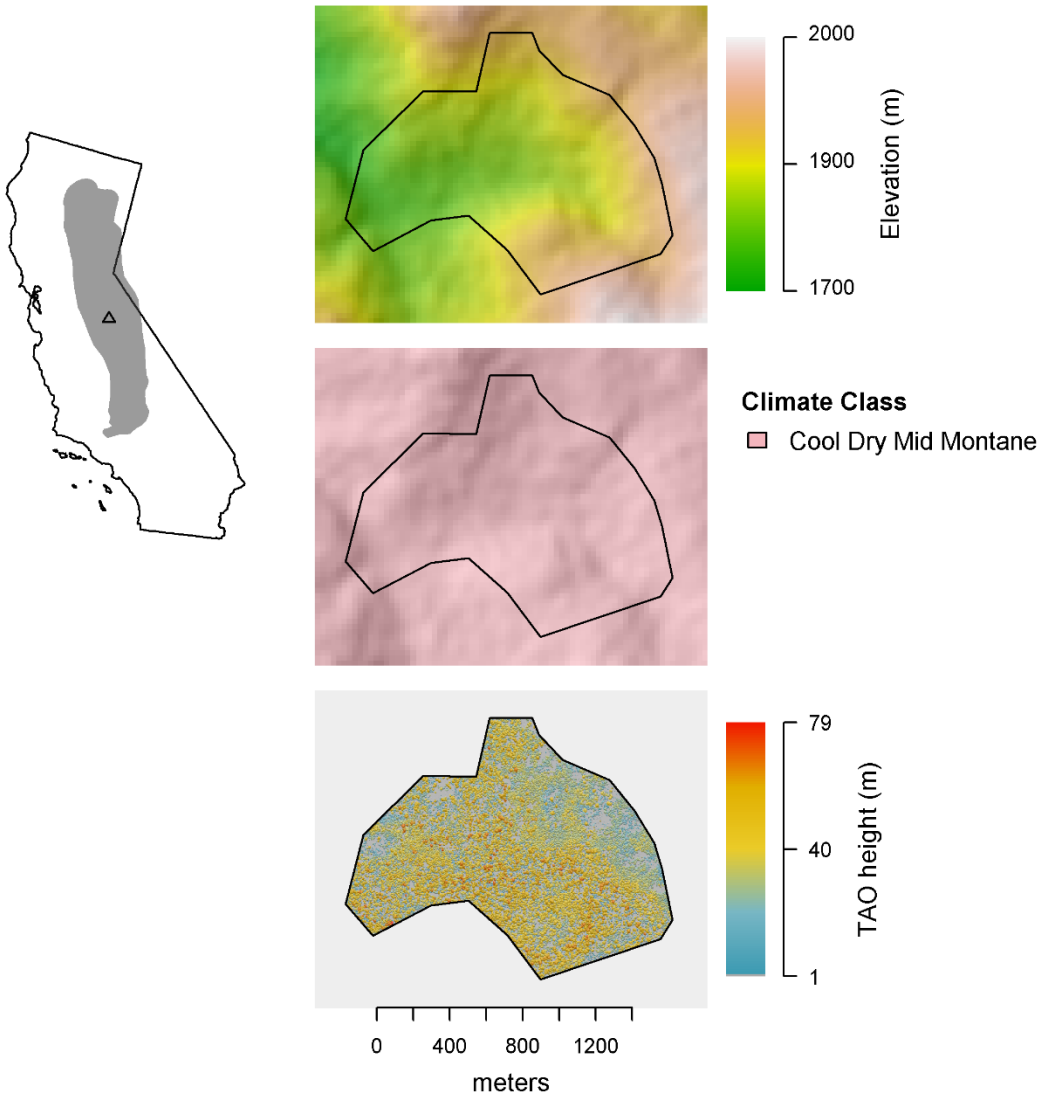

South Fork

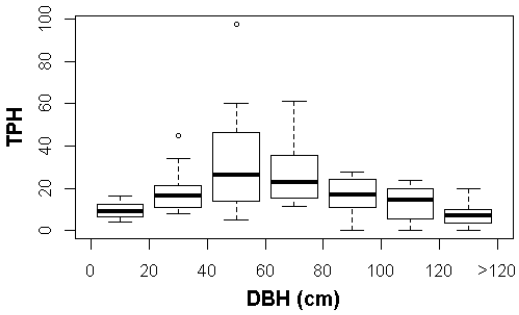
TPH
0 20 40 60 80 100
0 20 40 60 80 100 120 >120
DBH (cm)

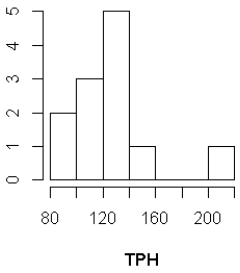
0 1 2 3 4 5
80 120 160 200
TPH

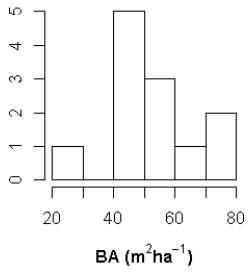
0 1 2 3 4 5
20 40 60 80
BA (m2ha-1)

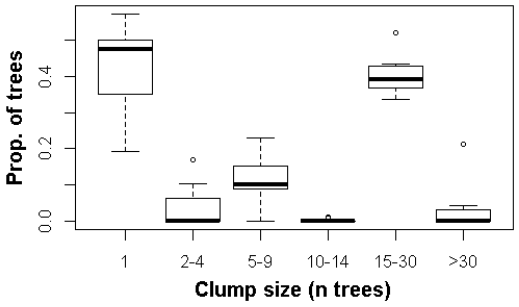
Prop. of trees
0.0 0.2 0.4
1 2-4 5-9 10-14 15-30 >30
Clump size (n trees)

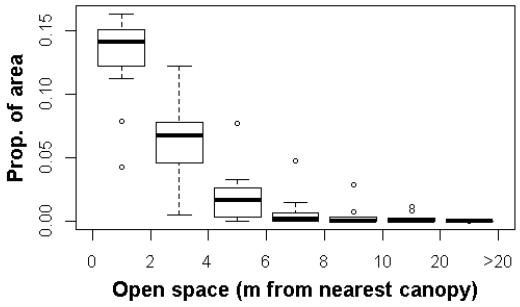
Prop. of area
0.00 0.05 0.10 0.15
0 2 4 6 8 10 20 >20
Open space (m from nearest canopy)

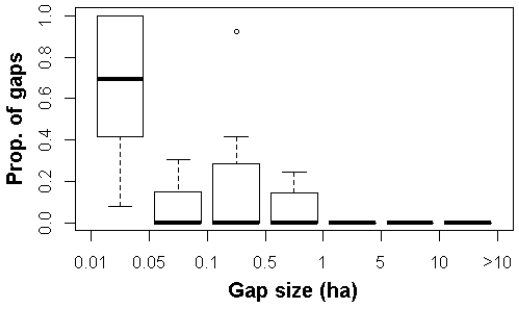
Prop. of gaps
0.0 0.2 0.4 0.6 0.8 1.0
0.01 0.05 0.1 0.5 1 5 10 >10
Gap size (ha)

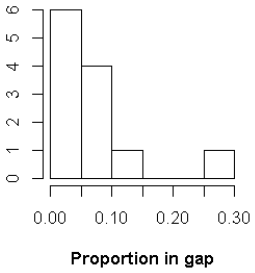
0 1 2 3 4 5 6
0.00 0.10 0.20 0.30
Proportion in gap

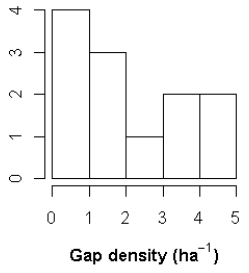
0 1 2 3 4
0 1 2 3 4 5
Gap density (ha-1)

Spring King

Ownership	Yosemite National Park			
Hectares	578			
	Ridges	**Valleys**	**NE slopes**	**SW slopes**
Landform proportions	0.35	0.20	0.20	0.25

	Minimum	**Mean**	**Maximum**
AET (mm)	251	364	412
Deficit (mm)	465	542	689
T_{min} (°C)	1.6	2.6	3.4
Elevation (m)	1747	1907	2037

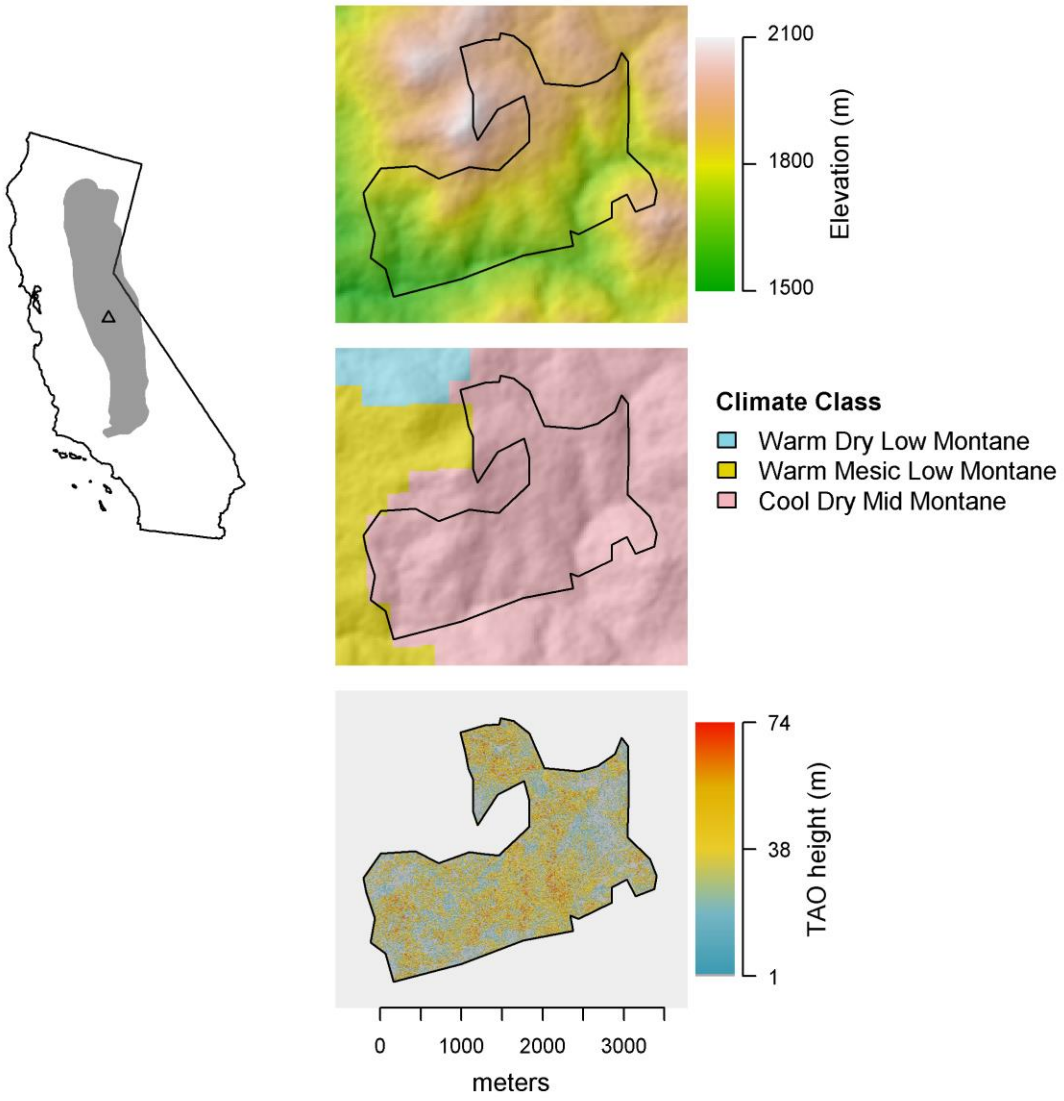

Spring King

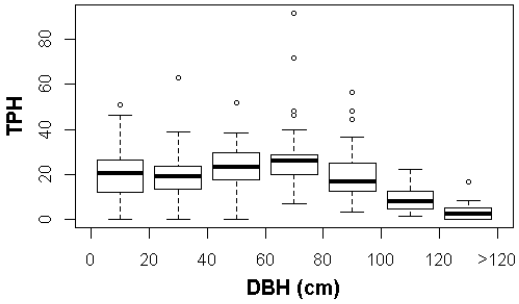
TPH
0 20 40 60 80
0 20 40 60 80 100 120 >120
DBH (cm)

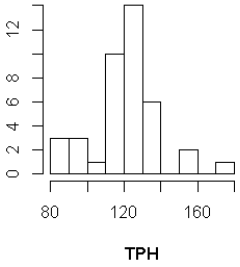
0 2 4 6 8 12
80 120 160
TPH

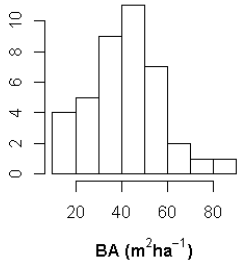
0 2 4 6 8 10
20 40 60 80
BA (m2ha−1)

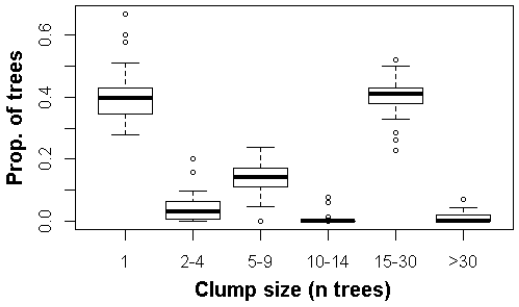
Prop. of trees
0.0 0.2 0.4 0.6
1 2-4 5-9 10-14 15-30 >30
Clump size (n trees)

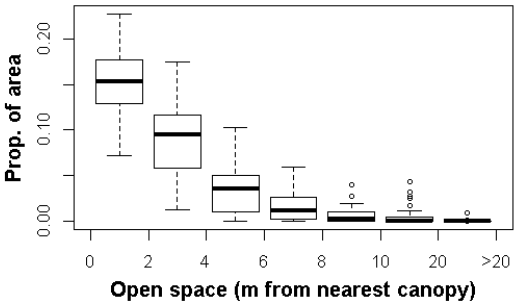
Prop. of area
0.00 0.10 0.20
0 2 4 6 8 10 20 >20
Open space (m from nearest canopy)

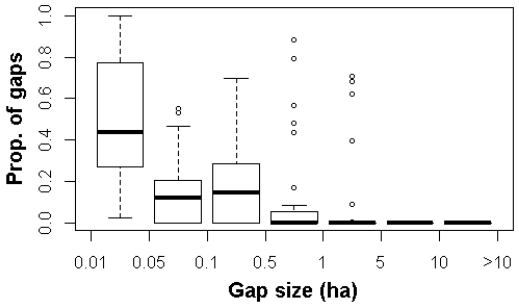
Prop. of gaps
0.0 0.2 0.4 0.6 0.8 1.0
0.01 0.05 0.1 0.5 1 5 10 >10
Gap size (ha)

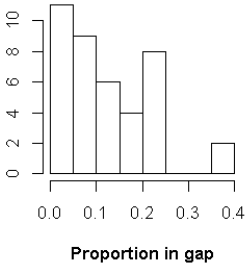
0 2 4 6 8 10
0.0 0.1 0.2 0.3 0.4
Proportion in gap

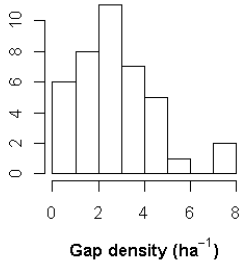
0 2 4 6 8 10
0 2 4 6 8
Gap density (ha−1)

Starr King

Ownership	Yosemite National Park			
Hectares	207			
	Ridges	**Valleys**	**NE slopes**	**SW slopes**
Landform proportions	0.34	0.08	0.08	0.50

	Minimum	**Mean**	**Maximum**
AET (mm)	229	256	338
Deficit (mm)	440	519	563
T_{min} (°C)	-0.78	-0.30	0.31
Elevation (m)	2476	2506	2608

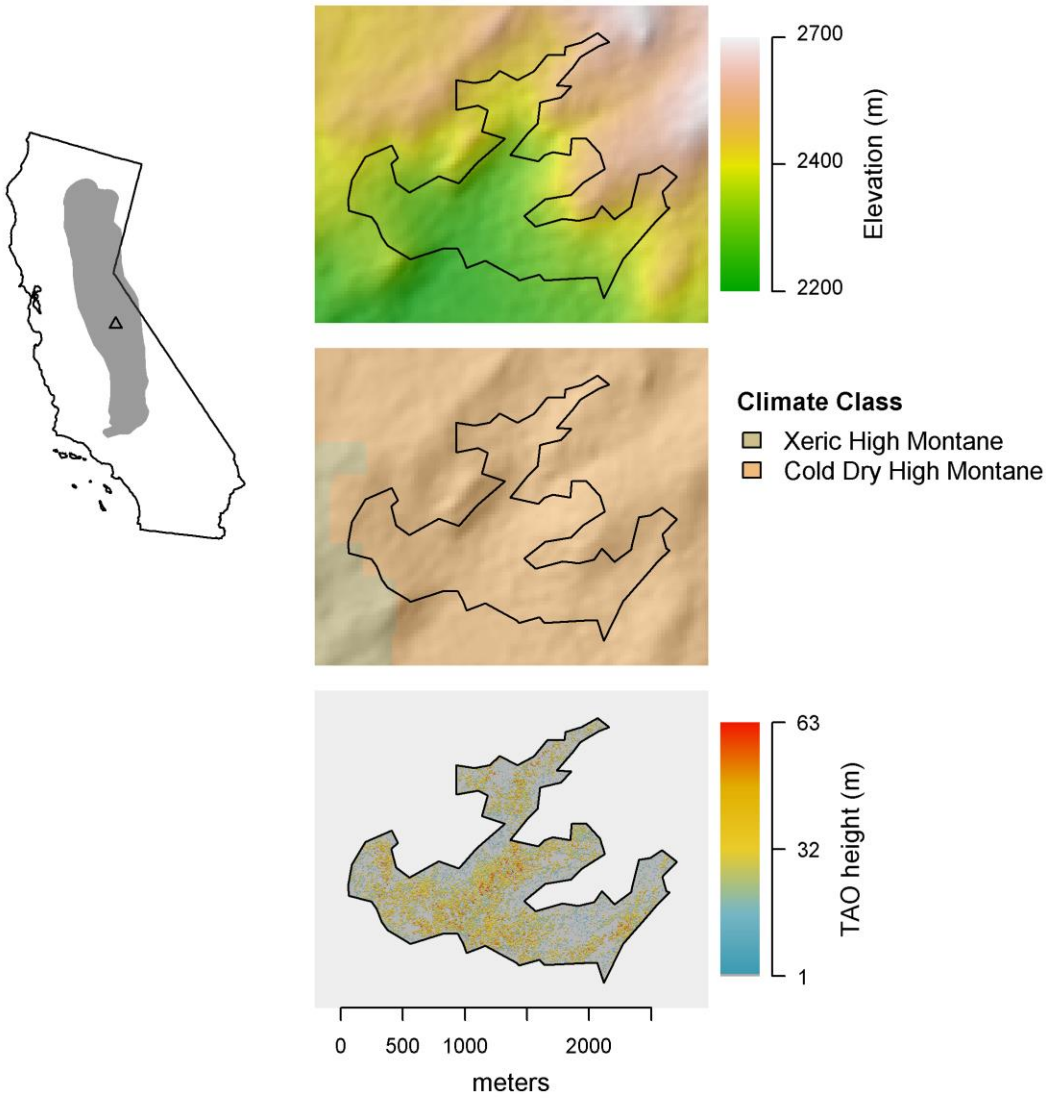

Starr King

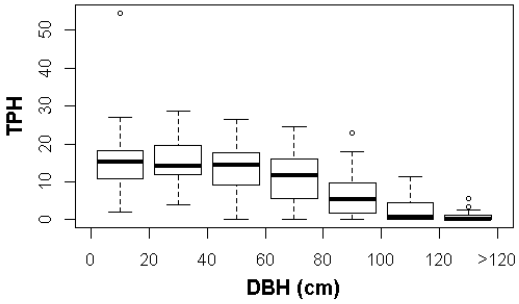
TPH
0 10 20 30 40 50
0 20 40 60 80 100 120 >120
DBH (cm)

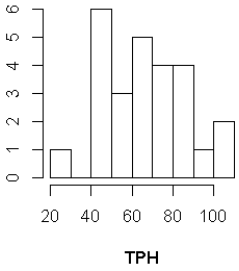
0 1 2 3 4 5 6
20 40 60 80 100
TPH

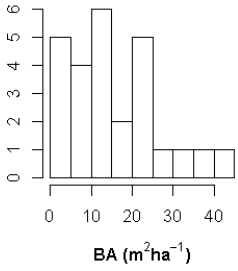
0 1 2 3 4 5 6
0 10 20 30 40
BA (m2ha-1)

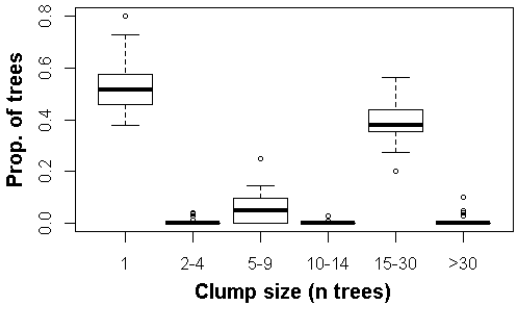
Prop. of trees
0.0 0.2 0.4 0.6 0.8
1 2-4 5-9 10-14 15-30 >30
Clump size (n trees)

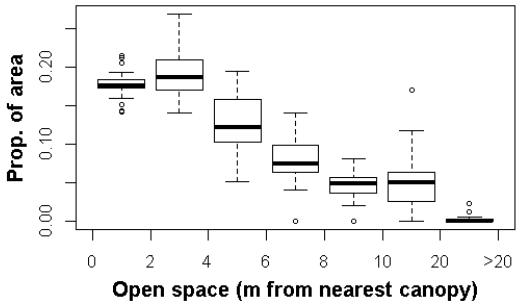
Prop. of area
0.00 0.10 0.20
0 2 4 6 8 10 20 >20
Open space (m from nearest canopy)

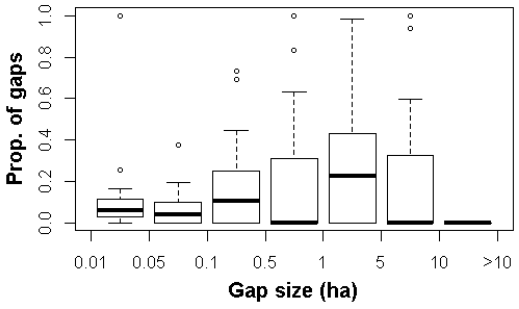
Prop. of gaps
0.0 0.2 0.4 0.6 0.8 1.0
0.01 0.05 0.1 0.5 1 5 10 >10
Gap size (ha)

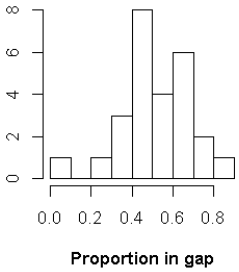
0 2 4 6 8
0.0 0.2 0.4 0.6 0.8
Proportion in gap

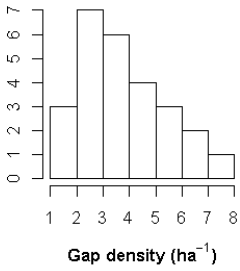
0 1 2 3 4 5 6 7
1 2 3 4 5 6 7 8
Gap density (ha-1)

Swamp

Ownership	Yosemite National Park
Hectares	178

	Ridges	**Valleys**	**NE slopes**	**SW slopes**
Landform proportions	0.32	0.16	0.20	0.32

	Minimum	**Mean**	**Maximum**
AET (mm)	269	289	424
Deficit (mm)	560	686	704
T_{min} (°C)	2.2	2.6	3.2
Elevation (m)	1585	1595	1610

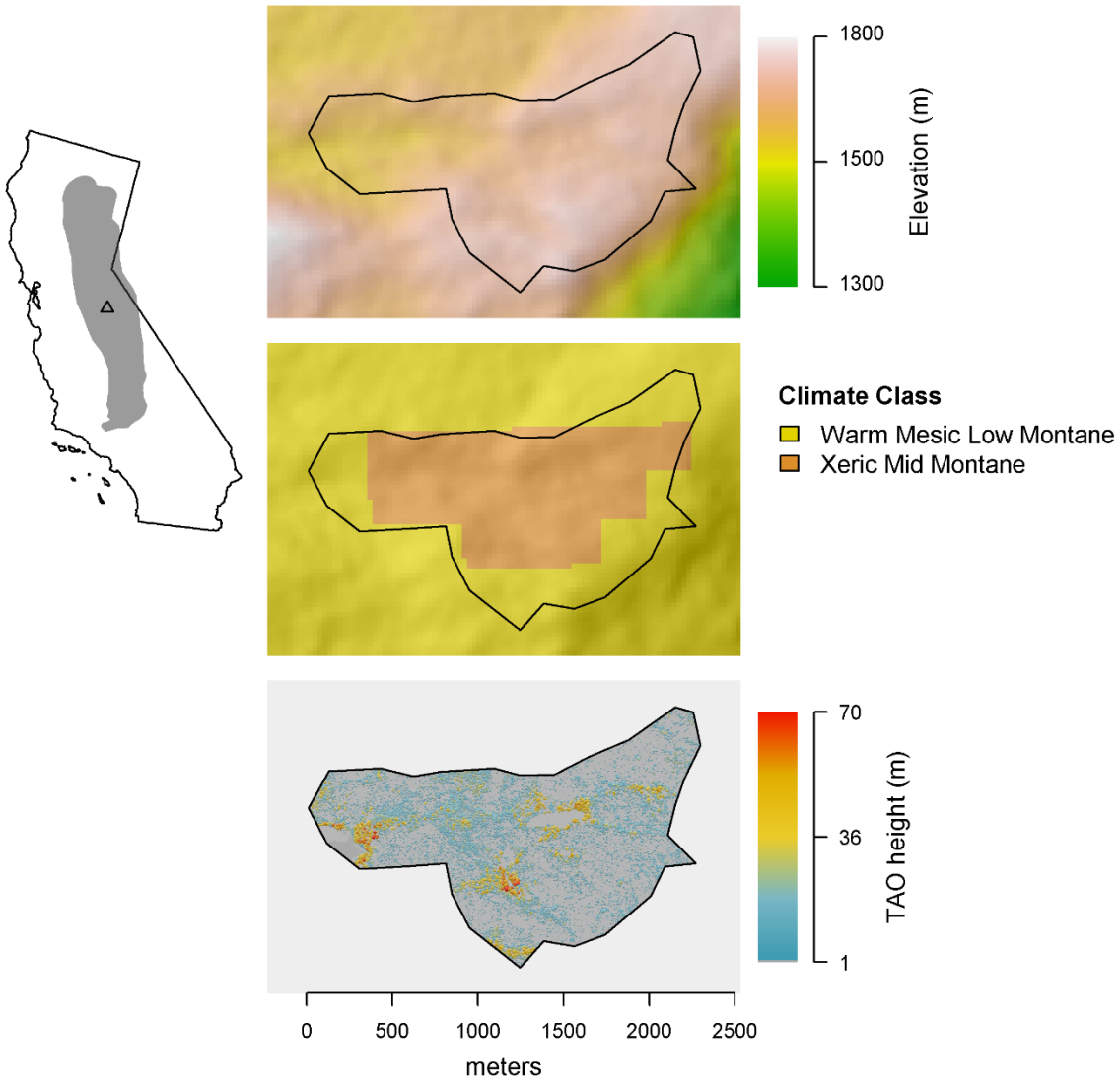

Swamp

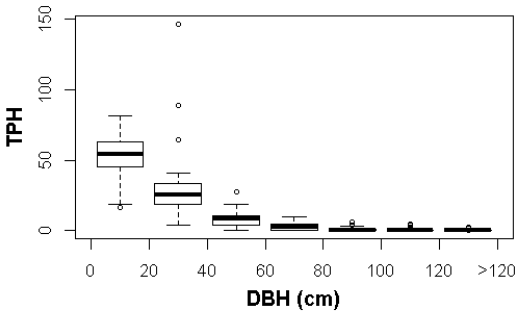
TPH
0
50
100
150
0
20
40
60
80
100
120
>120
DBH (cm)

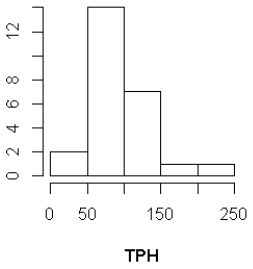
0
2
4
6
8
12
0
50
150
250
TPH

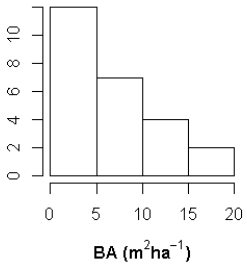
0
2
4
6
8
10
0
5
10
15
20
BA (m2ha−1)

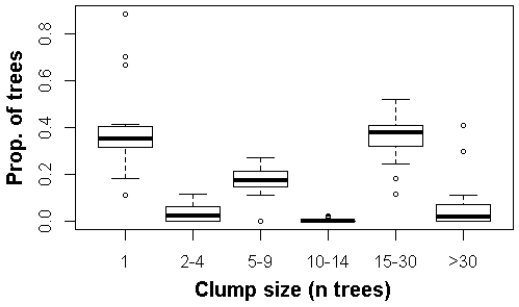
Prop. of trees
0.0
0.2
0.4
0.6
0.8
1
2-4
5-9
10-14
15-30
>30
Clump size (n trees)

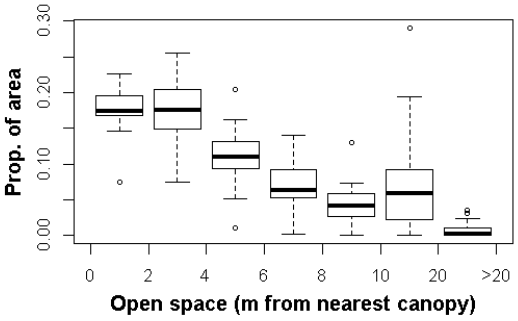
Prop. of area
0.00
0.10
0.20
0.30
0
2
4
6
8
10
20
>20
Open space (m from nearest canopy)

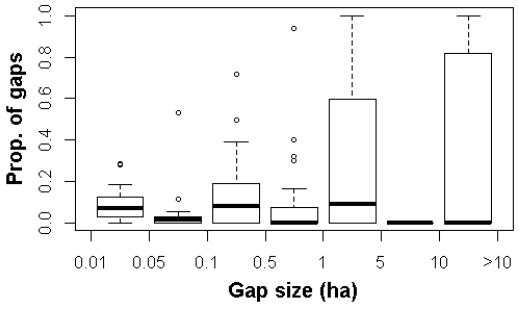
Prop. of gaps
0.0
0.2
0.4
0.6
0.8
1.0
0.01
0.05
0.1
0.5
1
5
10
>10
Gap size (ha)

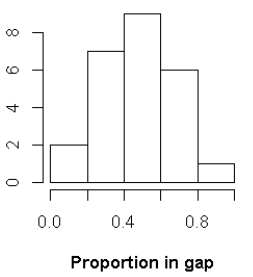
0
2
4
6
8
0.0
0.4
0.8
Proportion in gap

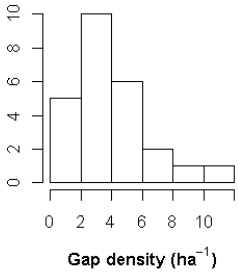
0
2
4
6
8
10
0
2
4
6
8
10
Gap density (ha−1)

T Grove

Ownership	Yosemite National Park
Hectares	167

	Ridges	**Valleys**	**NE slopes**	**SW slopes**
Landform proportions	0.14	0.14	0.38	0.34

	Minimum	**Mean**	**Maximum**
AET (mm)	365	390	407
Deficit (mm)	507	534	574
T_{min} (°C)	3.3	3.9	4.6
Elevation (m)	1618	1663	1683

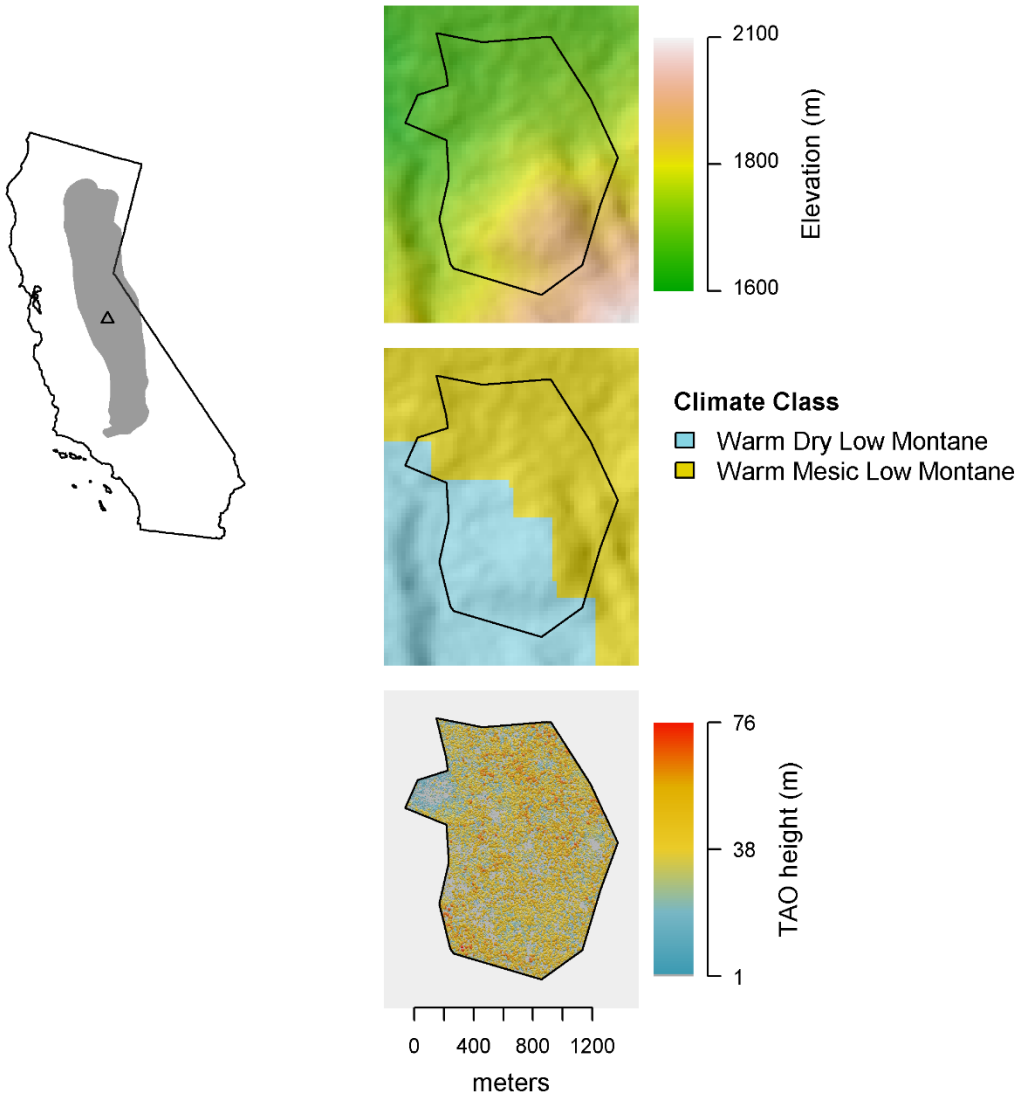

T Grove

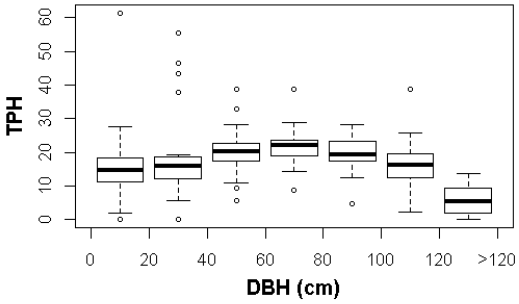
TPH
0 10 20 30 40 50 60
0 20 40 60 80 100 120 >120
DBH (cm)

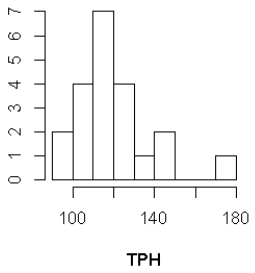
0 1 2 3 4 5 6 7
100 140 180
TPH

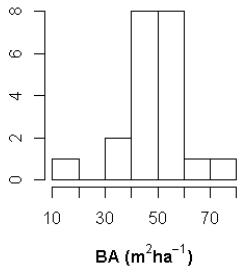
0 2 4 6 8
10 30 50 70
BA (m2ha-1)

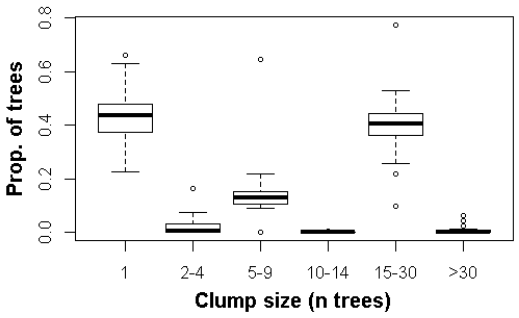
Prop. of trees
0.0 0.2 0.4 0.6 0.8
1 2-4 5-9 10-14 15-30 >30
Clump size (n trees)

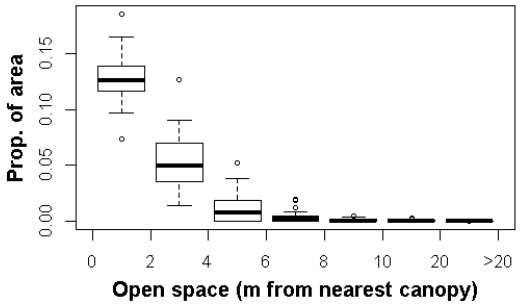
Prop. of area
0.00 0.05 0.10 0.15
0 2 4 6 8 10 20 >20
Open space (m from nearest canopy)

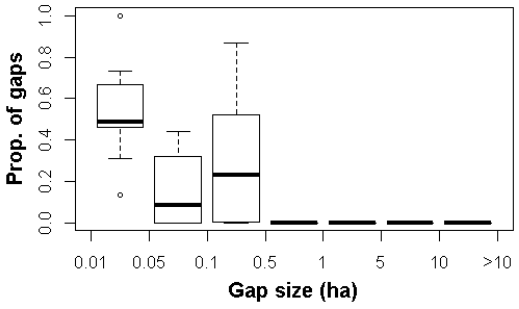
Prop. of gaps
0.0 0.2 0.4 0.6 0.8 1.0
0.01 0.05 0.1 0.5 1 5 10 >10
Gap size (ha)

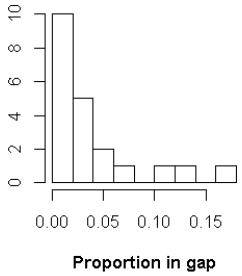
0 2 4 6 8 10
0.00 0.05 0.10 0.15
Proportion in gap

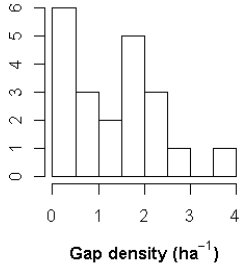
0 1 2 3 4 5 6
0 1 2 3 4
Gap density (ha-1)

Tamarack

Ownership	Yosemite?
Hectares	1025

	Ridges	**Valleys**	**NE slopes**	**SW slopes**
Landform proportions	0.37	0.23	0.25	0.15

	Minimum	**Mean**	**Maximum**
AET (mm)	259	360	472
Deficit (mm)	508	606	745
T_{min} (°C)	2.9	4.1	5.9
Elevation (m)	1902	2072	2166

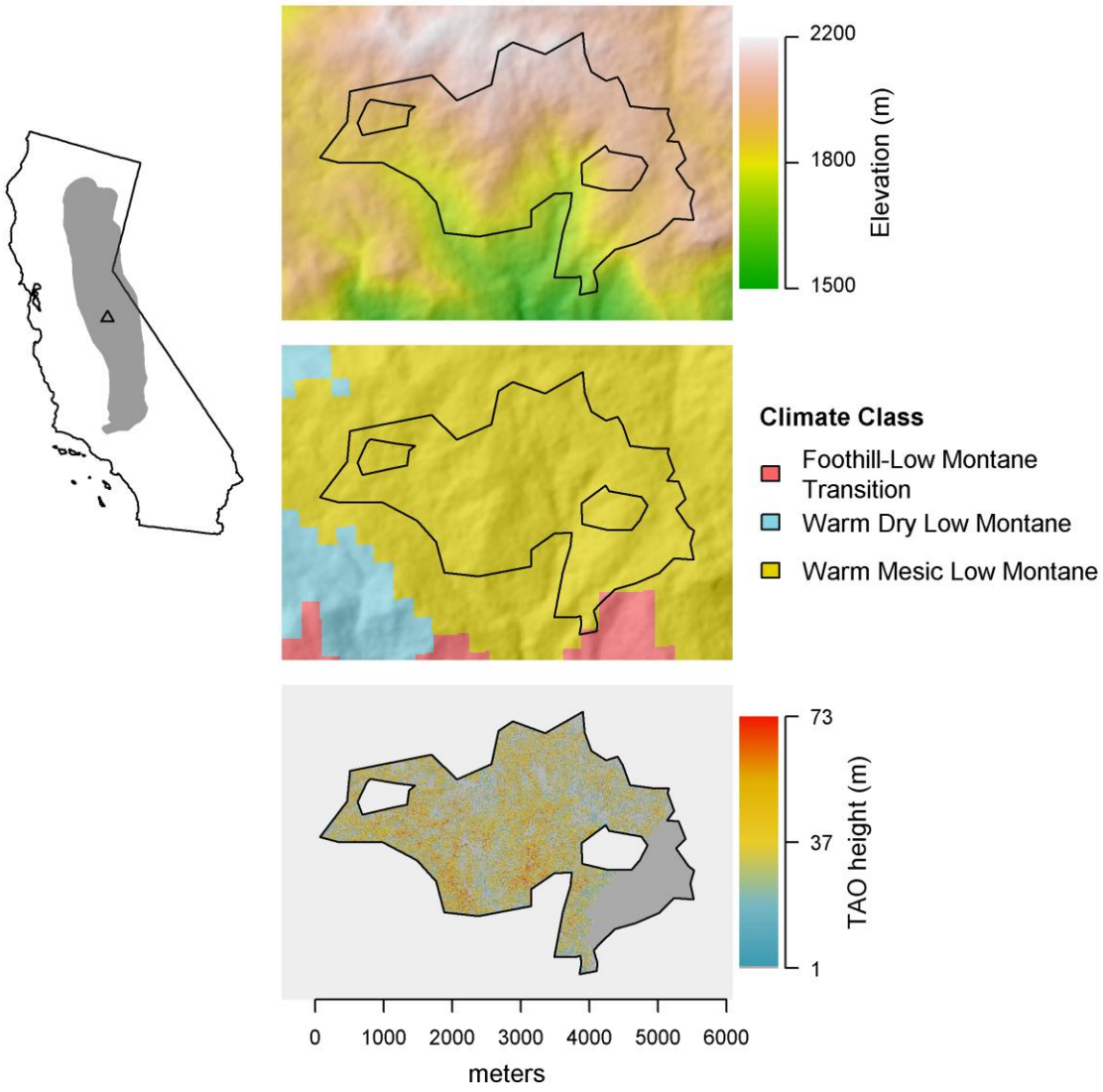

Tamarack

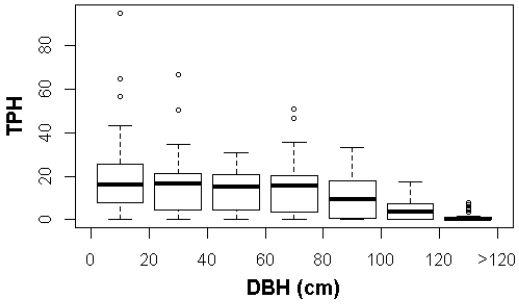
TPH
0
20
40
60
80
0
20
40
60
80
100
120
>120
DBH (cm)

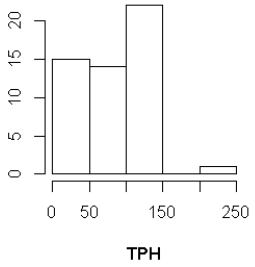
0
5
10
15
20
0
50
150
250
TPH

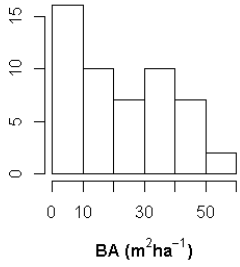
0
5
10
15
0
10
30
50
BA (m2ha−1)

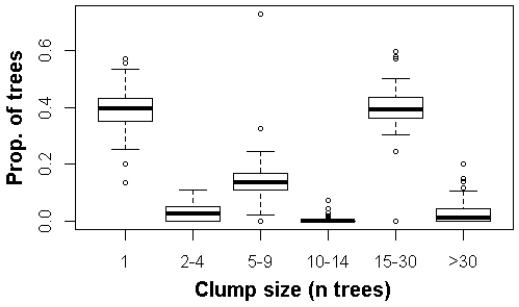
Prop. of trees
0.0
0.2
0.4
0.6
1
2-4
5-9
10-14
15-30
>30
Clump size (n trees)

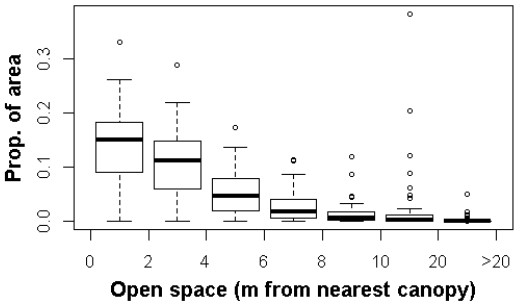
Prop. of area
0.0
0.1
0.2
0.3
0
2
4
6
8
10
20
>20
Open space (m from nearest canopy)

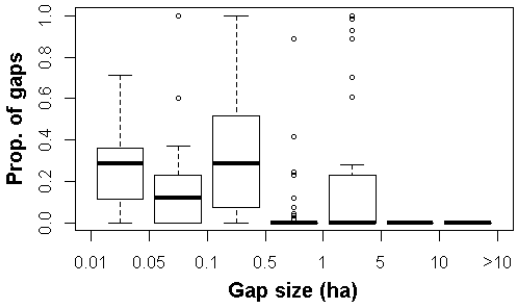
Prop. of gaps
0.0
0.2
0.4
0.6
0.8
1.0
0.01
0.05
0.1
0.5
1
5
10
>10
Gap size (ha)

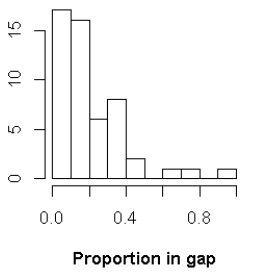
0
5
10
15
0.0
0.4
0.8
Proportion in gap

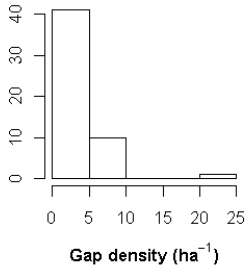
0
10
20
30
40
0
5
10
15
20
25
Gap density (ha−1)

Tueeulala

Ownership	?
Hectares	812

	Ridges	**Valleys**	**NE slopes**	**SW slopes**
Landform proportions	0.36	0.15	0.19	0.30

	Minimum	**Mean**	**Maximum**
AET (mm)	270	313	430
Deficit (mm)	541	682	741
T_{min} (°C)	1.7	3.0	5.8
Elevation (m)	1688	1871	2028

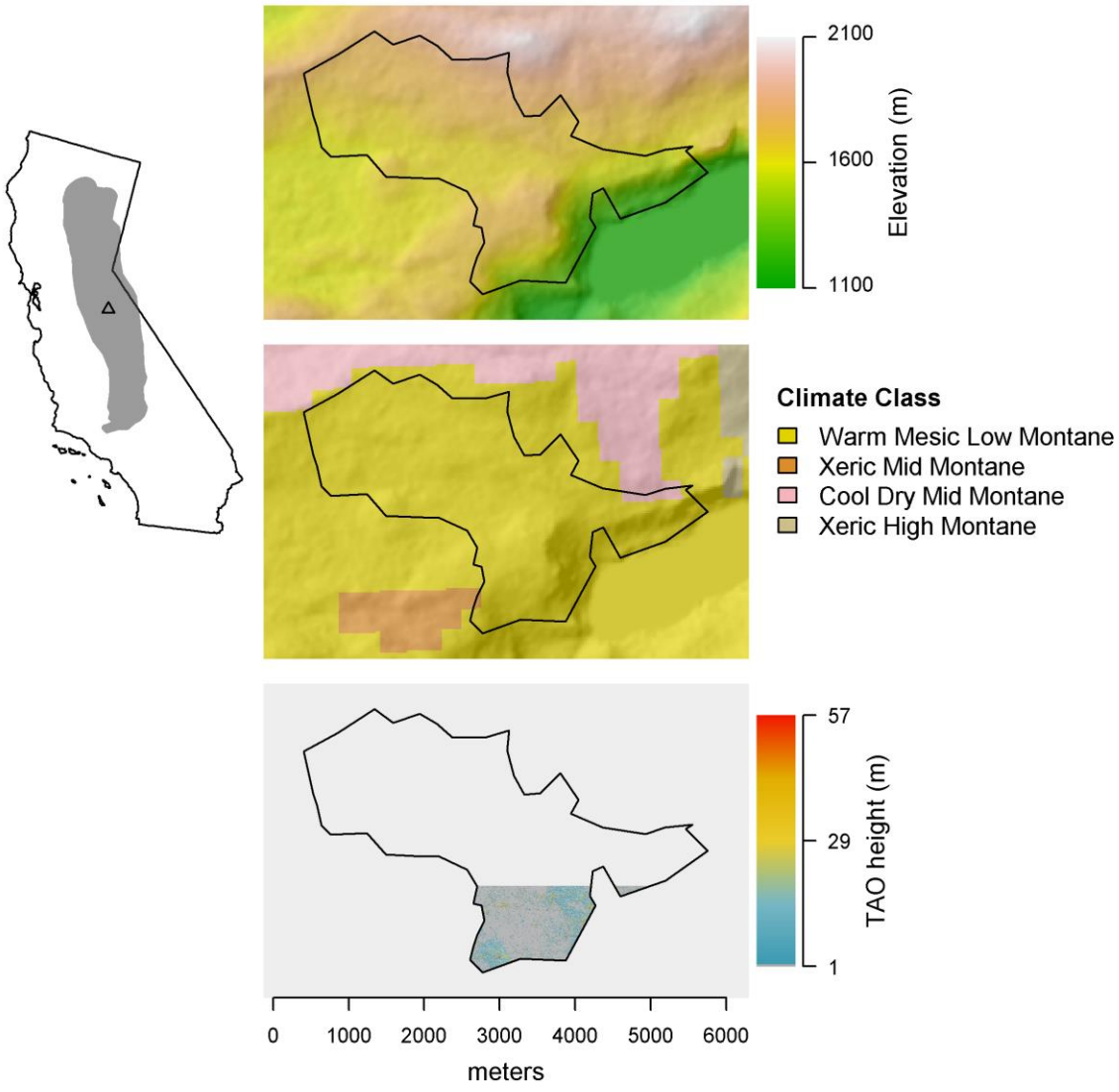

Tueeulala

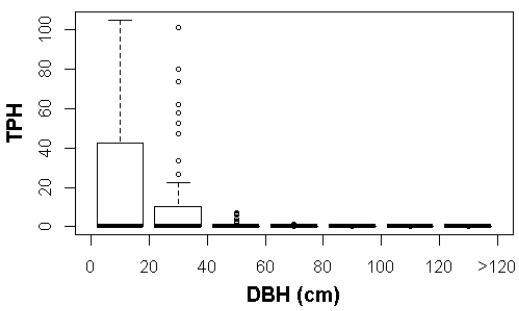
TPH
0 20 40 60 80 100
0 20 40 60 80 100 120 >120
DBH (cm)

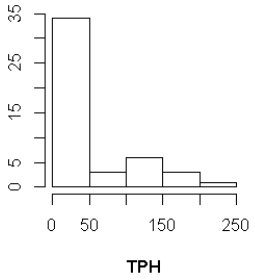
0 5 15 25 35
0 50 150 250
TPH

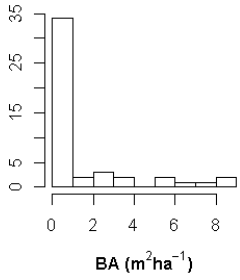
0 5 15 25 35
0 2 4 6 8
BA (m2ha-1)

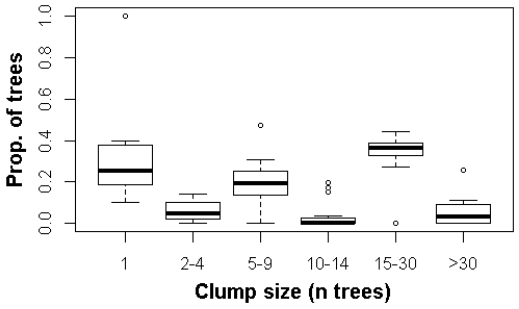
Prop. of trees
0.0 0.2 0.4 0.6 0.8 1.0
1 2-4 5-9 10-14 15-30 >30
Clump size (n trees)

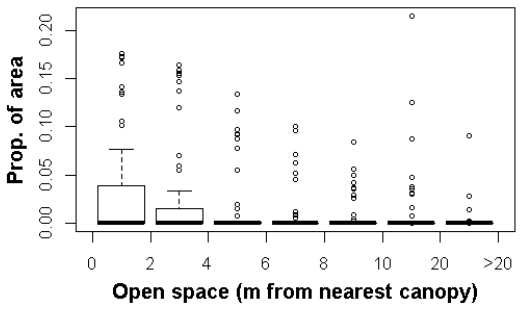
Prop. of area
0.00 0.05 0.10 0.15 0.20
0 2 4 6 8 10 20 >20
Open space (m from nearest canopy)

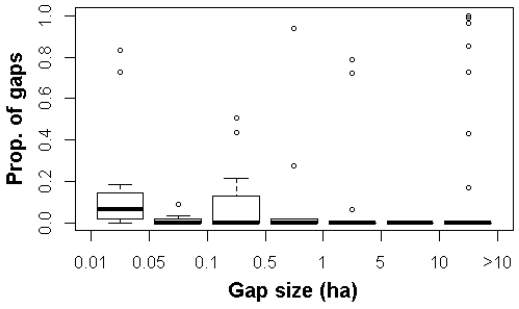
Prop. of gaps
0.0 0.2 0.4 0.6 0.8 1.0
0.01 0.05 0.1 0.5 1 5 10 >10
Gap size (ha)

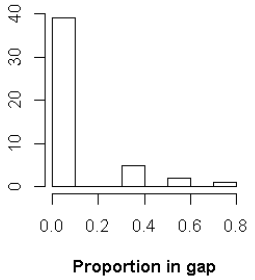
0 10 20 30 40
0.0 0.2 0.4 0.6 0.8
Proportion in gap

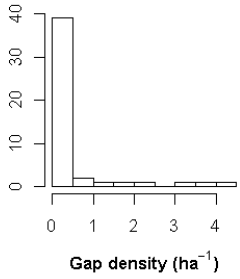
0 10 20 30 40
0 1 2 3 4
Gap density (ha-1)

Upper Cottonwood

Ownership	Yosemite National Park
Hectares	381

	Ridges	**Valleys**	**NE slopes**	**SW slopes**
Landform proportions	0.17	0.17	0.28	0.38

	Minimum	**Mean**	**Maximum**
AET (mm)	231	293	401
Deficit (mm)	405	516	576
T_{min} (°C)	-0.11	1.0	2.2
Elevation (m)	1679	2155	2280

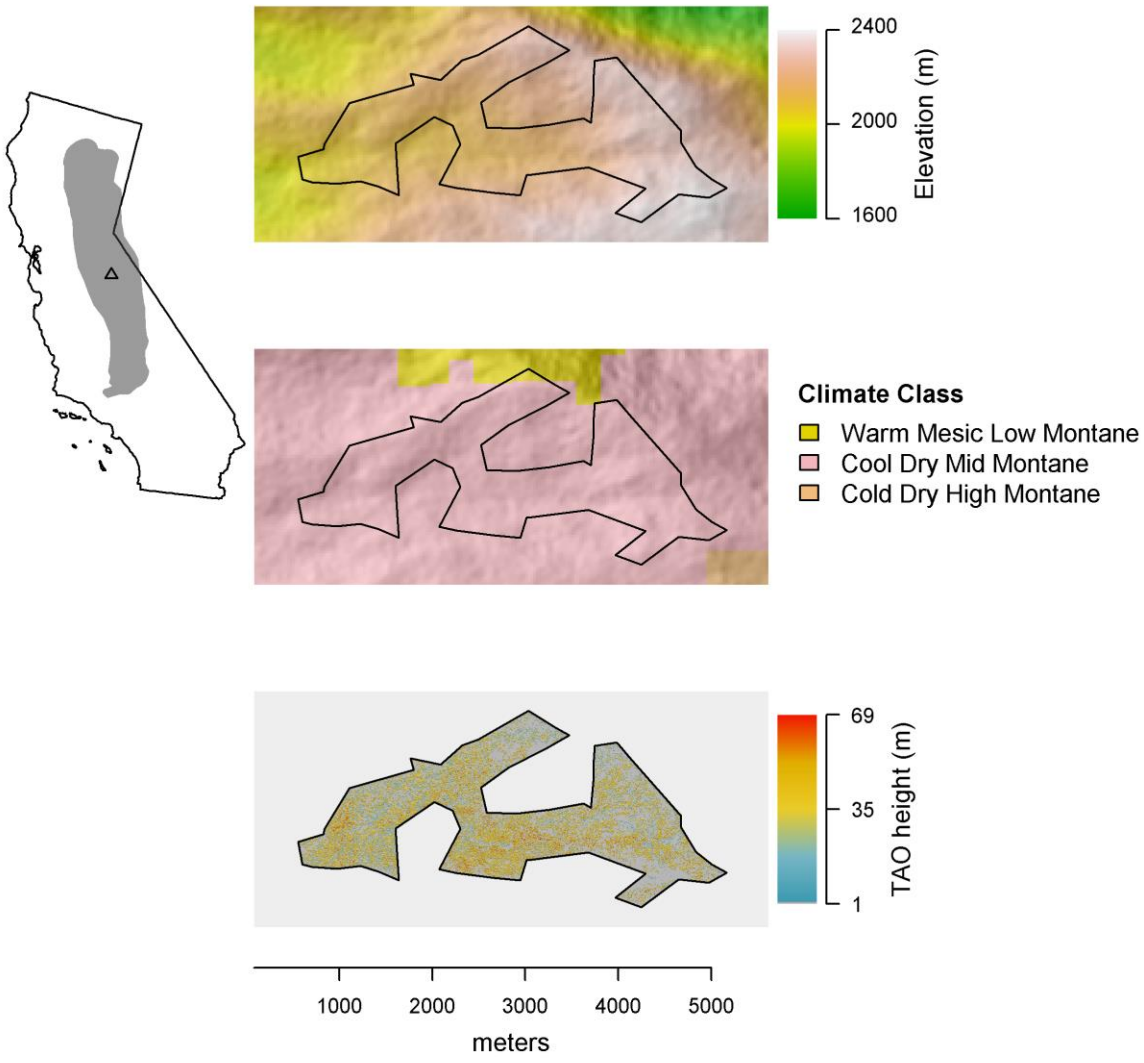

Upper Cottonwood

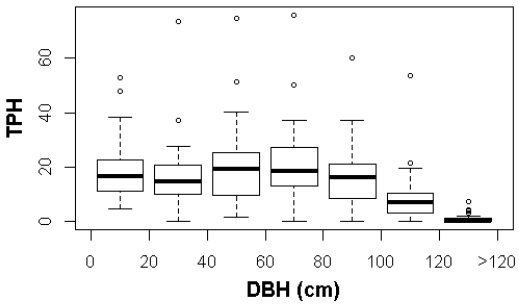

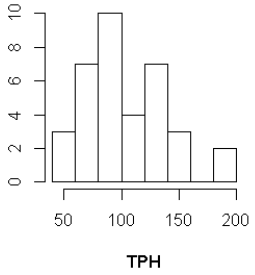

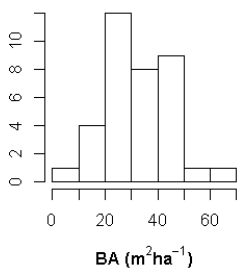

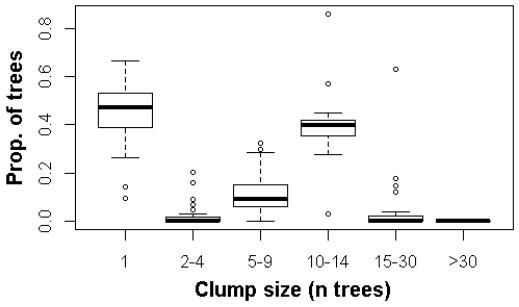

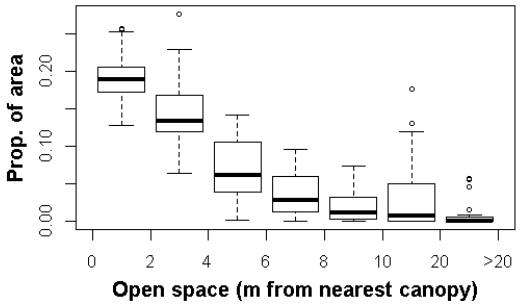

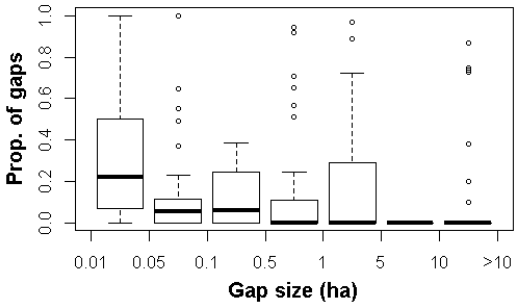

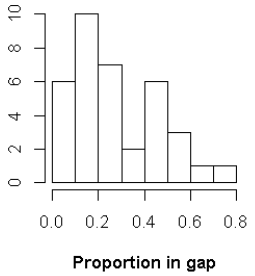

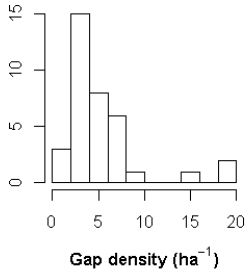

Chapter 2: Using lidar to guide development of restoration prescriptions in fire-prone forests

1. Introduction

Management of fire-adapted forests on public lands across the western United States is increasingly focused on restoration of resilience in areas that have been fire-suppressed, cut and replanted, or otherwise degraded (North *et al.*, 2009). The nominal goal of restoration, resilient forests, is taken to mean forests that experience minimal loss of function when disturbed (e.g., by wildfire or insects) and recover quickly from any losses that do occur (SER, 2002; DeRose and Long, 2014). In this context the functions that should be resilient to disturbance are those which forest managers value, such as hydraulic regulation and forest growth, at scales from management units (i.e., stands) to the Sierra Nevada region. Restoration work is typically done through a combination of mechanical treatment and prescribed fire, where mechanical treatment is more common on lands managed by the USDA Forest Service and fire use is more prevalent on lands managed by the USDI National Park Service (Stephens and Ruth, 2005; North *et al.*, 2009; Stephens *et al.*, 2013; North *et al.*, 2015).

Because restoration goals are broad and because there is a lack of silviculture research specifically investigating resilience (DeRose and Long, 2014), quantitative targets for mechanical treatments are most often drawn from reference datasets describing conditions across forests – historical or contemporary – that are considered functioning and resilient (Moore *et al.*, 1999; Keeley and Stephenson, 2000; Palik *et al.*, 2000; Larson and Churchill, 2012). Reference conditions are not necessarily used as exact targets to be replicated wholesale, but instead as benchmarks aiding in interpretation of current conditions (Churchill *et al.*, 2013). In fact, the best utility of reference conditions may be to provide a universe of discourse, or an envelope, describing the ranges of conditions that occur across a functioning landscape (Churchill *et al.*, 2013; Hessburg *et al.*, 2015;

Churchill *et al.*, 2017). Even reference landscapes show high degrees of variation driven by edaphic patterns, microclimate, and chance (Chapter 1; Lydersen and North, 2012; Hessburg *et al.*, 2015; Collins *et al.*, 2016). Reference conditions thus provide soft constraints on the realm of treatment options that can be considered restorative. Viewing reference conditions as a soft constraint is especially appropriate in light of expected changes in climate, since forests will be managed for future climates that are different than those under which reference forests have developed (Lutz *et al.*, 2010; Churchill *et al.*, 2013).

For reference condition data to be effective in guiding restoration of function and resilience, it is important that the measurements given actually correspond, ideally mechanistically, to desired functions and mechanisms of resilience. Some common measurements included in reference datasets are density, basal area, diameter distributions, and species composition (Fulé *et al.*, 1997; Collins *et al.*, 2011; Hagmann *et al.*, 2013, 2014; Collins *et al.*, 2015; Stephens *et al.*, 2015) since these metrics are variously correlated with drought stress, fuel laddering, fire tolerance, and insect/disease susceptibility (Agee and Skinner, 2005). It is increasingly recognized that spatial patterns of trees and canopy openings are also important dimensions to include (Churchill *et al.*, 2013; Lydersen *et al.*, 2013; Fry *et al.*, 2014; Churchill *et al.*, 2017), because these patterns drive other processes like horizontal fire movement, snow retention, insect dispersal, and regeneration of fire-tolerant tree species (Chapter 3; Larson and Churchill, 2012 and references therein).

Remote sensing tools have can provide larger spatial coverages of forest data for lower costs than ground-based field surveys (Reutebuch *et al.*, 2005), and these benefits have begun to be leveraged in restoration planning (e.g., at a state-wide scale; WA DNR, 2018). Airborne lidar has emerged as a key remote sensing technology able to make several measurements per square meter over tens or hundreds of thousands of contiguous hectares, and is applicable to both forest ecology (Hyde *et al.*, 2005; Hyde *et al.*, 2006; Falkowski *et al.*, 2009; Martinuzzi *et al.*, 2009; Kane *et al.*, 2011) and forest management (Næsset, 1997; Means *et al.*, 2000; Parker and Evans, 2009). The purpose of this study

is to take a step toward integrating lidar into forest restoration planning by introducing new methods using lidar for informing silvicultural aspects of restoration planning at treatment unit (operational) and project area (tactical) scales.

Aside from potentially reducing costs, using lidar in restoration planning could provide several unique benefits. In traditional silviculture planning, stands are treated as patches of homogeneous structure with one average value for measures like density and basal area taken from a sample of plots (Franklin *et al.*, 2018). In contrast, lidar's complete coverage captures the true, spatially explicit distributions of structural conditions which may be inadequately characterized by averages (Puettmann *et al.*, 2012). Because of its high resolution, lidar is also able to make fine-scale measurements of spatial patterns, i.e., the arrangement of tree clumps and canopy openings (Koukoulas and Blackburn, 2004; Kane *et al.*, 2013; Packalen *et al.*, 2013; Kane *et al.*, 2014). These kinds of data, despite representing key drivers of ecosystem function, are not captured by the Common Stand Exam or other typical resource inventory protocols (USDA Forest Service, 2013).

Another benefit of having accurate fine-scale measurements from lidar is the ability to define practical constraints on treatment options given current structural conditions. Reference conditions may provide soft bounds around the realm of potential restorative treatment outcomes, but prescriptions must also be subject to the hard constraint of what residual structural conditions are achievable given current stand structure. Lidar data could make it vastly easier to reconcile these constraints by explicitly evaluating potential transitions between current stand structure and residual structures on the bounds of the reference envelope.

Lidar data also offer some advantages at the scale of entire restoration project areas. Because lidar is often collected in contiguous acquisitions covering tens or hundreds of thousands of hectares, it allows for a complete view of structural conditions across a project area including both treatment units and the untreated matrix. This landscape context allows for assessment of processes that take

place at the scale of watersheds and groups of watersheds, such as fire sending, insect outbreak progression, and habitat for mammal and bird species (Hessburg *et al.*, 2013).

In this study, we develop new methods for integrating lidar data into silvicultural planning at stand and landscape scales, with a focus on restoration treatments in fire-prone forests. At the stand (i.e., treatment unit) scale, our objective is to delineate the decision space for prescription parameters like residual density, basal area, and spatial patterns given the soft constraints of reference condition envelopes and the hard constraint of current structural conditions. At the landscape (i.e., project area) scale, our objective is to provide a framework for selecting from the available treatment options, stand by stand, to meet different project-level goals. We first describe the new methods in concept, then apply them to a case study project area in the Lake Tahoe Basin, California. Within this case study we also ask: how do structural departures from reference conditions and the concomitant restoration treatment prescriptions vary with topographic position and aspect?

2. Theoretical Framework

2.1 Lidar individual tree detection and tree-approximate objects

Lidar data are most often integrated into forest planning and operations using an area-based approach, where statistics of the distribution of lidar return heights are summarized on a gridded basis (usually 10-30 m resolution) and used in models to predict traditional forest inventory metrics like density, basal area, or merchantable volume (White *et al.*, 2013). However, our objectives for this study have two key requirements that the area-based approach does not meet. First, we require a lidar data source that is able to capture not just density, basal area, and tree sizes, but also spatial patterns of tree clumps and canopy openings. The area-based approach is based solely on vertical distributions of lidar returns and thus cannot provide measurements of fine-scale horizontal pattern (Jeronimo *et al.*, 2018). Second, we require the ability to explicitly

evaluate whether particular combinations of prescribed density, basal area, and spatial pattern are actually possible to achieve simultaneously given the trees present in a treatment unit. This analysis is a key part of identifying constraints on treatment options. The area-based approach provides a suite of modeled or imputed values, but does not provide the explicit tree-based measurements that we require.

We chose to define our methods instead around an individual tree approach to lidar analysis. Individual tree detection refers to processing lidar data to pick out and delineate the crowns of each tree. Analyzing lidar on the basis of individual trees can provide estimates of forest inventory metrics comparable to the area-based approach (Breidenbach *et al.*, 2010; Lindberg *et al.*, 2010), but also enables characterization of the key features that the area-based approach cannot achieve, namely, tree-scale measurements including horizontal patterns.

However, lidar tree detection is not able to detect every tree, because many smaller tree crowns are hidden from lidar's view by the dominant canopy layer (Jeronimo *et al.*, 2018 and references therein). Thus, instead of thinking of tree detection results as a tree list, we adopt the tree-approximate object (TAO) paradigm (North *et al.*, 2017; Jeronimo *et al.*, 2018). TAOs are patches of connected canopy dominated by a single tree that was well-resolved by the lidar instrument, but may also encompass a few subordinate trees that could not be individually delineated. Treating tree detection results as TAOs is a way to make use of tree-scale measurements while explicitly recognizing that not every tree is being measured directly.

2.2 Backbone trees

Legacy trees, that is, old trees that established before significant impacts of Euro-American settlement, are typically the backbone of restoration prescriptions. Under most restoration treatment archetypes, legacy trees are always retained and non-legacy retention is structured

around them (Brown *et al.*, 2004; Agee and Skinner, 2005; Franklin *et al.*, 2007; Franklin *et al.*, 2013). Large non-legacy trees are also important ecosystem components (Lutz *et al.*, 2018b), since large trees contribute disproportionately to structural heterogeneity (Lutz *et al.*, 2013) and ecosystem functions such as biomass storage and accumulation, fire tolerance, reproduction, and habitat provision (van Wagtendonk and Moore, 2010; Lutz *et al.*, 2012; North *et al.*, 2017; Furniss *et al.*, in review). Therefore, we build this analysis around large trees, or backbone trees, representing the anchors of residual stand structure that would likely be retained in a restoration treatment.

Focusing on backbone trees is particularly advantageous when using lidar data, since these are the trees that lidar detects most accurately (Richardson and Moskal, 2011; Jeronimo *et al.*, 2018). Thus, the strengths and weaknesses of lidar tree detection are best incorporated into the analysis by focusing on residual structure compared to focusing on trees to be removed, which would on average be smaller and less accurately identified by lidar.

2.3 Prescription decision space

We developed a new method to simultaneously constrain the decision space of treatment options by reference conditions and current stand conditions by working in a pattern inspired by density management silviculture (Reineke, 1933; Drew and Flewelling, 1979; Curtis, 1982). In density management, stand conditions are characterized by plotting two stand-level average measurements against one another (Figure 1). One axis represents tree sizes and one represents density, e.g., density vs. quadratic mean diameter (Reineke, 1933), basal area vs. quadratic mean diameter (Briegleb, 1952), or density vs. mean tree volume (Drew and Flewelling, 1979). Within this 2-dimensional space, different regions or zones are defined, based on empirical trials, which correspond to different thinning treatment objectives, e.g., minimizing competition or

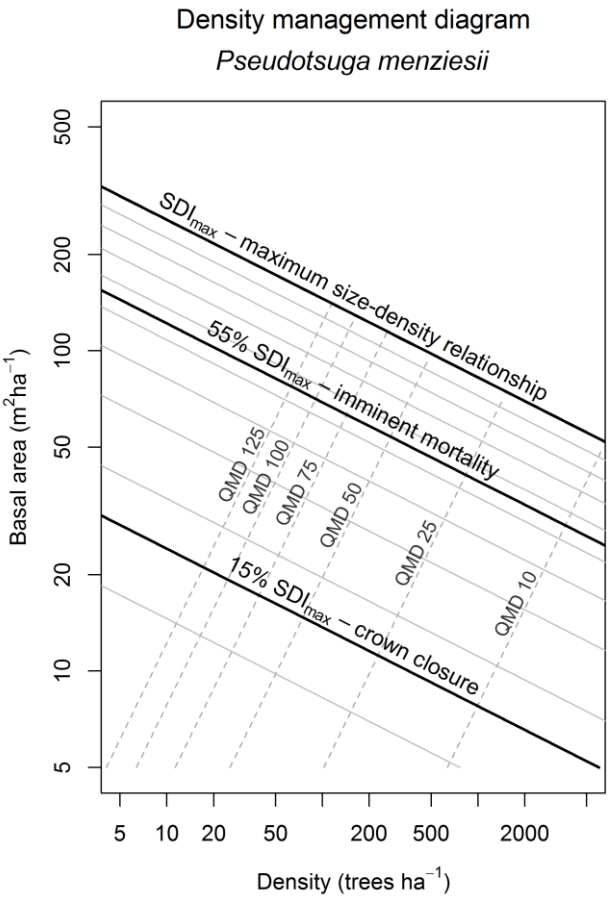

Figure 1 Example of a density management diagram (Drew and Flewelling, 1979), showing management zones delineated by relative stand density index (SDI) and quadratic mean diameter (QMD) isolines.

maximizing volume growth (Drew and Flewelling, 1979; Jack and Long, 1996; Powell, 1999). Single- and multiple-entry treatments or entire silviculture systems can be planned around a stand's trajectory through this 2D space, optimized depending on management objectives (Drew and Flewelling, 1979; Powell, 1999).

We extend and modify this idea in three ways. First, we expand the analysis from the two dimensions of density and tree size to include two additional spatial-pattern dimensions of tree clumping and canopy openings. Second, instead of defining management zones in terms of relative density thresholds (e.g., the -3/2 self-thinning law, Drew and Flewelling, 1979), we define them in terms of observed reference condition envelopes. Lastly, in traditional density

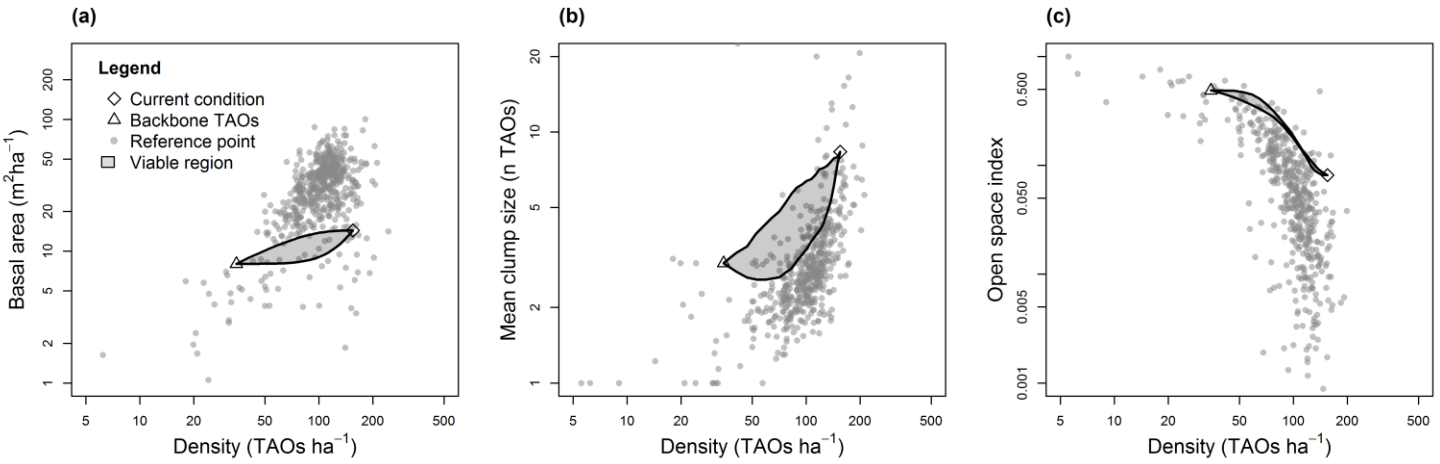

Figure 2 Example of an extended density diagram, building on the density management diagram in three ways: (1) instead of relying on density-based management zones, the desirable management zone is given by the range of variation of reference conditions, (2) the set of all possible treatment options that retain large and old "backbone" trees is shown as a hard constraint – the viable region – and (3) additional dimensions are included to represent spatial patterns, namely mean clump size and an open space index. The intersection between the viable region and the reference envelope is the target management zone. See text for details of these metrics.

management diagrams a treatment seeks to modify one axis (reducing density) with a small collateral effect on the second axis (usually a slight change in average tree size). The range of possible treatments can be expressed as a region in the density management space given the stand table, bounded below by strict thinning from above and bounded above by strict thinning from below (Figure 2a). A thinning target could be placed anywhere within the region of possible treatments; the choice of placement is based on management objectives. We extend this to include the two additional spatial pattern dimensions and the interactive constraints between spatial pattern targets and stocking targets (Figure 2b, c). The intersection of the region of possible treatments and the reference condition envelopes represents the set of treatment objectives that is simultaneously desirable and possible. We refer to these diagrams as extended density management diagrams.

This system for defining prescription decision spaces is general and can be applied to either field-collected stand tables or to measurements from lidar-detected TAOs. We demonstrate the latter in this study, but stress that the system we describe is not uniquely tied to lidar data.

2.4 Project area decision space

Once the decision space for each stand or treatment unit is defined in terms of an extended density management diagram, it remains to actually set objectives as points within the respective target regions. Because forest restoration goals often include modifying ecosystem processes that operate at watershed or trans-watershed scales it is necessary for stand-level restoration targets to be set within the context of the entire project area, emphasizing between-stand heterogeneity and strategic spatial configuration of different treatments across a project area (Gärtner *et al.*, 2008; Franklin and Johnson, 2012; North *et al.*, 2012; Hessburg *et al.*, 2015; North *et al.*, 2015).

Making decisions about geographic configuration of specific stand-level treatment targets in the context of a project area requires silvicultural discretion with an eye toward meeting project-level objectives (Franklin *et al.*, 2018). Thus, there is no general-purpose prescriptive system for making these decisions. However, the silvicultural choices involved are guided by landscape management principles (e.g., Hessburg *et al.*, 2015). Here we propose some ideas about how to bring landscape management principles into decisions about setting treatment targets.

Configuring treatments across a project area should follow common recommendations given for forests with historically low- and mixed-severity fire regimes. Previous research syntheses stress the need for patch heterogeneity at the landscape scale (Hessburg *et al.*, 2005; Franklin and Johnson, 2012), including some denser forest patches that provide habitat for wildlife species of concern (North *et al.*, 2009; Franklin and Johnson, 2012; Hessburg *et al.*, 2015), for example, the California spotted owl (*Strix occidentalis occidentalis*, North *et al.*, 2017), the Pacific fisher

(*Martes pennanti pacifica*, Purcell *et al.*, 2009), and the northern flying squirrel (*Glaucomys sabrinus*, Meyer *et al.*, 2007). The configuration of patches should be guided by physiographic variation, driven by topography (North *et al.*, 2009; Underwood *et al.*, 2010; Hessburg *et al.*, 2015). The ultimate landscape-level goal is often to create viable firesheds or firescapes, landscapes that are ready to accept fire without emergency suppression measures (North *et al.*, 2015), where ecosystem function can be maintained by the process of fire rather than mechanical treatment (Franklin and Johnson, 2012; North *et al.*, 2012). One step toward this is the establishment of fire anchor patches, mechanically treated areas that can serve as a starting point for prescribed fire and wildfire restoration (North *et al.*, 2015).

Based on these landscape restoration principles, the following steps should be taken when deciding on unit-level treatment targets:

(1) Distribute targets throughout the reference envelope to create and maintain landscape-level heterogeneity,

(2) Locate targets within the reference envelope according to unit-level physiography, e.g., set targets with lower density, smaller clumps, and more open space on ridgetops versus higher density, larger clumps, and less open space in valleys and on northerly slopes,

(3) Balance connectivity of dense habitat patches with continuity of fuels by placing dense patches in loose aggregates, and

(4) Identify one to a few fire anchor units within the project area to focus primarily on fuel objectives.

Given the decision space for a project area there may be many configurations of unit-level treatment targets that satisfy the landscape restoration principles. The methods presented here do

not attempt to optimize the best possible configuration; this decision is left up to the silviculturist.

3. Methods

3.1 Study area

As a case study, we piloted this new method in the Lake Tahoe West (LTW) Restoration Partnership planning area on National Forest lands within the Lake Tahoe Basin Management Unit (LTBMU) (Figure 3). The Lake Tahoe basin is an 82,000 ha watershed draining into Lake Tahoe. The basin was subject to heavy logging in the late 1800s to support silver mining and more moderate logging throughout the 20th century as the basin was developed into a recreation destination (Barbour *et al.*, 2002). As a result of logging, grazing, and a prolonged period of fire suppression, forest density in the mixed-conifer zone of the Lake Tahoe basin has tripled since the 1870s while basal area has doubled during the same period (Taylor *et al.*, 2014). These changes were driven by prolific white fir (*Abies concolor*) regeneration which, due to fire suppression, was allowed to recruit into intermediate size classes which are no longer susceptible to lower-severity fire (Beaty and Taylor, 2008; Becker and Lutz, 2016). Accordingly, surface and canopy fuel loads have approximately doubled (Taylor *et al.*, 2014), leaving forests of the basin very susceptible to high-severity fire effects. This pattern of increasing density and fuel loads is common across the Sierra Nevada (Collins *et al.*, 2011; North *et al.*, 2015; Stephens *et al.*, 2015; Becker and Lutz, 2016; Collins *et al.*, 2017).

Since the formation of the LTBMU in 1973, and especially in recent years, management goals in the basin have had a focus on restoration of forest resilience to fire through active management, including thinning, prescribed fire, and wildland fire use (Hymanson and Collopy, 2010). The LTW partnership is a collaborative restoration effort aimed at restoring resilience on

the west shore of Lake Tahoe. LTW is an interagency effort including federal, state, and private lands and agency, nonprofit and community stakeholders (Lake Tahoe West Restoration Partnership, 2017). The LTW planning area covers 23,900 ha stretching from the lake at 1,897 m elevation to the basin divide, rising to 3,043 m elevation at Pyramid Peak. The area experiences warm, dry summers with very little precipitation and cold, snowy winters with cumulative snow depths typically in excess of 4 m (Barbour *et al.*, 2002). The area includes Cool Dry High Montane, Cold Dry High Montane, and Cool Moist High Montane climate classes (Chapter 1).

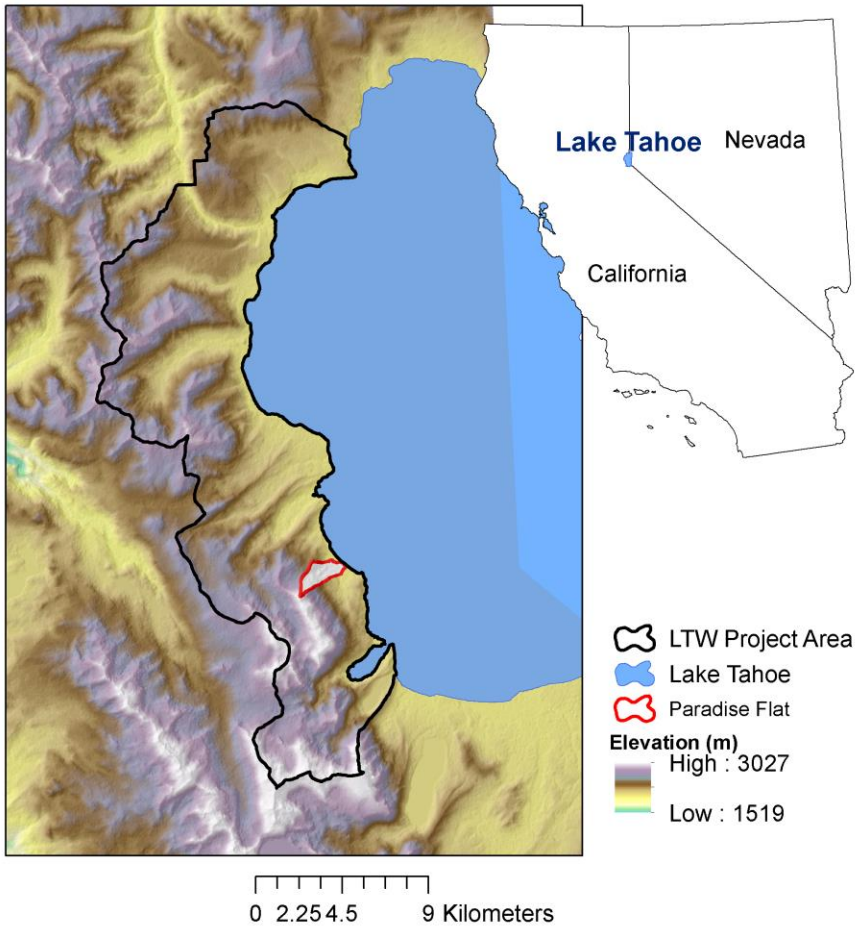

Figure 3 Map of the Lake Tahoe West project area on the west shore of Lake Tahoe in California, USA. The Paradise Flat catchment is the subject of this case study.

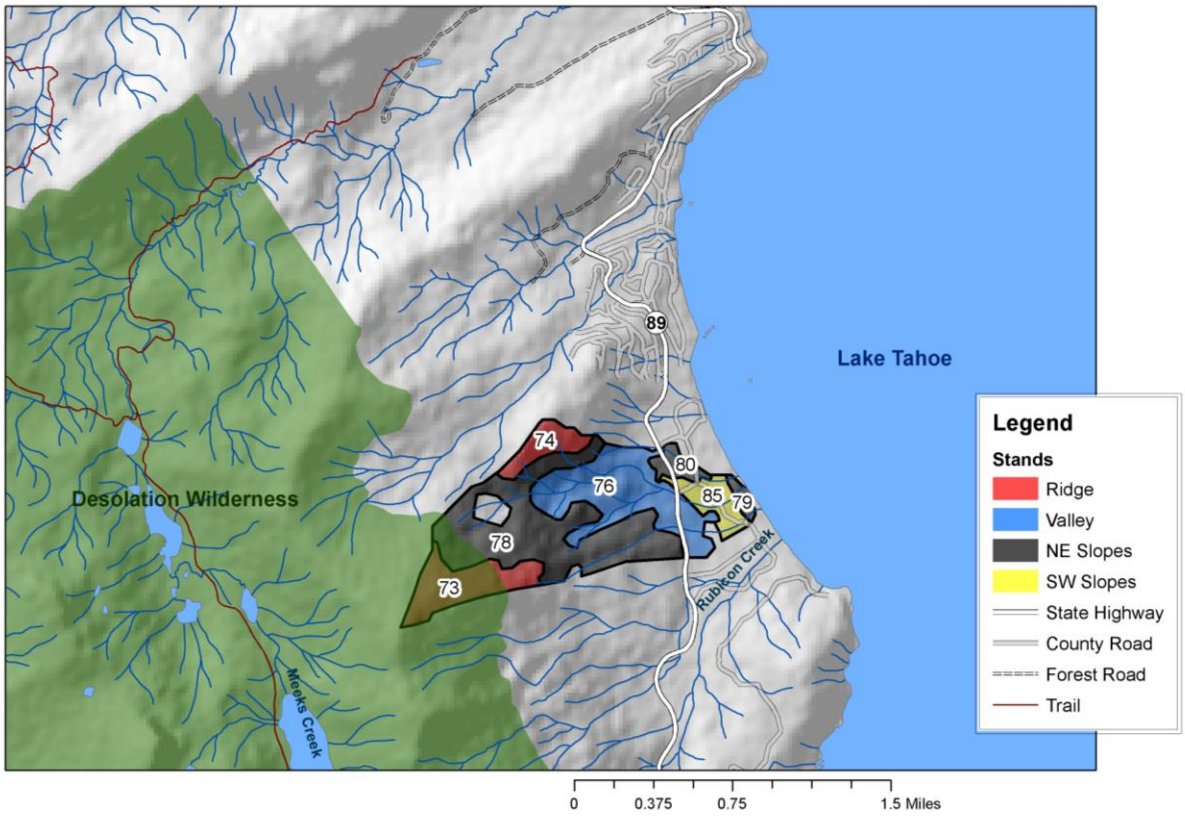

Figure 4 Map of the 215 ha Paradise Flat analysis area subdivided into stands based on landform, showing relevant geographic features. Paradise Flat ranges from 1,897-2,800 m elevation.

Within the LTW planning area we selected a 215 ha focal area to serve as an example project area for piloting our new method. The area comprises one catchment from the National Hydrography Dataset (EPA and USGS, 2018). The catchment extends down the northern flank of Rubicon Peak to the lake at Paradise Flat; this catchment is hereafter referred to as Paradise Flat (Figure 4). Paradise Flat is in the Cool Dry High Montane climate class and ranges in elevation from 1,897 m at lake level to 2,800 m at Rubicon Peak. The highest elevation 30 ha of Paradise lie within the Desolation Wilderness while the lowest elevation 30 ha are within the wildland-urban interface.

3.2 Lidar processing

3.2.1 Lidar data

Lidar data for the Lake Tahoe Basin were acquired on August 11-24, 2010 by Watershed Sciences, Inc. of Corvallis, Oregon. Data were acquired using two Leica ALS50 Phase II instruments flown at 900-1300 m above ground level. The instrument was able to record up to four returns per pulse with pulse rates of 83-105.9 kHz at a ±14º scan angle. Flight lines were flown with >50% sidelap yielding an average pulse density of 12 m^{-2}. Return location accuracy was 3.6 cm RMSE. The vendor created a bare-earth ground model using TerraScan and TerraModeler software (TerraSolid Oy, Helsinki, Finland).

3.2.2 Canopy height model

A canopy height model (CHM) is a 3-dimensional representation of the forest canopy surface with respect to the ground. A CHM was created for the focal areas using the FUSION Lidar Toolkit (McGaughey, 2018), based on lidar points normalized by the vendor-delivered ground model. The CHM was created as a 0.75 m resolution raster in which each cell took on the *z*-value of the highest lidar return in that cell. The CHM was smoothed with a 3x3 mean filter to remove noise (Jeronimo *et al.*, 2018).

3.2.3 Tree-approximate objects and backbone trees

Individual tree crowns were detected using the FUSION TreeSeg tool, an implementation of the watershed transform (Vincent and Soille, 1991; McGaughey, 2018). Detected trees were taken to be tree-approximate objects. Each TAO was assigned a georeferenced *xy*-location and a height corresponding to the highest lidar return in the TAO's crown.

To identify backbone trees we first subdivided Paradise Flat by landform, since fine-scale variability mediated by topographic position drives differences in resilient forest structures (Lydersen and North, 2012; Wiggins, 2017). We subdivided Paradise Flat into landscape management units (LMUs) (Underwood *et al.*, 2010) using the Landscape Management Unit

Tool version 2 (Boynton *et al.*, 2015), which segments a digital elevation model (DEM) into landscape facets. We used a 30 m resolution DEM with default parameters and classified the result into the following simplified classes: ridges, valleys, NE slopes (0-135° and 225-360° aspect), and SW slopes (135-225° aspect). We calculated 75th percentile TAO height (P75) pooled for each LMU facet within the subset of the LTW project area in the Cool Dry High Montane climate class. TAOs taller than their respective P75 thresholds were designated backbone trees (Table 1). The P75 threshold is derived from Van Pelt *et al.* (2016) as an indicator for emergent crowns in *Sequoia sempervirens* forests, but is also applicable to detecting large old trees Sierra Nevada mixed-conifer forests (R. Van Pelt, personal communication).

3.3 Stand-level density and pattern metrics

We took each of the seven delineated LMU patches within Paradise Flat to represent a stand, that is, a treatment unit with a single prescription. Stands ranged from 5.5 to 76 ha with a median size of 8.6 ha. We calculated the four variables required for the extended density management diagrams – density, basal area, tree clumping, and open space – for each stand. We calculated density in terms of TAOs per hectare. For basal area, we estimated dbh for the dominant tree of each TAO using height-diameter regressions from Jeronimo (Chapter 1); although TAOs do not represent every tree they capture dominant trees well, and so basal area estimates should be reasonably accurate (Jeronimo *et al.*, 2018), usually within 20% for mature Sierra Nevada mixed-conifer forests (S. Jeronimo, *unpublished data*).

We used the point pattern of the locations associated with each TAO to characterize clumping patterns. TAOs were assigned membership in a clump following methods developed for stem maps by Churchill *et al.* (2013) and adapted for TAOs by Jeronimo (Chapter 1). Any TAOs with high points within 6 m of one another were considered members of the same clump.

Table 1 Current structural conditions for the seven stands in the Paradise Flat analysis area as measured by lidar tree detection, along with structural metrics for only "backbone" trees. Abbreviations: LMU = landscape management unit, TAO = tree-approximate object, MCS = mean clump size, OSI = open space index. See text for full definitions of backbone trees and the abbreviated terms.

Stand ID	**73**	**74**	**76**	**78**	**79**	**80**	**85**
Area (ha)	26.5	5.5	57.5	76.2	5.9	7.7	9.3
LMU	Ridge	Ridge	Valley	NE Slope	NE Slope	NE Slope	SW Slope
Density (TAOs ha^{-1})	165	188	169	158	188	166	190
BA (m^2 ha^{-1})	21.1	16.2	38.5	38.4	27.1	23.4	19.8
MCS (TAOs)	8.5	9.7	7.0	6.4	8.3	7.6	12.9
OSI	0.02	0.01	0.01	0.01	0.00	0.01	0.04
Backbone threshold (m)	21.3	21.3	21.8	21.1	21.1	21.1	21.1
% Backbone	0.10	0.05	0.41	0.32	0.14	0.08	0.12
%BA Backbone	0.35	0.23	0.80	0.66	0.43	0.25	0.38
Backbone density (TAOs ha^{-1})	17	9	69	50	26	14	22
Backbone BA (m^2 ha^{-1})	7.3	3.8	30.9	25.4	11.6	5.8	7.5
MCS (TAOs)	2.3	1.6	2.7	2.1	1.8	1.6	2.0
OSI	0.65	0.64	0.16	0.24	0.34	0.53	0.50

1391 The 6 m distance is intended to represent the crown diameter of an average mature conifer.
1392 TAOs with no neighbors within 6 m were considered to be individual trees. We took the mean
1393 clump size (Plotkin *et al.*, 2002) as our metric of stand-level tree clumping.

1394 We quantified open space following Churchill *et al.* (2013), using the empty space function
1395 *F(t)*. The *F(t)* transform lays a grid over the analysis area – we used a 0.75 m grid to match the
1396 CHM and other rasters – and calculates the distance from each grid cell to the nearest tree stem
1397 location. In this case, we used TAO high points in lieu of tree positions. We calculated an open
1398 space index ranging from 0-1 and indicating what proportion of *F(t)* values are ≥9 m (Churchill
1399 *et al.*, 2013); this represents the amount of stand area in openings large enough to subside most
1400 crown fires, regenerate shade-intolerant species, and dissipate beetle aggregation pheromones
1401 (Churchill *et al.*, 2017).

1402 We set target ranges of variation based on reference data from Jeronimo (Chapter 1). This
1403 reference dataset summarizes stand structure and spatial pattern using TAO metrics for patches

of forest across the Sierra Nevada that have not been logged and have recently had active fire regimes. We selected reference patches within the same climate class as Paradise Flat – Cool Dry High Montane – and reduced the data in the same way to allow for direct comparison.

We delineated the range of possible treatments for each of the seven stands in Paradise Flat by simulating treatments under different prescriptions. For example, for the density vs. basal area panel of the extended density management diagram, we first simulated a strict thinning from below prescription. We deleted the shortest TAO, re-calculated density and basal area, deleted the second shortest TAO, re-calculated, etc., until we were left with only backbone trees. Next, we simulated a strict thinning from above prescription where we removed the largest non-backbone TAO first and worked down until only backbone TAOs remained. Each of these simulations yielded a curve between the current conditions and the backbone tree-only conditions; these curves delineate all possible treatment options for the given stand. We repeated this for mean clump size, simulating the maximum and minimum clumping options, and for the open space index, simulating the most open and least open options.

Lastly, we assessed departure of Paradise Flat stands numerically by comparing values against the distribution of reference data. We performed this comparison on the basis of LMUs, so, for example, ridgetop stands in Paradise Flat were compared to ranges of variation calculated from ridgetop LMUs in the reference dataset. We calculated the 10^{th} and 90^{th} percentile values of TAO density, basal area, mean clump size, and open space index across the reference areas to represent the low and high ends of the reference envelope, respectively. We then compared current conditions of the Paradise Flat stands to the ranges of variation, designating a stand as departed for a given metric if that metric fell outside of the reference envelope and nearly departed if it fell within 10% of the inter-percentile range of the edges of the reference envelope

(Hessburg *et al.*, 2013). For example, if the 10th and 90th percentile reference values for density were 5 and 55, then 10% of the inter-percentile range would be $0.1 \times (55 - 5) = 5$, so any values between 5-10 or 50-55 would be considered nearly departed.

3.3 Project area-level density management diagrams and prescriptions

We first visualized project area-wide departure from reference conditions by plotting current conditions of all seven stands colored by LMU in density-pattern space compared to the reference conditions. After using this view to set overarching goals, we proceeded to select stand-level treatment targets using extended density management diagrams showing the possible treatment space for each stand in the context of all other stands. We set targets for each stand in terms of density, basal area, mean clump size, and open space index according to the four principles given in Section 2.4. To help guide target selection according to principle 2 we colored each stand in the diagrams according to LMU type (ridge, valley, NE slope, or SW slope). According to principle 4, we assigned at least one unit a fire anchor status based on its LMU and geographic position within the project area. We then translated stand-level targets in terms of residual density, tree size, tree clumping, and canopy openings into rough marking guides by calculating differences between target conditions and current conditions. The steps involved with selecting treatment targets and translating these targets into marking guidelines are quite procedural. For clarity, we present them in a workbook style in Boxes 1 and 2.

4. Results

4.1 Current stand conditions

The seven LMU patches in Paradise Flat covering 189 ha had an average TAO density of 169 ha^{-1} (range of stand-level density: 130-190 TAOs ha^{-1}) with 24.5 $m^2\,ha^{-1}$ (11.7-38.5 $m^2\,ha^{-1}$) of

basal area. Mean clump size was 8.3 TAOs and the average open space index was 0.02. Backbone TAOs represented 16% of detected TAOs on average; these constituted 43% of estimated stand-level basal area. Backbone trees had an average mean clump size of 2.0 and an open space value of 0.45 (Table 1).

4.2 Departures from reference conditions

Tree-approximate object density was departed from the upper end of the reference envelope for five out of seven stands; however basal area was within the reference envelope for six out of seven stands (Table 2). The two stands with densities within the reference envelope were both NE slope LMUs. Mean clump size was high for four stands – all ridge and SW slope LMUs – all of which also had high density. Lastly, open space was low for six stands – very low for four of these – some of which simultaneously had departures for high density. The one stand which was not low on open space was a SW slope LMU.

In aggregate, current stand conditions across the project area had high density and moderate basal area compared to reference conditions, with more variability in basal area than in density (Figure 5a). Current clump sizes were clustered near the high end of the reference envelope while open space index values were spread throughout the lower half of the reference envelope (Figure 5b, c).

Ridgetop LMUs (17% of Paradise Flat) carried the lowest basal area followed by SW slopes (5% of area), NE slopes (48% of area), and then valleys (30% of area) (Figure 5a). Spatial patterns showed more mixed trends, with ridges and SW slopes exhibiting both larger clumps and more open space than NE slopes and valleys (Figure 5b, c). Density was not well-differentiated by LMU. Compared to the reference envelope, ridges and SW slopes were more departed than NE slopes and valleys in terms of density, basal area, and clump sizes.

Table 2 Low and high reference envelope values and current departures from reference conditions for the seven stands in the Paradise Flat analysis area. Departure key: -- = below P10 (10th percentile) of observed reference values, - = nearly below P10 of observed reference values, + = nearly above P90 (90th percentile) of observed reference values, ++ = above P90 of observed reference values. See Table 1 legend for definition of abbreviations.

Stand ID		73	74	76	78	79	80	85
Density P10	TPH	45	45	45	78	78	78	54
Density P90	TPH	138	138	138	179	179	179	165
Current Density	TPH	165	188	169	158	188	166	190
Density departure		++	++	++		++		++
BA P10	m^2 ha^{-1}	3.1	3.1	3.1	11.1	11.1	11.1	7.2
BA P90	m^2 ha^{-1}	25.5	25.5	25.5	40.7	40.7	40.7	46.5
Current BA	m^2 ha^{-1}	21.1	16.2	38.5	38.4	27.1	23.4	19.8
BA departure				++	+			
MCS P10	n TAOs	1.4	1.4	1.4	2.4	2.4	2.4	1.8
MCS P90	n TAOs	5.1	5.1	5.1	10.0	10.0	10.0	10.2
Current MCS	n TAOs	8.5	9.7	7.0	6.4	8.3	7.6	12.9
MCS departure		++	++	++				++
OSI P10		0.02	0.02	0.02	0.00	0.00	0.00	0.00
OSI P90		0.28	0.28	0.28	0.26	0.26	0.26	0.24
Current OSI		0.02	0.01	0.01	0.01	0.00	0.01	0.04
OSI departure		--	--	--	-	--	-	

4.3 Stand-level treatment targets

Stand-level targets were set according to current conditions and treatment objectives (Box 1). Target density ranged from 40-120 TAOs ha^{-1} and target basal area ranged from 10-38 m^2 ha^{-1}. These targets represented reductions in density of 38-145 TAOs ha^{-1} and in basal area of 0.4-9.4 m^2 ha^{-1}. Mean clump sizes targets were between 2.1 and 4.9 while open space index targets were between 0.06 and 0.42 (Table 3).

Ridges were prescribed the lowest densities and basal areas (40-55 TAOs ha^{-1} and 10-12 m^2 ha^{-1}, respectively) and NE slopes were prescribed the highest (65-120 TAOs ha^{-1} and 14-38 m^2 ha^{-1}). This corresponded to lower mean clump sizes on ridges and SW slopes (2.1-2.4 TAOs) and higher mean clump sizes in valleys and on NE slopes (2.8-4.9 TAOs). Open space targets were highly variable, mainly according to spatial patterns of backbone TAOs.

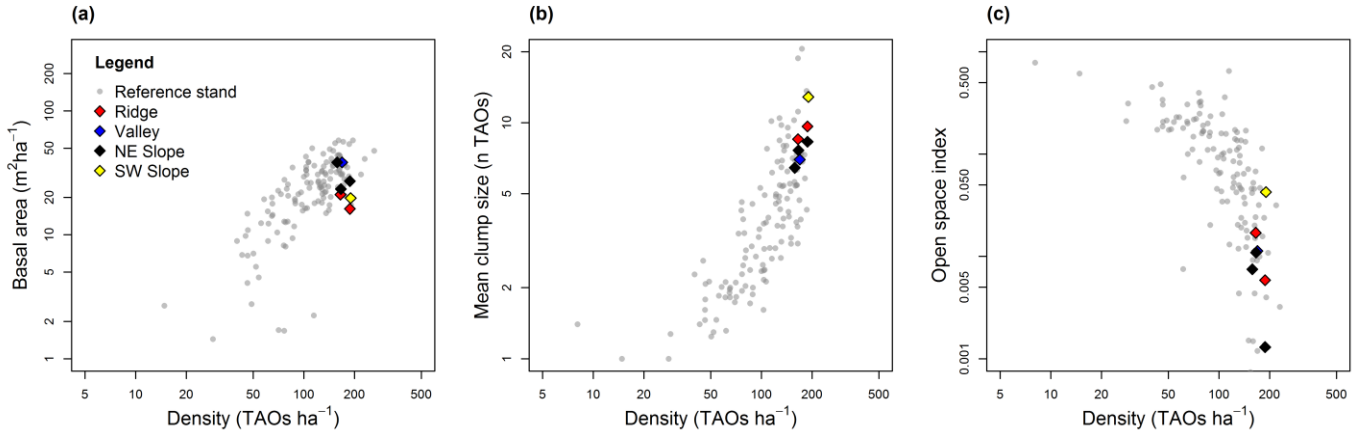

Figure 5 Current conditions for the seven Paradise Flat stands under study compared to reference conditions. Each stand is represented by one point colored according to its topographic position. Ridges and SW slopes are outside of the reference envelope for basal area and mean clump size, while valleys and NE slopes are on the low end of the reference envelope for open space.

5. Discussion

5.1 Departures and prescriptions varying with landform

Departures varied by landform. In particular, drier and more exposed landforms – ridgetops and SW slopes – were more departed from reference conditions, having lower basal area and higher mean clump sizes given their current density (Figure 5, Table 2). Forest change with fire suppression is the result of a complex combination of several concurrent processes including increased recruitment rates, shifts toward shade-tolerant species composition, increased competition due to higher density, and declines in large trees (Lutz *et al.*, 2009; McIntyre *et al.*, 2015; Becker and Lutz, 2016; Levine *et al.*, 2016; Collins *et al.*, 2017; Young *et al.*, 2017). In the coastal and inland Pacific Northwest and in the Southwestern United States, several studies have found that lower productivity sites experience slower growth and thus a lower velocity of departure from reference conditions. For example, Larson *et al.* (2008) described a negative relationship between productivity and structural development rates, Johnston (2017) observed a 1400% increase in moist mixed-conifer forest density for trees ≥15

cm compared to a 216% increase in density on dry pine sites, Rodman *et al.* (2017) found average density increases of 47% in mixed-conifer forests for trees >1.37 m tall compared to 37% for pine forests, and O'Connor *et al.* (2017) found that intermediate productivity sites had higher rates of increasing density for trees ≥1 cm than low productivity sites. In contrast, studies in the Sierra Nevada have found the opposite trend, for example, Stephens *et al.* (2015) found a 78% increase in density in mixed-conifer forests for trees ≥30.4 cm compared to a 331% increase for pine forests and Taylor *et al.* (2014) found three-fold increases in density of trees ≥10 cm for mixed-conifer and red fir forests compared to a five-fold increase for pine forests. Our results align with other studies from the Sierra Nevada, indicating that dry landforms may be a restoration priority in this region because of an enhanced mismatch between contemporary structure and biophysical conditions. The reasons for the disparity between the Sierra Nevada compared to the cooler, moister Pacific Northwest and the hotter, drier Southwest are not apparent. This observation merits further study.

Backbone tree density also varied by landform (Student's *t* test comparing ridges and SW slopes vs. valleys and NE slopes; n = 131 LMUs across LTW Cool Dry High Montane zone; p = 0.011) while overall density did not (p = 0.996). This could be because dry landforms had lower densities during the active fire period before the onset of fire suppression (Lydersen and North,

Table 3 Stand-level treatment targets for the seven stands in the Paradise Flat analysis area. See Table 1 legend for definition of abbreviations.

Stand ID	Density target (TAOs ha^{-1})	BA target (m^2 ha^{-1})	MCS target (n TAOs)	OSI target
73	40	12	2.2	0.42
74	55	10	2.4	0.22
76	75	32	2.8	0.15
78	120	38	4.1	0.04
79	65	20	2.5	0.12
80	100	14	4.9	0.06
85	45	12	2.1	0.27

2012; Rodman *et al.*, 2017), but could additionally be due to differential rates of large-tree decline between contrasting environmental conditions. For instance, Lutz *et al.* (2009) found that proportional density of Jeffrey pine – which dominates both historical and contemporary forest composition in the study area (Taylor *et al.*, 2014) – has decreased more at lower elevations (i.e., warmer/drier habitat) during the 20th century fire suppression period.

There was a strong correlation between basal area and backbone tree density (Pearson's r = 0.94) (Table 1), which, because basal area varied by landform, translated to a disparity in ranges of treatment options between landforms. Stands with a larger difference between current density and backbone density had a wider range of options available (e.g., compare Figure 12 vs. Figure 8), since backbone tree presence effectively constrains treatment options. These constraints applied not just to possible targets for density and basal area, but also for spatial patterns (e.g., Figure 8b, c). This pattern highlights the utility of the extended density management diagram, where the interactions between stand density and spatial patterns can be visualized, enabling realistic treatment targets to be set.

Valleys and NE slopes were often within the reference envelope (Table 2) and were prescribed modest reductions in density (38-123 TAOs ha^{-1}). Because departure of the drier landforms was greater than that of the more mesic landforms, the prescriptions for these stands called for more trees to be removed (125-145 TAOs ha^{-1} for ridges and SW slopes).

5.2 The treatment decision space

Backbone tree populations had lower density and smaller mean clump sizes than reference conditions (Figures 6, 8, 10, 12, 14, 16, 18). If backbone trees are taken to be roughly equivalent to legacy trees, then this may indicate that increases in stand density and stress associated with prolonged fire suppression have led to density-dependent mortality of old trees, altering the

legacy tree pattern to be sparse and regular relative to active-fire reference conditions. This indicates that a radial release thinning approach would not be sufficient to restore spatial patterns to within the reference envelopes (Hood *et al.*, 2017). Instead, some backbone trees would need to be left in clumps together with smaller trees to meet clumping targets. This is not out of the ordinary, since mixed-age tree clumps are commonly observed in reference datasets (Larson and Churchill, 2012 and references therein).

Explicitly prescribing openings is difficult since canopy openings are not straightforward to count or measure (Schneider and Larson, 2017) and, especially in low-density forests, it can be difficult to even distinguish openings from the low-density forest matrix (McGuire *et al.*, 2001; Churchill *et al.*, 2013). Visualizing treatment targets in the context of the range of possible treatment options for the open space index allowed us enough insight into canopy openings in the stands to provide some general marking guidelines (e.g., Box 2). We suggest that the general guidelines can indicate one of the following: (1) backbone trees are very evenly spaced throughout the unit and there is simply not much opportunity for creating open space, (2) there is some opportunity for creating open space if careful, so leave retention clumps in loosely associated patches rather than scattered throughout the stand, (3) there is adequate space in openings so any implementation of clumping targets will probably achieve open space targets, or (4) there is a possibility for the catchment to be too open after harvest, so be sure to retain clumps in a way that breaks up the largest openings. Specific guidelines as to how many openings to create and of what sizes could be given in case (2).

Although we did not analyze the merchantability of wood removed in these hypothetical treatments, it could be possible to separate commercial thinning opportunities from non-commercial treatments based on TAO height-diameter relationships (Popescu *et al.*, 2004).

5.3 Limitations of lidar data

Measurements using lidar individual tree detection were able to provide insight into stand structural conditions relevant to silviculture planning, including density, basal area, and clumping and opening patterns. However, there are several remaining points of uncertainty that cannot yet be fully assessed using only lidar data. These include the inexact equivalency of backbone trees and legacy trees; incomplete knowledge of trees in subordinate canopy positions; lack of knowledge about species composition; and the omission of data about biological hotspots like wetland areas, hardwood clones, or rock outcroppings.

The backbone trees identified in this study were selected with a height threshold that varied by climate and landform. However, restoration treatments are, in practice, anchored around old trees, not just large trees (Van Pelt, 2008; North *et al.*, 2009; Franklin and Johnson, 2012; Franklin *et al.*, 2013; Hessburg *et al.*, 2015). Old trees, even when small, provide several desirable characteristics that large young trees do not, including unique and functionally valuable crown structures (Ishii and McDowell, 2002; Van Pelt and Sillett, 2008; Kramer *et al.*, 2014; Kramer *et al.*, 2018; Sillett *et al.*, 2018), lower sapwood-to-heartwood ratios (Sillett *et al.*, 2015) and correspondingly higher water use efficiency (Moore *et al.*, 2004), lower mortality rates (Lutz and Halpern, 2006; Larson *et al.*, 2015; Das *et al.*, 2016), higher fire resistance (Agee and Skinner, 2005; Taylor, 2010), and a higher number of high-quality habitat-providing cavities (Lindenmayer *et al.*, 2012) as well as snags and logs composed of more durable wood (Sillett *et al.*, 2018). In light of this, it is always important to distinguish between old trees and large trees; correspondingly, age class characteristics should be included in forest inventory.

The inability to fully characterize subordinate trees and other understory vegetation is a consistent issue in lidar application (Martinuzzi *et al.*, 2009; Richardson and Moskal, 2011; but

see Wing *et al.*, 2012). This issue is more pronounced in areas where high canopy cover in large trees obscures lidar's view of understory structure (Falkowski *et al.*, 2008; Jeronimo, 2015; Jeronimo *et al.*, 2018). This is not a major issue when it comes to defining the desired structural conditions since those conditions are driven by the larger trees in the stand; however, it is an issue in terms of assessing economic viability of the restoration treatments at both unit and project area scales. Lidar's inability to characterize the shrub layer in detail is also problematic for assessing pre- and post-treatment habitat value, since shrubs are important dietary components for many vertebrate wildlife species (Lutz *et al.*, 2014; Lutz *et al.*, 2017).

Species composition is a major element of forest restoration that has not been accounted for in this work. Fire-suppressed mixed-conifer forests have shifted from historical dominance by fire-tolerant *Pinus* spp. and old individuals of other genera to contemporary dominance by fire-intolerant young *Abies* spp. and *Calocedrus decurrens* (Collins *et al.*, 2011; Barth *et al.*, 2015; Stephens *et al.*, 2015; Becker and Lutz, 2016; Collins *et al.*, 2017). Although some work has been done using lidar to differentiate species based on crown morphology (Brandtberg, 2007; Heinzel and Koch, 2011) the results have not been particularly strong and, more importantly, there is little prospect of successfully identifying species of trees in subordinate canopy positions using this type of approach.

Lastly, forest restoration typically includes the goal of maintaining unique micro-environments that may occur across a landscape. Examples of these include aspen clones, moist swales supporting different vegetation than the surrounding matrix, rock outcrops and other areas of unique geologic or pedologic significance, and patches of snags or decadent wildlife trees (Franklin *et al.*, 2013; Hessburg *et al.*, 2015). There also may be forest health issues to address, such as pockets of infection by root rots, mistletoe, or insect activity. There is evidence that some

of these micro-environments can be detected with lidar (Wing *et al.*, 2015; Barbosa *et al.*, 2016), but no such methods have yet been operationalized over watershed or larger scales.

Filling these data gaps and developing a prescriptions would require additional fieldwork. In particular, the actual density and stocking of legacy trees (as compared to backbone trees) should be evaluated to verify the appropriateness of the recommended treatments. Some inventory or cruise data must be gathered to estimate the volume and grade of material to be removed, as well as to ensure that there are enough non-legacy trees of desirable species to meet the prescribed residual density and clumping targets. Each unit should be evaluated to determine specific non-commercial treatments of understory trees and fine fuels and estimate costs associated with these treatments. Lastly, it is important to identify locations for retention patches focused on different biological hotspots along with areas to focus on improvement of forest health.

5.4 Comparison to the traditional approach

For forest restoration projects carried out to date, planning activities have been approached using the tools of traditional forestry. This includes delineating stands using aerial photos and ground truth surveys, timber and resource inventories on a grid of plots, a silvicultural assessment based on field surveys, and presale layout (e.g., USDA, 2008, 2013). The methods applied in this study augment the traditional approach. Using TAOs to estimate certain attributes of forest structure and spatial pattern, as well as to visualize patterns and potential treatment options, provides an additional level of knowledge before groundwork for a project even begins. The traditional steps of stand delineation, timber inventory, silvicultural assessment, and layout can all be made more efficient and effective using TAOs. For stand delineation, densities and clump/opening patterns of backbone trees could be taken into account along with aerial photos in order to better define units with homogeneous prescriptions. Timber inventory designs can be

guided by pre-existing knowledge of forest structure, for example: sampling effort in different stands can be scaled proportionally to structural variability; sampling can potentially be foregone or modified in homogeneous patches of pre-forest or non-commercial trees; and specific locations of rare and unique features – which may be missed in a gridded inventory – can be identified and visited. As demonstrated in this report, the structural data provided by TAOs can be used to outline much of a prescription for each treatment unit, leaving only a few details to be filled in using ground observations and inventory data. Finally, layout can be improved using TAO maps to pre-identify locations for openings and potentially skips, which can also inform placement of landings and yarding corridors.

Along with supplementing traditional approaches, the methods in this study make a new level of sophistication available to silviculturists and other restoration planners. Since lidar data can provide total coverage of project areas and their surrounding landscapes, lidar tools enable analyses that are not otherwise possible. For example, inventory plots are not large enough to capture patterns of tree clumps and openings, since these patterns are structured at a scale of 0.5-5 hectares (North *et al.*, 2007; Churchill *et al.*, 2013; Lutz, 2015; Lutz *et al.*, 2018a). The extensive coverage of lidar data allows for spatially explicit assessment of clump and opening pattern that would not otherwise be feasible.

5.5 Next steps for incorporating lidar into silviculture planning

The methods applied in this study could be built upon to improve accuracy of legacy tree detection, incorporate new remote sensing technologies for identifying tree species, and relate density of TAOs to density of trees.

Legacy tree detection could be improved by including a tree age or age class estimate in the timber inventory so that a better basis is available for modeling legacy status. Another

improvement could come from using tree height, crown size, and crown shape (which can be measured from TAOs) together in a logistic regression model to predict legacy tree status. This approach would make more complete use of the available TAO measurements.

There are several technologies that are beginning to be leveraged for resolving individual tree identity to the genus or species level, including geographically co-registered lidar and high-resolution hyperspectral orthophotos, full-waveform lidar, and multi-spectral lidar. Alonzo *et al.* (2014) demonstrated using hyperspectral data to identify 29 species of street trees in Santa Barbara, CA with better than 80% accuracy, and Hovi *et al.* (2016) identified three boreal conifer and hardwood species in Hyytiälä, Finland also with better than 80% accuracy. Budei *et al.* (2018) performed a similar study using multi-spectral lidar in Toronto, Ontario, Canada and identified 10 species with 75% accuracy. However, these methods have not yet been operationalized because (1) they require extensive parameter tuning to achieve high accuracy and (2) the data are not widely collected and, in some cases, the sensors are not widely available.

The comparisons made in this study between TAO metrics in the LTW project area and TAO metrics for reference areas across the Sierra Nevada are fair comparisons of structural departure, since TAO measurements are consistent across the range of conditions present in the Sierra Nevada mixed-conifer zone (Jeronimo *et al.*, 2018). However, the treatment targets given here in terms of TAOs may be difficult to translate into actual prescriptions, since silviculture operates on the basis of trees, not TAOs. Measurements of basal area and open space should not be very sensitive to omission of small trees, but density and mean clump size usually will be. The disparity between prescribed residual tree density versus TAO density has not been studied, but it is conceivable that it is not significant since most restoration treatments aim to remove fuel ladders, which logically should be roughly equivalent to lidar-omitted trees. However,

quantifying these relationships is a necessary next step in incorporating lidar tree detection into silviculture planning.

The methods introduced in this study could be built upon to become a valuable tool for gaining public support for forest restoration projects. Implementation of restoration on public lands in the United States has often been slower than desired or necessary to meet management objectives before ecosystems reach tipping points and experience profound changes (North *et al.*, 2012; Adams, 2013; North *et al.*, 2015; Trumbore *et al.*, 2015), and social acceptance, support, and advocacy for restoration projects are major dynamics that affect project success (Long, 2009; Franklin *et al.*, 2014; Urgenson *et al.*, 2017). Providing renderings of treatments has been shown to be an effective way to increase public support for ecosystem management (Sheppard, 2005). The methods introduced here could provide the foundation for a treatment simulation tool allowing visualization of a range of potential treatment options that are simultaneously possible and restorative, and these options could be visualized at multiple scales with real structural data.

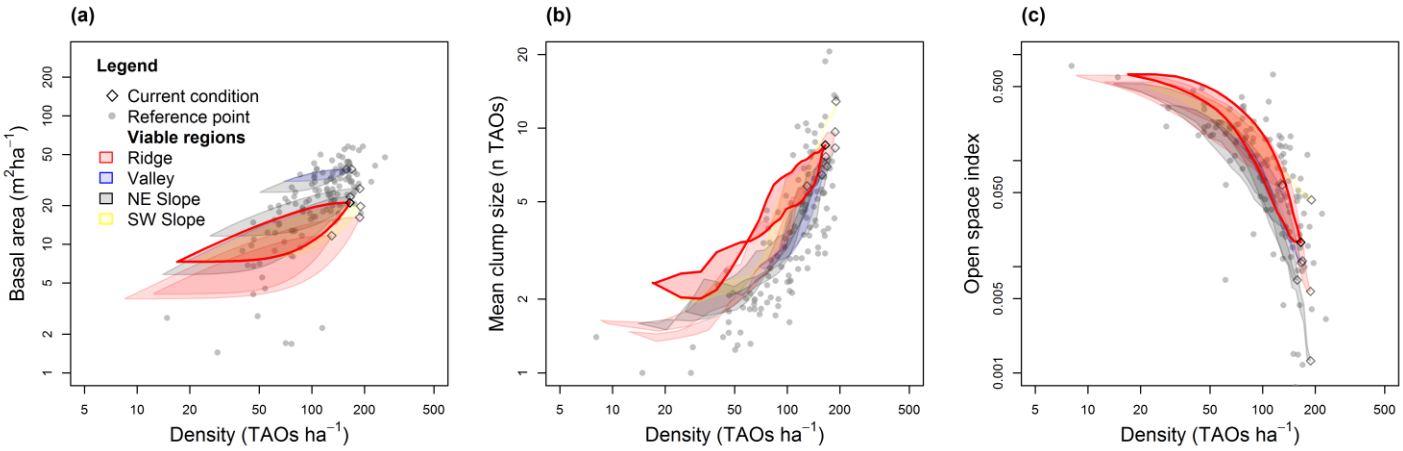

Figure 6 Extended density management diagram for Paradise Flat, highlighting stand 73. In this stand, density is higher than the reference range of variation, basal area is within the range, mean clump sizes is high, and open space is low.

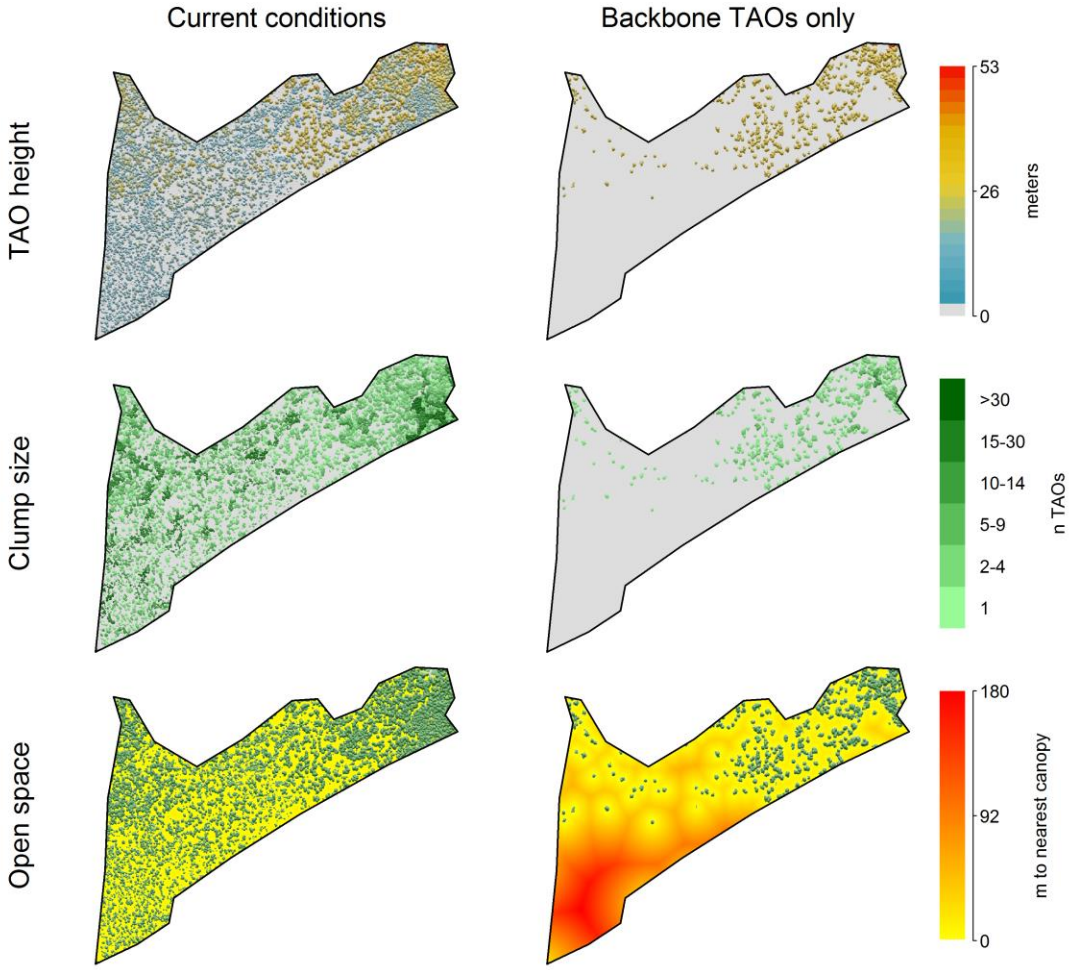

Figure 7 Maps of the 26.5 ha ridgetop stand 73 showing pertinent lidar data products describing current stand structure and pattern, as well as potential structure and pattern if all trees were removed except the backbone trees. The backbone tree height threshold for this stand is 21.3 m and 10% of TAOs are backbone trees.

1689

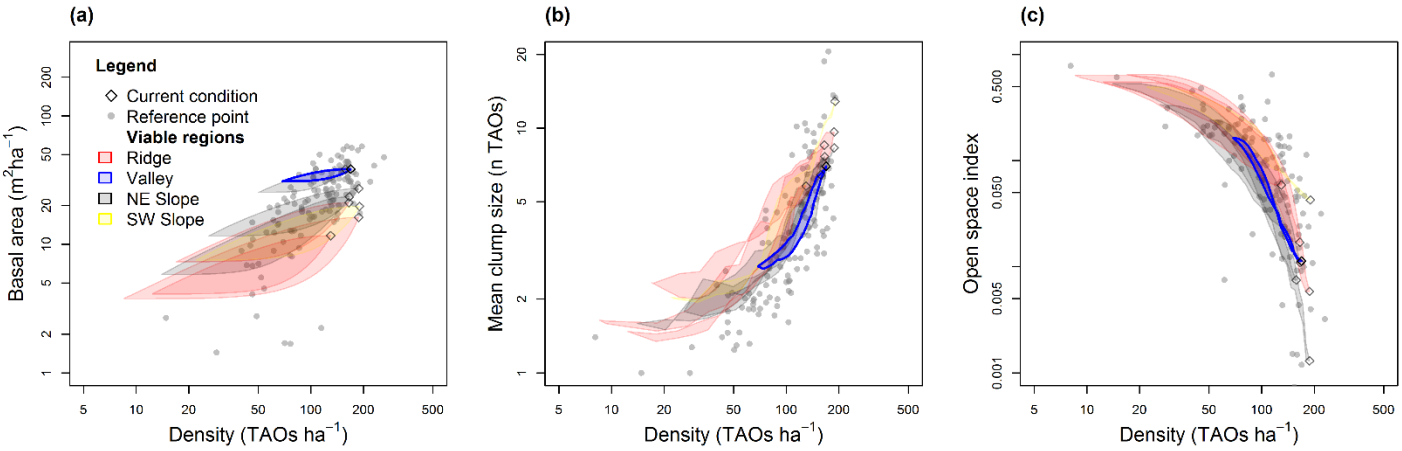

Figure 8 Extended density management diagram for Paradise Flat, highlighting stand 76. In this stand, density is higher than the reference range of variation, basal area is high, mean clump size is high, and open space is low.

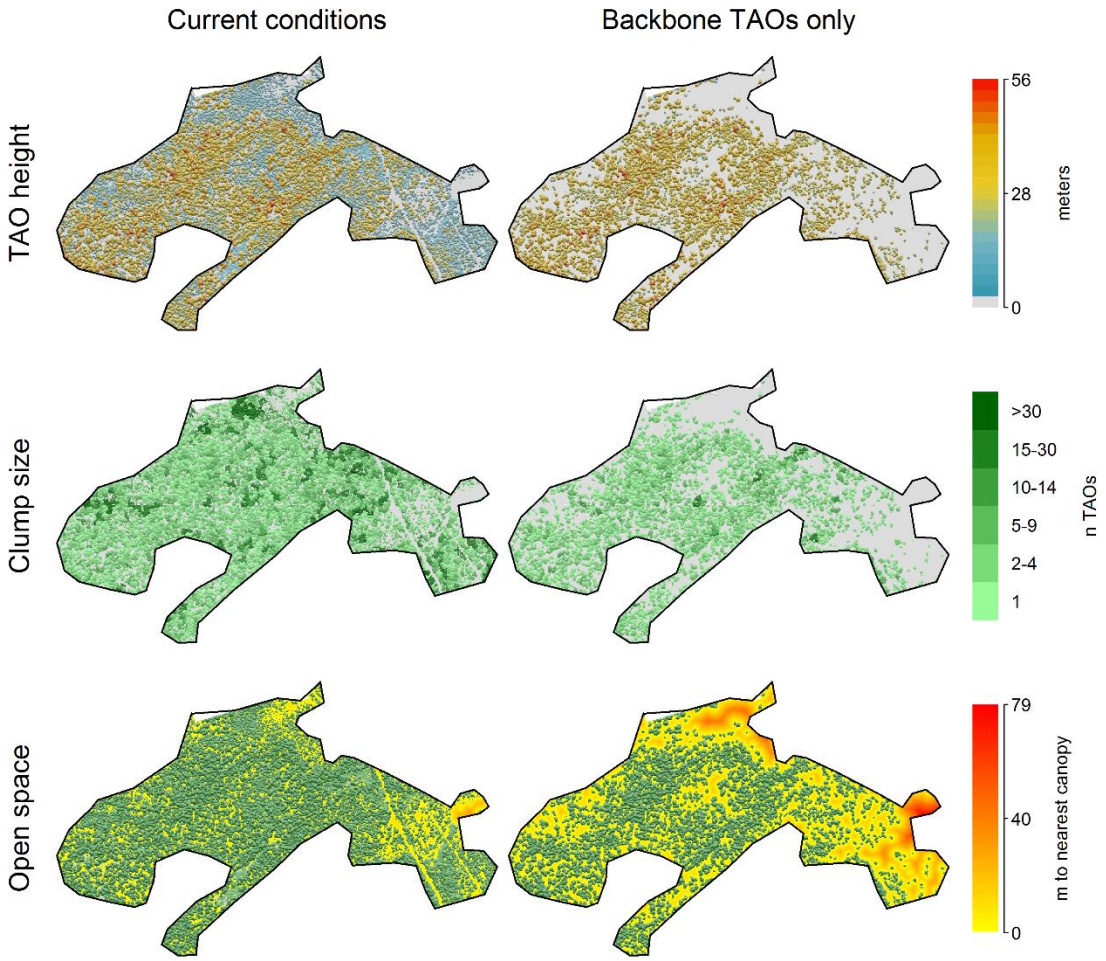

Figure 9 Maps of the 57.5 ha valley stand 76 showing pertinent lidar data products describing current stand structure and pattern, as well as potential structure and pattern if all trees were removed except the backbone trees. The backbone tree height threshold for this stand is 21.8 m and 41% of TAOs are backbone trees.

1690

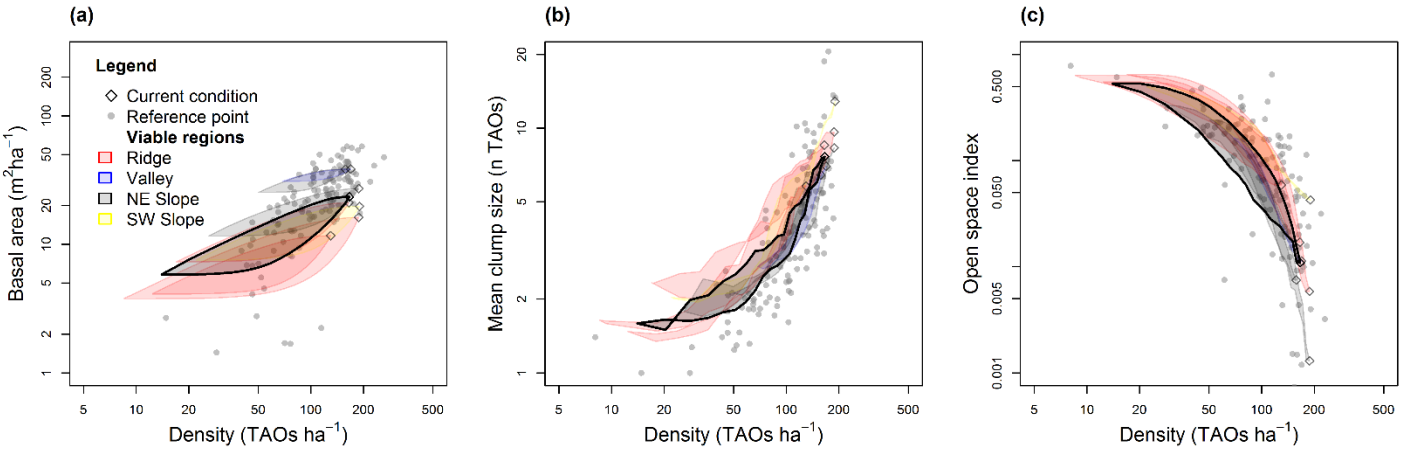

Figure 10 Extended density management diagram for Paradise Flat, highlighting stand 80. In this stand, density, basal area, mean clump size, and open space are all within the range of variation; open space is on the low end of the range.

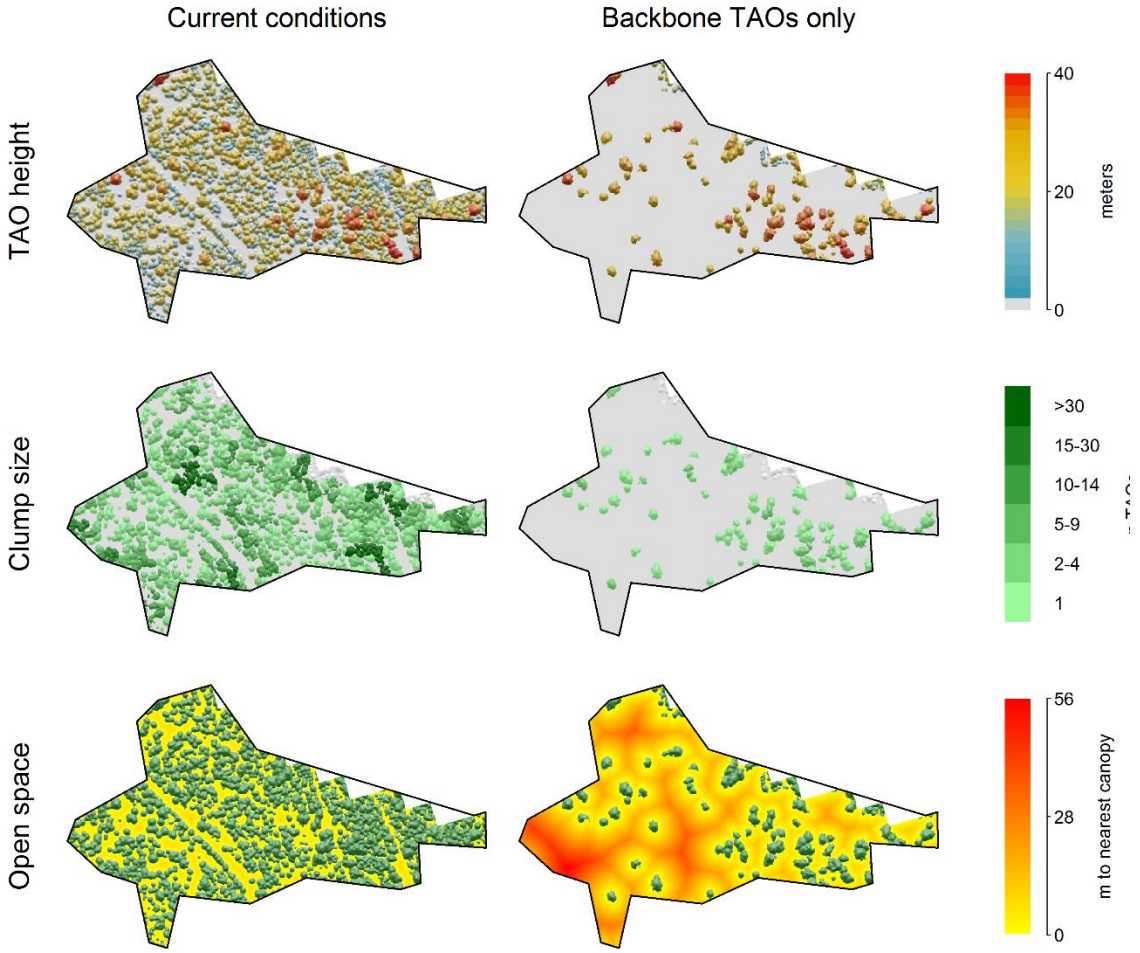

Figure 11 Maps of the 7.7 ha NE slope stand 80 showing pertinent lidar data products describing current stand structure and pattern, as well as potential structure and pattern if all trees were removed except the backbone trees. The backbone tree height threshold for this stand is 21.1 m and 8% of TAOs are backbone trees.

1691

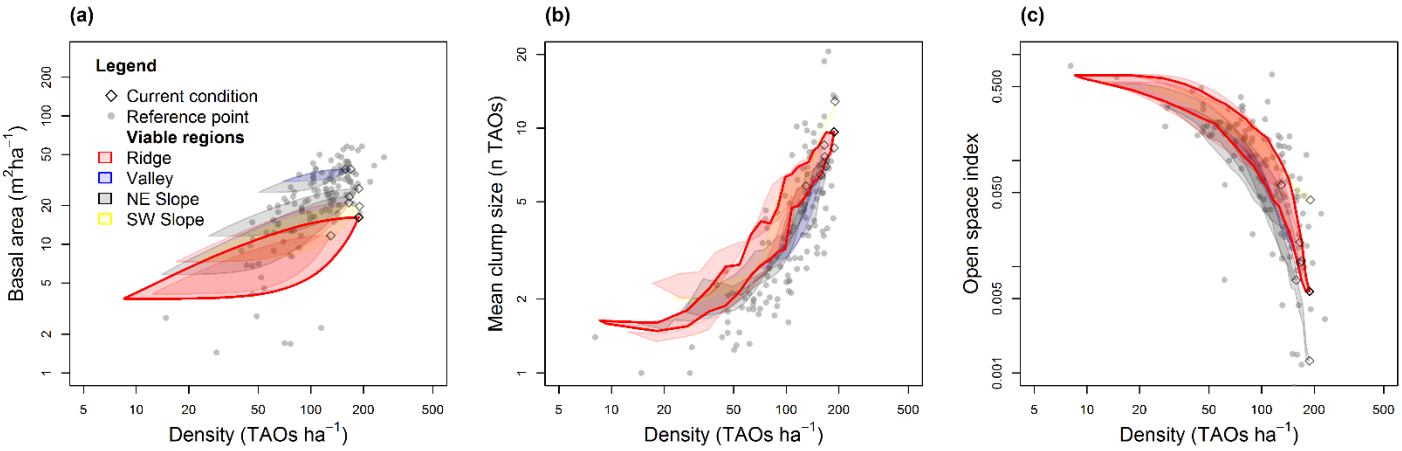

Figure 12 Extended density management diagram for Paradise Flat, highlighting stand 74. In this stand, density is higher than the reference range of variation, basal area is within the range, mean clump size is high, and open space is low.

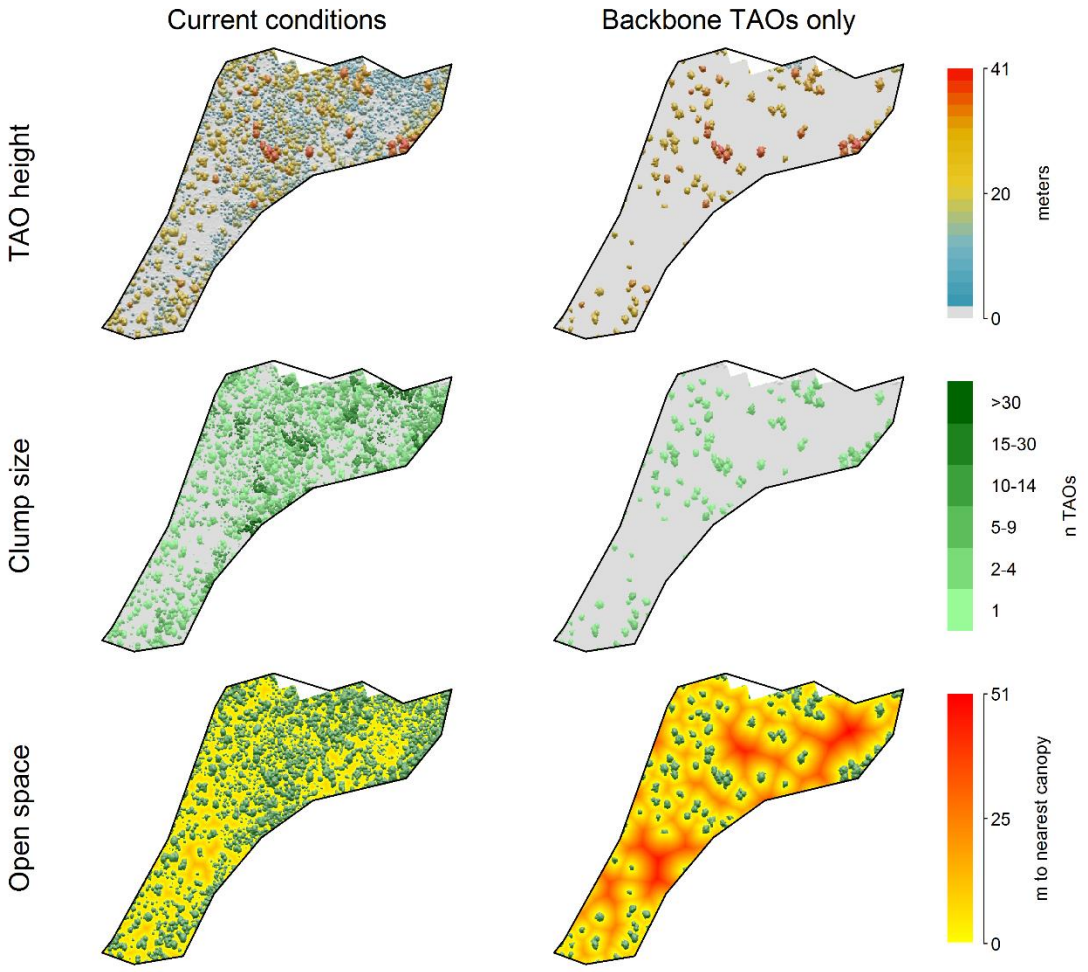

Figure 13 Maps of the 5.5 ha ridgetop stand 74 showing pertinent lidar data products describing current stand structure and pattern, as well as potential structure and pattern if all trees were removed except the backbone trees. The backbone tree height threshold for this stand is 21.3 m and 5% of TAOs are backbone trees.

1692

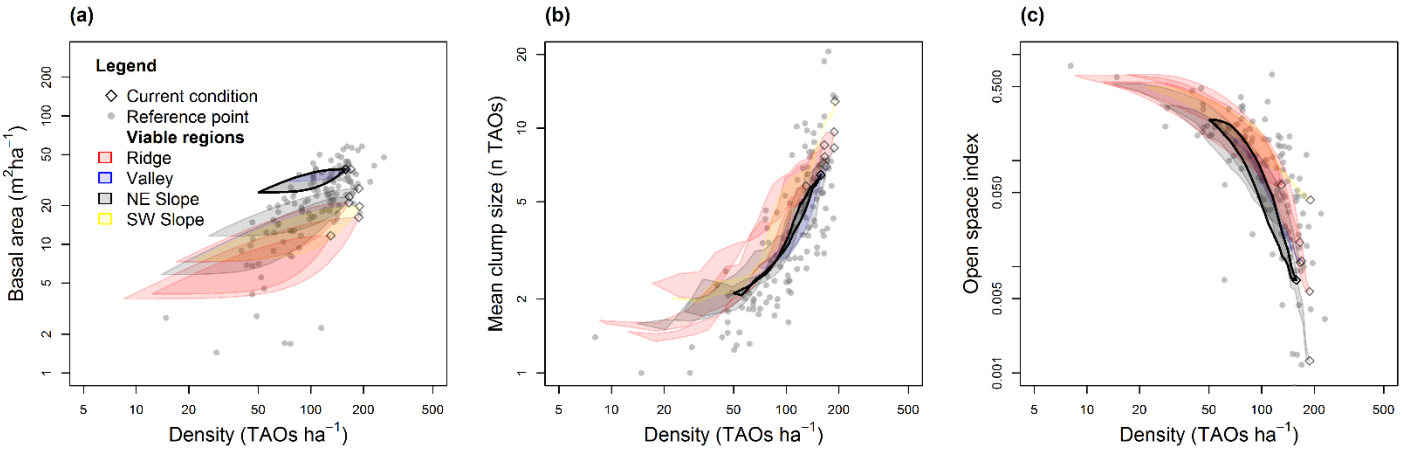

Figure 14 Extended density management diagram for Paradise Flat, highlighting stand 78. In this stand density and mean clump size are within the range of variation, basal area is within on the high end, and open space is within on the low end.

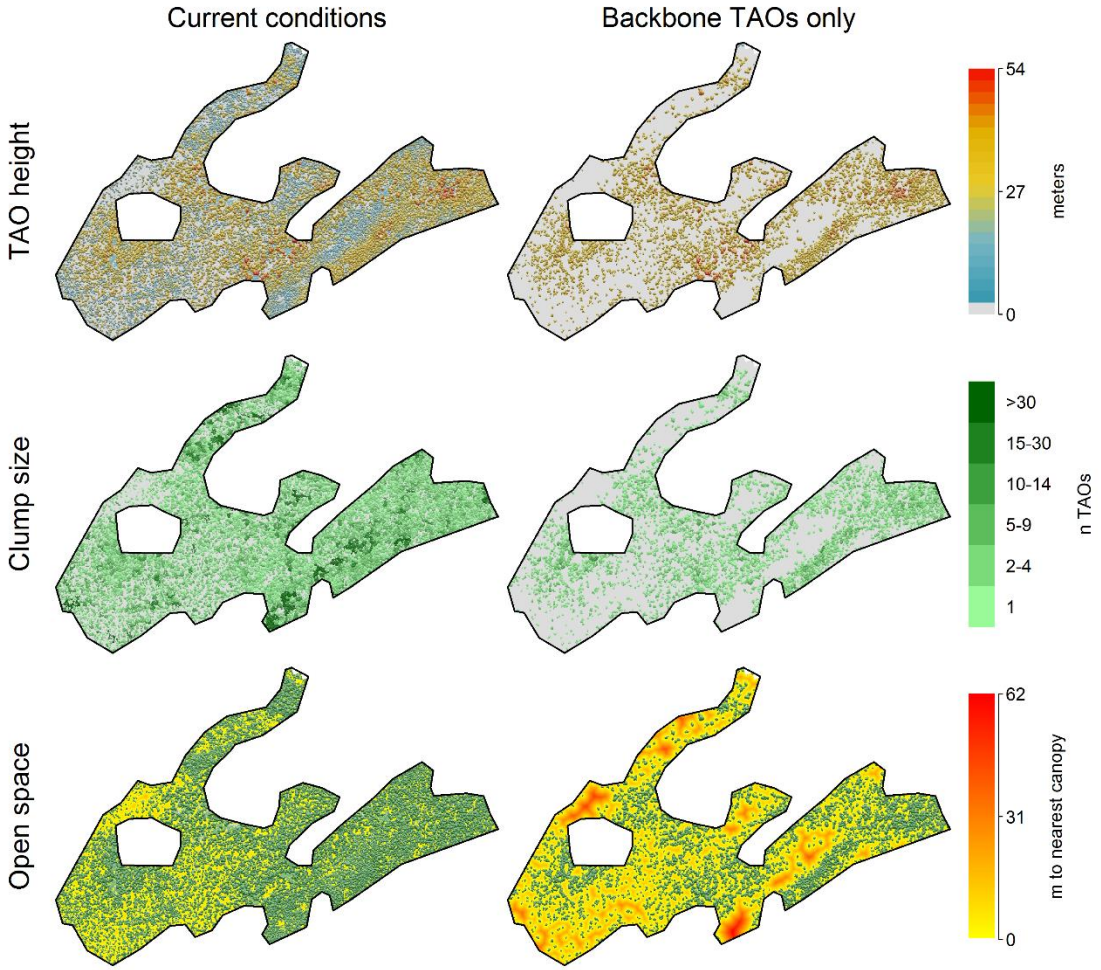

Figure 15 Maps of the 76.2 ha NE slope stand 78 showing pertinent lidar data products describing current stand structure and pattern, as well as potential structure and pattern if all trees were removed except the backbone trees. The backbone tree height threshold for this stand is 21.1 m and 32% of TAOs are backbone trees.

1693

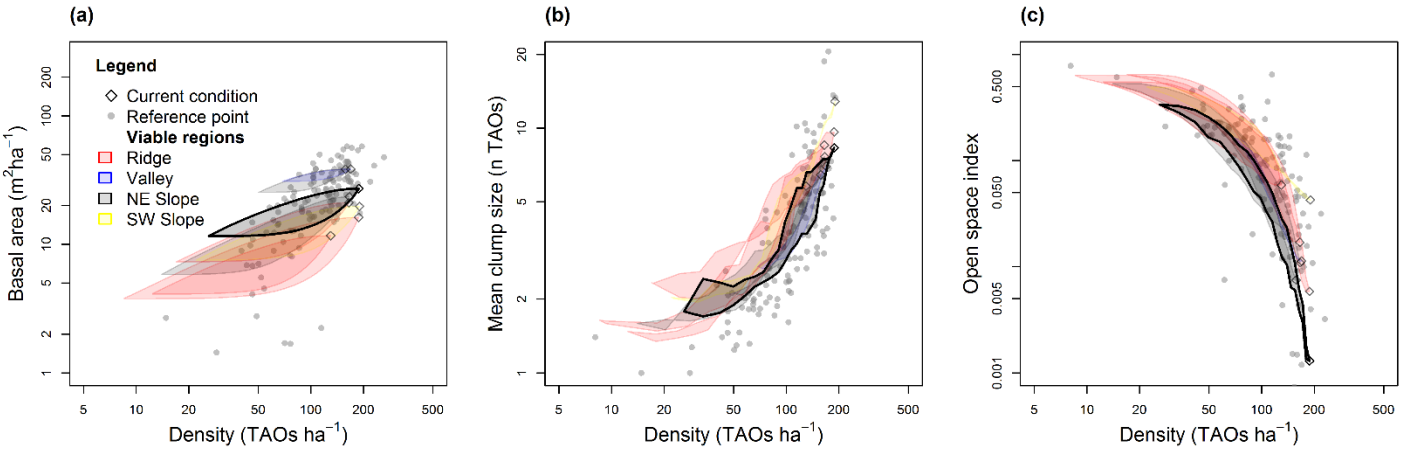

Figure 16 Extended density management diagram for Paradise Flat, highlighting stand 79. In this stand density is above the reference range of variation, basal area and mean clump size are within the range, and open space is low.

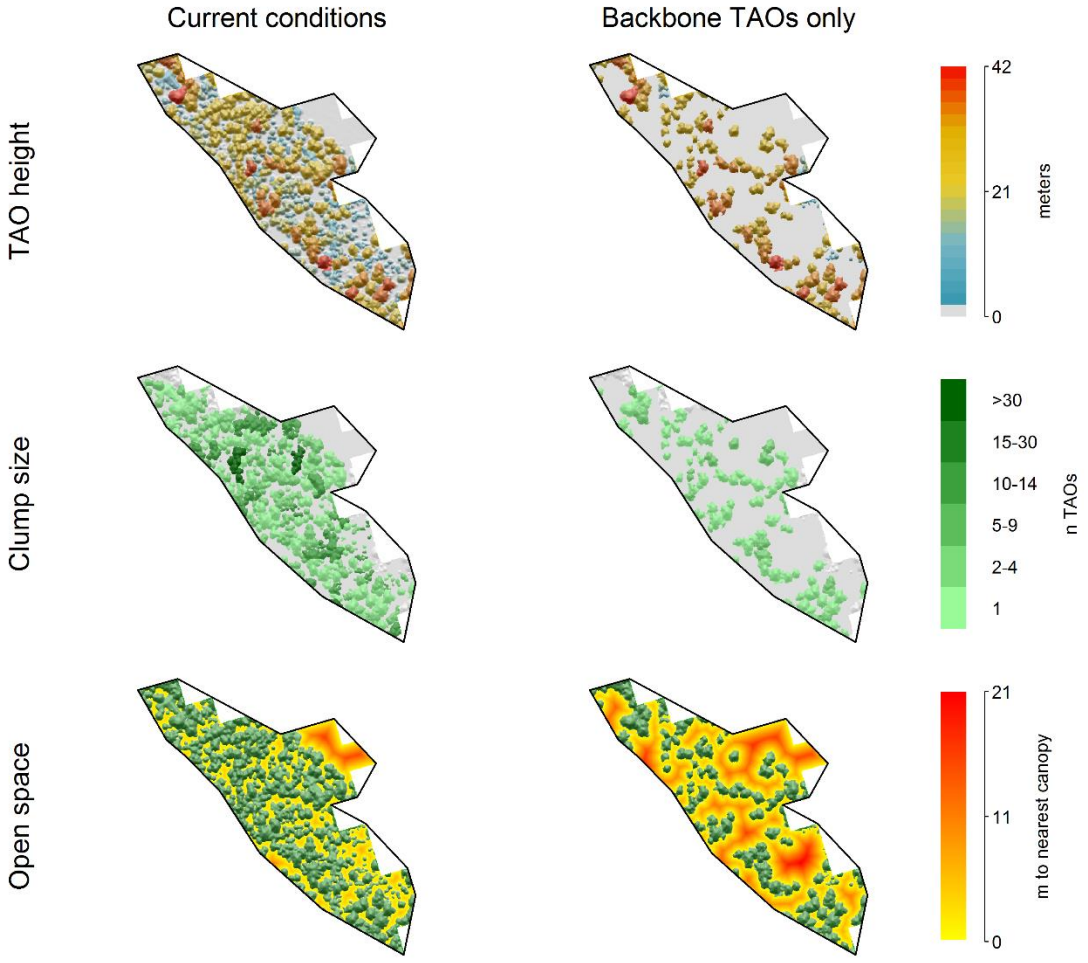

Figure 17 Maps of the 5.9 ha NE slope stand 79 showing pertinent lidar data products describing current stand structure and pattern, as well as potential structure and pattern if all trees were removed except the backbone trees. The backbone tree height threshold for this stand is 21.1 m and 14% of TAOs are backbone trees.

1694

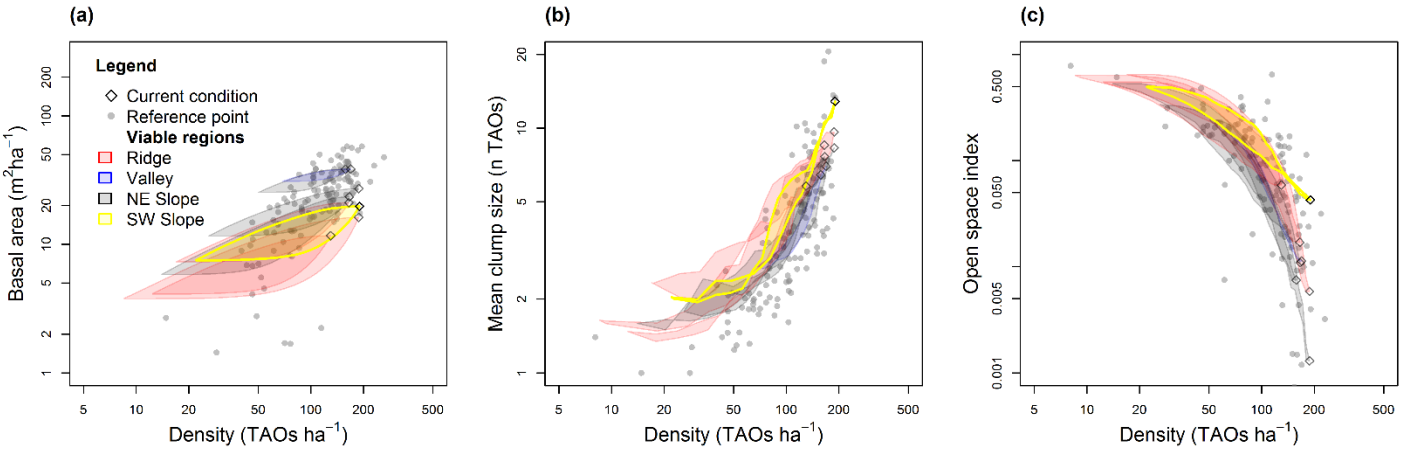

Figure 18 Extended density management diagram for Paradise Flat, highlighting stand 85. In this stand density and mean clump size are above the reference range of variation and basal area and open space are within the range.

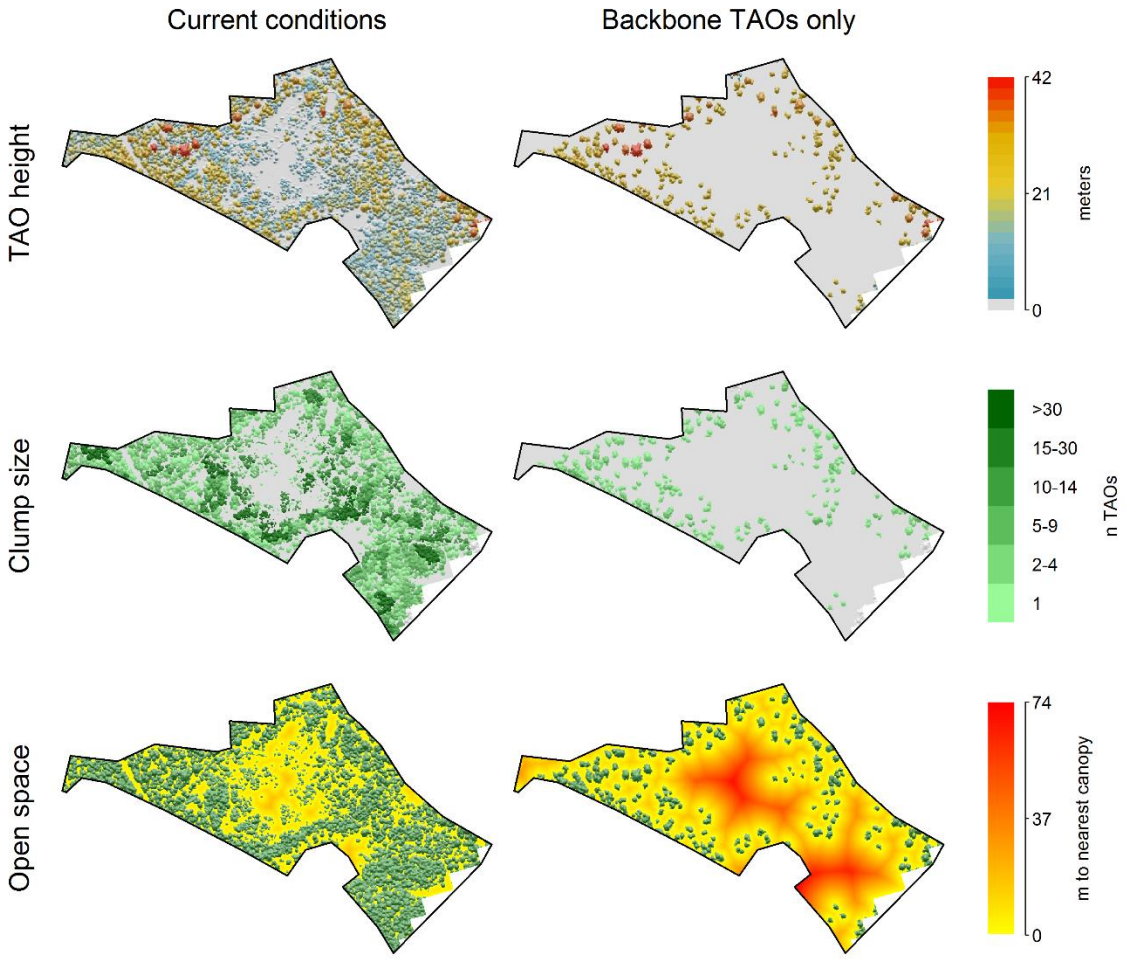

Figure 19 Maps of the 9.3 ha SW slope stand 85 showing pertinent lidar data products describing current stand structure and pattern, as well as potential structure and pattern if all trees were removed except the backbone trees. The backbone tree height threshold for this stand is 21.1 m and 12% of TAOs are backbone trees.

1695

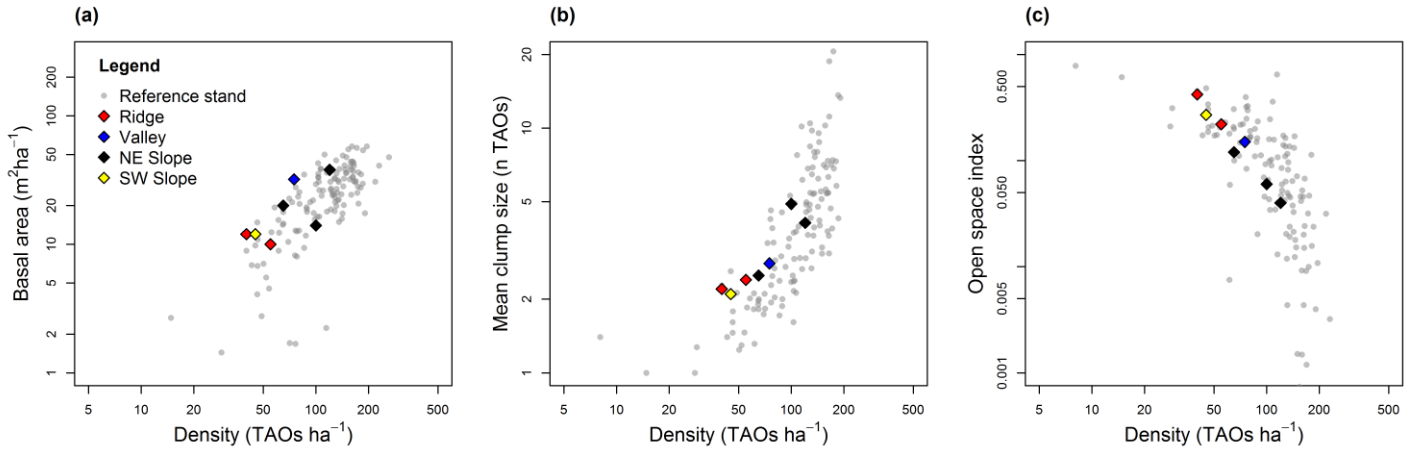

Figure 20 Hypothetical post-treatment conditions for the seven Paradise Flat stands under study compared to reference conditions. Each stand is represented by one point colored according to its topographic position. Compared to Figure 5, all stands have moved to within the reference envelope. The stands are distributed throughout the reference envelope and located within the density-pattern space according to physiography, with lower density, smaller clumps, and more open space on warm, dry sites and higher density, larger clumps, and less open space on more mesic sites.

1696

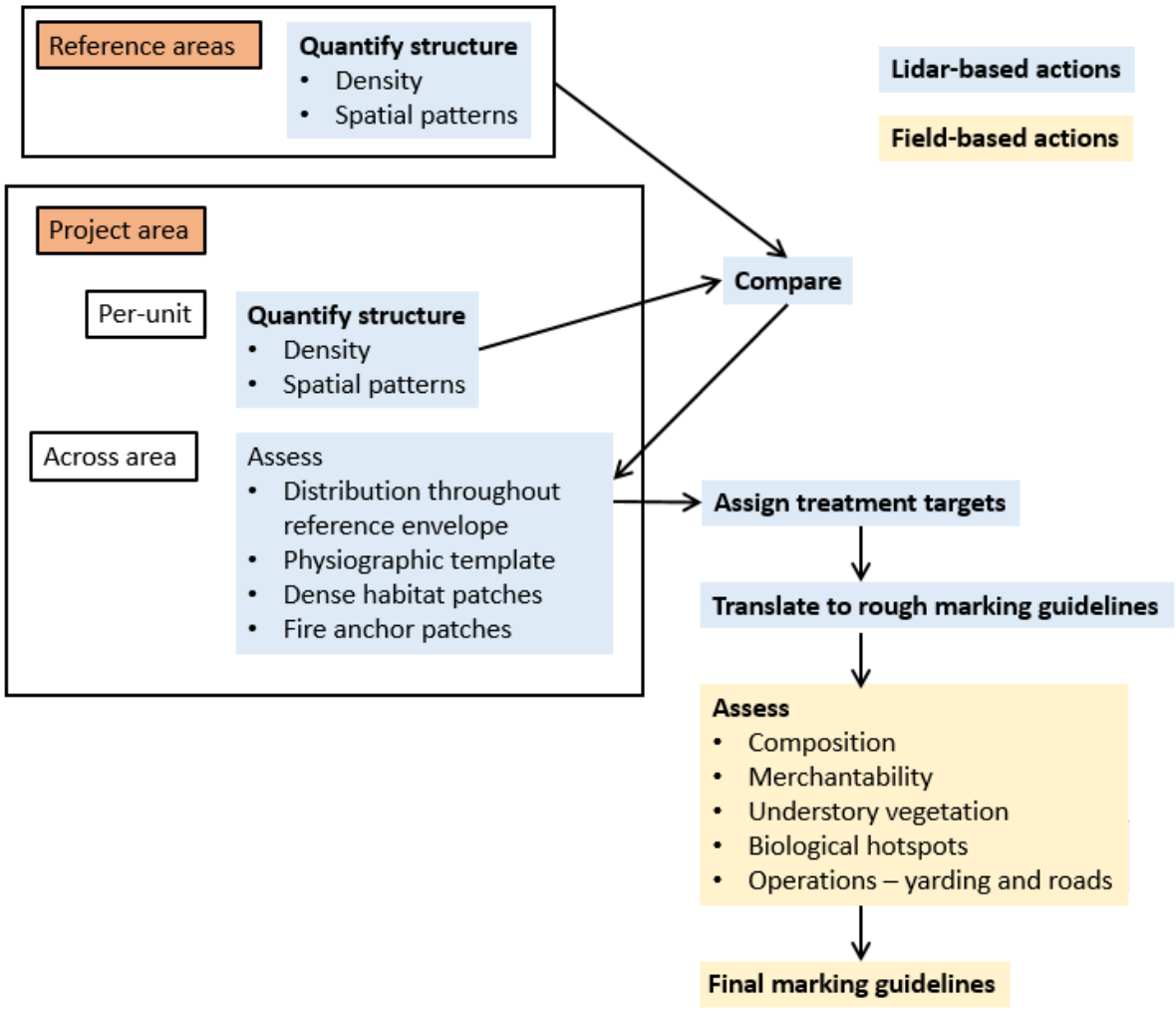

Figure 21 Flowchart describing the steps involved in comparing reference conditions to current conditions in restoration project areas and translating comparisons to marking guidelines.

1697

Box 1 Selecting stand-level targets given current conditions, reference conditions, and project area-level context

The lidar TAO departure analysis we have described provides an array of useful metrics and visualization techniques for assessing forest landscape structure relative to reference conditions. However, integrating these data to make specific decisions about stand-level treatment targets is not an algorithmic process; instead, the various lines of quantitative evidence must be brought together with other knowledge about the site and considered with some silvicultural expertise. Here we walk through an example of selecting stand-level targets for the seven stands in the Paradise Flat catchment. We suppose that objectives for treatment of this project area are to reduce fuels while maintaining forest structure and pattern that is characteristic of active-fire areas in the same climate zone.

We stress that the targets we decide on here are only one of many possible effective configurations. Our goal is not to provide the ultimate analysis of the Paradise Flat area, rather it is to demonstrating the utility of our TAO departure analysis results in the context of silviculture planning.

We begin by observing the basic patterns of departure from reference conditions (Sections 4.2, 5.1, Table 2, Figure 5). From this, we decide on some specific goals by LMU:

	LMU(s)	Observed departure	Treatment goals
1	Ridges, SW slopes	Most departed in terms of high density, misalignment of structure and biophysical template	Reduce density to lower 50% of reference envelope
2	Valleys, NE slopes	Density, basal area on high end or slightly above reference ranges of variation	Reduce density by 20-40%
3	Ridges, Valleys, SW slopes	Mean clump size 26-89% above reference range of variation	Reduce mean clump sizes to within reference envelope
4	All	Open space below or on low end of reference range for all stands	Increase amount of open space as much as possible given density and clump size targets

Next, we decide which stand will be our fire anchor unit (see Section 2.4). We select stand 76, since this stand strategically buffers the upland/wilderness areas from the state highway and wildland-urban interface stands (79, 80, and 85) (Figure 4). It may often be preferable to select a more warm/dry LMU to serve as a fire anchor, but in this case we choose strategic placement over the biophysical template.

With this in mind, we begin looking at maps and density management diagrams for individual units. We start with stand 73 (Figures 6, 7). According to treatment goal 1, we set the density target near the lower end of the intersection of the reference envelope and the range of possible densities: 40 TAOs ha^{-1}. The basal area of stand 73 is not higher than the reference envelope, so we choose to thin from below to maintain the largest trees. The thin-from-below line (upper boundary of the possible region, Figure 6a) indicates that 40 TAOS ha^{-1} is associated with a basal area of 12 m^2 ha^{-1}. Possible mean clump sizes at 40 TAOs ha^{-1} range from 2.2 to 3.1 TAOs (Figure 6b); we select 2.2 to stay within the reference envelope at the given density (treatment goal 3). Possible open space index values range from 0.42 to 0.56 (Figure 6c); we choose the highest possible value, 0.56, in accordance with treatment goal 4.

Next we jump to stand 76 (Figures 8, 9). This stand is our fire anchor stand, and so treatment will focus more on reducing density and fuel connectivity than on creating spatial patterns. Fortunately, since 41% of the TAOs are backbone trees – and since backbone trees tend to retain legacy spatial heterogeneity – nearly any treatment that retains all backbone trees will land within the spatial pattern envelopes (Figure 8b, c). We set the density target for this stand at 75 TAOs ha^{-1}, retaining just 6 non-backbone TAOs ha^{-1}. We choose to thin from below to reduce ladder fuels as much as possible. Thinning from below, 75 TAOs ha^{-1} corresponds to 32 m^2 ha^{-1} of basal area (Figure 8a). Spatial pattern options are limited due to high backbone density: target

mean clump size is set at 2.8 TAOs and target open space index is set at 0.15 (Figure 8b, c). These targets may seem to have high density and low open space for a fire anchor unit; however, 91% of TAOs and 97% of basal area will be represented by backbone TAOs, which should represent the largest, most fire-tolerant trees.

Next we will look at stand 80 (Figures 10, 11). According to treatment goal 2, we choose to reduce density to 100 TAOs ha^{-1}, a 24% reduction. Because the thin-from-above and thin-from-below lines for basal area are both within the reference envelope at 100 TAOs ha^{-1} (Table 2, Figure 10) we have more options in setting a basal area target than for previous stands. We choose to generally thin from below but allow for removal of some larger trees, since – although we are not performing an economic analysis – this is an opportunity to recuperate costs incurred on other parts of the project area. Correspondingly, we set a target of 14 m^2 ha^{-1} of basal area. At the target density options for mean clump size are between 4.2 and 4.9 TAOs and options for open space index are between 0.03 and 0.07 (Figure 10). We set targets at 4.9 TAOs for mean clump size, since we are not trying to reduce clump sizes on NE slopes, and 0.07 for open space (treatment goal 4).

We set targets for the remaining units following similar logic and relying on the guidelines from Section 2.4 (Figures 12-19). The results are given in Table 3 and a hypothetical post-treatment diagram is shown in Figure 20.

Box 2 Working from stand-level average targets to prescription outlines

Once a treatment unit is assigned a specific target in terms of residual density, tree size, tree clumping, and canopy openings, a rough marking guide can be developed by comparing targets to current conditions. We will walk through the steps using stand 85.

Stand data	
Size (ha)	9.3
Backbone density (TAOs ha^{-1})	22.1
Backbone basal area (m^2 ha^{-1})	7.5
Non-backbone density (TAOs ha^{-1})	167.8
Target density (TAOs ha^{-1})	45
Target basal area (m^2 ha^{-1})	12
Target mean clump size (n TAOs)	2.1
Target open space index	0.27

1. Calculate non-backbone retention density

Since backbone trees are detected by lidar with a high accuracy, counts of backbone TAOs can be directly interpreted in terms of density. Subtracting backbone tree density from target density for each stand gives the target number of non-backbone trees to retain: $45 - 22.1 = 22.9$. This provides the first marking guideline:

- Retain all old trees, plus 22.9 younger trees per hectare

2. Figure clumping targets

To define targets for spatial patterns, we follow the individuals, clumps, and openings approach (ICO, Churchill *et al.*, 2013). In this method a number of clump size bins are defined and each bin is allocated a certain share of the residual density. We translate the target mean clump sizes as defined in section 2.3 to ICO clump bin proportions using the empirical relationships between these quantities observed in the reference condition dataset (Supplementary Table 1):

MCS: 2.1	Clump size (n TAOs)					
	1	2-4	5-9	10-14	15-30	>30
Proportion of TAOs	0.49	0	0.08	0.02	0.41	0

As with density, the non-backbone retention is assessed by subtracting clumping proportions for backbone TAOs from the target proportions:

Backbone proportions	0.68	0	0.05	0	0.27	0
Target Δ (prop. of TAOs)	-0.19	0	0.03	0.02	0.14	0

Multiplying the target non-backbone retention density by these proportions yields the target number of TAOs per hectare to add in each clump size bin:

Target Δ (TAOs ha^{-1})	-4.4	0	0.7	0.5	3.2	0

Dividing this by the midpoint of each bin yields the number of clumps per hectare to retain in each bin:

Target Δ (clumps ha^{-1})	-4.4	0	0.1	0.04	0.15	0

Negative numbers for clump targets indicate that numbers in a given bin should be reduced. This can be achieved by either breaking a clump into two or more smaller clumps or by leaving a non-backbone tree to link clumps together, bringing both into a larger size class.

These targets can then be rounded off and expressed as clear directives:

- Bring 4.4 individual backbone trees per hectare into clumps of 5-14 TAOs

In addition to backbone trees:

- Add 1 clump of 5-9 TAOs per 10 hectares
- Add 1 clump of 10-14 TAOs per 25 hectares
- Add 1 clump of 15-30 TAOs per 7 hectares

Because the unit size (9.3 ha) is less than some of the clump retention rates, the last three directives can be simplified:

- Add 1 clump of 5-9 TAOs in the unit
- Add 1 clump of 10-14 TAOs in the unit if an obvious choice exists
- Add 1 clump of 15-30 TAOs in the unit

3. Set guidelines for canopy openings

The opening target, set in terms of the open space index, is difficult to prescribe directly; however, the knowing the relative position of the target within the range of possible treatment options is sufficient to provide marking guidelines. Open space can be modified by varying second-order patterns, that is, whether the clumps themselves are aggregated versus being dispersed throughout the stand. When the target is on the high (more open) end of the range of possibilities then the second-order pattern should be aggregated with plenty of space left between loose aggregates of clumps. When the target is on the low (less open) end then the second-order pattern should be dispersed to break up the open space. It is also helpful to look at the map to see where current openings exist and where openings are easy to make without removing backbone trees.

In this example, the target of 0.27 is on the low end of the possible range at the target density (0.27-0.40). We can see from the map (Figure 19) that there is a large opening in the center of the unit as well as an area in the SE corner that would become very open if all backbone trees were removed. Thus, we give this directive:

- Retain clumps in loose aggregates to break up large openings

If we instead set the target on the high end, e.g., 0.40, then we would give this directive instead:

- Expand the existing opening in the center of the unit and create a new opening 0.1-0.25 ha in size in the SE corner of the unit

The steps involved with translating reference conditions and current conditions to implemented treatments are outlined graphically in Figure 21.

Supplementary Table 1 Empirical relationships between mean clump size and clump size distributions derived from Sierra Nevada reference areas (Chapter 1). Values are stand-level averages. Each cell gives the proportion of TAOs in the clump size indicated by the column label when the mean clump size is as given by the row label. For example, if the stand-level mean clump size is 3.6, then 17% of TAOs should be in clumps of 5-9.

	Clump size (n TAOs)					
MCS	**1.00**	**2-4**	**5-9**	**10-13**	**15-30**	**>30**
1-1.25	0.94	0.00	0.00	0.00	0.06	0.00
1.25-1.5	0.69	0.00	0.00	0.02	0.29	0.00
1.5-1.75	0.60	0.00	0.02	0.01	0.37	0.00
1.75-2	0.53	0.00	0.03	0.05	0.39	0.00
2-2.25	0.49	0.00	0.08	0.02	0.41	0.00
2.25-2.5	0.46	0.01	0.10	0.04	0.39	0.00
2.5-2.75	0.43	0.02	0.14	0.03	0.38	0.00
2.75-3	0.41	0.03	0.15	0.04	0.36	0.01
3-3.25	0.37	0.03	0.16	0.03	0.40	0.01
3.25-3.5	0.38	0.04	0.17	0.01	0.38	0.02
3.5-3.75	0.35	0.06	0.18	0.00	0.40	0.01
3.75-4	0.36	0.05	0.18	0.01	0.37	0.03
4-4.25	0.33	0.05	0.21	0.03	0.35	0.03
4.25-4.5	0.33	0.05	0.20	0.00	0.37	0.05
4.5-4.75	0.30	0.09	0.18	0.00	0.38	0.05
4.75-5	0.30	0.07	0.20	0.01	0.36	0.06
5-6	0.29	0.09	0.21	0.03	0.31	0.07
6-7	0.24	0.10	0.21	0.02	0.34	0.09
7-8	0.25	0.08	0.19	0.02	0.31	0.15
8-9	0.25	0.10	0.18	0.04	0.31	0.12
9-10	0.25	0.08	0.18	0.05	0.27	0.17
10-15	0.22	0.09	0.17	0.11	0.27	0.14
15-20	0.24	0.04	0.13	0.17	0.27	0.15
20-25	0.19	0.07	0.14	0.22	0.27	0.11
25-50	0.15	0.08	0.15	0.28	0.24	0.10
50-75	0.13	0.09	0.13	0.37	0.19	0.09
75-100	0.15	0.04	0.11	0.41	0.20	0.09
100-200	0.10	0.03	0.08	0.59	0.12	0.08

References

Adams, M.A., 2013. Mega-fires, tipping points and ecosystem services: Managing forests and woodlands in an uncertain future. Forest Ecology and Management 294, 250-261.

Agee, J.K., Skinner, C.N., 2005. Basic principles of forest fuel reduction treatments. Forest Ecology and Management 211, 83-96.

Alonzo, M., Bookhagen, B., Roberts, D.A., 2014. Urban tree species mapping using hyperspectral and lidar data fusion. Remote Sensing of Environment 148, 70-83.

Barbosa, J.M., Sebastián-González, E., Asner, G.P., Knapp, D.E., Anderson, C., Martin, R.E., Dirzo, R., 2016. Hemiparasite–host plant interactions in a fragmented landscape assessed via imaging spectroscopy and LiDAR. Ecological Applications 26, 55-66.

Barbour, M., Kelley, E., Maloney, P., Rizzo, D., Royce, E., Fites-Kaufmann, J., 2002. Present and past old-growth forests of the Lake Tahoe Basin, Sierra Nevada, US. Journal of Vegetation Science 13, 461-472.

Barth, M.A., Larson, A.J., Lutz, J.A., 2015. A forest reconstruction model to assess changes to Sierra Nevada mixed-conifer forest during the fire suppression era. Forest Ecology and Management 354, 104-118.

Beaty, R.M., Taylor, A.H., 2008. Fire history and the structure and dynamics of a mixed conifer forest landscape in the northern Sierra Nevada, Lake Tahoe Basin, California, USA. Forest Ecology and Management 255, 707-719.

Becker, K.M., Lutz, J.A., 2016. Can low-severity fire reverse compositional change in montane forests of the Sierra Nevada, California, USA? Ecosphere 7.

Boynton, R., Shipley, K., Roth, N., Underwood, E., 2015. The Landscape Management Unit (LMU) Tool. URL: http://ice.ucdavis.edu/project/landscape_management_unit_lmu_tool. Accessed 12/1/2017.

Brandtberg, T., 2007. Classifying individual tree species under leaf-off and leaf-on conditions using airborne lidar. ISPRS Journal of Photogrammetry and Remote Sensing 61, 325-340.

Breidenbach, J., Næsset, E., Lien, V., Gobakken, T., Solberg, S., 2010. Prediction of species specific forest inventory attributes using a nonparametric semi-individual tree crown approach based on fused airborne laser scanning and multispectral data. Remote Sensing of Environment 114, 911-924.

Briegleb, P.A., 1952. An approach to density measurement in Douglas-fir. Journal of Forestry 50, 529-536.

Brown, J.H., Gillooly, J.F., Allen, A.P., Savage, V.M., West, G.B., 2004. Toward a metabolic theory of ecology. Ecology 85, 1771-1789.

Budei, B.C., St-Onge, B., Hopkinson, C., Audet, F.-A., 2018. Identifying the genus or species of individual trees using a three-wavelength airborne lidar system. Remote Sensing of Environment 204, 632-647.

Churchill, D.J., Carnwath, G.C., Larson, A.J., Jeronimo, S.M.A., 2017. Historical forest structure, composition, and spatial pattern in dry conifer forests of the western Blue Mountains, Oregon. General Technical Report PNW-GTR-956. USDA Forest Service Pacific Northwest Research Station, Portland, OR.

Churchill, D.J., Larson, A.J., Dahlgreen, M.C., Franklin, J.F., Hessburg, P.F., Lutz, J.A., 2013. Restoring forest resilience: from reference spatial patterns to silvicultural prescriptions and monitoring. Forest Ecology and Management 291, 442-457.

Collins, B.M., Everett, R.G., Stephens, S.L., 2011. Impacts of fire exclusion and recent managed fire on forest structure in old growth Sierra Nevada mixed-conifer forests. Ecosphere 2, 1-14.

Collins, B.M., Fry, D.L., Lydersen, J.M., Everett, R., Stephens, S.L., 2017. Impacts of different land management histories on forest change. Ecological Applications 27, 2475-2486.

Collins, B.M., Lydersen, J.M., Everett, R.G., Fry, D.L., Stephens, S.L., 2015. Novel characterization of landscape-level variability in historical vegetation structure. In.

Collins, B.M., Lydersen, J.M., Fry, D.L., Wilkin, K., Moody, T., Stephens, S.L., 2016. Variability in vegetation and surface fuels across mixed-conifer-dominated landscapes with over 40 years of natural fire. Forest Ecology and Management 381, 74-83.

Curtis, R.O., 1982. A simple index of stand density for Douglas-fir. Forest Science 28, 92-94.

Das, A.J., Stephenson, N.L., Davis, K.P., 2016. Why do trees die? Characterizing the drivers of background tree mortality. Ecology 97, 2616-2627.

DeRose, R.J., Long, J.N., 2014. Resistance and resilience: A conceptual framework for silviculture. Forest Science 60, 1205-1212.

Drew, T.J., Flewelling, J.W., 1979. Stand density management: an alternative approach and its application to Douglas-fir plantations. Forest Science 25, 518-532.

EPA, USGS, 2018. National Hydrography Dataset Plus Version 2. URL: https://www.epa.gov/waterdata/nhdplus-national-hydrography-dataset-plus. Accessed 12/1/2017.

Falkowski, M.J., Evans, J.S., Martinuzzi, S., Gessler, P.E., Hudak, A.T., 2009. Characterizing forest succession with lidar data: An evaluation for the Inland Northwest, USA. Remote Sensing of Environment 113, 946-956.

Falkowski, M.J., Smith, A.M., Gessler, P.E., Hudak, A.T., Vierling, L.A., Evans, J.S., 2008. The influence of conifer forest canopy cover on the accuracy of two individual tree measurement algorithms using lidar data. Canadian Journal of Remote Sensing 34, S338-S350.

Franklin, J., Johnson, K., Churchill, D., Hagmann, K., Johnson, D., Johnston, J., 2013. Restoration of dry forests in eastern Oregon: a field guide. The Nature Conservancy, Portland, OR 202.

Franklin, J.F., Hagmann, R.K., Urgenson, L.S., 2014. Interactions between societal goals and restoration of dry forest landscapes in western North America. Landscape Ecology 29, 1645-1655.

Franklin, J.F., Johnson, K.N., 2012. A restoration framework for federal forests in the Pacific Northwest. Journal of Forestry 110, 429-439.

Franklin, J.F., Johnson, K.N., Johnson, D.L., 2018. Larger Spatial-Scale Concerns: Landscapes and Regions. In, Ecological Forest Management. Waveland Press, Long Grove, Illinois, pp. 117-146.

Franklin, J.F., Mitchell, R.J., Palik, B.J., 2007. Natural disturbance and stand development principles for ecological forestry.

Fry, D.L., Stephens, S.L., Collins, B.M., North, M.P., Franco-Vizcaíno, E., Gill, S.J., 2014. Contrasting spatial patterns in active-fire and fire-suppressed Mediterranean climate old-growth mixed conifer forests. PLoS One 9, e88985.

Fulé, P.Z., Covington, W.W., Moore, M.M., 1997. Determining reference conditions for ecosystem management of southwestern ponderosa pine forests. Ecological Applications 7, 895-908.

Furniss, T.J., Larson, A.J., Kane, V.R., Lutz, J.A., in review. Multi-scale validation of post-fire tree mortality models. International Journal of Wildland Fire.

Gärtner, S., Reynolds, K., Hessburg, P., Hummel, S., Twery, M., 2008. Decision support for evaluating landscape departure and prioritizing forest management activities in a changing environment. Forest Ecology and Management 256, 1666-1676.

Hagmann, R.K., Franklin, J.F., Johnson, K.N., 2013. Historical structure and composition of ponderosa pine and mixed-conifer forests in south-central Oregon. Forest Ecology and Management 304, 492-504.

Hagmann, R.K., Franklin, J.F., Johnson, K.N., 2014. Historical conditions in mixed-conifer forests on the eastern slopes of the northern Oregon Cascade Range, USA. Forest Ecology and Management 330, 158-170.

Heinzel, J., Koch, B., 2011. Exploring full-waveform LiDAR parameters for tree species classification. International Journal of Applied Earth Observation and Geoinformation 13, 152-160.

Hessburg, P., Reynolds, K., Salter, R., Dickinson, J., Gaines, W., Harrod, R., 2013. Landscape Evaluation for Restoration Planning on the Okanogan-Wenatchee National Forest, USA. Sustainability 5, 805.

Hessburg, P.F., Agee, J.K., Franklin, J.F., 2005. Dry forests and wildland fires of the inland Northwest USA: contrasting the landscape ecology of the pre-settlement and modern eras. Forest Ecology and Management 211, 117-139.

1935 Hessburg, P.F., Churchill, D.J., Larson, A.J., Haugo, R.D., Miller, C., Spies, T.A., North, M.P.,
1936 Povak, N.A., Belote, R.T., Singleton, P.H., Gaines, W.L., Keane, R.E., Aplet, G.H.,
1937 Stephens, S.L., Morgan, P., Bisson, P.A., Rieman, B.E., Salter, R.B., Reeves, G.H., 2015.
1938 Restoring fire-prone Inland Pacific landscapes: seven core principles. Landscape Ecology
1939 30, 1805-1835.
1940 Hood, S.M., Cluck, D.R., Jones, B.E., Pinnell, S., 2017. Radial and stand-level thinning
1941 treatments: 15-year growth response of legacy ponderosa and Jeffrey pine trees.
1942 Restoration Ecology.
1943 Hovi, A., Korhonen, L., Vauhkonen, J., Korpela, I., 2016. LiDAR waveform features for tree
1944 species classification and their sensitivity to tree- and acquisition related parameters.
1945 Remote Sensing of Environment 173, 224-237.
1946 Hyde, P., Dubayah, R., Peterson, B., Blair, J., Hofton, M., Hunsaker, C., Knox, R., Walker, W.,
1947 2005. Mapping forest structure for wildlife habitat analysis using waveform lidar:
1948 Validation of montane ecosystems. Remote Sensing of Environment 96, 427-437.
1949 Hyde, P., Dubayah, R., Walker, W., Blair, J.B., Hofton, M., Hunsaker, C., 2006. Mapping forest
1950 structure for wildlife habitat analysis using multi-sensor (LiDAR, SAR/InSAR, ETM+,
1951 Quickbird) synergy. Remote Sensing of Environment 102, 63-73.
1952 Hymanson, Z.P., Collopy, M.W., 2010. An integrated science plan for the Lake Tahoe basin:
1953 conceptual framework and research strategies. General Technical Report-Pacific
1954 Southwest Research Station, USDA Forest Service.
1955 Ishii, H., McDowell, N., 2002. Age-related development of crown structure in coastal Douglas-
1956 fir trees. Forest Ecology and Management 169, 257-270.

Jack, S.B., Long, J.N., 1996. Linkages between silviculture and ecology: an analysis of density management diagrams. Forest Ecology and Management 86, 205-220.

Jeronimo, S.M.A., 2015. LiDAR individual tree detection for assessing structurally diverse forest landscapes. MS thesis. University of Washington, Seattle, WA.

Jeronimo, S.M.A., Kane, V.R., Churchill, D.J., McGaughey, R.J., Franklin, J.F., 2018. Applying lidar individual tree detection to management of structurally diverse forest landscapes. Journal of Forestry 116, 336-346.

Johnston, J.D., 2017. Forest succession along a productivity gradient following fire exclusion. Forest Ecology and Management 392, 45-57.

Kane, V.R., Gersonde, R.F., Lutz, J.A., McGaughey, R.J., Bakker, J.D., Franklin, J.F., 2011. Patch dynamics and the development of structural and spatial heterogeneity in Pacific Northwest forests. Canadian Journal of Forest Research 41, 2276-2291.

Kane, V.R., Lutz, J.A., Roberts, S.L., Smith, D.F., McGaughey, R.J., Povak, N.A., Brooks, M.L., 2013. Landscape-scale effects of fire severity on mixed-conifer and red fir forest structure in Yosemite National Park. Forest Ecology and Management 287, 17-31.

Kane, V.R., North, M.P., Lutz, J.A., Churchill, D.J., Roberts, S.L., Smith, D.F., McGaughey, R.J., Kane, J.T., Brooks, M.L., 2014. Assessing fire effects on forest spatial structure using a fusion of Landsat and airborne LiDAR data in Yosemite National Park. Remote Sensing of Environment 151, 89-101.

Keeley, J.E., Stephenson, N.L., 2000. Restoring natural fire regimes to the Sierra Nevada in an era of global change. In: Cole, D.N., McCool, S.F., Borrie, W.T., O'Loughlin, J. (Eds.), Wilderness science in a time of change conference Volume 5: Wilderness ecosystems,

threats, and management. Proceedings. RMRS-P-15-VOL5. USDA Forest Service Rocky Mountain Research Station, Missoula, MT.

Koukoulas, S., Blackburn, G.A., 2004. Quantifying the spatial properties of forest canopy gaps using LiDAR imagery and GIS. International Journal of Remote Sensing 25, 3049-3072.

Kramer, R.D., Sillett, S.C., Carroll, A.L., 2014. Structural development of redwood branches and its effects on wood growth. Tree Physiology 34, 314-330.

Kramer, R.D., Sillett, S.C., Van Pelt, R., 2018. Quantifying aboveground components of Picea sitchensis for allometric comparisons among tall conifers in North American rainforests. Forest Ecology and Management 430, 59-77.

Lake Tahoe West Restoration Partnership, 2017. Agency and Stakeholder Charter.

Larson, A.J., Churchill, D.J., 2012. Tree spatial patterns in fire-frequent forests of western North America, including mechanisms of pattern formation and implications for designing fuel reduction and restoration treatments. Forest Ecology and Management 267, 74-92.

Larson, A.J., Lutz, J.A., Donato, D.C., Freund, J.A., Swanson, M.E., HilleRisLambers, J., Sprugel, D.G., Franklin, J.F., 2015. Spatial aspects of tree mortality strongly differ between young and old-growth forests. Ecology 96, 2855-2861.

Larson, A.J., Lutz, J.A., Gersonde, R.F., Franklin, J.F., Hietpas, F.F., 2008. Potential site productivity influences the rate of forest structural development. Ecological Applications 18, 899-910.

Levine, C.R., Krivak-Tetley, F., van Doorn, N.S., Ansley, J.-A.S., Battles, J.J., 2016. Long-term demographic trends in a fire-suppressed mixed-conifer forest. Canadian Journal of Forest Research 46, 745-752.

Lindberg, E., Holmgren, J., Olofsson, K., Wallerman, J., Olsson, H., 2010. Estimation of tree lists from airborne laser scanning by combining single-tree and area-based methods. International Journal of Remote Sensing 31, 1175-1192.

Lindenmayer, D.B., Laurance, W.F., Franklin, J.F., 2012. Global decline in large old trees. Science 338, 1305-1306.

Long, J.N., 2009. Emulating natural disturbance regimes as a basis for forest management: a North American view. Forest Ecology and Management 257, 1868-1873.

Lutz, J., Larson, A., Swanson, M., 2018a. Advancing Fire Science with Large Forest Plots and a Long-Term Multidisciplinary Approach. Fire 1, 5.

Lutz, J., Van Wagtendonk, J., Franklin, J., 2009. Twentieth-century decline of large-diameter trees in Yosemite National Park, California, USA. Forest Ecology and Management 257, 2296-2307.

Lutz, J.A., 2015. The evolution of long-term data for forestry: large temperate research plots in an era of global change. Northwest Science 89, 255-269.

Lutz, J.A., Furniss, T.J., Germain, S.J., Becker, K.M., Blomdahl, E.M., Jeronimo, S., Cansler, C.A., Freund, J.A., Swanson, M.E., Larson, A.J., 2017. Shrub communities, spa-tial patterns, and shrub-mediated tree mortality following reintroduced fire in Yosemite National Park, California, USA. Fire Ecology 13, 104-126.

Lutz, J.A., Furniss, T.J., Johnson, D.J., Davies, S.J., Allen, D., Alonso, A., Anderson-Teixeira, K.J., Andrade, A., Baltzer, J., Becker, K.M.L., Blomdahl, E.M., Bourg, N.A., Bunyavejchewin, S., Burslem, D.F.R.P., Cansler, C.A., Cao, K., Cao, M., Cárdenas, D., Chang, L.W., Chao, K.J., Chao, W.C., Chiang, J.M., Chu, C., Chuyong, G.B., Clay, K., Condit, R., Cordell, S., Dattaraja, H.S., Duque, A., Ewango, C.E.N., Fischer, G.A.,

Fletcher, C., Freund, J.A., Giardina, C., Germain, S.J., Gilbert, G.S., Hao, Z., Hart, T., Hau, B.C.H., He, F., Hector, A., Howe, R.W., Hsieh, C.F., Hu, Y.H., Hubbell, S.P., Inman-Narahari, F.M., Itoh, A., Janík, D., Kassim, A.R., Kenfack, D., Korte, L., Král, K., Larson, A.J., Li, Y., Lin, Y., Liu, S., Lum, S., Ma, K., Makana, J.R., Malhi, Y., McMahon, S.M., McShea, W.J., Memiaghe, H.R., Mi, X., Morecroft, M., Musili, P.M., Myers, J.A., Novotny, V., de Oliveira, A., Ong, P., Orwig, D.A., Ostertag, R., Parker, G.G., Patankar, R., Phillips, R.P., Reynolds, G., Sack, L., Song, G.Z.M., Su, S.H., Sukumar, R., Sun, I.F., Suresh, H.S., Swanson, M.E., Tan, S., Thomas, D.W., Thompson, J., Uriarte, M., Valencia, R., Vicentini, A., Vrška, T., Wang, X., Weiblen, G.D., Wolf, A., Wu, S.H., Xu, H., Yamakura, T., Yap, S., Zimmerman, J.K., 2018b. Global importance of large-diameter trees. Global Ecology and Biogeography 27, 849-864.

Lutz, J.A., Halpern, C.B., 2006. Tree mortality during early forest development: A long-term study of rates, causes, and consequences. Ecological Monographs 76, 257-275.

Lutz, J.A., Larson, A.J., Freund, J.A., Swanson, M.E., Bible, K.J., 2013. The importance of large-diameter trees to forest structural heterogeneity. PLoS One 8, e82784.

Lutz, J.A., Larson, A.J., Swanson, M.E., Freund, J.A., 2012. Ecological importance of large-diameter trees in a temperate mixed-conifer forest. PLoS One 7, e36131.

Lutz, J.A., Schwindt, K.A., Furniss, T.J., Freund, J.A., Swanson, M.E., Hogan, K.I., Kenagy, G.E., Larson, A.J., 2014. Community composition and allometry of Leucothoe davisiae, Cornus sericea, and Chrysolepis sempervirens. Canadian Journal of Forest Research 44, 677-683.

Lutz, J.A., van Wagtendonk, J.W., Franklin, J.F., 2010. Climatic water deficit, tree species ranges, and climate change in Yosemite National Park. Journal of Biogeography 37, 936-950.

Lydersen, J., North, M., 2012. Topographic variation in structure of mixed-conifer forests under an active-fire regime. Ecosystems 15, 1134-1146.

Lydersen, J.M., North, M.P., Knapp, E.E., Collins, B.M., 2013. Quantifying spatial patterns of tree groups and gaps in mixed-conifer forests: reference conditions and long-term changes following fire suppression and logging. Forest Ecology and Management 304, 370-382.

Martinuzzi, S., Vierling, L.A., Gould, W.A., Falkowski, M.J., Evans, J.S., Hudak, A.T., Vierling, K.T., 2009. Mapping snags and understory shrubs for a LiDAR-based assessment of wildlife habitat suitability. Remote Sensing of Environment 113, 2533-2546.

McGaughey, R.J., 2018. FUSION/LDV: Software for LIDAR Data Analysis and Visualization: Version 3.70. USDA Forest Service Pacific Northwest Research Station, Seattle, WA.

McGuire, J.P., Mitchell, R.J., Moser, E.B., Pecot, S.D., Gjerstad, D.H., Hedman, C.W., 2001. Gaps in a gappy forest: plant resources, longleaf pine regeneration, and understory response to tree removal in longleaf pine savannas. Canadian Journal of Forest Research 31, 765-778.

McIntyre, P.J., Thorne, J.H., Dolanc, C.R., Flint, A.L., Flint, L.E., Kelly, M., Ackerly, D.D., 2015. Twentieth-century shifts in forest structure in California: Denser forests, smaller trees, and increased dominance of oaks. Proceedings of the National Academy of Sciences.

2067 Means, J.E., Acker, S.A., Fitt, B.J., Renslow, M., Emerson, L., Hendrix, C.J., 2000. Predicting
2068 forest stand characteristics with airborne scanning lidar. Photogrammetric Engineering
2069 and Remote Sensing 66, 1367-1372.
2070 Meyer, M.D., Kelt, D.A., North, M.P., 2007. Microhabitat associations of northern flying
2071 squirrels in burned and thinned forest stands of the Sierra Nevada. The American
2072 Midland Naturalist 157, 202-211.
2073 Moore, G.W., Bond, B.J., Jones, J.A., Phillips, N., Meinzer, F.C., 2004. Structural and
2074 compositional controls on transpiration in 40-and 450-year-old riparian forests in western
2075 Oregon, USA. Tree Physiology 24, 481-491.
2076 Moore, M.M., Wallace Covington, W., Fule, P.Z., 1999. Reference conditions and ecological
2077 restoration: a southwestern ponderosa pine perspective. Ecological Applications 9, 1266-
2078 1277.
2079 Næsset, E., 1997. Estimating timber volume of forest stands using airborne laser scanner data.
2080 Remote Sensing of Environment 61, 246-253.
2081 North, M., Brough, A., Long, J., Collins, B., Bowden, P., Yasuda, D., Miller, J., Sugihara, N.,
2082 2015. Constraints on mechanized treatment significantly limit mechanical fuels reduction
2083 extent in the Sierra Nevada. Journal of Forestry 113, 40-48.
2084 North, M., Collins, B.M., Stephens, S., 2012. Using fire to increase the scale, benefits, and future
2085 maintenance of fuels treatments. Journal of Forestry 110, 392-401.
2086 North, M., Innes, J., Zald, H., 2007. Comparison of thinning and prescribed fire restoration
2087 treatments to Sierran mixed-conifer historic conditions. Canadian Journal of Forest
2088 Research 37, 331-342.

North, M., Stine, P., O'Hara, K., Zielinski, W., Stephens, S., 2009. An ecosystem management strategy for Sierran mixed-conifer forests, General Technical Report PSW-GTR-220. USDA Forest Service Pacific Southwest Research Station. Albany, CA.

North, M.P., Kane, J.T., Kane, V.R., Asner, G.P., Berigan, W., Churchill, D.J., Conway, S., Gutiérrez, R.J., Jeronimo, S., Keane, J., Koltunov, A., Mark, T., Moskal, M., Munton, T., Peery, Z., Ramirez, C., Sollmann, R., White, A., Whitmore, S., 2017. Cover of tall trees best predicts California spotted owl habitat. Forest Ecology and Management 405, 166-178.

O'Connor, C.D., Falk, D.A., Lynch, A.M., Swetnam, T.W., Wilcox, C.P., 2017. Disturbance and productivity interactions mediate stability of forest composition and structure. Ecological Applications 27, 900-915.

Packalen, P., Vauhkonen, J., Kallio, E., Peuhkurinen, J., Pitkänen, J., Pippuri, I., Strunk, J., Maltamo, M., 2013. Predicting the spatial pattern of trees by airborne laser scanning. International Journal of Remote Sensing 34, 5154-5165.

Palik, B.J., Goebel, P.C., Kirkman, L.K., West, L., 2000. Using landscape hierarchies to guide restoration of disturbed ecosystems. Ecological Applications 10, 189-202.

Parker, R.C., Evans, D.L., 2009. LiDAR forest inventory with single-tree, double-, and single-phase procedures. International Journal of Forestry Research 2009.

Plotkin, J.B., Chave, J., Ashton, P.S., 2002. Cluster analysis of spatial patterns in Malaysian tree species. The American Naturalist 160, 629-644.

Popescu, S.C., Wynne, R.H., Scrivani, J.A., 2004. Fusion of small-footprint lidar and multispectral data to estimate plot-level volume and biomass in deciduous and pine forests in Virginia, USA. Forest Science 50, 551-565.

Powell, D.C., 1999. Suggested stocking levels for forest stands in northeastern Oregon and southeastern Washington: an implementation guide for the Umatilla National Forest. Technical Publication F14-SO-TP-03-99. USDA Forest Service, Pacific Northwest Region. Portland, OR.

Puettmann, K.J., Coates, K.D., Messier, C.C., 2012. A critique of silviculture: managing for complexity. Island press. Washington, DC.

Purcell, K.L., Mazzoni, A.K., Mori, S.R., Boroski, B.B., 2009. Resting structures and resting habitat of fishers in the southern Sierra Nevada, California. Forest Ecology and Management 258, 2696-2706.

Reineke, L.H., 1933. Perfecting a stand-density index for even-aged forests. Journal of Agricultural Research 46, 627-638.

Reutebuch, S.E., Andersen, H.-E., McGaughey, R.J., 2005. Light Detection and Ranging (LIDAR): An Emerging Tool for Multiple Resource Inventory. Journal of Forestry 103, 286-292.

Richardson, J.J., Moskal, L.M., 2011. Strengths and limitations of assessing forest density and spatial configuration with aerial LiDAR. Remote Sensing of Environment 115, 2640-2651.

Rodman, K.C., Meador, A.J.S., Moore, M.M., Huffman, D.W., 2017. Reference conditions are influenced by the physical template and vary by forest type: A synthesis of Pinus ponderosa-dominated sites in the southwestern United States. Forest Ecology and Management 404, 316-329.

Schneider, E.E., Larson, A.J., 2017. Spatial aspects of structural complexity in Sitka spruce–western hemlock forests, including evaluation of a new canopy gap delineation method. Canadian Journal of Forest Research 47, 1033-1044.

SER, 2002. Society for Ecological Restoration Science & Policy Working Group: The SER Primer on Ecological Restoration.

Sheppard, S.R., 2005. Landscape visualisation and climate change: the potential for influencing perceptions and behaviour. Environmental Science & Policy 8, 637-654.

Sillett, S.C., Van Pelt, R., Carroll, A.L., Kramer, R.D., Ambrose, A.R., Trask, D.A., 2015. How do tree structure and old age affect growth potential of California redwoods? Ecological Monographs 85, 181-212.

Sillett, S.C., Van Pelt, R., Freund, J.A., Campbell-Spickler, J., Carroll, A.L., Kramer, R.D., 2018. Development and dominance of Dougals-fir in North American rainforests. Forest Ecology and Management 429, 93-114.

Stephens, S.L., Agee, J.K., Fulé, P., North, M., Romme, W., Swetnam, T., Turner, M.G., 2013. Managing forests and fire in changing climates. Science 342, 41-42.

Stephens, S.L., Lydersen, J.M., Collins, B.M., Fry, D.L., Meyer, M.D., 2015. Historical and current landscape-scale ponderosa pine and mixed conifer forest structure in the Southern Sierra Nevada. Ecosphere 6, 1-63.

Stephens, S.L., Ruth, L.W., 2005. FEDERAL FOREST-FIRE POLICY IN THE UNITED STATES. Ecological Applications 15, 532-542.

Taylor, A.H., 2010. Fire disturbance and forest structure in an old-growth Pinus ponderosa forest, southern Cascades, USA. Journal of Vegetation Science 21, 561-572.

Taylor, A.H., Vandervlugt, A.M., Maxwell, R.S., Beaty, R.M., Airey, C., Skinner, C.N., 2014. Changes in forest structure, fuels and potential fire behaviour since 1873 in the Lake Tahoe Basin, USA. Applied Vegetation Science 17, 17-31.

Trumbore, S., Brando, P., Hartmann, H., 2015. Forest health and global change. Science 349, 814-818.

Underwood, E.C., Viers, J.H., Quinn, J.F., North, M., 2010. Using topography to meet wildlife and fuels treatment objectives in fire-suppressed landscapes. Environmental Management 46, 809-819.

Urgenson, L.S., Nelson, C.R., Haugo, R.D., Halpern, C.B., Bakker, J.D., Ryan, C.M., Waltz, A.E., Belote, R.T., Alvarado, E., 2017. Social perspectives on the use of reference conditions in restoration of fire-adapted forest landscapes. Restoration Ecology.

USDA, 2008. Environmental Assessment: Glaze Forest Restoration Project. USDA Forest Service, Deschutes National Forest, Sisters Ranger District, Deschutes County, Oregon.

USDA, 2013. Red Knight Restoration Project: Environmental Assessment. USDA Forest Service, Fremont-Winema National Forest, Chemult Ranger District, Klamath County, Oregon.

USDA Forest Service, 2013. Region 5 - Common Stand Exam Field Guide.

Van Pelt, R., 2008. Identifying old trees and forests in eastern Washington. Washington State Department of Natural Resources.

Van Pelt, R., Sillett, S.C., 2008. Crown development of coastal Pseudotsuga menziesii, including a conceptual model for tall conifers. Ecological Monographs 78, 283-311.

Van Pelt, R., Sillett, S.C., Kruse, W.A., Freund, J.A., Kramer, R.D., 2016. Emergent crowns and light-use complementarity lead to global maximum biomass and leaf area in Sequoia sempervirens forests. Forest Ecology and Management 375, 279-308.

van Wagtendonk, J.W., Moore, P.E., 2010. Fuel deposition rates of montane and subalpine conifers in the central Sierra Nevada, California, USA. Forest Ecology and Management 259, 2122-2132.

Vincent, L., Soille, P., 1991. Watersheds in digital spaces: an efficient algorithm based on immersion simulations. IEEE Transactions on Pattern Analysis & Machine Intelligence, 583-598.

WA DNR, 2018. 20-Year Forest Health Strategic Plan: Eastern Washington. Washington State Department of Natural Resources, Olympia, WA. URL: http://www.dnr.wa.gov/ForestHealthPlan. Accessed 1/9/2018.

White, J.C., Wulder, M.A., Varhola, A., Vastaranta, M., Coops, N.C., Cook, B.D., Pitt, D., Woods, M., 2013. A best practices guide for generating forest inventory attributes from airborne laser scanning data using an area-based approach. The Forestry Chronicle 89, 722-723.

Wiggins, H.L., 2017. The influence of tree height on lidar's ability to accurately characterize forest structure and spatial pattern across reference landscapes. Master of Science Thesis. University of Montana, Missoula, MT.

Wing, B.M., Ritchie, M.W., Boston, K., Cohen, W.B., Gitelman, A., Olsen, M.J., 2012. Prediction of understory vegetation cover with airborne lidar in an interior ponderosa pine forest. Remote Sensing of Environment 124, 730-741.

Wing, B.M., Ritchie, M.W., Boston, K., Cohen, W.B., Olsen, M.J., 2015. Individual snag detection using neighborhood attribute filtered airborne lidar data. Remote Sensing of Environment 163, 165-179.

Young, D.J., Stevens, J.T., Earles, J.M., Moore, J., Ellis, A., Jirka, A.L., Latimer, A.M., 2017. Long-term climate and competition explain forest mortality patterns under extreme drought. Ecology Letters 20, 78-86.

Chapter 3: Structural drivers of immediate and delayed fire mortality: modeling tree death in a landscape context

1. Introduction

Forest fire behavior is driven by topography, burning weather, and fuels, i.e., stand structure. Structure is the only one of these components that can be directly manipulated and therefore constitutes the means by which fire behavior can be managed (Agee, 1993). Modifying structure by thinning, prescribed burning, and wildland fire use are effective ways to reduce the severity of future fires (Graham *et al.*, 2004; Kalies and Kent, 2016), especially when post-treatment structure is spatially heterogeneous (Kennedy and Johnson, 2014). Very hot and dry weather can negate the effects of these treatments to some extent, but even under extreme burning conditions structural modifications do act to reduce burn severity (Collins *et al.*, 2009; Parks *et al.*, 2015; Lydersen *et al.*, 2017). Because forest structure is the only modifiable variable driving fire severity it is important to understand the pattern-process linkages between elements of structure and tree mortality.

The effects of fire on tree mortality (i.e., fire severity) vary depending on resistance characteristics of individual trees (Belote *et al.*, 2015), but also on vertical and horizontal spatial patterns (Agee and Skinner, 2005; Hessburg *et al.*, 2005; Larson and Churchill, 2012; Kennedy and Johnson, 2014). Mechanisms of resistant for individual trees include thick bark and well-pruned crowns (Ryan *et al.*, 1988; Ryan and Reinhardt, 1988; Hood *et al.*, 2007; Hood *et al.*, 2010). These characteristics typically express themselves with age but are very much related to species identity (Ryan and Reinhardt, 1988; Belote *et al.*, 2015). Vertical canopy structure affects fire behavior, and thus fire severity, primarily via ladder fuels that can carry surface fires

into the canopy, leading to high-severity crown fires (Agee and Skinner, 2005). Horizontal patterns of trees can modify the way fire moves through a stand or across a landscape. Heterogeneous patterns, such as closely-spaced aggregates of trees and canopy openings larger than the average mature tree crown, induce varied and aggregated fire effects such as small-group torching, survival of dense regeneration patches that have little or no surface fuels, and survival of topographically protected patches or areas (Fulé and Covington, 1998; Stephens and Fry, 2005; Kolden *et al.*, 2012; Meddens *et al.*, in press).

Individual tree structure and spatial patterns in vertical and horizontal dimensions can also have effects on delayed fire mortality. Delayed mortality, which occurs following fires of all severities (Miller *et al.*, 2016), usually takes place within 4-5 years post-fire and can represent over 40% of total fire mortality (Youngblood *et al.*, 2009; Fettig *et al.*, 2010; Hood *et al.*, 2010; Van Mantgem *et al.*, 2011; Prichard and Kennedy, 2012). Delayed mortality can occur after fire causes damage to or partial necrosis of a tree's cambium and/or crown and the tree enters a death spiral, succumbing some years later from carbon starvation, hydraulic failure, decay, bark beetles, wind, competition, or some combination of these (Filip *et al.*, 2007; Smith *et al.*, 2016). Many of these factors – especially pests, pathogens, and competition – are density-dependent agents of mortality. High stand density can additionally predispose trees to compounding stressors such as drought and bark beetles (Guarín and Taylor, 2005; Hood and Bentz, 2007; Das *et al.*, 2008).

Patterns in forest structure emerge in the context of a hierarchy of nested spatial scales (Kotliar and Wiens, 1990; Palik *et al.*, 2000; Boyden *et al.*, 2012; Hessburg *et al.*, 2015). The elements of structure that influence immediate and delayed fire mortality occur in a narrow sense at the individual tree scale but integrate into community-level effects at the scales of tree clumps

and larger neighborhoods (Belote *et al.*, 2015). For example, fire mortality at the individual tree scale is broadly reported to be due to crown and stem injuries, which occur in accordance with individual tree structure (Woolley *et al.*, 2012; Smith *et al.*, 2016); fire mortality at the scale of tree clumps and openings acts to maintain and enhance clump-opening patterns (Kane *et al.*, 2013); and at the scale of a larger neighborhood, beetle-induced delayed can increase with stand density (Hood and Bentz, 2007). Pattern-process linkages like these also interact across hierarchical scales (Kotliar and Wiens, 1990); however, previous research has focused on one scale at a time and has not characterized the cross-scale linkages.

Despite theoretical and empirical evidence that both immediate and delayed fire mortality vary in response to multi-scale spatial structure, the effects of spatial pattern on fire mortality have not been explicitly quantified. Kane *et al.* (2013) described fire effects in terms of spatial pattern classes and presented a framework for predicting how patterns might respond to fires of varying severity, but did not explicitly identify mechanisms of pattern change. This and other Landsat-based studies are also limited in their ability to characterize delayed mortality since Landsat fire severity indices rely on post-fire scenes captured immediately to one year after the fire. It may, however, be possible to predict delayed effects from one year post-fire Landsat severity measures (Miller *et al.*, 2016).

In light of drying climates (Battles *et al.*, 2008; Collins, 2014; Young *et al.*, 2017), increased fuel loads (van Wagtendonk and Moore, 2010; Van de Water and North, 2011; Stephens *et al.*, 2012), and increasing fire severity (Miller *et al.*, 2009; Stevens *et al.*, 2017) across the Western US, major restoration efforts are underway to treat fuels and improve forest resistance to fire with a primary goal of reducing fire-caused tree mortality (Hessburg *et al.*, 2005; Miller *et al.*, 2009; North *et al.*, 2009; Collins *et al.*, 2010). These treatments are often guided in concept by

historical or contemporary reference condition datasets (Chapters 1, 2), but specific details for landscape-level treatment design and prioritization as well as stand-level thinning and prescribed fire prescriptions are generally arrived at using modeling tools such as the Fire and Fuels extension to the Forest Vegetation Simulator, the First-Order Fire Effects Model (FOFEM), and BehavePlus (Hood *et al.*, 2007). The mortality model underlying these tools is not parameterized on spatial pattern and so does not account for the effects of pattern on immediate or delayed fire mortality (Ryan and Reinhardt, 1988; Hood *et al.*, 2010), even while many restoration treatments feature prescriptions with explicit spatial pattern targets (e.g., increasing spatial heterogeneity and creating a fine-scale mosaic of tree clumps and canopy openings) (USDA, 2008; Churchill *et al.*, 2013; USDA, 2013). This leaves silviculturists with the imperative to prescribe heterogeneous spatial patterns that reduce fire behavior, encourage survival of green tree refugia, and buffer against agents of delayed mortality without having adequate modeling tools to support their decisions.

The objective of this study is to investigate the effects of spatial patterns at multiple nested scales on probabilities of immediate and delayed fire mortality in Sierra Nevada mixed-conifer forests, which are characterized by high levels of spatial heterogeneity (Franklin and Fites-Kaufmann, 1996). We aim to quantify these effects for the dual purposes of ecological understanding of pattern-process linkages and to develop modeling options for use by forest managers. Our research questions for this study are:

(1) How does mortality progress 1-4 years post-fire in terms of rates, demographics, and agents?

(2) What elements of forest structure and pattern predict immediate and delayed post-fire mortality at scales from small groups of trees to larger neighborhood patches?

(3) How does the prevalence of different mortality agents vary with changes in the important fine-scale predictors of fire mortality?

2. Methods

2.1 Study area

Our study area was within the footprint of the 2013 Rim Fire in Yosemite National Park, California (Figure 1). The Rim Fire started on August 17, 2013 and burned a total of 104,131 ha, including 31,519 ha in Yosemite National Park, before being declared out on October 23, 2013. This was the largest fire recorded in Sierra Nevada history at that time. While fire effects on the adjacent Stanislaus National Forest included very large high severity patches that burned under extreme weather conditions (Lydersen *et al.*, 2014), effects on the structurally variable forests of Yosemite were more mixed and provide an excellent opportunity to study the effects of structure and pattern on tree mortality (Kane *et al.*, 2015a).

We used fire mortality data from the Yosemite Forest Dynamics Plot (YFDP; Lutz *et al.*, 2012), a 25.6 ha stem mapped permanent plot affiliated with the Smithsonian ForestGEO network (Anderson-Teixeira *et al.*, 2015; Lutz, 2015). The YFDP is an old-growth sugar pine-white fir (*Pinus lambertiana-Abies concolor*) forest ranging from 1774 to 1911 m in elevation and is characterized by a Mediterranean climate with cool moist winters and warm dry summers. Normal temperatures range from a July maximum of 26 ºC to a February minimum of -3 ºC. Winters are moderately snowy, developing a typical springtime snowpack depth of approximately 1 m, and summers consistently include a several-month drought period. The YFDP was established in 2009-2010 and has been censused annually for recruitment and mortality since 2011.

The YFDP was burned in the Rim Fire as part of backfiring operations started on August 31, 2013. The backfire was lit approximately 1 km south of the plot and backed downslope, entering the plot around 1:30 am on September 1. The plot burned through the night and completed active burning by 11:30 on the morning of September 2. Fire effects were mixed with mainly low and moderate severities. The YFDP was censused and remeasured after the fire in May 2014 and annual mortality and ingrowth surveys have continued since that time (Lutz *et al.*, 2017).

2.2 Spatial pattern predictor variables

We used lidar-based pre-fire measurements of structure and pattern to predict fire mortality. We restricted this study to using lidar-based predictor variables to allow the resultant model to be predicted across Sierra Nevada mixed-conifer forests without additional ground measurements.

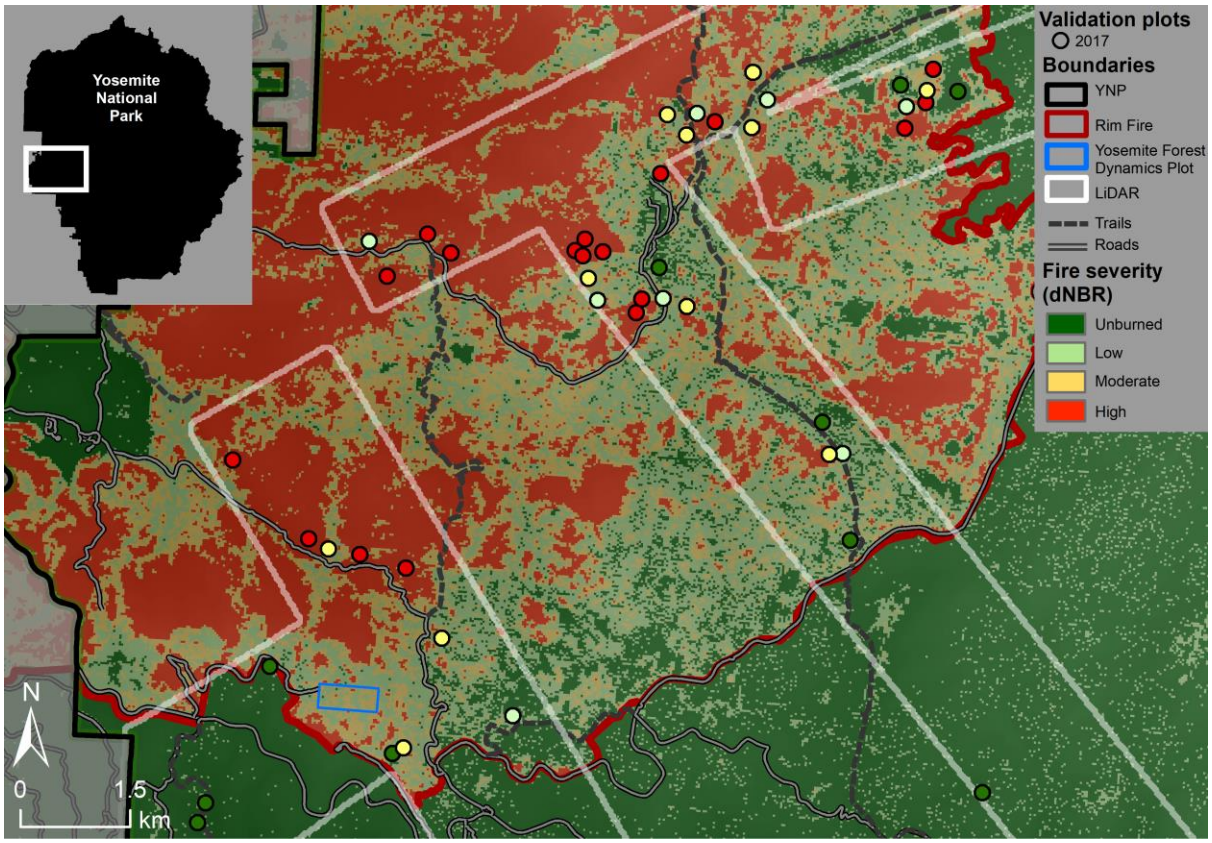

Figure 1 Map of study area showing the Yosemite Forest Dynamics Plot, Rim Fire severity, the 2010 lidar acquisition, and validation plot locations. Validation plots are colored by the fire severity. Map by Tucker Furniss.

We used lidar data acquired on July 21-22, 2010 by Watershed Sciences, Inc. of Corvallis, Oregon. Data were collected using dual-mounted Leica ALS50 Phase II instruments flown at 1300 m above ground. The instrument was capable of capturing up to 4 returns per pulse at a pulse rate of ≥85 kHz with a ±14º scan angle. Pulse density was approximately 11 points m^{-2} across the acquisition with an increased density of >30 points m^{-2} on the YFDP. Absolute survey accuracy was 4.4 cm root mean squared error. The vendor created and delivered a ground model using TerraScan and TerraModeler software (TerraSolid Oy, Helsinki, Finland).

We used FUSION software (McGaughey, 2018) to create a canopy height raster at 0.75 m resolution with a 3×3 mean smoothing filter (Jeronimo *et al.*, 2018), normalizing by the vendor-delivered ground model. We used this canopy height model (CHM) as an input into the FUSION TreeSeg tool, which segments the CHM into tree-approximate objects (TAOs). TAOs represent objects resolvable by lidar, which are canopy dominants along with any potential subordinate trees that may be hidden by the dominant tree's foliage (Jeronimo *et al.*, 2018). All subsequent lidar analysis was done in the R environment (R Core Team, 2016).

We analyzed structure and mortality at three scales: the TAO, the local area, and the neighborhood. TAO crown areas are delineated by the TreeSeg tool; we used those areas directly. The "local area" refers to a virtual 0.1 ha circular plot centered on each TAO. We segmented the YFDP into 24 90×90m subplots with 10 m of buffer between each; we refer to this as the neighborhood scale (Figure 2a). We created predictor variables at each scale from the lidar point cloud, CHM, and TAO data.

To create predictor variables at the TAO scale we clipped the lidar point cloud by each TAO footprint and calculated point cloud statistics that correspond to structure, namely, the height of the highest return and canopy cover in strata from 0.25-2 m, 2-4 m, 4-8 m, 8-16 m, 16-32 m, and

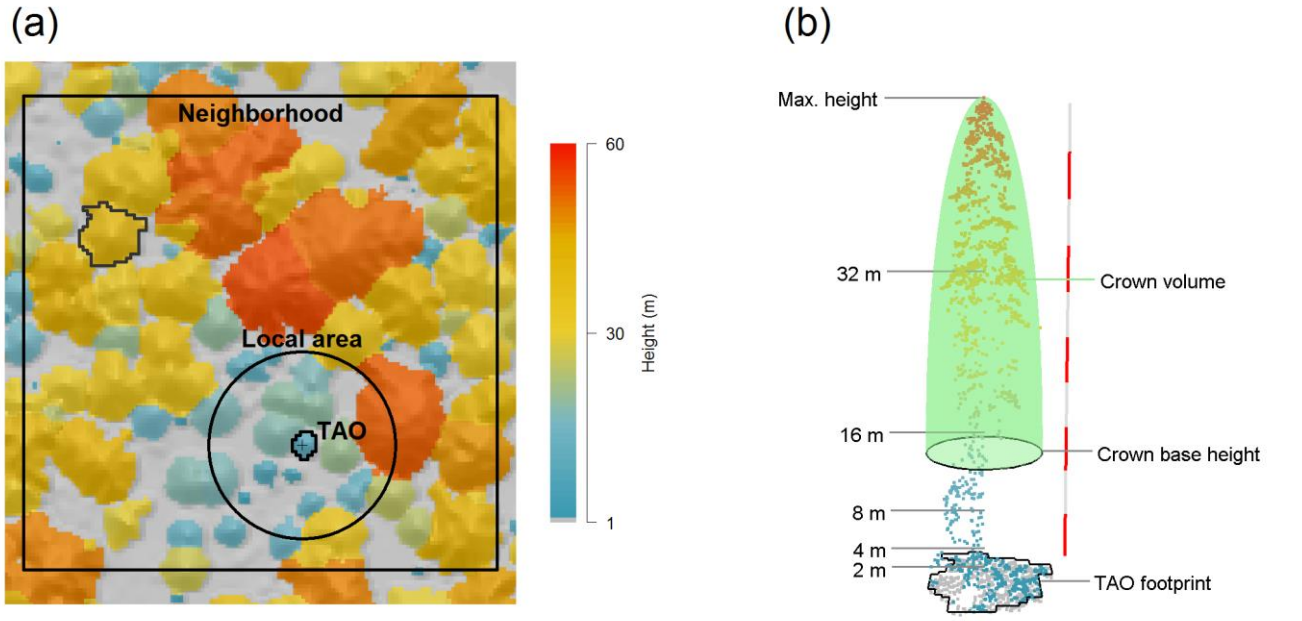

Figure 2 (a) Schematic of scales used in this study. The tree-approximate object (TAO) scale represents individual trees or closely related clusters of trees identified by lidar. The local area scale is a 0.1 ha circular plot placed around each TAO. The neighborhood scale is a 90×90 m fixed window. The Yosemite Forest Dynamics Plot was subdivided into 24 such neighborhoods and 48 more neighborhoods were sampled centered on our validation plot dataset. (b) Annotated TAO point cloud clipped from dark grey outline in panel (a). Canopy cover is calculated in bins shown by the markings on the left side. Crown volume is estimated using a paraboloid extending from the TAO high point to the estimated crown base (Table 2), and with a radius such that the circle shown at the crown base has area equal to the TAO footprint. Height pole is in 5 m increments.

>32 m (Kane *et al.*, 2013). We calculated additional predictors based on published models. Crown base height, crown fuel weight, and crown bulk density were estimated following Erdody and Moskal (2010). Leaf area index was estimated following Model D from Richardson *et al.* (2009) (Table 1). We estimated crown volume by idealizing each TAO crown as a paraboloid with crown length equal to TAO height minus estimated crown base height, and crown spread equal to the radius of a circle with an area equivalent to the TAO's footprint area (Figure 2b). Lastly, we assigned each TAO membership in a clump following methods developed for stem maps by Churchill *et al.* (2013) and adapted for TAOs by Jeronimo (Chapter 1). In this method, TAOs are considered members of the same clump if their high points are within 6 m of one another. We clump size as an additional TAO-level predictor.

Table 1 Published models used to create some of the tree-approximate object-scale predictor variables. Abbreviations: P25, P50, P90 = 25th, 50th, and 90th percentile lidar return heights, respectively; CC = canopy cover, or proportion of lidar first returns with heights over 2 m.

Structural metric	**Crown base height (m)**
Model form	((3.254 + 0.13 * P25 - 0.021 * P90 - 0.039 * CC) + 0.214)^2
Ecoregion	East Cascades, Washington
Citation	Erdody and Moskal (2010)
Structural metric	**Crown fuel weight (kg ha^-1)***
Model form	exp((-0.536 + 0.031 * CC) * 1.028) * 1000
Ecoregion	East Cascades, Washington
Citation	Erdody and Moskal (2010)
Structural metric	**Crown bulk density (kg m^-3)**
Model form	exp((-3.696 + 0.025 * P25 - 0.03 * P50 + 0.029 * CC) * 1.032)
Ecoregion	East Cascades, Washington
Citation	Erdody and Moskal (2010)
Structural metric	**Leaf area index**
Model form	-2.907 * ln(1 - CC)
Ecoregion	Puget Lowlands, Washington
Citation	Richardson *et al.* (2009)

* Note: for model input, values are multiplied by TAO area to represent kg per TAO

At the local area scale we calculated measures of density and canopy openings. We calculated TAO density within the 0.1 ha plot and estimated basal area using height-diameter regressions from Jeronimo (Chapter 1). We quantified open space using the open space transform (Churchill *et al.*, 2013); we overlaid a 0.5 m grid on each plot and calculated the distance from each grid cell to the nearest TAO high point. We also delineated gaps using methods from (Churchill *et al.*, 2017). This method uses image morphology operators to delineate gaps that are at least 5 m^2 in size with a core that is at least 9 m from the nearest TAO high point. Predictor variables tested for characterizing openings were (1) mean of the open space transform within the 0.1 ha plot, (2) maximum value of the open space transform within the plot, and (3) percent of plot in a delineated gap. Since these measures were highly correlated we proceeded using only the first option, hereafter referred to as simply "open space."

Lastly, we calculated metrics for each 90×90 m neighborhood. We calculated TAO density, canopy cover from 0.25-2 m, and canopy cover >2 m (the latter following Kane *et al.* (2010)). We used rumple (Kane *et al.*, 2010) as an index of structural complexity. To characterize spatial pattern we calculated the mean clump size, the proportion of area >9 m from a TAO high point, and open space (Chapter 1).

To correct for edge effects, i.e., TAOs spanning a plot boundary and containing unsampled trees outside the plot, we only considered TAOs whose high points were at least 5 m from the edge of the 90×90 m neighborhood. This removed 489 TAOs from analysis.

2.3 Fire mortality response variables

The YFDP was surveyed for tree mortality in each post-fire year 2014-2017, allowing determination of immediate mortality (dead by the time of May 2014 census) versus delayed mortality (alive in 2014 but dead by May 2017 census) and survivorship (alive at May 2017 census). Each tree was assigned one or more causes of mortality based on observable conditions. For this study we focused on trees at ≥10 cm dbh to match commonly used fire mortality models (e.g., FOFEM; Ryan and Reinhardt, 1988); this excluded 22,528 trees between 1 and 9.9 cm from our analysis. We removed 49 trees with mortality causes that could have been affected by the fire, e.g., small trees crushed by falling debris. We also did not consider trees that were dead pre-fire or trees that showed low vigor (imminent mortality) in the 2017 survey (n = 4,358). An additional 2,925 trees landed within the buffer zones between neighborhoods and 1,323 trees were removed from analysis due to the edge corrections.

In preliminary analyses we did not have success directly predicting mortality rates in terms of proportions of trees killed. We chose instead to focus on modeling numbers of trees killed; this approach was much more successful. To allow for indirect calculations of mortality rates we also

simultaneously modeled numbers of live trees pre-fire; the ratio of modeled mortality to modeled density gives a normalized estimate of mortality rates.

We prepared response variables at two scales. At the TAO scale we counted the number of trees per TAO, matching stem mapped trees to TAOs by finding minimum distances between mapped treetops and TAO high points in 3D space (Jeronimo *et al.*, 2018). We then partitioned these counts into counts of immediate mortality, delayed mortality, and survivorship for each TAO. At the neighborhood scale we calculated the number of trees per hectare and the number of killed trees per hectare, without separating immediate from delayed mortalities. This study is focused on the mortality models. The pre-fire density models are reported in Appendix A.

2.4 Independent validation plots

We installed 48, ¼-ha validation plots covering the full elevational and fire severity ranges of the Rim Fire in Yosemite, as far as could be sampled using the 2010 lidar acquisition (Figure 1). The range of sampling for the validation plots intentionally included much warmer, drier, and more *Pinus ponderosa*-dominated sites as well as much cooler, wetter *Abies magnifica*-dominated sites compared to the YFDP. The goal of this was to "bookend" the range of conditions where a model built from the YFDP is likely to behave well.

Plots were located by random selection in clustered locations within 200 m of road or trail access, stratified by Landsat-derived burn severity as calculated by Blomdahl *et al.* (in review) (Figure 1), and were installed in May-July 2017. Each plot was navigated to using a handheld GPS. Plots were laid out as 50×50 m squares oriented to the cardinal directions. Field crews had discretion to rotate plots around the pre-located corner in 90º increments to ensure that plots were good representations of their local area. One corner of each plot was geolocated using a Topcon HiPer V GPS recording at 1 Hz for between 17 and 120 minutes, 60 minutes on average. The

base of each tree ≥10 cm dbh, whether living or dead, standing or down was measured and mapped. Tree status was recorded as one of the following: healthy, declining, nearly dead, recent non-fire mortality, immediate fire mortality, delayed fire mortality, or dead pre-fire. Status calls for dead trees were made from visual cues such as remnant foliage, bole and basal charring and consumption, presence of pitch on the bole, and qualitative assessment of local soil burn severity.

We derived all of the lidar-based predictors and field-based response variables for the validation plots to match the YFDP data. We calculated lidar metrics on 90×90 m squares centered on each 50×50 m plot. Similar to the edge correction used for the YFDP data, we only included TAOs with high points at least 5 m from the edge of the stem maps.

2.5 Water balance, topography and burn weather predictors

Along with structural predictors from lidar, we collected climatic, topographic, and burning weather predictors for each neighborhood in the YFDP and validation plot datasets, since these variables have been shown to be important predictors of fire severity (Miller and Urban, 1999; Kane *et al.*, 2015b). We included actual evapotranspiration and climatic water deficit data from Flint *et al.* (2014). We calculated slope at 30 m and 270 m scales and topographic position index at 500 m, 1 km, and 2 km scales (Weiss, 2001; Kane *et al.*, 2015b). We used FireFamilyPlus version 4.2 (USDA, 2016) to calculate daily burning index, energy release component, maximum temperature, minimum relative humidity, and mean wind speed from the Crane Flat weather station (Station ID 044102). We assigned these values to each neighborhood according to the date of burning, which was taken from daily fire progression maps (Lydersen *et al.*, 2014).

2.6 Statistical analysis

We modeled post-fire tree mortality as a set of generalized linear models in a Bayesian framework. At the TAO scale, we modeled the number of trees per TAO partitioned into immediate mortality, delayed mortality, and survivor classes. At the neighborhood scale we modeled the number of mortalities at the neighborhood level, first using only structural predictors and then additionally including water balance and topography predictors (collectively, topoedaphic predictors) and burn weather predictors. Lastly, we tested a formulation of the full model – including topoedaphic and burn weather predictors – that was hierarchically structured across scales compared to separate models for each scale. The hierarchically structured model included an interaction term between number of trees killed at the neighborhood level and the TAO level (Figure 3). Table 2 summarizes the models we tested and Appendix A gives complete model definitions.

Because water balance, topography, and burning weather had a low range of variation across the YFDP relative to ranges that occur across the Sierra Nevada mixed-conifer zone, we combined the validation plots with the YFDP data for the neighborhood-level modeling to capture more representative ranges of variation. For the TAO-scale models, however, we used only the YFDP data and retained the validation plots as an independent testing data set.

Sample sizes for neighborhood-level models were 72 neighborhoods, 2,620 TAOs and associated local areas, and 10,767 trees ≥10 cm dbh. Sample sizes for the TAO-level models, which did not include the validation plots, were 24 neighborhoods, 1,773 TAOs and local areas, and 7,488 trees.

We estimated posterior distributions of parameters for all models using JAGS 4.2.0 (Plummer 2016) Markov chain Monte Carlo sampling software within the rjags package (version 4.6, Plummer 2016) in the R statistical programming environment (version 3.3.2, R Core Team

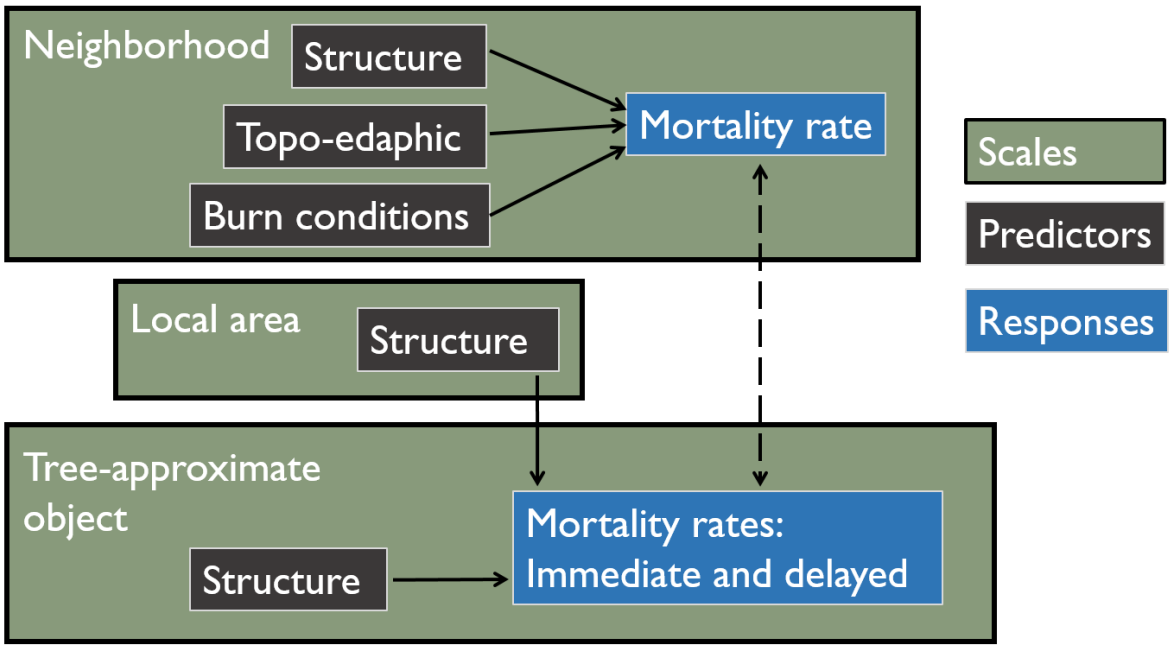

Figure 3 Conceptual formulation of mortality model. Arrows represent explanatory variables being used to predict a response variable; the dashed arrow between response variables represents a cross-scale linkage where an interaction term was included between neighborhood-level mortality and TAO-level mortality. Models were tested both with and without this term.

2016). For initial testing each model was run with two chains, 500 adaptation iterations, 500 burn-in iterations, and 5000 sampling iterations. These runs were judged to have converged based on visual assessment of the posterior distributions for the model coefficients and by the Gelman-Rubin diagnostic (Gelman and Rubin, 1992). Parameters were estimated as the mean of the combined distributions of the two chains. We used posterior predictive checks to confirm that the posterior distributions represented the data well (Gelman *et al.*, 2004); Bayesian *p*-values were all between 0.45 and 0.55.

We used a stochastic search variable selection (SSVS) procedure (George and McCulloch, 1993) to narrow down the list of variables used in the models (Appendix A). This procedure pairs each predictor with a Bernoulli-distributed inclusion parameter that indicates whether the variable is a likely predictor for each link in the Monte Carlo chain given the observed data. The posterior estimates for the Bernoulli distributions' inclusion parameters represent the proportion

Table 2 Four tree mortality model formulations tested in this study. See text section 2.6 for a description of the different components. See Figure 2 for a graphical representation of modeling relationships.

Model	Structural predictors	Topo-edaphic and burn predictors	Cross-scale linkage
A	Yes	No	No
B	Yes	Yes	No
C	Yes	No	Yes
D	Yes	Yes	Yes

of links where the given variable was a likely predictor, and can be interpreted as importance values. We tuned the SSVS to select 4 predictors per link on average.

We selected the final set of models from among the tested options (Table 2) using two criteria. For the TAO-level models, which had separate training and testing data, we used the log predictive density scoring function (LPD) (Gelman *et al.*, 2014) to select the best model. For the neighborhood-level models, which did not have separate training and testing data, we used the posterior predictive loss function (D_{sel}) (Gelfand and Ghosh, 1998). After choosing a model form with these criteria, we chose subsets of predictor variables by iteratively removing those with the lowest importance values until all predictors were included in at least 60% of Monte Carlo links.

We performed final model runs using the same procedures described above for the model selection runs, but with three chains, 2000 adaptation iterations, 2000 burn-in iterations, and 20000 sampling iterations. We then evaluated absolute accuracy by calculating the root mean squared prediction errors on both training and testing datasets.

2.7 Mechanistic interpretation of model results

We took the most important predictor at each of the TAO and local area scales for both immediate and delayed TAO mortality to investigate possible mechanisms through which these structural characteristics affect fire mortality at fine scales. We stratified the range of each of these predictor variables into 10 bins set so that each bin contained an approximately equal number of trees. We compiled the list of causes of mortality – of which each tree could have

several – for each bin and normalized this list to sum to one to get proportions of mortality factors in different categories.

For immediate mortalities we used the following categories of mortality agents: suppression, rot, beetle, mechanical, fire: crown kill, fire: stem kill, and fire: mechanical, the latter of which refers to trees that suffered mechanical failures due to fire removal of structural tissue, but which otherwise would probably have survived. Fire: crown kill and fire: stem kill were almost always recorded together. To help differentiate between them we only included the one that was recorded as more severe in the field survey. For delayed mortalities we first compared fire-related factors to non-fire related factors, then evaluated relative proportions of non-fire-related factors alone.

We took these mortality proportion data to represent contingency tables (i.e., a matrix where each cell gives the number of mortalities related to a given agent within a given structural stratum). We calculated χ^2 statistics for these tables and performed an iterative procedure to reduce the 10 bins to the two most highly contrasting bins possible. At each step we tested every pair of adjacent bins to see which yielded the highest χ^2 statistic when combined. We repeated this until we were left with only two bins, ensuring that the χ^2 statistic was significant at each step. From this we were able to identify a threshold for each of the structural predictors tested along with an effect on causes of mortality at that threshold.

3. Results

3.1 Immediate and delayed mortality on the YFDP

Of trees ≥10 cm DBH on the YFDP that were alive in 2013 (n = 11,974), 39% died immediately after fire, 24% died 2-4 years post-fire, and the remaining 37% were alive in May 2017. Mortality decreased monotonically over time: 62% of mortalities occurred in the first year

(2013-2014) followed by 22% in the second year, 12% in the third year, and 4% in the fourth year. Mortality rates decreased similarly, with a rate of 39% the first year, 23% of remaining live trees the second year, 16% the third year, and 6% the fourth year (Figure 4). In general, smaller trees died earlier on and larger trees died in later years (Figure 4). The quadratic mean diameter of trees that died in the first year was 21.0 cm, followed by 27.6 in the second year, 57.8 in the third year, and 55.1 in the fourth year.

3.2 Validation plots

The 48 validation plots installed spanned a range of elevations from 1430 to 2250 m and covered forest types ranging from low montane *Pinus ponderosa-Quercus chrysolepis* to high montane *Abies magnifica* (Table 3). Density of trees ≥10 cm dbh ranged from 85 to 1005 trees ha^{-1} and basal area ranged from 14 to 122 m^2 ha^{-1}. Species included all those found in the YFDP

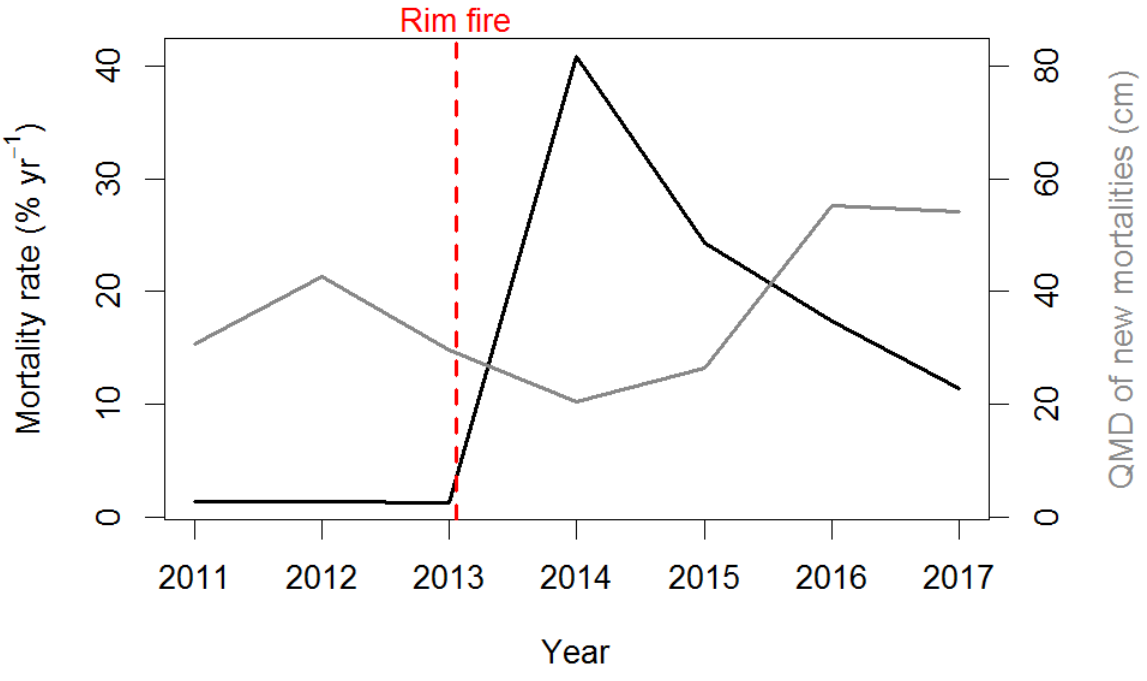

Figure 4 Rates and demographics of tree mortality for trees ≥10 cm dbh on the Yosemite Forest Dynamics Plot for three pre-fire censuses and four post-fire censuses. QMD refers to quadratic mean diameter.

Table 3 Characteristics of 48 validation plots installed across the footprint of the Rim fire within Yosemite National Park, where lidar data were available. Abbreviations: BA = basal area, ABCO = Abies concolor, ABMA = A. magnifica, CADE = Calocedrus decurrens, CONU = Cornus nuttallii, PICO = Pinus contorta, PIJE = P. jeffreyi, PILA = P. lambertiana, PIPO = P. ponderosa, QUCH = Quercus chrysolepis, QUKE = Q. kelloggii, UNKN = unknown charred remnant.

						Proportions of basal area										
Plot	**Elevation (m)**	**Density (trees ha^{-1})**	**BA (m^2 ha^{-1})**	**Immediate mortality**	**Delayed mortality**	**ABCO**	**ABMA**	**CADE**	**CONU**	**PICO**	**PIJE**	**PILA**	**PIPO**	**QUCH**	**QUKE**	**UNKN**
G1-P1	1976	309	71.1	17%	14%	0.70		0.15				0.14	0.01			
G1-P2	1592	567	49.1	48%	45%	<0.01		0.15				0.09	0.68	<0.01	0.07	
G1-P3	1632	471	99.2	43%	38%	0.88		0.06				0.02			0.04	<0.01
G1-P4	1659	729	73.1	49%	43%	0.30		0.29				0.22	0.20			
G1-P5	1575	511	90.9	46%	44%	0.45	<0.01	0.18				0.07	0.16		0.12	0.01
G1-P6	1924	753	70.4	38%	27%	0.61		0.11	<0.01			0.28				
G1-P7	1944	565	91.3	41%	38%	0.53		<0.01				0.47			<0.01	
G1-P8	1623	712	70.9	65%	35%	0.58		0.19				0.09	0.09		0.01	0.06
G2-P1	1545	601	49.3	63%	37%	0.06		0.22				0.14	0.45	0.05	0.08	
G2-P2	1569	860	46.7	44%	47%	0.13		0.17				0.14	0.43	0.01	0.03	0.08
G2-P3	1470	580	30.6	29%	33%			0.49					0.40		0.05	0.07
G2-P4	1689	141	73.8	16%	12%	0.34		0.20				0.43			0.03	
G2-P5	1743	416	89.8	33%	25%	0.18		0.19	0.01			0.62				<0.01
G2-P7	2057	404	93.6	50%	33%	0.32	0.10	0.01				0.50				0.08
G3-P1	1900	587	89.7	20%	18%	0.22	0.08	0.17				0.50				0.02
G3-P2	1744	327	65.0	45%	45%	0.01		0.35					0.51		0.05	0.08
G3-P3	1958	305	107.9	26%	21%	0.39	0.22	0.26				0.13				
G3-P4	2044	505	121.7	33%	31%	0.13	0.37	0.33				0.16				
G3-P5	1956	742	80.1	47%	34%	0.81		0.08				0.01				0.10
G3-P6	1629	516	69.4	25%	22%	0.09		0.49				<0.01	0.23		0.18	
G3-P7	1668	1005	94.9	62%	38%	0.26		0.31				0.30	0.06			0.06
G4-P1	1855	519	19.3	27%	19%			0.14			0.80					0.06
G4-P2	1899	112	76.5	15%	15%	0.88		0.04			0.09					
G4-P3	1929	389	93.1	44%	39%	0.37		0.12				0.16	0.31			0.03

Table 3, continued Characteristics of 48 validation plots installed across the footprint of the Rim fire within Yosemite National Park, where lidar data were available. Abbreviations: BA = basal area, ABCO = Abies concolor, ABMA = A. magnifica, CADE = Calocedrus decurrens, CONU = Cornus nuttallii, PICO = Pinus contorta, PIJE = P. jeffreyi, PILA = P. lambertiana, PIPO = P. ponderosa, QUCH = Quercus chrysolepis, QUKE = Q. kelloggii, UNKN = unknown charred remnant.

						Proportions of basal area										
Plot	**Elevation (m)**	**Density (trees ha^{-1})**	**BA (m^2 ha^{-1})**	**Immediate mortality**	**Delayed mortality**	**ABCO**	**ABMA**	**CADE**	**CONU**	**PICO**	**PIJE**	**PILA**	**PIPO**	**QUCH**	**QUKE**	**UNKN**
G4-P4	1939	427	61.1	48%	43%	0.50		0.34				0.10	0.04		0.01	<0.01
G4-P5	1944	443	85.1	51%	37%	0.99						0.01				
G4-P6	1907	388	69.9	29%	24%	0.90		0.03			0.02	0.05	<0.01			<0.01
G4-P7	1909	389	104.4	39%	35%	0.78	0.15	<0.01				0.07				
G4-P8	1894	589	95.6	30%	31%	0.81		0.04				0.04				0.11
G5-P1	2018	718	74.5	48%	39%	0.31					0.24	0.44			0.01	
G5-P2	1992	378	65.2	47%	29%	0.58	0.01	0.27				0.12				0.01
G5-P3	1961	317	83.3	52%	42%	0.57	0.30	<0.01			0.02	0.10				<0.01
G5-P4	1971	568	70.4	24%	21%	0.74					0.25	0.01			0.01	
G5-P5	1959	252	107.3	37%	31%	0.59					0.09	0.32				
G5-P6	1960	493	59.5	33%	30%	0.82		0.18								
G5-P7	1974	150	99.3	34%	29%	0.81	<0.01	<0.01			<0.01	0.17				0.01
G6-P1	2011	602	59.3	28%	28%	0.80		<0.01				0.20				
G6-P2	1969	323	81.3	32%	27%	0.71		0.05				0.25				
G6-P3	1992	351	101.1	51%	45%	0.39		0.29				0.32				
G6-P4	1965	312	97.7	54%	41%	0.77		0.07				0.16				
G6-P5	2010	385	92.4	61%	39%	0.47		0.01				0.52			<0.01	
G6-P7	2006	215	80.6	65%	33%	0.74		0.01				0.19			0.01	0.06
G7-P1	2240	434	18.7	6%	4%	0.04		0.08			0.83	0.05				
G7-P2	2276	85	14.1	4%	3%		0.01			0.53	0.38	0.08				
G7-P3	2212	129	81.9	64%	33%	0.30	0.64				0.01	0.04				0.01
G7-P4	2225	393	43.1	23%	17%	0.15	0.68				0.16	<0.01			<0.01	0.01
G7-P5	2234	163	73.7	66%	34%	0.62	0.20					0.07				0.12
G7-P8	2227	107	26.5	18%	9%	0.24					0.47	0.19	0.10			

as well as *Pinus contorta*, *P. jeffreyi*, and *Quercus chrysolepis*. Mortality was classified in the field as 47% immediate and 53% delayed; after applying a correction factor for misidentified mortality status (Appendix A), we estimated that 56% of mortality was immediate and 44% was delayed. In total, 5,686 trees were sampled on the validation plots of which 3,279 were included for analysis after the edge correction.

Overall, the 24 90×90 m neighborhoods from the YFDP and the 48 neighborhoods from the validation plots spanned a wide range of conditions in terms of burn weather, topography, and climate (Table 4). Neighborhoods burned in the Rim fire between August 27 and September 9, 2013 at burning indices from 54 to 83, energy release component values from 70 to 80, maximum air temperatures from 22 to 26 °C, minimum relative humidities from 14 to 45%, and mean wind speeds from 2.2 to 5.8 m s^{-1} (Table 5). In terms of topography, neighborhood-level slope ranged from 5% to 100% and topographic position index ranged from −100 m to 180 m. Actual evapotranspiration ranged between 260 and 500 mm while climatic water deficit ranged between 380 and 630 mm.

3.3 Model results

Model D, which included topoedaphic and burn predictors as well as the cross-scale linkages between neighborhood models and TAO models, performed best (Table 6). Including the topoedaphic and burn predictors had the largest effect on neighborhood-level models, improving D_{sel} values by 54%. The cross-scale linkage did not have a measurable effect on the neighborhood-level models. In contrast, the cross-scale linkage had a substantial effect on the TAO-level mortality model, improving the LPD value by 18%. Including topoedaphic and burning predictors had a smaller effect, improving LPD by 6%.

Table 4 Characteristics of "neighborhoods," 90×90 m windows comprising the largest scale explicitly incorporated in this study. Twenty-four neighborhoods were tiled within the Yosemite Forest Dynamics plot and 48 additional neighborhoods were centered on the validation plots (Table 2). Abbreviations: TPI = topographic position index (Weiss, 2001), AET = actual evapotranspiration, Deficit = climatic water deficit.

Neighborhood	Burn Day	Slope, 30 m radius (%)	Slope, 270 m radius (%)	TPI, 500 m radius (m)	TPI, 1 km radius (m)	TPI, 2 km radius (m)	AET (mm)	Deficit (mm)
YFDP-01	31-Aug	63.4	23.6	-4.3	32.5	114.3	440	552
YFDP-02	31-Aug	24.0	28.3	-5.1	27.0	104.6	440	552
YFDP-03	1-Sep	40.9	33.1	18.9	47.2	118.9	440	552
YFDP-04	31-Aug	45.5	28.8	4.2	39.8	118.1	436	543
YFDP-05	1-Sep	53.7	33.7	-5.1	24.3	96.9	436	543
YFDP-06	1-Sep	57.7	37.9	-3.5	21.7	87.4	436	543
YFDP-07	1-Sep	40.3	33.2	-1.3	31.5	105.7	436	543
YFDP-08	1-Sep	60.4	36.5	-8.1	17.9	86.0	436	543
YFDP-09	1-Sep	53.9	38.9	-16.7	4.8	64.9	436	543
YFDP-10	1-Sep	28.8	36.4	4.2	33.1	102.6	436	543
YFDP-11	1-Sep	64.0	39.7	-0.6	21.4	84.0	428	530
YFDP-12	1-Sep	56.4	40.7	-7.7	8.9	62.4	428	530
YFDP-13	1-Sep	34.7	39.3	14.2	38.4	102.2	428	530
YFDP-14	1-Sep	48.7	43.2	12.1	29.3	85.7	428	530
YFDP-15	1-Sep	48.1	43.1	8.9	20.6	67.0	428	530
YFDP-16	1-Sep	54.6	41.5	14.2	33.2	91.0	428	530
YFDP-17	1-Sep	71.2	45.0	10.0	22.3	72.4	428	530
YFDP-18	1-Sep	56.2	45.1	6.4	13.6	53.4	428	530
YFDP-19	1-Sep	59.0	44.0	10.2	24.6	76.2	420	518
YFDP-20	1-Sep	51.5	47.0	-1.0	6.5	49.7	420	518
YFDP-21	1-Sep	47.4	47.9	1.3	4.3	37.6	420	518
YFDP-22	1-Sep	67.1	47.4	12.4	21.8	66.4	420	518
YFDP-23	1-Sep	61.3	48.1	0.4	3.8	40.5	420	518
YFDP-24	1-Sep	62.4	47.1	-4.6	-5.3	21.2	420	518
G1-P1	3-Sep	40.1	25.1	28.9	59.7	106.8	465	488
G1-P2	31-Aug	54.1	27.4	16.1	7.9	-32.1	387	573
G1-P3	31-Aug	36.9	34.4	-12.6	-43.3	-104.0	404	514
G1-P4	31-Aug	14.2	11.9	0.9	11.9	4.6	375	556
G1-P5	31-Aug	33.1	32.1	-7.8	-38.3	-94.2	376	549
G1-P6	30-Aug	9.4	17.0	2.1	38.8	125.8	440	552
G1-P7	3-Sep	77.3	37.2	16.3	31.6	69.5	432	539
G1-P8	31-Aug	36.3	25.1	-8.3	-9.7	-42.2	375	554
G2-P1	31-Aug	51.7	33.0	22.6	7.6	-40.3	369	593
G2-P2	31-Aug	96.0	28.1	26.6	13.9	-37.1	446	505
G2-P3	31-Aug	63.1	37.4	7.9	11.4	-26.6	410	634
G2-P4	31-Aug	13.5	17.1	-9.8	-14.5	-48.6	410	517

2552

Table 4, continued Characteristics of "neighborhoods," 90×90 m windows comprising the largest scale explicitly incorporated in this study. Twenty-four neighborhoods were tiled within the Yosemite Forest Dynamics plot and 48 additional neighborhoods were centered on the validation plots (Table 2). Abbreviations: TPI = topographic position index (Weiss, 2001), AET = actual evapotranspiration, Deficit = climatic water deficit.

Neighborhood	Burn Day	Slope, 30 m radius (%)	Slope, 270 m radius (%)	TPI, 500 m radius (m)	TPI, 1 km radius (m)	TPI, 2 km radius (m)	AET (mm)	Deficit (mm)
G2-P5	1-Sep	53.5	50.3	-12.0	-12.3	-48.9	408	499
G2-P7	4-Sep	30.5	29.2	34.2	66.1	120.7	403	504
G3-P1	6-Sep	46.3	31.4	6.8	-3.1	-37.4	372	451
G3-P2	30-Aug	31.6	28.4	7.9	18.8	25.0	404	508
G3-P3	8-Sep	36.8	28.7	10.2	25.5	-7.1	435	382
G3-P4	12-Sep	20.9	31.4	-4.3	8.1	38.6	387	478
G3-P5	8-Sep	30.4	18.1	10.6	35.5	9.0	371	460
G3-P6	30-Aug	45.2	32.7	9.6	19.3	10.2	421	499
G3-P7	30-Aug	31.6	11.3	-2.5	5.0	29.6	429	517
G4-P1	30-Aug	42.7	22.1	-15.7	-9.0	-38.6	405	462
G4-P2	29-Aug	25.5	6.5	-14.2	-17.4	-11.4	401	482
G4-P3	28-Aug	31.7	25.8	5.0	19.4	57.1	412	487
G4-P4	28-Aug	22.9	21.0	19.0	22.1	54.1	416	473
G4-P5	27-Aug	29.2	18.1	-0.9	-8.5	-1.9	423	448
G4-P6	27-Aug	29.3	8.6	-16.5	-29.3	-16.3	409	440
G4-P7	28-Aug	37.9	6.7	-1.7	-5.3	-28.8	409	450
G4-P8	29-Aug	37.7	14.4	-3.2	2.0	0.9	394	478
G5-P1	27-Aug	70.0	42.3	-9.9	-24.8	-9.0	405	450
G5-P2	27-Aug	33.5	17.5	-2.1	1.8	26.4	417	462
G5-P3	28-Aug	46.7	18.1	-13.6	-28.4	-38.3	398	454
G5-P4	28-Aug	50.4	26.6	-29.7	-59.3	-47.1	401	451
G5-P5	27-Aug	17.3	19.1	-1.3	-24.1	-31.0	415	439
G5-P6	27-Aug	43.1	17.1	-3.3	-11.2	-12.7	419	444
G5-P7	27-Aug	11.0	17.8	-2.6	-19.0	-10.5	429	438
G6-P1	27-Aug	46.6	20.2	30.6	62.5	147.6	426	503
G6-P2	28-Aug	22.9	14.3	-11.1	8.0	93.6	426	503
G6-P3	28-Aug	34.8	11.0	9.7	34.4	109.4	413	487
G6-P4	28-Aug	31.0	19.7	-2.2	6.6	67.6	407	486
G6-P5	28-Aug	11.7	12.9	30.0	56.0	121.3	413	487
G6-P7	28-Aug	12.1	6.9	21.9	53.8	127.6	472	440
G7-P1	29-Aug	21.0	20.9	47.7	89.8	127.0	283	545
G7-P2	12-Sep	12.3	17.5	11.9	45.1	122.5	288	509
G7-P3	3-Sep	19.1	29.5	-1.9	20.1	70.3	397	425
G7-P4	3-Sep	23.8	13.6	-1.0	33.8	93.3	404	409
G7-P5	4-Sep	35.3	22.4	16.6	46.2	105.3	284	524
G7-P8	1-Sep	19.2	30.2	42.0	72.7	113.0	345	485

2554 The top predictors for the neighborhood-level mortality model were AET, open space, energy
2555 release component, maximum burning day temperature, canopy cover >2 m, and rumple.
2556 Immediate mortality at the TAO level was predicted best by maximum TAO height, canopy
2557 cover <8 m, mean clump size in local area, open space in local area, and leaf are index. Number
2558 of delayed mortalities was predicted best by local TAO density, canopy cover 8-16 m and <2 m,
2559 canopy fuel weight, crown base height, and open space in local area (Table 7).
2560 Root mean squared prediction error (RMSE) for the final parsimonious set of models was 70
2561 trees ha^{-1} ≥10 cm dbh for the neighborhood mortality model. When predicted back on the YFDP
2562 training data, the number of immediate mortalities ≥10 cm dbh per TAO had an RMSE of 1.6
2563 trees and the number of delayed mortalities had an RMSE of 1.7 trees. Predicting on the out-of-
2564 sample validation plots, RMSE for number of immediate mortalities ≥10 cm dbh was 1.9 trees
2565 and RMSE for delayed mortalities was 1.4 trees. When these numbers were summarized up to
2566 the neighborhood scale, the RMSE for immediate mortalities ≥10 cm dbh was 70 trees ha^{-1} and
2567 was 44 trees ha^{-1} for delayed mortalities.

2568 *3.4 Relationships between fine-scale structure and mortality agents*

2569 Immediate mortalities were overwhelmingly fire-related, with nearly 98% of the mortality
2570 factor records analyzed attributed to stem kill, crown kill, and fire-mechanical damage (n =

Table 5 Burning weather metrics given for days on which one or more of the neighborhoods analyzed burned in the Rim fire.

Date	27-Aug	28-Aug	30-Aug	31-Aug	2-Sep	3-Sep	4-Sep	6-Sep	8-Sep	12-Sep
Burning index	73	83	68	54	70	69	62	70	67	61
Energy release component	78	76	80	77	72	70	71	72	77	77
Maximum temperature (°F)	72	74	80	80	76	73	76	75	78	75
Maximum temperature (°C)	22.2	23.3	26.7	26.7	24.4	22.8	24.4	23.9	25.6	23.9
Minimum relative humidity (%)	26	35	24	16	35	45	42	33	14	29
Average wind speed (mph)	10	13	7	5	11	11	8	10	7	7
Average wind speed (m/s)	4.5	5.8	3.1	2.2	4.9	4.9	3.6	4.5	3.1	3.1
Number of neighborhoods burned	8	10	5	12	1	4	2	1	2	2

Table 6 Model assessment statistics for the four tested model formulations. The best statistic for each column is in bold italic face. Abbreviations: RMSE = root mean squared error; D_{sel} = posterior predictive loss function (Gelfand and Ghosh, 1998), where lower numbers represent a better and more parsimonious model fit; LPD = log predictive density (Gelman *et al.*, 2014), where higher (less negative) numbers represent a better and more parsimonious model fit.

Neighborhood scale			**RMSE (trees ha^{-1})**		
	Model	**D_{sel}**	**Immediate mortality**	**Delayed mortality**	**Total mortality**
	A	926699	78.7	63.4	89.4
	B	426853	70.8	44.3	84.8
	C	924992	76.8	63.4	89.4
	D	***426432***	***70.1***	***43.9***	***84.4***
Tree-approximate object scale			**RMSE (n trees)**		
			In-sample		**Out-of-sample**
	Model	**LPD**	**Immediate mortality**	**Delayed mortality**	**Immediate mortality**	**Delayed mortality**
	A	-5716	1.693	1.759	1.898	1.388
	B	-5394	1.693	1.759	1.897	1.387
	C	-4842	1.638	1.734	1.886	***1.398***
	D	***-4793***	***1.613***	***1.706***	***1.885***	1.403

1321). At the TAO scale, the proportion of mortalities attributed to crown kill was significantly higher when the dominant canopy of a TAO was <51 m tall (66% vs. 74%; $p < 0.001$). The increase in crown kill was mirrored by a decrease in stem kill of similar magnitude (Figure 5). At the local area scale, crown kill decreased and stem kill increased by five percentage points when mean clump size was >23 TAOs ($p < 0.05$). Fire-mechanical mortalities (total n = 12) were five times more common when TAO height was >51 m and when local area mean clump size was >23 TAOs (Figure 5).

Delayed mortalities were also dominated by fire-related mortality factors (71%, n = 1206). At the TAO scale the proportion of mortality factor records that were fire-related was 14 percentage points lower when crown base height was >28 m ($p < 0.001$). At the local area scale fire-related mortality was 22 percentage points higher when TAO density was >170 ha^{-1}($p <$ 0.001) (Figure 5).

Of the non-fire related factors, bark beetles and rots accounted for the most mortality, 46% and 34% respectively, followed by suppression with 16% of mortality records and mechanical

Table 7 Predictors selected for the final models along with importance values resulting from the stochastic search variable selection procedure (George and McCulloch, 1993). The importance values represent the proportion of times in a Monte Carlo chain that the variable in question was selected to be included in the model, based on the likelihood of the predictor variable given the observed data.

Sub-model	Predictor	Importance value
Neighborhood mortality	AET	1.00
	Open space	1.00
	Energy release component	0.99
	Maximum burn day temperature	0.96
	Canopy cover >2 m	0.88
	Rumple	0.80
TAO immediate mortality	Maximum height	1.00
	Canopy cover <8 m	1.00
	Mean clump size in local area	0.99
	Local area open space	0.89
	Leaf area index	0.73
TAO delayed mortality	Local density	1.00
	Canopy cover 8-16 m	0.99
	Canopy cover <2 m	0.99
	Canopy fuel weight	0.88
	Crown base height	0.86
	Local area open space	0.75

damage with the remaining 4%. Proportions of mortality agents responded to crown base height at the TAO scale (Figure 5). When crown bases were higher than 18 m, beetle mortalities were 11 percentage points higher, rot mortalities were 7 percentage points lower, and mechanical mortalities decreased from 6.4% to 2.7% ($p < 0.001$). Suppression mortalities did not differ with crown base height. At the local area scale, TAO densities greater than 180 ha^{-1} were associated with less beetle kill (48% reduced to 23%), more rot (32% to 50%), and more suppression (15% to 22%). The share of mortalities attributed to mechanical damage did not differ with TAO density.

4. Discussion

4.1 Mortality rates and agents over time

Patterns of mortality on the YFDP over time generally followed the paradigm outlined by many other studies, where most mortality occurred in the first year (62% of mortalities compared to 55-90% in the literature) and subsequent years showed monotonically decreasing amounts of tree death (Figure 4) (Keyser *et al.*, 2006; Hood and Bentz, 2007; Hood *et al.*, 2010; Prichard and Kennedy, 2012). Also following past studies, first-year mortality occurred disproportionately in small trees and mortality in subsequent years advanced through larger size classes (Figure 4) (Breece *et al.*, 2008; Youngblood *et al.*, 2009; Van Mantgem *et al.*, 2011). The basic explanation for this pattern is that immediate mortality is due mainly to direct fire effects – i.e., crown and cambium damage – which smaller trees are more susceptible to, while delayed mortality is due to stress from non-lethal damage predisposing trees to other agents of mortality (Youngblood *et al.*, 2009; Woolley *et al.*, 2012; Smith *et al.*, 2016). Not only are larger trees more likely to be damaged than immediately killed, but also many agents of delayed mortality, particularly bark beetles, tend to favor larger trees (Breece *et al.*, 2008; Hood *et al.*, 2010; Jenkins *et al.*, 2014). Our results partially support this line of reasoning, but suggest that mortality patterns are more complex than this model supposes. In particular, direct effects of fire damage to vascular and foliar tissue often lead to mortality 2-4 years post-fire with no other apparent mortality agents (Figure 6).

4.2 Model accuracy in context

Model results were reasonably accurate, especially in the context of results achieved from past studies focusing on predicting fire mortality given pre-fire data. For example, at scales of tens of thousands of hectares, Kane *et al.* (2015b) predicted fire severity at a 30 m grain size resulting in a pseudo-r^2 value of 0.50 and Lydersen *et al.* (2017) created a similar model with a pseudo-r^2 value of 0.46. At finer scales, Furniss *et al.* (in review) predicted death of individual

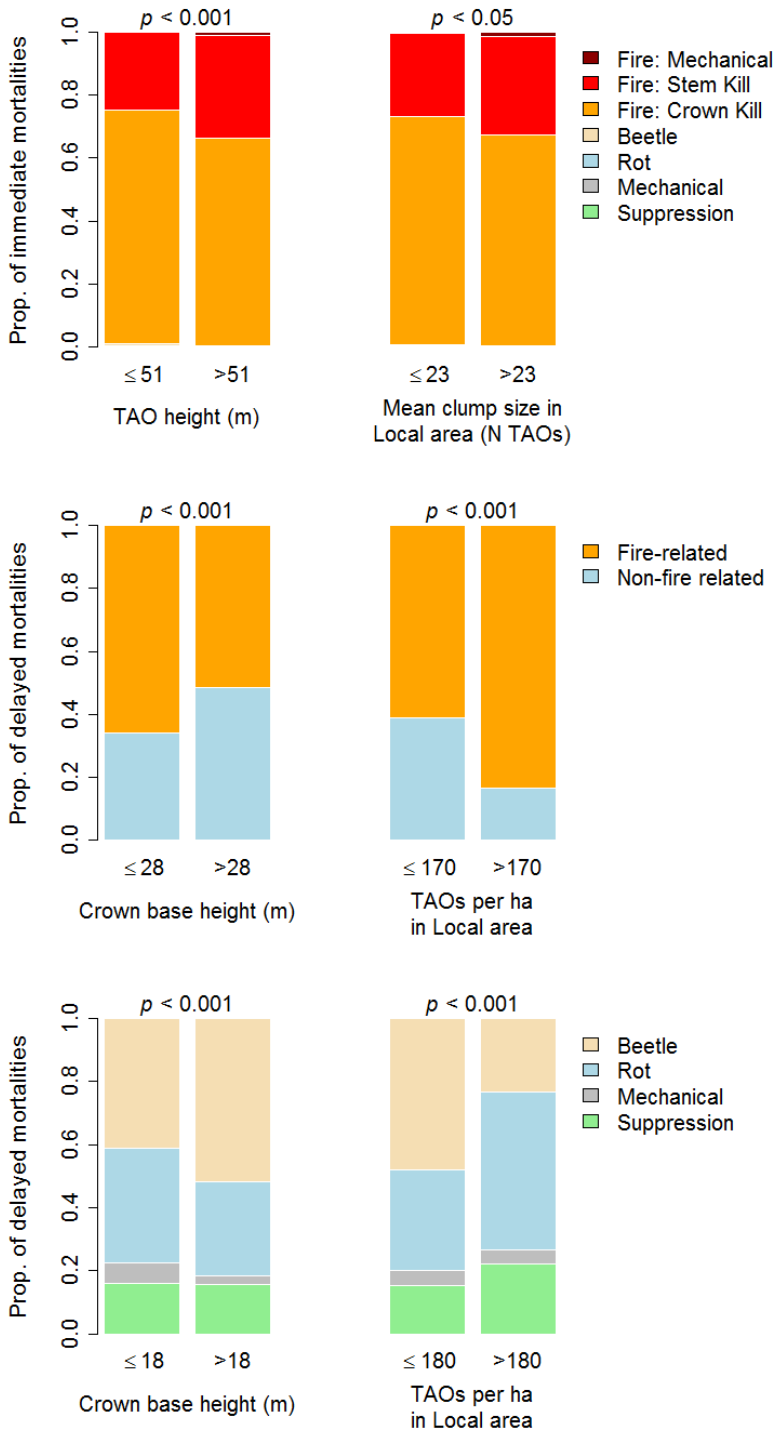

Figure 5 Factors associated with mortality for trees ≥10 cm dbh on the Yosemite Forest Dynamics Plot killed since the 2013 Rim fire that were included in model analysis, stratified by structural conditions that were found to be important predictors of mortality at the TAO scale (left column) and the local area scale (right column). Each killed tree had one or more factors associated with death recorded; we normalized these to 0-1 to improve comparison. The p-values refer to $\chi 2$ tests comparing the distributions of mortality factors for each structural strata.

2618

trees from pre-fire structure with accuracies ranging from 75-88%. In comparison, our neighborhood-level mortality model had an r^2 value of 0.67 and our TAO-level immediate mortality and delayed mortality models had r^2 values of 0.55 and 0.48, respectively. A major limitation of this model's potential accuracy is that it does not include any species data directly, since airborne lidar does not measure composition. This limits the model because tree physiological responses to fire vary among species, and so species exhibit differential rates of fire mortality under the same circumstances (Ryan and Reinhardt, 1988). Furthermore, due to a

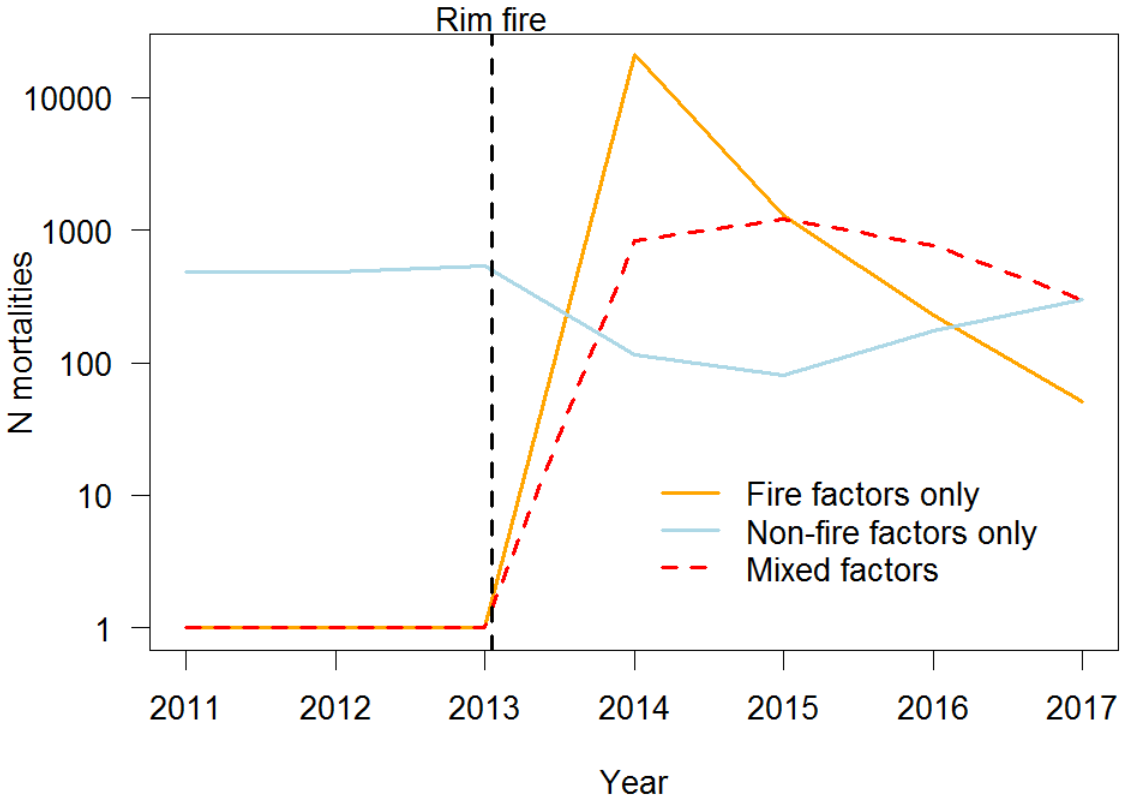

Figure 6 Predominance of mortality factor classes for trees ≥10 cm dbh on the Yosemite Forest Dynamics plot for three pre-fire censuses and four post-fire censuses reported on the basis of individual trees. "Fire factors only" refers to trees that had no observable conditions contributing to death except fire damage, "non-fire factors only" refers to trees that had no observable fire damage, and "mixed factors" refers to trees for which both fire-related and non-fire related conditions contributing to death were observed.

long history of fire exclusion across much of the Sierra Nevada mixed-conifer zone the species composition of the diameter distribution has been changing (Becker and Lutz, 2016). This study included plots with a variety of burn histories: for some plots the Rim Fire was a first-entry fire after 80-100 years of fire exclusion (e.g., the YFDP) while for others it was the third fire in the last 30 years (e.g., validation plot G3-P4). These varying histories certainly led to differing amounts of compositional change and restoration since the onset of fire suppression which are sure to affect fire mortality patterns.

An important characteristic of this model is that model accuracy in terms of RMSE was nearly identical for predictions on in-sample training data compared to predictions on out-of-sample testing data (Table 6). Our validation plot dataset, which was not used to fit TAO-level models, covers a wide range of environmental conditions spanning the range of elevation, aspect, and fire severity that the Rim fire burned through in Yosemite. The fact that predictions on this holdout dataset are similarly accurate to predictions on the geographically constrained training dataset suggests that the model properly captures some mechanisms driving tree mortality and can be applied throughout the mid-montane Sierra Nevada mixed-conifer zone, within the environmental bounds captured by our validation plots.

4.2 Multi-scale drivers of fire mortality

The predictors associated with neighborhood-scale mortality fell into three basic categories. Canopy cover and AET are measures of fuel amounts, where canopy cover gives the amount of canopy fuels and AET is related to site productivity and thus shrub and herb fuel loads as well as proportions of shade-tolerant understory trees (Lutz *et al.*, 2010; Kane *et al.*, 2015b). Fuel configuration was characterized by open space proportion and rumple, measures of overstory fuel breaks and canopy complexity, respectively (Kane *et al.*, 2010; Kane *et al.*, 2014). Lastly,

burn weather was described by maximum temperature on burn day and energy release component. Topographic predictors like slope and topographic position were not themselves important predictors, but do affect AET. This suggests that the importance of these conditions is mainly expressed through their role in modulating growing conditions, and that the signal of burn weather overwhelms the signal of slope and topographic position in terms of fire severity.

Structural conditions within TAOs and within local areas both offered important predictors of TAO-scale mortality. Immediate mortality was lower within TAOs with a taller maximum height, with less ladder fuels, and with less leaf area. This is consistent with common understanding of fire mortality. Larger trees are more likely to survive (Ryan and Reinhardt, 1988; Hood *et al.*, 2007; Furniss *et al.*, in review), ladder fuels carry surface fires into the canopy (Stephens, 1998; Agee and Skinner, 2005), and high leaf area usually indicates shade-tolerant, fire-intolerant species (Lusk, 2002; Gersonde and O'Hara, 2005). At the local area scale, larger openings led to decreased immediate mortality, presumably since openings act as overstory fuel breaks. About one third of delayed mortalities were attributed to fire effects alone, and some important predictors of delayed mortality did seem to relate to fire behavior. For example, canopy cover 0-2 m represents surface fuel loads, crown base height represents the ease with which fire can transition from the surface to the canopy, and the amount of open space in the local area was also important for delayed mortality. However, many of the important predictors of delayed mortality were associated with other agents of mortality. For example, canopy fuel weight at the TAO level may be associated with the size of crown that a tree must support, and larger crowns are more difficult to maintain under drought conditions (Donovan and Ehleringer, 1991; Martínez-Vilalta and Piñol, 2002; Tang *et al.*, 2005). Local TAO density may represent nearby competition, especially for moisture resources (Young *et al.*, 2017).

Explicitly including cross-scale linkages between neighborhood-level and TAO-level models substantially improved model fits (Table 6). This aligns with the theoretical understanding of fire's landscape ecology, where different scales rest within a hierarchical structure with cross-scale interactions (Kotliar and Wiens, 1990; Hessburg *et al.*, 2015). The degree of improvement realized at the TAO scale was more than at the neighborhood scale, suggesting that cross-scale interactive drivers of fire severity exert a stronger influence from the top down than from the bottom up. This agrees with past studies that have identified weather and climatic water balance as the most important drivers of fire severity, upon which variation due to finer-scale structure is arranged (Gill and Taylor, 2009; Lutz *et al.*, 2009b; Kane *et al.*, 2015b; Lydersen *et al.*, 2017). However, we found that spatial configuration of fuels at the neighborhood scale was also an important driver: model C performed nearly as well as model D for TAO mortality, despite not including burn weather, water balance, or topography predictors (Table 6). It appears that, rather than fine-scale effects integrating up to form a broad-scale result, the broad-scale conditions instead form the basic template that is locally modified by fine-scale conditions.

Including the burn weather, water balance, and topography predictors had an effect on the neighborhood-level models that did not carry down to the TAO-level models. This makes sense, since the topoedaphic predictors were covariates only at the neighborhood scale. Nevertheless, it is interesting that the TAO-level models including a cross-scale linkage performed similarly regardless of whether topoedaphic predictors were included. This indicates, perhaps, that the useful information garnered from the cross-scale linkage does not necessarily have to be highly accurate; a simple indication of low, moderate, or high neighborhood-level severity may be enough to inform and improve TAO-level results. For future modeling applications at tree or tree-approximate scales, including an interaction term representing simple fire severity classes at

a neighborhood-like scale – such as data derived from satellite remote sensing – may be helpful. Of the three categories of important neighborhood-level predictors, two (fuel amount and configuration) were partially or fully represented in the structure-only model, model A (Table 1). It appears, then, that the improvement achieved by model D was mainly due to the addition of burn weather parameters.

Although the spatial extent of this study covered tens of thousands of hectares and included a wide range of environmental conditions, we did not explicitly analyze processes occurring at scales larger than the 90×90 m neighborhood. Our analysis captured the variation that may occur at the 1000-10,000 ha scale by virtue of plot placement. However, we did not capture processes like day-to-day fire spread, which can be driven by synoptic weather patterns and watershed-scale topography; other research focusing on these scales suggests that the pattern we observed – significant top-down effects – would hold upon expanding the hierarchy of scales to include larger scales like watersheds (Gill and Taylor, 2009; Collins, 2014; Lydersen *et al.*, 2017).

4.3 Relationships between fine-scale structure and mortality agents

The balance between immediate mortalities caused by stem kill versus crown kill is a rough indicator of fine-scale flame lengths relative to canopy height, since crown scorch and consumption require flames to reach into the canopy. Trees within taller TAOs suffered less crown kill than trees in shorter TAOs; the same was true for trees in larger clumps (Figure 5). This could be because the shade under spreading tree crowns and within large clumps excludes understory vegetation; however, it could also be that larger trees and trees in clumps experienced similar levels of damage to smaller trees in smaller clumps, but were able to recover better. Larger trees have more developed root systems and are more resilient to damage, and trees in clumps have mutually supportive root grafting and mycorrhizal relationships that can help

provide clump-level resilience (Warren *et al.*, 2008; Simard, 2009; Salomón *et al.*, 2016). It is also possible that trees within larger clumps are less exposed to convection currents that carry damaging heat into the canopy (Smith *et al.*, 2016; Parsons *et al.*, 2018). Fire-mechanical mortality was not especially common one year post-fire, but occurred almost exclusively in large trees with previous fire scars. This is important, because large trees that established before the modern fire suppression era are irreplaceable anchors of ecosystem function (Lutz *et al.*, 2018b) and their numbers have declined over time (Lutz *et al.*, 2009a). The risk of fire-mechanical mortality was much greater in large clumps with large trees present, perhaps because of deeper organic matter accumulations.

Of delayed mortalities occurring 2-4 years post-fire, 35% had no indications of mortality agents other than fire damage and 59% of mortality factors in total were fire-related. Higher crown base heights shifted the balance of delayed mortality causes away from fire effects, as would be expected since fire effects should be more severe when crown bases are lower (more fuel laddering) and a lower TAO-level crown base height indicates more leaf area and thus more crowding in the lower canopy, increasing fine-scale stresses. An interesting result is that the amount of fire-related mortality was significantly higher in high-density local areas. This indicates that the ability of trees to recover from fire damage, even without subsequent stresses by beetles, rot, mechanical damage, or suppression, is density-dependent and specifically is impeded by high local density. High density local areas are competitive environments and fire damage reduces trees' abilities to compete, resulting in more first-order delayed mortality.

Associations between fine-scale structure and mortality agents mostly took the form of tradeoffs between mortality dominated by rot and mortality dominated by beetles. Structural factors that shifted the balance toward beetle kill were things that aided beetle flights, such as

higher crown bases and lower local density. The same conditions that aided successful beetle flights also may have contributed to a more difficult environment for rots to persist, since high crown bases and lower density reduce soil moisture by providing reduced shading, decreased soil organic matter, and less hydraulic redistribution (Pugnaire *et al.*, 2004; Domingo *et al.*, 2011; Prieto *et al.*, 2011).

Furniss *et al.* (in review) found that spatial correlation was essentially inescapable in fire-mortality models. Our results provide insight into several possible reasons for this. First, first-order delayed mortality was density-dependent, which, in spatially heterogeneous forests like those characteristic of the Sierra Nevada mixed-conifer zone, implies patchiness. Second, the most important non-fire mortality factors 2-4 years post-fire were rot and bark beetles, both of which are biologically inclined to spatial correlation, either through continuous mycelial patches or tree-switching host selection behavior (Bruhn *et al.*, 1996; Powell and Bentz, 2014). Together, fire effects, rot, and bark beetles account for over 96% of delayed mortalities. It is no surprise, then, that mortality should be spatially correlated at multiple scales. Indeed, fire is fundamentally a spatially structured process (Sugihara *et al.*, 2006).

4.4 Management implications and conclusions

The process of post-fire tree mortality is complex and depends on a variety of factors at many scales. Structural conditions that improve resistance against one type of mortality agent often have collateral effects of reducing resistance against another mortality agent. However, some trends emerge that can be generally applied when managing for fire resistant forests.

We found that neighborhood-scale conditions provide the template for fire severity upon which TAO-scale fire effects play out. This finding indicates that it is important for forest managers to spend at least an equal amount of effort considering meso-scale conditions such as

canopy openings >0.1 ha and spatial complexity as is spent considering residual tree sizes and spacing. Additionally, spatial patterns including tree clumps and openings were important determinants of both immediate and delayed fire mortality; incorporating explicit spatial pattern targets into restoration treatments is an important aspect of managing for fire.

This research confirms that reducing ladder fuels and leaf area/density, along with creating more open space, are effective ways to reduce both immediate and delayed fire mortality. However, these same actions do have some potential negative consequences. Specifically, higher crown bases and lower densities are favorable for bark beetles, especially so when all residual trees are in larger size classes that are viable host trees. Creating stand conditions that favor bark beetles could be problematic if populations were able to reach epidemic levels. Thus, it may improve overall stand resilience to retain a wide variety of trees, including small non-host trees, and arrange structures in space to break up tree-switching flight lines and induce long-distance dispersal (Powell and Bentz, 2014).

Our findings suggest that it may be advantageous to leave at least some large trees together in clumps of 10-30 TAOs, since these conditions both led to reduced crown damage. This recommendation also comes with a tradeoff, however, since the same condition is more susceptible to fire-mechanical mortality in the largest size classes. Thus it is advisable to retain large trees together in large clumps only when the trees do not have fire scars predisposing them to fire-mechanical failure.

Because we validated this model across a wide range of environmental and burn conditions, it should be applicable to much of the Sierra Nevada mixed-conifer zone. Fire mortality risk could be assessed over any area in this zone with lidar data under various hypothetical burn conditions. This would be a valuable tool for prioritizing restoration treatment areas. Evaluating

model results to identify specific structural risk factors could also be helpful as a way to identify conditions that should be focused on for silvicultural treatment.

One complication of this model is that the fire it was built on, the Rim fire, occurred in the midst of a several year long extreme drought (Lydersen *et al.*, 2014). The drought probably exacerbated the stresses caused by fire damage and may have resulted in somewhat higher mortality rates than would have been observed without a drought. However, the 2013-2015 drought was similarly hot and dry as projected future conditions for the 2050's (Cayan *et al.*, 2008). In this sense the post-fire climate conditions may actually be helpful, since the model inherently incorporates some of the effects of a more extreme future climate.

This study demonstrates the importance of large, spatially explicit, long-term forest plots (sensu Lutz *et al.*, 2018a). The measurements of pre-fire forest conditions, factors associated with mortality, and spatial patterns were key components enabling this study.

References

Agee, J.K., 1993. Fire ecology of Pacific Northwest forests. Island press.

Agee, J.K., Skinner, C.N., 2005. Basic principles of forest fuel reduction treatments. Forest Ecology and Management 211, 83-96.

Anderson-Teixeira, K.J., Davies, S.J., Bennett, A.C., Gonzalez-Akre, E.B., Muller-Landau, H.C., Joseph Wright, S., Abu Salim, K., Almeyda Zambrano, A.M., Alonso, A., Baltzer, J.L., 2015. CTFS-ForestGEO: a worldwide network monitoring forests in an era of global change. Global Change Biology 21, 528-549.

Battles, J.J., Robards, T., Das, A., Waring, K., Gilless, J.K., Biging, G., Schurr, F., 2008. Climate change impacts on forest growth and tree mortality: a data-driven modeling study in the mixed-conifer forest of the Sierra Nevada, California. Climatic change 87, 193-213.

Becker, K.M., Lutz, J.A., 2016. Can low-severity fire reverse compositional change in montane forests of the Sierra Nevada, California, USA? Ecosphere 7.

Belote, R.T., Larson, A.J., Dietz, M.S., 2015. Tree survival scales to community-level effects following mixed-severity fire in a mixed-conifer forest. Forest Ecology and Management 353, 221-231.

Blomdahl, E.M., Kolden, C.A., Meddens, A.J.H., Lutz, J.A., in review. The importance of small fire refugia in the central Sierra Nevada, California, USA. Forest Ecology and Management.

Boyden, S., Montgomery, R., Reich, P.B., Palik, B., 2012. Seeing the forest for the heterogeneous trees: stand-scale resource distributions emerge from tree-scale structure. Ecological Applications 22, 1578-1588.

Breece, C., Kolb, T., Dickson, B., McMillin, J., Clancy, K., 2008. Prescribed fire effects on bark beetle activity and tree mortality in southwestern ponderosa pine forests. Forest Ecology and Management 255, 119-128.

Bruhn, J.N., Mihail, J.D., Meyer, T.R., 1996. Using spatial and temporal patterns of Armillaria root disease to formulate management recommendations for Ontario's black spruce (Piceamariana) seed orchards. Canadian Journal of Forest Research 26, 298-305.

Cayan, D.R., Maurer, E.P., Dettinger, M.D., Tyree, M., Hayhoe, K., 2008. Climate change scenarios for the California region. Climatic change 87, 21-42.

Churchill, D.J., Carnwath, G.C., Larson, A.J., Jeronimo, S.M.A., 2017. Historical forest structure, composition, and spatial pattern in dry conifer forests of the western Blue Mountains, Oregon. General Technical Report PNW-GTR-956. USDA Forest Service Pacific Northwest Research Station, Portland, OR.

Churchill, D.J., Larson, A.J., Dahlgreen, M.C., Franklin, J.F., Hessburg, P.F., Lutz, J.A., 2013. Restoring forest resilience: from reference spatial patterns to silvicultural prescriptions and monitoring. Forest Ecology and Management 291, 442-457.

Collins, B.M., 2014. Fire weather and large fire potential in the northern Sierra Nevada. Agricultural and Forest Meteorology 189–190, 30-35.

Collins, B.M., Miller, J.D., Thode, A.E., Kelly, M., Van Wagtendonk, J.W., Stephens, S.L., 2009. Interactions among wildland fires in a long-established Sierra Nevada natural fire area. Ecosystems 12, 114-128.

Collins, B.M., Stephens, S.L., Moghaddas, J.J., Battles, J., 2010. Challenges and approaches in planning fuel treatments across fire-excluded forested landscapes. Journal of Forestry 108, 24-31.

2845 Das, A., Battles, J., van Mantgem, P.J., Stephenson, N.L., 2008. Spatial elements of mortality
2846 risk in old-growth forests. Ecology 89, 1744-1756.
2847 Domingo, F., Serrano-Ortiz, P., Were, A., Villagarcía, L., García, M., Ramírez, D., Kowalski,
2848 A., Moro, M., Rey, A., Oyonarte, C., 2011. Carbon and water exchange in semiarid
2849 ecosystems in SE Spain. Journal of Arid Environments 75, 1271-1281.
2850 Donovan, L.A., Ehleringer, J.R., 1991. Ecophysiological differences among juvenile and
2851 reproductive plants of several woody species. Oecologia 86, 594-597.
2852 Erdody, T.L., Moskal, L.M., 2010. Fusion of LiDAR and imagery for estimating forest canopy
2853 fuels. Remote Sensing of Environment 114, 725-737.
2854 Fettig, C.J., McKelvey, S.R., Cluck, D.R., Smith, S.L., Otrosina, W.J., 2010. Effects of
2855 prescribed fire and season of burn on direct and indirect levels of tree mortality in
2856 ponderosa and Jeffrey pine forests in California, USA. Forest Ecology and Management
2857 260, 207-218.
2858 Filip, G.M., Schmitt, C.L., Scott, D.W., Fitzgerald, S.A., 2007. Understanding and defining
2859 mortality in western conifer forests. Western Journal of Applied Forestry 22, 105-115.
2860 Flint, L.E., Flint, A.L., Thorne, J.H., Boynton, R., 2014. 2014 California BCM (Basin
2861 Characterization Model) Downscaled Climate and Hydrology - 30-year Summaries.
2862 California Climate Commons.
2863 Franklin, J.F., Fites-Kaufmann, J., 1996. Assessment of late-successional forests of the Sierra
2864 Nevada. In, Sierra Nevada ecosystem project, final report to Congress, pp. 627-662.
2865 Fulé, P.Z., Covington, W.W., 1998. Spatial patterns of Mexican pine-oak forests under different
2866 recent fire regimes. Plant Ecology 134, 197-209.

Furniss, T.J., Larson, A.J., Kane, V.R., Lutz, J.A., in review. Multi-scale validation of post-fire tree mortality models. International Journal of Wildland Fire.

Gelfand, A.E., Ghosh, S.K., 1998. Model choice: a minimum posterior predictive loss approach. Biometrika 85, 1-11.

Gelman, A., Carlin, J.B., Stern, H.S., Rubin, D.B., 2004. Bayesian data analysis. Texts in statistical science series. Chapman & Hall/CRC, Boca Raton, FL.

Gelman, A., Hwang, J., Vehtari, A., 2014. Understanding predictive information criteria for Bayesian models. Statistics and Computing 24, 997-1016.

Gelman, A., Rubin, D.B., 1992. Inference from iterative simulation using multiple sequences. Statistical Science, 457-472.

George, E.I., McCulloch, R.E., 1993. Variable selection via Gibbs sampling. Journal of the American Statistical Association 88, 881-889.

Gersonde, R.F., O'Hara, K.L., 2005. Comparative tree growth efficiency in Sierra Nevada mixed-conifer forests. Forest Ecology and Management 219, 95-108.

Gill, L., Taylor, A.H., 2009. Top-down and bottom-up controls on fire regimes along an elevational gradient on the east slope of the Sierra Nevada, California, USA. Fire Ecology 5, 57-75.

Graham, R.T., McCaffrey, S., Jain, T.B.t.e., 2004. Science Basis for Changing Forest Structure to Modify Wildfire Behavior and Severity. General Technical Report RMRS-GTR-120. USDA Forest Service Rocky Mountain Research Station. Fort Collins, CO.

Guarín, A., Taylor, A.H., 2005. Drought triggered tree mortality in mixed conifer forests in Yosemite National Park, California, USA. Forest Ecology and Management 218, 229-244.

Hessburg, P.F., Agee, J.K., Franklin, J.F., 2005. Dry forests and wildland fires of the inland Northwest USA: contrasting the landscape ecology of the pre-settlement and modern eras. Forest Ecology and Management 211, 117-139.

Hessburg, P.F., Churchill, D.J., Larson, A.J., Haugo, R.D., Miller, C., Spies, T.A., North, M.P., Povak, N.A., Belote, R.T., Singleton, P.H., Gaines, W.L., Keane, R.E., Aplet, G.H., Stephens, S.L., Morgan, P., Bisson, P.A., Rieman, B.E., Salter, R.B., Reeves, G.H., 2015. Restoring fire-prone Inland Pacific landscapes: seven core principles. Landscape Ecology 30, 1805-1835.

Hood, S., Bentz, B., 2007. Predicting postfire Douglas-fir beetle attacks and tree mortality in the northern Rocky Mountains. Canadian Journal of Forest Research 37, 1058-1069.

Hood, S.M., McHugh, C.W., Ryan, K.C., Reinhardt, E., Smith, S.L., 2007. Evaluation of a post-fire tree mortality model for western USA conifers. International Journal of Wildland Fire 16, 679-689.

Hood, S.M., Smith, S.L., Cluck, D.R., 2010. Predicting mortality for five California conifers following wildfire. Forest Ecology and Management 260, 750-762.

Jenkins, M.J., Runyon, J.B., Fettig, C.J., Page, W.G., Bentz, B.J., 2014. Interactions among the mountain pine beetle, fires, and fuels. Forest Science 60, 489-501.

Jeronimo, S.M.A., Kane, V.R., Churchill, D.J., McGaughey, R.J., Franklin, J.F., 2018. Applying lidar individual tree detection to management of structurally diverse forest landscapes. Journal of Forestry 116, 336-346.

Kalies, E.L., Kent, L.L.Y., 2016. Tamm Review: Are fuel treatments effective at achieving ecological and social objectives? A systematic review. Forest Ecology and Management 375, 84-95.

Kane, V.R., Cansler, C.A., Povak, N.A., Kane, J.T., McGaughey, R.J., Lutz, J.A., Churchill, D.J., North, M.P., 2015a. Mixed severity fire effects within the Rim fire: relative importance of local climate, fire weather, topography, and forest structure. Forest Ecology and Management 358, 62-79.

Kane, V.R., Lutz, J.A., Cansler, C.A., Povak, N.A., Churchill, D.J., Smith, D.F., Kane, J.T., North, M.P., 2015b. Water balance and topography predict fire and forest structure patterns. Forest Ecology and Management 338, 1-13.

Kane, V.R., Lutz, J.A., Roberts, S.L., Smith, D.F., McGaughey, R.J., Povak, N.A., Brooks, M.L., 2013. Landscape-scale effects of fire severity on mixed-conifer and red fir forest structure in Yosemite National Park. Forest Ecology and Management 287, 17-31.

Kane, V.R., McGaughey, R.J., Bakker, J.D., Gersonde, R.F., Lutz, J.A., Franklin, J.F., 2010. Comparisons between field- and LiDAR-based measures of stand structural complexity. Canadian Journal of Forest Research 40, 761-773.

Kane, V.R., North, M.P., Lutz, J.A., Churchill, D.J., Roberts, S.L., Smith, D.F., McGaughey, R.J., Kane, J.T., Brooks, M.L., 2014. Assessing fire effects on forest spatial structure using a fusion of Landsat and airborne LiDAR data in Yosemite National Park. Remote Sensing of Environment 151, 89-101.

Kennedy, M.C., Johnson, M.C., 2014. Fuel treatment prescriptions alter spatial patterns of fire severity around the wildland–urban interface during the Wallow Fire, Arizona, USA. Forest Ecology and Management 318, 122-132.

Keyser, T.L., Smith, F.W., Lentile, L.B., Shepperd, W.D., 2006. Modeling postfire mortality of ponderosa pine following a mixed-severity wildfire in the Black Hills: the role of tree morphology and direct fire effects. Forest Science 52, 530-539.

Kolden, C.A., Lutz, J.A., Key, C.H., Kane, J.T., van Wagtendonk, J.W., 2012. Mapped versus actual burned area within wildfire perimeters: characterizing the unburned. Forest Ecology and Management 286, 38-47.

Kotliar, N.B., Wiens, J.A., 1990. Multiple scales of patchiness and patch structure: a hierarchical framework for the study of heterogeneity. Oikos, 253-260.

Larson, A.J., Churchill, D.J., 2012. Tree spatial patterns in fire-frequent forests of western North America, including mechanisms of pattern formation and implications for designing fuel reduction and restoration treatments. Forest Ecology and Management 267, 74-92.

Lusk, C.H., 2002. Leaf area accumulation helps juvenile evergreen trees tolerate shade in a temperate rainforest. Oecologia 132, 188-196.

Lutz, J., Larson, A., Swanson, M., 2018a. Advancing Fire Science with Large Forest Plots and a Long-Term Multidisciplinary Approach. Fire 1, 5.

Lutz, J., Van Wagtendonk, J., Franklin, J., 2009a. Twentieth-century decline of large-diameter trees in Yosemite National Park, California, USA. Forest Ecology and Management 257, 2296-2307.

Lutz, J.A., 2015. The evolution of long-term data for forestry: large temperate research plots in an era of global change. Northwest Science 89, 255-269.

Lutz, J.A., Furniss, T.J., Germain, S.J., Becker, K.M., Blomdahl, E.M., Jeronimo, S., Cansler, C.A., Freund, J.A., Swanson, M.E., Larson, A.J., 2017. Shrub communities, spa-tial patterns, and shrub-mediated tree mortality following reintroduced fire in Yosemite National Park, California, USA. Fire Ecology 13, 104-126.

Lutz, J.A., Furniss, T.J., Johnson, D.J., Davies, S.J., Allen, D., Alonso, A., Anderson-Teixeira, K.J., Andrade, A., Baltzer, J., Becker, K.M.L., Blomdahl, E.M., Bourg, N.A.,

Bunyavejchewin, S., Burslem, D.F.R.P., Cansler, C.A., Cao, K., Cao, M., Cárdenas, D., Chang, L.W., Chao, K.J., Chao, W.C., Chiang, J.M., Chu, C., Chuyong, G.B., Clay, K., Condit, R., Cordell, S., Dattaraja, H.S., Duque, A., Ewango, C.E.N., Fischer, G.A., Fletcher, C., Freund, J.A., Giardina, C., Germain, S.J., Gilbert, G.S., Hao, Z., Hart, T., Hau, B.C.H., He, F., Hector, A., Howe, R.W., Hsieh, C.F., Hu, Y.H., Hubbell, S.P., Inman-Narahari, F.M., Itoh, A., Janík, D., Kassim, A.R., Kenfack, D., Korte, L., Král, K., Larson, A.J., Li, Y., Lin, Y., Liu, S., Lum, S., Ma, K., Makana, J.R., Malhi, Y., McMahon, S.M., McShea, W.J., Memiaghe, H.R., Mi, X., Morecroft, M., Musili, P.M., Myers, J.A., Novotny, V., de Oliveira, A., Ong, P., Orwig, D.A., Ostertag, R., Parker, G.G., Patankar, R., Phillips, R.P., Reynolds, G., Sack, L., Song, G.Z.M., Su, S.H., Sukumar, R., Sun, I.F., Suresh, H.S., Swanson, M.E., Tan, S., Thomas, D.W., Thompson, J., Uriarte, M., Valencia, R., Vicentini, A., Vrška, T., Wang, X., Weiblen, G.D., Wolf, A., Wu, S.H., Xu, H., Yamakura, T., Yap, S., Zimmerman, J.K., 2018b. Global importance of large-diameter trees. Global Ecology and Biogeography 27, 849-864.

Lutz, J.A., Larson, A.J., Swanson, M.E., Freund, J.A., 2012. Ecological importance of large-diameter trees in a temperate mixed-conifer forest. PLoS One 7, e36131.

Lutz, J.A., van Wagtendonk, J.W., Franklin, J.F., 2010. Climatic water deficit, tree species ranges, and climate change in Yosemite National Park. Journal of Biogeography 37, 936-950.

Lutz, J.A., Van Wagtendonk, J.W., Thode, A.E., Miller, J.D., Franklin, J.F., 2009b. Climate, lightning ignitions, and fire severity in Yosemite National Park, California, USA. International Journal of Wildland Fire 18, 765-774.

Lydersen, J.M., Collins, B.M., Brooks, M.L., Matchett, J.R., Shive, K.L., Povak, N.A., Kane, V.R., Smith, D.F., 2017. Evidence of fuels management and fire weather influencing fire severity in an extreme fire event. Ecological Applications.

Lydersen, J.M., North, M.P., Collins, B.M., 2014. Severity of an uncharacteristically large wildfire, the Rim Fire, in forests with relatively restored frequent fire regimes. Forest Ecology and Management 328, 326-334.

Martínez-Vilalta, J., Piñol, J., 2002. Drought-induced mortality and hydraulic architecture in pine populations of the NE Iberian Peninsula. Forest Ecology and Management 161, 247-256.

McGaughey, R.J., 2018. FUSION/LDV: Software for LIDAR Data Analysis and Visualization: Version 3.70. USDA Forest Service Pacific Northwest Research Station, Seattle, WA.

Meddens, A.J., Kolden, C.A., Lutz, J., Smith, A.M., Cansler, C.A., Abatzoglou, J., Meigs, G.W., Downing, W., Krawchuck, M., in press. Fire refugia: What are they and why do they matter for global change? BioScience.

Miller, C., Urban, D.L., 1999. A model of surface fire, climate and forest pattern in the Sierra Nevada, California. Ecological Modelling 114, 113-135.

Miller, J.D., Safford, H., Crimmins, M., Thode, A., 2009. Quantitative evidence for increasing forest fire severity in the Sierra Nevada and southern Cascade Mountains, California and Nevada, USA. Ecosystems 12, 16-32.

Miller, J.D., Safford, H.D., Welch, K.R., 2016. Using one year post-fire fire severity assessments to estimate longer-term effects of fire in conifer forests of northern and eastern California, USA. Forest Ecology and Management 382, 168-183.

North, M., Stine, P., O'Hara, K., Zielinski, W., Stephens, S., 2009. An ecosystem management strategy for Sierran mixed-conifer forests, General Technical Report PSW-GTR-220. USDA Forest Service Pacific Southwest Research Station. Albany, CA.

Palik, B.J., Goebel, P.C., Kirkman, L.K., West, L., 2000. Using landscape hierarchies to guide restoration of disturbed ecosystems. Ecological Applications 10, 189-202.

Parks, S.A., Holsinger, L.M., Miller, C., Nelson, C.R., 2015. Wildland fire as a self-regulating mechanism: the role of previous burns and weather in limiting fire progression. Ecological Applications 25, 1478-1492.

Parsons, R.A., Pimont, F., Wells, L., Cohn, G., Jolly, W.M., de Coligny, F., Rigolot, E., Dupuy, J.-L., Mell, W., Linn, R.R., 2018. Modeling thinning effects on fire behavior with STANDFIRE. Annals of Forest Science 75, 7.

Powell, J.A., Bentz, B.J., 2014. Phenology and density-dependent dispersal predict patterns of mountain pine beetle (Dendroctonus ponderosae) impact. Ecological Modelling 273, 173-185.

Prichard, S.J., Kennedy, M.C., 2012. Fuel treatment effects on tree mortality following wildfire in dry mixed conifer forests, Washington State, USA. International Journal of Wildland Fire 21, 1004-1013.

Prieto, I., Padilla, F.M., Armas, C., Pugnaire, F.I., 2011. The role of hydraulic lift on seedling establishment under a nurse plant species in a semi-arid environment. Perspectives in Plant Ecology, Evolution and Systematics 13, 181-187.

Pugnaire, F.I., Armas, C., Valladares, F., 2004. Soil as a mediator in plant-plant interactions in a semi-arid community. Journal of Vegetation Science 15, 85-92.

R Core Team, 2016. R: A language and environment for statistical computing. R Foundation for Statistical Computing, Vienna, Austria.

Richardson, J.J., Moskal, L.M., Kim, S.-H., 2009. Modeling approaches to estimate effective leaf area index from aerial discrete-return LIDAR. Agricultural and Forest Meteorology 149, 1152-1160.

Ryan, K.C., Peterson, D.L., Reinhardt, E.D., 1988. Modeling long-term fire-caused mortality of Douglas-fir. Forest Science 34, 190-199.

Ryan, K.C., Reinhardt, E.D., 1988. Predicting postfire mortality of seven western conifers. Canadian Journal of Forest Research 18, 1291-1297.

Salomón, R.L., Tarroux, E., DesRochers, A., 2016. Natural root grafting in Picea mariana to cope with spruce budworm outbreaks. Canadian Journal of Forest Research 46, 1059-1066.

Simard, S.W., 2009. The foundational role of mycorrhizal networks in self-organization of interior Douglas-fir forests. Forest Ecology and Management 258, S95-S107.

Smith, A.M.S., Sparks, A.M., Kolden, C.A., Abatzoglou, J.T., Talhelm, A.F., Johnson, D.M., Boschetti, L., Lutz, J.A., Apostol, K.G., Yedinak, K.M., Tinkham, W.T., Kremens, R.J., 2016. Towards a new paradigm in fire severity research using dose–response experiments. International Journal of Wildland Fire 25, 158-166.

Stephens, S., Fry, D., 2005. Spatial distribution of regeneration patches in an old-growth Pinus jeffreyi-mixed conifer forest in northwestern Mexico. Journal of Vegetation Science 16, 693-702.

Stephens, S.L., 1998. Evaluation of the effects of silvicultural and fuels treatments on potential fire behaviour in Sierra Nevada mixed-conifer forests. Forest Ecology and Management 105, 21-35.

Stephens, S.L., Collins, B.M., Roller, G., 2012. Fuel treatment longevity in a Sierra Nevada mixed conifer forest. Forest Ecology and Management 285, 204-212.

Stevens, J.T., Collins, B.M., Miller, J.D., North, M.P., Stephens, S.L., 2017. Changing spatial patterns of stand-replacing fire in California conifer forests. Forest Ecology and Management 406, 28-36.

Sugihara, N.G., Van Wagtendonk, J.W., Fites-Kaufman, J., 2006. Fire as and Ecological Process. In: Sugihara, N.G., Van Wagtendonk, J.W., Fites-Kaufman, J., Shaffer, K.E., Thode, A.E. (Eds.), Fire in California's Ecosystems. University of California Press, Berkeley, California, p. 596.

Tang, J., Qi, Y., Xu, M., Misson, L., Goldstein, A.H., 2005. Forest thinning and soil respiration in a ponderosa pine plantation in the Sierra Nevada. Tree Physiology 25, 57-66.

USDA, 2008. Environmental Assessment: Glaze Forest Restoration Project. USDA Forest Service, Deschutes National Forest, Sisters Ranger District, Deschutes County, Oregon.

USDA, 2013. Red Knight Restoration Project: Environmental Assessment. USDA Forest Service, Fremont-Winema National Forest, Chemult Ranger District, Klamath County, Oregon.

USDA, 2016. FireFamilyPlus. URL: https://www.firelab.org/document/firefamilyplus-software. Accessed 1/12/2017.

Van de Water, K., North, M., 2011. Stand structure, fuel loads, and fire behavior in riparian and upland forests, Sierra Nevada Mountains, USA; a comparison of current and reconstructed conditions. Forest Ecology and Management 262, 215-228.

Van Mantgem, P.J., Stephenson, N.L., Knapp, E., Battles, J., Keeley, J.E., 2011. Long-term effects of prescribed fire on mixed conifer forest structure in the Sierra Nevada, California. Forest Ecology and Management 261, 989-994.

van Wagtendonk, J.W., Moore, P.E., 2010. Fuel deposition rates of montane and subalpine conifers in the central Sierra Nevada, California, USA. Forest Ecology and Management 259, 2122-2132.

Warren, J.M., Brooks, J.R., Meinzer, F.C., Eberhart, J.L., 2008. Hydraulic redistribution of water from Pinus ponderosa trees to seedlings: evidence for an ectomycorrhizal pathway. New Phytologist 178, 382-394.

Weiss, A., 2001. Topographic position and landforms analysis. Poster presentation, ESRI user conference, San Diego, CA.

Woolley, T., Shaw, D.C., Ganio, L.M., Fitzgerald, S., 2012. A review of logistic regression models used to predict post-fire tree mortality of western North American conifers. International Journal of Wildland Fire 21, 1-35.

Young, D.J., Stevens, J.T., Earles, J.M., Moore, J., Ellis, A., Jirka, A.L., Latimer, A.M., 2017. Long-term climate and competition explain forest mortality patterns under extreme drought. Ecology Letters 20, 78-86.

Youngblood, A., Grace, J.B., McIver, J.D., 2009. Delayed conifer mortality after fuel reduction treatments: interactive effects of fuel, fire intensity, and bark beetles. Ecological Applications 19, 321-337.

Appendix A: Complete model definitions for Chapter 3, Structural drivers of immediate and delayed fire mortality: modeling tree death in a landscape context

Submodel 1. TAO-level number of trees model

Symbol	Definition
i	Index for neighborhood
j	Index for TAO
$N_{T,ij}$	Observed number of trees in neighborhood i, TAO j
$\mu_{T,ij}$	Estimate for number of trees in neighborhood i, TAO j
$\beta_0^{N_T}$	Intercept for TAO-level number of trees model
$\boldsymbol{\beta}^{\boldsymbol{N_T}}$	Coefficient vector for TAO-level number of trees model
n_T	Number of TAO-level structure predictors
n_L	Number of local area-level structure predictors
$\boldsymbol{S_{ij}^T}$	Matrix of TAO-level structure predictors for neighborhood i, TAO j
$\boldsymbol{S_{ij}^L}$	Matrix of local area-level structure predictors for neighborhood i, TAO j

$$N_{T,ij} \sim \text{Poisson}\left(\mu_{T,ij}\right)$$

$$\log\left(\mu_{T,ij}\right) = \beta_0^{N_T} + \beta_{1\cdots n_T}^{N_T}\boldsymbol{S_{ij}^T} + \boldsymbol{\beta}_{(\boldsymbol{n_T}+\mathbf{1})\cdots \boldsymbol{n_L}}^{\boldsymbol{N_T}}\boldsymbol{S_{ij}^L}$$

Submodel 2. TAO-level mortality class model: non-hierarchical

Symbol	Definition
i	Index for neighborhood
j	Index for TAO
$M_{T,ij}$	Observed mortality class for TAO j in neighborhood i
$\boldsymbol{\pi_{ij}}$	Vector of estimates for proportions of trees in neighborhood i, TAO j in each of the mortality classes
$\boldsymbol{\varphi_{ij}}$	Unnormalized vector of estimates for relative amounts of trees in neighborhood i, TAO j in each of the mortality classes
$\beta_n^{DM_T}$	Coefficient vector for TAO-level mortality class model, immediate mortality class
$\beta_n^{IM_T}$	Coefficient vector for TAO-level mortality class model, delayed mortality class
n_T	Number of TAO-level structure predictors
n_L	Number of local area-level structure predictors
$\boldsymbol{S_{ij}^T}$	Matrix of TAO-level structure predictors for neighborhood i, TAO j
$\boldsymbol{S_{ij}^L}$	Matrix of local area-level structure predictors for neighborhood i, TAO j

$$M_{T,ij} \sim \text{Multinomial}\left(\boldsymbol{\pi_{ij}}, N_{T,ij}\right)$$

$$\boldsymbol{\pi_{ij}} = \frac{\boldsymbol{\varphi_{ij}}}{\sum_{k=1}^{3} \varphi_{ij,k}}$$

$$\varphi_{ij,1} = 1$$

$$\varphi_{ij,2} = \beta_{1\cdots n_T}^{DM_T} \boldsymbol{S_{ij}^T} + \boldsymbol{\beta}_{(\boldsymbol{n_T}+\boldsymbol{1})\cdots \boldsymbol{n_L}}^{\boldsymbol{DM_T}} \boldsymbol{S_{ij}^L}$$

$$\varphi_{ij,2} = \beta_{1\cdots n_T}^{IM_T} \boldsymbol{S_{ij}^T} + \boldsymbol{\beta}_{(\boldsymbol{n_T}+\boldsymbol{1})\cdots \boldsymbol{n_L}}^{\boldsymbol{IM_T}} \boldsymbol{S_{ij}^L}$$

Submodel 3. TAO-level mortality class model: hierarchical

Symbol	Definition
i	Index for neighborhood
j	Index for TAO
$M_{T,ij}$	Observed mortality class for TAO j in neighborhood i
$\boldsymbol{\pi_{ij}}$	Vector of estimates for proportions of trees in neighborhood i, TAO j in each of the mortality classes
$\boldsymbol{\varphi_{ij}}$	Unnormalized vector of estimates for relative amounts of trees in neighborhood i, TAO j in each of the mortality classes
$\beta_n^{DM_T}$	Coefficient vector for TAO-level mortality class model, immediate mortality class
$\beta_n^{IM_T}$	Coefficient vector for TAO-level mortality class model, delayed mortality class
n_T	Number of TAO-level structure predictors
n_L	Number of local area-level structure predictors
$\boldsymbol{S_{ij}^T}$	Matrix of TAO-level structure predictors for neighborhood i, TAO j
$\boldsymbol{S_{ij}^L}$	Matrix of local area-level structure predictors for neighborhood i, TAO j
M_{N_i}	Estimated number of mortalities for neighborhood i, from Submodel 6 or 7

$$M_{T.ij} \sim \text{Multinomial}\left(\boldsymbol{\pi_{ij}}, N_{T,ij}\right)$$

$$\boldsymbol{\pi_{ij}} = \frac{\boldsymbol{\varphi_{ij}}}{\sum_{k=1}^{3} \varphi_{ij,k}}$$

$$\varphi_{ij,1} = 1$$

$$\varphi_{ij,2} = M_{N_i}\left(\beta_{1\cdots n_T}^{DM_T}\boldsymbol{S_{ij}^T} + \boldsymbol{\beta}_{(\boldsymbol{n_T}+\boldsymbol{1})\cdots \boldsymbol{n_L}}^{\boldsymbol{DM_T}}\boldsymbol{S_{ij}^L}\right)$$

$$\varphi_{ij,2} = M_{N_i}\left(\beta_{1\cdots n_T}^{IM_T}\boldsymbol{S_{ij}^T} + \boldsymbol{\beta}_{(\boldsymbol{n_T}+\boldsymbol{1})\cdots \boldsymbol{n_L}}^{\boldsymbol{IM_T}}\boldsymbol{S_{ij}^L}\right)$$

Submodel 4. Neighborhood-level density model: without topoedaphic and burn weather

Symbol	Definition
i	Index for neighborhood
$N_{N,i}$	Observed density for neighborhood i
$\mu_{N,i}$	Estimate for number of trees in neighborhood i
$\beta_0^{N_N}$	Intercept for Neighborhood-level density model
$\beta_n^{N_N}$	Coefficient vector for Neighborhood-level density model
n_N	Number of neighborhood-level structure predictors
$\boldsymbol{S_i^N}$	Matrix of neighborhood-level structure predictors for neighborhood i

$$N_{N,i} \sim \text{Poisson}(\mu_{N,i})$$

$$\log(\mu_{N,i}) = \beta_0^{N_N} + \beta_{1\cdots n_N}^{N_N} \boldsymbol{S_i^N}$$

Submodel 5. Neighborhood-level density model: with topoedaphic and burn weather

Symbol	Definition
i	Index for neighborhood
$N_{N,i}$	Observed density for neighborhood i
$\mu_{N,i}$	Estimate for number of trees in neighborhood i
$\beta_0^{N_N}$	Intercept for neighborhood-level density model
$\beta_n^{N_N}$	Coefficient vector for neighborhood-level density model
n_N	Number of neighborhood-level structure predictors
n_T	Number of neighborhood-level topoedaphic and burn predictors
$\boldsymbol{S_i^N}$	Matrix of neighborhood-level structure predictors for neighborhood i
$\boldsymbol{T_i^N}$	Matrix of neighborhood-level topoedaphic and burn weather predictors for neighborhood i

$$N_{N,i} \sim \text{Poisson}(\mu_{N,i})$$

$$\log(\mu_{N,i}) = \beta_0^{N_N} + \beta_{1 \cdots n_N}^{N_N} \boldsymbol{S_i^N} + \beta_{(n_N+1) \cdots n_T}^{N_N} \boldsymbol{T_i^N}$$

Submodel 6. Neighborhood-level mortality model: without topoedaphic and burn weather

Symbol	Definition
i	Index for neighborhood
j	Index for TAO
$M_{N,i}$	Observed number of mortalities per ha for neighborhood i
$\mu_{N_M,i}$	Estimate for number of mortalities per ha in neighborhood i
$\beta_0^{M_N}$	Intercept for neighborhood-level mortality model
$\beta_n^{M_N}$	Coefficient vector for neighborhood-level mortality model
n_N	Number of neighborhood-level structure predictors
$\boldsymbol{S_i^N}$	Matrix of neighborhood-level structure predictors for neighborhood i

$$M_{N,i} \sim \text{Poisson}\left(\mu_{N_M,i}\right)$$

$$\log\left(\mu_{N_M,i}\right) = \beta_0^{M_N} + \beta_{1\cdots n_N}^{M_N} \boldsymbol{S_i^N}$$

Submodel 7. Neighborhood-level mortality model: with topoedaphic and burn weather

Symbol	Definition
i	Index for neighborhood
j	Index for TAO
$M_{N,i}$	Observed number of mortalities per ha for neighborhood i
$\mu_{N_M,i}$	Estimate for number of mortalities per ha in neighborhood i
$\beta_0^{M_N}$	Intercept for neighborhood-level mortality model
$\beta_n^{M_N}$	Coefficient vector for neighborhood-level mortality model
n_N	Number of neighborhood-level structure predictors
n_T	Number of neighborhood-level topoedaphic and burn predictors
$\boldsymbol{S_i^N}$	Matrix of neighborhood-level structure predictors for neighborhood i
$\boldsymbol{T_i^N}$	Matrix of neighborhood-level topoedaphic and burn weather predictors for neighborhood i

$$M_{N,i} \sim \text{Poisson}\left(\mu_{N_M,i}\right)$$

$$\log\left(\mu_{N_M,i}\right) = \beta_0^{M_N} + \beta_{1\cdots n_N}^{M_N} \boldsymbol{S_i^N} + \beta_{(n_N+1)\cdots n_T}^{M_N} \boldsymbol{T_i^N}$$

Common priors

All intercepts for all applicable models had the following vague prior:

$$\beta_0 \sim \text{Normal}(0, 10)$$

All coefficients for all models had priors of the following form:

$$\beta_n \sim \text{Normal}(0, \sigma c_\tau)$$

$$\tau \sim \text{Bernoulli}(4/n),$$

where σ is a tuning parameter, $\boldsymbol{c_{1...2}}$ is a vector of tuning parameters, and n is the number of coefficients. This set of priors targets selection of 4 coefficients for each Monte Carlo chain iteration.

σ is set to 4 for Submodels 1, 4, 5, 6, 7. For Submodels 2 and 3 σ is 0.005 for the delayed mortality model and 0.01 for the immediate mortality model.

c is set to 0.2 for Submodel 1, 0.12 for Submodels 4 and 5, and 0.19 for Submodels 6 and 7. For Submodels 2 and 3 c is set to 0.1.

Models

Model A = Submodels 1, 2, 4, and 6

Model B = Submodels 1, 2, 5, and 7

Model C = Submodels 1, 3, 4, and 6

Model D = Submodels 1, 3, 5, and 7

Mortality class error correction

To assess error in tree status calls we performed a blind validation exercise on the YFDP. We visited 32 of the 640 sub-quadrats across YFDP spanning a range of fire severities. We assigned each dead tree to one of the status classes used for the validation plots using the same qualitative classification criteria. This resulted in an error assessment sample of 327 trees over 1.28 ha. We used these data to build the following model.

Symbol	Definition
$\boldsymbol{y_i}$	Field-observed mortality class for tree i. Vector of length four; three zeroes with a single one indicating the observed class among: surviving, delayed mortality, immediate mortality, and dead pre-fire.
$\boldsymbol{h_i}$	Estimate for field-observation
$\boldsymbol{z_i}$	Actual mortality class vector, from annual census
$\boldsymbol{a}$	Coefficients for transition matrix between actual and observed quantities

$$\boldsymbol{y_i} \sim \text{Multinomial}(\boldsymbol{h_i}, 1)$$

$$\boldsymbol{h_i} = \boldsymbol{z_i} \times \boldsymbol{a}$$

$$\boldsymbol{a_{1\cdots4,1\cdots4}} \sim \text{Dirichlet}(1, 1, 1, 1)$$

We estimated a value for $\boldsymbol{a}$ using Bayesian analysis methods followed in the main study. We then used $\boldsymbol{a}$ as a correction factor on field-identified mortality classes on the validation plots. For example:

$$\hat{\boldsymbol{z}}_{\boldsymbol{i}} = \boldsymbol{a}\boldsymbol{y}_{\boldsymbol{i}}^{-\boldsymbol{1}},$$

where $\hat{\boldsymbol{z}}_{\boldsymbol{i}}$ is the corrected estimate of mortality class and $\boldsymbol{y_i}$ is a field observation of mortality class on a validation plot for tree i.